Turbulent flow of Generalised Newtonian fluids through pipes and open channels

Jagmohan Singh

Department of Mechanical and Aerospace Engineering

Monash University

This dissertation is submitted for the degree of
Doctor of Philosophy

April 2017

Copyright notice

Declaration

I hereby declare that this thesis contains no material which has been accepted for the award of any other degree or diploma at any university or equivalent institution and that, to the best of my knowledge and belief, this thesis contains no material previously published or written by another person, except where due reference is made in the text of the thesis.

This thesis includes one original paper published in a peer reviewed journal. The ideas, development and writing up of all the papers in the thesis were the principal responsibility of myself, the student, working within the department of mechanical and aerospace engineering under the supervision of Prof. Murray Rudman.

In the case of the publication in Chapter 4, the nature and extent of my contribution to the work was the following:

Thesis chapter	Publication title	Publication status	Nature and extent of student's contribution
4	The importance of rheology characterization in predicting turbulent flows of generalized Newtonian fluids	Published	Performing simulations, data analysis, writing and editing. 85%

I have not renumbered sections of the published paper.

Candidate's Signature: ██████████   Date: 27/04/2017

The undersigned hereby certify that the above declaration correctly reflects the n███████████████ nd co-authors contributions to this work.
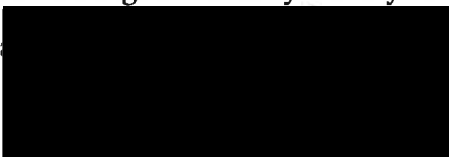
Main Supervisor's Signature: ██████   Date: 27/04/2017

Acknowledgements

This thesis would not have been possible without the inspiration and support of many wonderful individuals – my thanks and appreciation to all of them for making this thesis possible. I would like to thank Monash University and AMIRA international and the sponsors of the project AMIRA P1087 for their financial support over the course of my Ph.D.

I would like to express my warmest gratitude to my principal supervisor Prof. Murray Rudman. Without his enthusiasm, encouragement, support and continuous optimism this thesis would hardly have been completed. I have been extremely lucky to have a supervisor who cared so much about my work, and who responded to my questions and queries so promptly.

I would like to thank my associate supervisors; Prof. Hugh Blackburn and Dr. Andrew Chryss; for their continuous support. Hugh's guidance and immense knowledge helped me in all the time of research and writing journal articles. I would like to thank Andrew and Commonwealth Scientific and Industrial Research Organisation (CSIRO), Australia for letting me join experimental campaigns at Clayton and Highett facilities. I would like to thank Dr. Lionel Pullum and Dr. Lachlan Graham from CSIRO for explaining me the experiments in detail and patiently.

I would like to thank the Computational Mechanics Laboratory group for tolerating my presentations during weekly meetings. I would like to thank Mechanical Engineering Graduate association (MEGA) and Monash postgraduate association (MPA) for organising social and recreational activities throughout the year, which were antidote to stress from the research work. I am thankful to Bev Pearce, Jacelyn Tan and Nancy Hawe, Fiona Pyrczak and Stelios Konstantinidis from the departmental office for their continuous support during the candidature.

I would like to thank my friends Anchal Sareen, Shantanu Bhat, Meghna Kulkarni, Methma Rajamuni, Chandi sasmal, Shravan Kairy and Parthan Kasarapu

Abstract

Turbulent flow of non-Newtonian liquids has practical applications (e.g. polymer processing, mining and waste water treatment industries) but has received little attention. Much of the attention has gone to viscoelastic liquids which are attractive for engineering applications due to their drag reducing properties. In contrast, the turbulent flow of generalised Newtonian (GN) liquids has been little studied.

In this thesis, turbulent flows of GN liquids are studied for pipes and open channels using direct numerical simulations (DNS). High shear rate rheology data is found to be essential for reducing discrepancies between DNS and experiments observed in the past DNS studies. A criterion for the maximum shear rate required in rheology characterisation is proposed for getting good agreement between DNS and experiments. Shear thinning and yield stress are found to similarly affect a turbulent pipe flow, however, the effect of shear thinning is found to be greatest inside the viscous sublayer whereas yield stress affected flow the most outside the viscous sublayer. The effect of both shear thinning and yield stress is found to be confined in the inner layers.

The mean axial velocity profiles of power-law liquids are found to deviate from the Newtonian law of wall $U_z^+ = y^+$. This is due to a new mean shear stress, the turbulent viscous stress which arises in the mean momentum equation due to viscosity fluctuations. A new scaling is proposed to recover the law of wall but this new scaling can not determined *a priori* and is difficult to obtain in experiments. The turbulent pipe flow of both Newtonian and shear-thinning liquids are affected similarly by increasing Reynolds number.

For rectangular open channels of GN liquids, the flow rate is found independent of the channel aspect ratio for a fixed hydraulic radius. The effect of varying aspect ratio is found similar for both Newtonian and shear-thinning liquids. However, secondary flows which are known to occur in non-axisymmetric

ducts are found to penetrate more deeply into the flow for a shear-thinning fluid compared to Newtonian fluid. The scaling based on mean viscosity and mean axial velocity gradient at the wall is found to collapse the near wall mean axial velocity profiles for different aspect ratio for both Newtonian and shear-thinning liquids. Shear thinning is shown to decrease the turbulent friction factor (drag-reduction) in both pipes and open channels compared to Newtonian fluids for a fixed Reynolds number (Re_τ or Re_G). The signature of the drag reduction is also found in other data, as in the enhanced axial turbulence intensity, reduced Reynolds shear stress, radial and azimuthal turbulence intensities and reduces viscous dissipation of the turbulent kinetic energy.

The current work will give a direction to the development of Reynolds averaged Navier–Stokes simulations and large-eddy simulations for GN liquids. The results presented will also be helpful to practitioners for improving the existing methods for designing fluid systems for GN liquids.

Table of contents

List of figures

xviii

List of tables

Nomenclature

Roman Symbols

s shear rate tensor

$\mathcal{A}$ advection

$\mathcal{D}$ transport due to mean viscosity

$\mathcal{P}$ production

$\mathcal{T}$ transport due to Reynolds stress

Re_τ friction Reynolds number $= u^* R / \nu_w$

Re Newtonian Reynolds number

Re_G generalised Reynolds number $= U_b D / \nu_w$

u^* friction velocity $= (\tau_w / \rho)^{1/2}$

A cross-sectional area of the channel

AR aspect ratio of the channel

b channel width

D pipe diameter

D_h hydraulic diameter $= 2R_h$

f fanning friction factor

Fr Froude number $= U_b / (gh)^{1/2}$

g gravitational acceleration $= 9.81 \ \mathrm{m\,s^{-2}}$

h fluid depth in open channel

K mean flow kinetic energy

k turbulent kinetic energy

P_w wetted perimeter

q total kinetic energy

R pipe radius

r radial distance

R_h hydraulic radius = A/P_w

U mean axial velocity

u velocity

U_b superficial or bulk velocity

W work

x direction parallel to the channel bed

y direction nomal to the channel bed

y distance from the wall $(R - r)$

z axial direction

Greek Symbols

χ transport due to fluctuating viscosity and mean shear

$\dot{\gamma}$ second invariant of shear rate tensor

ϵ dissipation

ν fluid kinematic viscosity

Π turbulent transport due to pressure fluctuations

ρ fluid density

Υ transport due to fluctuating viscosity and mean shear

Ξ	turbulent transport due to viscosity fluctuations
τ	shear stress magnitude
τ	shear stress

Superscripts

$+$	wall unit
k	turbulent flow quantity
m	mean flow quantity

Subscripts

$'$	root mean square quantity
θ	azimuthal component
dp/dz	pressure gradient dependent quantity
nn	non-Newtonian quantity
r	radial component
t	time rate
w	wall quantity
x	component parallel to the channel bed
y	component normal to the channel bed
z	axial component

1

Introduction

Tailings disposal in the mining industries is at a crossroads. Tailings from mining operations, which are fine particles suspensions in water with potentially harmful chemicals used in the process, are typically stored in large dams at low volume concentrations. Events such as high rainfall, earthquake can turn a tailings storage facility into an environmental disaster. Even today when significant advances have been made in technology, two to three major incidents every year related to tailings storage facilities are very common [82]. In 2015 itself, more than hundred people were killed by just two of such incidents. The loss of wealth caused by such incidents is huge and the environmental impact is devastating.

Alternate disposal methods are being explored to make tailings management safer and to reduce their environmental impact. One such alternate method is paste and thickened tailings (P & TT) disposal in which tailings are dewatered significantly before sending to a tailings storage facility where it further dries and becomes less susceptible to flow. Other than being environmental safe, P & TT also improves the water efficiency of the operations because the water recovered from de-watering can be reused in other parts of the process.

Although, P & TT is attractive alternative to the current tailings disposal method, there are still many uncertainties involved in its use in practice. Most

of the uncertainties arise due to the change in the rheological nature of tailings due to dewatering. De-watered tailings (also called thickened tailings) show non-Newtonian behaviour i.e. they do not show a uniform viscosity. For these liquids, hydraulic design methods are not well developed and often design practices for Newtonian liquids are followed which are not accurate for tailings.

Tailings (slurries) can be homogeneous, settling or mixed depending on the particle size of solids and their settling behaviour (see table 1.1). The simplest of them are homogeneous tailings which can be treated as single phase liquids [102]. These are characterised by solid particles much smaller than the flow length scales and a carrier fluid velocity significantly higher than the particle settling velocity. Homogeneous tailings often show generalised Newtonian (GN) behaviour for which shear stress tensor $\boldsymbol{\tau}$ can be modelled as:

$$\boldsymbol{\tau} = \rho\nu(\dot{\gamma})\boldsymbol{s}. \tag{1.1}$$

Here $\dot{\gamma}$ is the second invariant of the shear rate tensor $\boldsymbol{s} = (1/2)(\boldsymbol{\nabla v} + \boldsymbol{\nabla v}^T)$, $\boldsymbol{v}$ is the velocity vector and ν is fluid's effective kinematic viscosity, $\tau/\rho\dot{\gamma}$. Equation 1.1 assumes an instantaneous response of the fluid to an applied shear stress. Viscosity in Eq 1.1 is modelled via a rheology model, the parameters of which are usually determined from the experimentally measured shear stress versus shear rate curve (rheogram) via regression. Model parameters determined via such regressions have no intrinsic physical meaning, but nevertheless are very useful in predicting flow behaviour and are extensively used. Other than thickened tailings, other liquids in biological and industrial applications such as blood, tomato ketchup, mayonnaise cheese, paint and waste water sludge can also be modelled via the GN assumption. GN liquids can be shear-thinning or shear-thickening depending on whether the fluid's effective viscosity decreases or increases with increasing shear rate. Most GN liquids show shear-thinning behaviour.

Pipelines and open channels are common methods of transporting GN liquids at industrial sites. Although laminar flows are more commonly observed in pipes of small diameters, the flow can be turbulent in pipes of large diameters or

Table 1.1 Classification of mining tailings or slurries [104]

Category	Description
Homogeneous slurries	Also referred as "slow settling slurries", characterised by fine solid particles kept in suspension by carrier fluid (normally water). These particles may settle partially when there is no flow.
Settling slurries	Also called rapid settling slurries, characterised by relatively larger solid particles.
Mixed slurries	These slurries are the mixture of homogeneous and settling slurries.

in open channels. Since Osborne Reynolds demonstrated transition to turbulence in 1893 and Prandtl proposed the boundary layer theory in 1904, significant advances have been made towards understanding turbulent flows of Newtonian liquids, however, the turbulent flow of GN liquids has received scant attention.

GN liquids are usually opaque which makes experimental investigation of their flow using optical measurements techniques such as particle image velocimetry (PIV) almost impossible. There have been a few experimental studies [12, 35, 86] but they reported only the pressure drop versus flow rate data. In other studies [76] where higher order turbulent statistics were measured, it is not clear whether the liquids were really GN liquids or if they also showed some other non-Newtonian effects such as viscoelasticity.

Compared to experiments, numerical simulations are more promising for studying the flow of GN liquids. This is because the fluid opacity does not affect numerical simulations and vicoelastic effects are avoided easily. Additionally, it is possible to disentangle the effect of rheology model parameters which is not possible in experiments because the rheology model parameters are usually intercorrelated. Despite numerical simulations being used extensively for studying turbulence in Newtonian liquids, studies of GN liquids are rare. Reynolds-averaged-Navier–Stokes (RANS) and large-eddy simulations (LES) capture only large scales of flow motion and use some special models (e.g turbulence or sub-grid stress models) for modelling the effect of smaller turbulent length scales. Although attempts have been made to develop turbulence or subgrid

models for GN liquids [30, 42, 73, 75] there are no universally accepted models yet available.

Direct numerical simulations (DNS) is another numerical technique widely used for Newtonian liquids. Once validated, it can be used reliably to provide a detailed picture of turbulence in the flow that is almost impossible to obtain in experiments. For GN liquids, it has an advantage over RANS and LES that it does not require any special model and captures finest time and spatial length scales in the flow. If used carefully, DNS shows excellent convergence properties and accuracy which is further increased with high-order methods such as spectral-element methods for discretisation. A downside of DNS is that it becomes computationally very demanding with increasing Reynolds number. DNS has been used for GN liquids [40, 83–85], but significant discrepancies were observed compared to experiments for even first-order statistics [83] the reason for which is yet to be confirmed.

This thesis is a step forward towards understanding turbulence in the flow of GN liquids. The effect of GN rheology is studied for pipes and rectangular open channel flows using DNS. It is shown that high shear rate data is essential in rheology characterisation to get a good agreement between DNS of GN liquids and experiments. The statistics of mean flow and turbulent kinetic energy budgets is presented for GN liquids for the first time which shows that the effect of GN rheology are significant only near the wall. For open channel flows, the effect of GN rheology is found similar to that seen in pipe flows.

2

Literature review

Study of non-Newtonian liquids goes back to 1916 when Bingham [10] investigated plasticity in flows through capillaries and proposed the Bingham rheology model for clay suspensions. Since then many rheology models have been proposed which present the rheology of a wide range of generalised Newtonian (GN) liquids [50]. The first experimental study of GN liquids is by Brautlecht and Sethi [15] in 1933 who studied the power required to pump paper pulps through a pipeline. Since then quite a few studies have been conducted for GN liquids. In this chapter, the studies of GN liquids through pipes and open channels are reviewed and the laminar flow is discussed only in brief. Only the studies of liquids relevant to this PhD study i.e. Herschel–Bulkley (HB) and its subsets – Bingham and power-law (PL) liquids are reviewed. The chapter is divided into three sections. First the constitutive equation of the Herschel–Bulkley model is presented and then the studies of pipe and open channel flows are reviewed in subsequent sections.

2.1   Herschel–Bulkley rheology model

The Herschel–Bulkley rheology model is a widely used rheology model for GN liquids. It represents the rheology of liquids such as mining and waste water

slurries quite well [31, 50, 55, 89]. The Herschel–Bulkley model defines the fluid's effective kinematic viscosity as:

$$\nu = \rho^{-1}(\tau_y/\dot\gamma + K\dot\gamma^{n-1}) \tag{2.1}$$

Here, ρ is the density, $\dot\gamma$ is shear rate – the second invariant of the strain rate tensor $\boldsymbol{s} = [\boldsymbol{\nabla v} + \boldsymbol{\nabla v}^T]/2$ and $\boldsymbol{v}$ is the velocity. In Eq. 2.1, τ_y, K and n are model parameters known as yield stress, consistency and flow index. For shear stress $\tau < \tau_y$, the fluid does not shear, and there is deformation only for $\tau > \tau_y$. The Herschel–Bulkley rheology model represents shear-thinning behaviour for $n < 1$ i.e. the fluid viscosity decreases with increasing shear rate and for $n > 1$ the opposite, shear-thickening behaviour is observed. Other widely used rheology models are the power-law rheology model and the Bingham rheology models. The Herschel–Bulkley rheology model reduces to a power-law rheology model, $\nu = \rho^{-1}(K\dot\gamma^{n-1})$, when $\tau_y = 0$ and to the Bingham rheology model, $\nu = \rho^{-1}(\tau_y/\dot\gamma + K)$, when $n = 1.0$.

Although the Herschel–Bulkley, power-law and Bingham rheology models are widely used, they have two common limitations. They show an infinite viscosity for shear rate $\dot\gamma \to 0$ and a zero viscosity for $\dot\gamma \to \infty$ neither of which is physically possible. However, in industrially relevant turbulent flows only a limited range of shear rate is covered and therefore, these rheology models can be used reliably for such applications provided they accurately represent viscosity over the range of relevant shear rates.

In the following sections and chapters, a term 'Herschel–Bulkley (HB) fluid' is used for a fluid whose rheology is modelled by the Herschel–Bulkley rheology model. Similarly, the terms 'power-law (PL) fluid' and 'Bingham fluid' are used for liquids whose rheology is modelled by the power-law and Bingham rheology models.

2.2 Pipe flow

2.2.1 Laminar flow

For a steady, incompressible, fully developed laminar pipe flow (radius R, diameter $D = 2R$), the shear stress τ_{rz} (see Figure 2.1) at a distance r from the pipe centre is given by

$$\tau_{rz} = (r/2)(-dp/dz) \tag{2.2}$$

where, dp/dz is the pressure gradient driving the flow. For a fixed dp/dz, an expression for the nominal wall shear stress τ_w is obtained by substituting $r = R$ in Eq. 2.2 giving

$$\tau_w = (R/2)(-dp/dz). \tag{2.3}$$

For a given rheology model, τ_{rz} in Eq. 2.2 can be expressed in terms of the axial
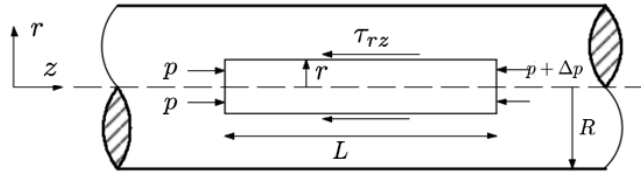
Fig. 2.1 Force balance for a pipe flow in the streamwise direction

velocity gradient $\partial u_z / \partial y$. An expression for the axial velocity u_z is obtained by integrating Eq. 2.2 with the no-slip boundary condition, $u_z = 0$, at the wall and zero gradient boundary condition, $\partial u_z / \partial r = 0$ at the centre. For a HB fluid, this gives [91]

$$u_z = \frac{2}{(dp/dz)(1 + 1/n)K^{1/n}} \left[(\tau_w - \tau_y)^{1+1/n} - \left(\frac{r}{2} \frac{dp}{dz} - \tau_y \right)^{1+1/n} \right]. \tag{2.4}$$

The above equation is valid only for the region where $\tau \geq \tau_y$. The area weighted average of Eq. 2.4 gives an expression for the bulk velocity (flow rate per unit area) as:

$$U_b = nR \left(\frac{\tau_w}{K} \right)^{1/n} (1 - \phi)^{n+1/n} \left\{ \frac{(1-\phi)^2}{3n+1} + \frac{2\phi(1-\phi)}{2n+1} + \frac{\phi^2}{n+1} \right\} \tag{2.5}$$

7

where $\phi = \tau_y/\tau_w$. Equivalent expressions for u_z and U_b for PL and Bingham liquids can be obtained from Eq. 2.4 and 2.5 by substituting $\phi = 0$ for a PL fluid and $n = 1.0$ for a Bingham fluid. For these liquids, the normalised axial velocity (u_z/U_b) profiles are plotted in figure 2.2 where flattening of the velocity profiles with both shear thinning (decreasing n) and increasing the yield stress τ_y can be seen. In contrast, shear thickening results in fuller and sharper velocity profiles near the pipe centre compared to Newtonian fluid. Since Bingham and HB liquids deform only for $\tau > \tau_y$ and τ_{rz} decreases with the distance from the wall $y = R - r$, there exists a plug region near the pipe centre where the fluid does not deform and moves like a solid. The radius of this plug region can be found by substituting $\tau_{rz} = \tau_y$ in Eq. 2.2.
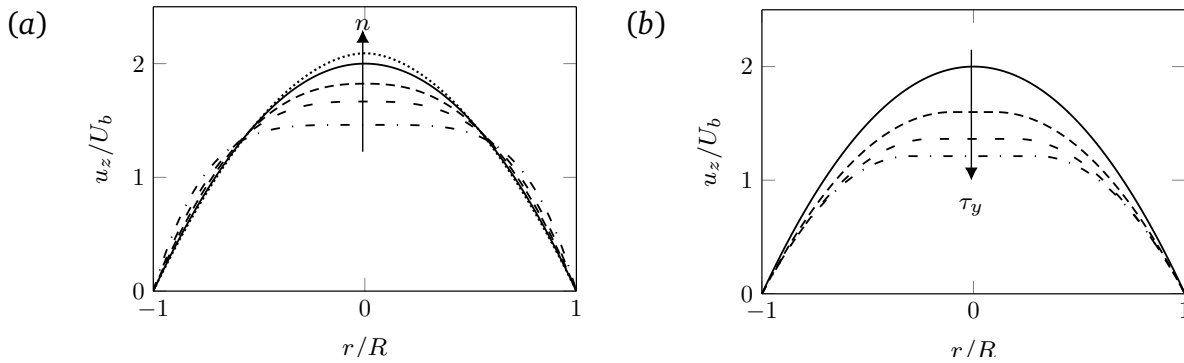
Fig. 2.2 Laminar velocity profiles for (*a*) power-law and (*b*) Bingham liquids. Consistency K is fixed for all liquids.

PL liquids deform for all shear rates and therefore, do not show a plug region. However, for low shear stresses such as those expected near the pipe centre, PL liquids similar to HB liquids with $\tau_y \neq 0$ show very high viscosity which leads to very low shear rates there. Therefore, despite lack of a plug region PL liquids show nearly uniform velocity close to the pipe centre. Similar to increasing τ_y in a Bingham fluid, the region of this uniform velocity region increases with shear thinning. Overall, shear thinning in PL liquids and increasing yield stress in Bingham liquids similarly affect a laminar pipe flow.

2.2.2 Reynolds number for GN liquids

The non-uniform viscosity of GN liquids makes the choice of an appropriate viscosity scale unclear. Metzner & Reed [70] proposed a Reynolds number definition (widely referred to as Metzner–Reed Reynolds number) for PL liquids by collapsing their laminar friction factor curves on the Newtonian curve $f = 16/Re$ where

$$f = 2\tau_w/\rho U_b^2 \tag{2.6}$$

The Metzner–Reed Reynolds number is defined as:

$$Re_{\text{MR}} = \frac{8\rho U_b^{2-n} D^n}{K(6 + 2/n)^n} \tag{2.7}$$

Metzner and Reed also proposed a generalised version of this definition for non-PL liquids by replacing n with n' and K with K' where

$$n' = \frac{d(\log(D\Delta P/4L))}{d(\log(8U_b/D))}, \quad K' = \frac{D\Delta P/4L}{(8U_b/D)^{n'}}. \tag{2.8}$$

Following the same procedure as used by Metzner & Reed [70] for PL liquids, Madlener et al. [66] proposed a similar Reynolds number definition for HB liquids as:

$$Re_{HB} = \frac{\rho U_b^{2-n} D^n}{(\tau_y/8)(D/U_b)^n + K((3m + 1)/(4m))^n 8^{n-1}} \tag{2.9}$$

where

$$m = \frac{nK(8U_b/D)^n}{\tau_y + K(8U_b/D)^n}. \tag{2.10}$$

As in Eq. 2.9, the Metzner–Reed Reynolds number definition becomes complex when extended to other rheologies , therefore this definition is primarily used for PL liquids. The use of this definition for turbulent flows is debated. Guzel et al. [45] argued that since the Metzner–Reed Reynolds number was derived from a laminar flow analysis, care must be taken when it is used for turbulent flows. Chilton and Stainsby [22] also presented similar arguments and suggested that

since in turbulent flow of GN liquids, the effective viscosity would be different from that in a laminar flow, the Re_{MR} definition was not physically realistic for turbulent flows. They proposed an alternate Reynolds number definition (see table 2.1) which arguably was more realistic for turbulent flows compared to Re_{MR} but was very complex and is therefore rarely used in the literature.

Another definition of the Reynolds number popularly used for GN liquids is based on the nominal wall viscosity $\nu_w = \nu(\dot{\gamma}_w)$ which can be obtained from the rheology model and the corresponding laminar flow velocity expression. For HB liquids, ν_w is given as:

$$\nu_w = \rho^{-1}K^{1/n}\tau_w/(\tau_w - \tau_y)^{1/n} \tag{2.11}$$

Using this nominal wall viscosity ν_w, the generalised Reynolds number is defined as:

$$Re_G = U_bD/\nu_w \tag{2.12}$$

Although Re_G is also obtained from the laminar flow analysis, it is widely used for turbulent flow of GN liquids [12, 83, 84] and also for other rheologies [33, 79, 80]. There are also many other Reynolds number definitions available for turbulent pipe flows of GN liquids, a few of which are mentioned in table 2.1 but none of them is universally accepted. For turbulent flow of Newtonian fluids it is common to use a Reynolds number definition based on the friction velocity $u^* = (\tau_w/\rho)^{1/2}$. A friction Reynolds number definition similar to the Newtonian definition is used in this thesis for GN liquids as:

$$Re_\tau = u^*R/\nu_w \tag{2.13}$$

and is called friction Reynolds number.

2.2.3 Turbulent flow

Turbulent flows are inherently unsteady and analytical solutions of the mean flow do not exist even for Newtonian liquids. Non-Newtonian viscosity in GN liquids further increases the complexities in the governing equations (discussed

10

Table 2.1 Different Reynolds number definitions for GN liquids. Here U_b is the bulk velocity, U_c is the centreline velocity and Re_{MR} is the Metzner–Reed Reynolds number (Eq. 2.7).

Proposed by	Reynolds number definition
Tomita [95]	$\left(\dfrac{3+9n}{4+8n}\right)Re_{MR}$
Clapp [26]	$\dfrac{8\rho U_b^2}{K(8U_b/D)^n}$
Chilton and Stainsby [22]	$\dfrac{U_b D}{\nu_w\left(\frac{3n'+1}{4n'}\right)}$
Guzel et al. [45]	$\dfrac{4\rho U_c^2}{R\lvert \partial p/\partial x\rvert}$
Slatter and Lazarus [90]	$\dfrac{8\rho U_b^2}{\tau_y + k(8U_b/D)^n}$

in chapter 3). Experiments or simulations are needed to study the flow of these liquids. In the following, first the experimental studies are reviewed followed by numerical studies.

Theoretical and experimental studies

Most experimental studies of GN liquids were focused on determining a turbulent friction factor correlation. An early study of this nature is by Metzner and Reed [70] which measured the friction factor for sixteen different GN liquids over a wide range of Reynolds number ($Re_{MR} = 10^{-3} - 10^5$). Correlations for laminar and turbulent friction factors ($f = 2\tau_w/\rho U_b^2$) were proposed in which the laminar friction factor was derived analytically whereas the turbulent friction factor was an empirical correlation. These were given as:

$$f = \begin{cases} \dfrac{16}{Re_{MR}} & \text{for Laminar flow} \\[2mm] 0.000140 + \dfrac{0.125}{(Re_{MR})^{0.32}} & \text{For turbulent flow.} \end{cases} \tag{2.14}$$

Experiments were conducted to test these correlations. Similar to Newtonian liquids, the transition to turbulence was assumed to occur when the friction factor f first dropped to 0.008. This gave a transition Reynolds number in the range $Re_{\mathrm{MR}} \in [2000, 2500]$ which is close to the Newtonian transition Reynolds number 2100. The predictions of Eq. 2.14 agreed with experiments to within 10% for laminar flows but for turbulent flows, data was scattered. Only for very high Re_{MR}, $Re_{\mathrm{MR}} \gtrsim 50\,000$, did the predictions of the correlation agree well with experiments.

Dodge and Metzner [35] proposed an empirical expression for the mean axial velocity which was later corrected by Skelland [88]. The correct expression reads

$$U_z^+ = \frac{5.657}{n^{0.75}} \log \hat{y} - \frac{0.566}{n^{1.2}} + \frac{3.475}{n^{0.75}} \left[1.96 + 0.816n - 1.628n \log \left(3 + \frac{1}{n} \right) \right] \quad (2.15)$$

where $\hat{y} = \left[(\rho^n \tau_w^{2-n})^{1/2} / K \right] y^n$ is the non-dimensional distance from the wall and U_z^+ is the mean axial velocity normalised by the friction velocity $u^* = (\tau_w/\rho)^{1/2}$. Eq. 2.15 was integrated and rearranged to give the following expression for the friction factor (referred to as the Dodge and Metzner correlation)

$$\frac{1}{\sqrt{f}} = \frac{4.0}{(n')^{0.75}} \log_{10}[Re_{MR}(f)^{1-n'/2}] - \frac{0.4}{(n')^{1.2}}. \quad (2.16)$$

with n' given by Eq. 2.8. Dodge and Metzner conducted experiments using a wide range of liquids including Carbopol and Carboxymethylcellulose (CMC) solutions for Re_{MR} upto $36\,000$ and found a good agreement between the predictions of Eq. 2.16 and the experimental results (within 2%) for Carbopol liquids. CMC solutions showed an abnormal capability to suppress the formation and propagation of turbulence which Dodge and Metzner suggested to be a result of viscoelasticity possessed by these liquids. A delay in transition to turbulence to a higher Re_{MR} and a decrease in the friction factor for a given Re_{MR} (drag reduction) with shear thinning were also reported.

Researchers continued exploring alternate and simpler turbulent friction factor correlations. Shaver and Merrill [86] proposed the following correlation

$$f = \frac{0.079}{n^5 Re^\gamma} \quad \text{where} \quad \gamma = \frac{2.63}{10.5^n}.$$ (2.17)

This correlation was determined empirically using the experimental turbulent flow data of CMC solutions with the rheology approximated by a PL rheology model. Shaver and Merrill confirmed the findings of Dodge and Metzner of drag reduction by shear thinning which was suggested to be due to a progressively decreasing frequency of vortex formation at the pipe wall. Less blunt velocity profiles were reported in the turbulent flow of shear-thinning liquids than Newtonian liquids. Unlike Newtonian liquids, profiles of the velocity defect $((u_{max} - u)/u^*)$ when plotted as a function of y did not collapse on a single curve and instead presented a series of curves that depended on the value of flow index n.

Clapp [26] used a three zone model similar to Newtonian liquids – laminar sublayer ($\hat{y} < 5^n$), Buffer layer ($5 < \hat{y} < y_2$), turbulent core ($\hat{y} > y_2$) where y_2 was determined from the mean axial velocity profiles measured experimentally. For these layers, the mean axial velocity correlations were proposed as:

$$U_z^+ = \begin{cases} (\hat{y})^{1/n} & \text{Laminar sublayer} \\ 5/n \ln \hat{y} - 3.05 & \text{buffer layer}. \\ 2.78/n \ln \hat{y} + 3.8/n & \text{turbulent core}. \end{cases}$$ (2.18)

For the turbulent core, the coefficients were derived empirically. By integrating the above velocity distributions, a turbulent friction factor correlation was proposed as:

$$1/\sqrt{f} = (4.53/n) \log[Re_{\text{MR}} f^{1-n/2}] + 2.69/n + 0.68(5n - 8/n)$$ (2.19)

Although Eq. 2.19 predicted f within 4% of the experimental values, the experimental database used for testing included only weakly shear-thinning liquids ($n = 0.69 - 0.81$). Therefore, Eq. 2.18 and 2.19 can give erroneous predictions for more shear-thinning liquids.

Bogue and Metzner [13] tested both the Dodge & Metzner and Shaver & Merrill correlations (Eq. 2.15 and 2.17) using experimental data from clay suspensions and Carbopol solutions. The prediction of the Dodge and Metzner correlation were found to agree better with experiments compared to that of Shaver & Merrill. Large deviations between the predictions of Shaver & Merrill correlation and the experiments was suggested to be a result of viscoelasticity of the liquids used in developing the correlation. By using the nominal wall viscosity ν_w for the viscosity scale, Bogue and Metzner proposed a Reynolds number definition Re_G (see Eq. 2.12) and the non-dimensional distance from the wall (Eq. 2.20)

$$y^+ = yu^*/\nu_w. \tag{2.20}$$

For PL liquids, y^+ can be shown to be related to the Dodge & Metzner scaling $\hat{y}$ via $y^+ = \hat{y}^{1/n}$. Bogue and Metzner reported that for turbulent flows at relatively low Reynolds number, the use of ν_w reduced the dependence of the friction factor correlation on the rheology model parameters. They suggested that at very high Reynolds number, ν_w might be enough to completely characterise the turbulent flow of GN liquids. Bogue and Metzner further observed that the turbulent mean axial velocity profiles when normalised by the bulk velocity were almost insensitive to the non-Newtonian character of the fluid but showed a remarkable difference when plotted in wall coordinates using the generalised U_z^+ and y^+. They suggested that this could be because the $U_z^+ - y^+$ relation implicitly used the friction factor–Reynolds number relationship. The change in friction factor with varying rheology model parameters such as flow index n in case of PL liquids, resulted in a significant variation in the $U_z^+ - y^+$ relationship which was reflected in the mean axial velocity profiles.

Alternate turbulent friction factor correlations were proposed by other researchers for PL liquids [26, 52, 58, 62, 87, 92, 95, 106] and for HB liquids [51, 96]. El-Emam et al. [37] summarised more than fourteen turbulent friction factor correlations for GN liquids. Garcia and Steffe [39] compared the available correlations and found that for PL liquids, the correlations proposed by Dodge and Metzner [35], Clapp [27] and Hanks and Ricks [52] agreed with each other.

Hartnett and Kostic [54] also found the Dodge & Metzner correlation agreeing the best with the available experimental measurements. For HB liquids, Garcia and Steffe found the analysis of Hanks [51] to be the most comprehensive. They also reported large errors in predicting the friction factor for a yield stress fluid using a correlation developed for PL liquids.

The studies mentioned above were focused on defining the turbulent friction factor as a function of a Reynolds number. Wilson and Thomas [103] argued that earlier studies did not consider the drag reduction arising from shear thinning. Instead they simply sought to define a reduced effective viscosity which would give a larger Reynolds number and hence produce a smaller friction factor. Wilson and Thomas suggested that turbulent drag reduction by shear thinning was associated with thickening of the viscous sublayer, such as proposed by Lumley [65] in the context of viscoelastic liquids. By considering the modification to the velocity profiles associated with thickening of the viscous sublayer, Wilson and Thomas proposed a new correlation (referred to as the Wilson–Thomas correlation) for predicting the bulk velocity U_b as:

$$\frac{U_b}{u^*} = \frac{V_N}{u^*} + 11.6(\alpha - 1) - 2.5\ln(\alpha) - \Omega \qquad (2.21)$$

where V_N is the bulk velocity for a Newtonian fluid with the same ν_w as the non-Newtonian fluid. In Eq. 2.21, α is the ratio of the area under the Newtonian and non-Newtonian rheogram evaluated for $\tau = \tau_w$ and Ω included any effect of possible blunting of velocity profile in the logarithmic or core region of the flow. Wilson and Thomas derived the following expression for Ω for HB liquids:

$$\Omega = -2.5\ln(1 - \xi) - 2.5\xi(1 + 0.5\xi), \quad \text{with} \quad \xi = \tau_y/\tau_w. \qquad (2.22)$$

Compared to the Dodge and Metzner correlation, the predictions of the Wilson–Thomas correlation were approximately 15% lower for shear-thinning liquids with the error decreasing as n approached to the Newtonian value ($n = 1$). It was argued by Wilson and Thomas that the experimental uncertainty in Dodge and Metzner [35] was of the similar order. They observed a similar agreement for

Bingham liquids between the predictions of the correlation and the experimental measurements.

Anbarlooei et al. [5] argued that although turbulent friction factor correlations such as Dodge & Metzner correlations were frequently used, these were empirically derived and lacked a solid physical basis. They proposed a Blasius-type turbulent friction factor correlation (Eq. 2.23) by adapting Kolmogorov's phenomenology to a power-law fluid.

$$f = \left(0.102 - 0.033n + \frac{0.01}{n}\right) \frac{1}{Re_{\mathrm{MR}}^{\frac{1}{2(n+1)}}} \qquad (2.23)$$

A large experimental data set (more than 80 points) was used to test this correlation, which showed a better agreement between experiments and the predictions of Eq. 2.23 than the Dodge and Metzner correlation.

As mentioned earlier, most of the experimental and theoretical studies aimed at deriving a turbulent friction factor correlation for GN fluid and did not report turbulent statistics such as the distribution of turbulent intensities and Reynolds shear stress. Park et al. [74] was the first study which reported the results of mean flow and turbulence intensities for shear-thinning HB liquids (Carbopol solutions with rheology approximated by the Herschel–Bulkley rheology model), however, their measurements were limited to only weakly turbulent flows ($Re_G \leq 3500$). Transition to turbulence occurs over a range of the Reynolds number. Park et al. observed a much narrower transition region for HB liquids compared to Newtonian liquids. The mean axial velocity profiles closely followed the Newtonian 1/7 power-law velocity profile. The axial turbulence intensity was higher but the tangential component was lower in more than 80% of the flow region for a HB fluid compared to a Newtonian fluid. The yield stress was found to have a negligible effect on the mean flow statistics. Similar findings were reported by Pinho and Whitelaw [76] for PL liquids (CMC solutions) for Re_G up to $111\,000$.

Turbulent flow predictions using the correlations discussed above rely on rheology characterisation which use a measured shear rheogram. Therefore, a

poor rheology characterisation can lead to significant errors in the predictions. A turbulent pipe flow covers a wide range of shear rates, however, typically only a limited range of shear rate is covered in rheology measurements [8]. Slatter [89] discussed the importance of shear rate range for pipe flow predictions of GN liquids and suggested that very low shear rate rheology measurements were unimportant for pipe flow engineering and therefore, could be ignored in rheology characterisation. Ignoring the very low shear rate data was also required to get a satisfactory fit of the rheological model with measurements in the medium and high shear rate range. The HB rheology model provided the best fit over the greatest range of shear rate for the liquids they considered (mineral slurries). Slatter showed that the predictions of turbulent flow correlations such as mentioned above were sensitive to the rheology characterisation of the fluid. The rheology model parameters determined from a laminar pipe flow curve (bulk velocity vs. pressure drop) were found to give errors as large as 50% compared to the experiments. Guzel et al. [45] also emphasised the importance of rheology measurements. They showed that using differing range of shear rates could give different rheology parameters suggesting that a poor rheology characterisation could lead to significant errors in theoretical or numerical analysis.

Summary

All of the studies summarised above discussed friction factor in turbulent flow of GN liquids. In all of these studies, the rheology characterisation considered either a laminar pipe flow curve or a shear rheogram which was measured for shear rates much lower than those relevant to turbulent flows. Studies such as Shaver and Merrill [86] and Pinho and Whitelaw [76] used CMC solutions which are known to show viscoelastic effects and therefore, were not simple GN liquids especially at the high shear rates relevant to turbulent flows. Turbulence intensities and Reynolds shear stress are important in understanding turbulent flows but unfortunately except Park et al. [74] and Pinho and Whitelaw [76], no other study reported these results. Only a little discussion is available on the effect of yield stress on turbulent behaviour in Park et al. [74] and Slatter [89].

Numerical studies

Although numerical investigations can give great insight to fluid flow, there are only a few published numerical studies of turbulent flow of GN liquids. Many of these were focused on developing a numerical technique for these liquids. Malin [67] modified the Newtonian Lam-Bremhorst $k - \epsilon$ turbulence model for Reynolds-averaged Navier–Stokes (RANS) simulations by introducing a viscous damping for GN liquids. He used the modified RANS to study the flow of PL liquids for Re_{MR} up to 1×10^5. The friction factor predictions were found in a good agreement with the Dodge & Metzner correlation (Eq. 2.16). For very high Re_{MR}, a good agreement was also observed between the predicted mean axial velocity and Eq. 2.15. The turbulent kinetic energy was found to increase with shear thinning for a given Re_{MR}. Later using the same turbulence model, Malin performed simulations for HB liquids [68] for Re_{MR} up to 1×10^5. For these simulations, the numerical predictions of the friction factor agreed with the Dodge & Metzner correlation only for very high Re_{MR} and low yield stress. The results reported in these studies were limited to the mean flow and the turbulent kinetic energy profiles. The statistics of viscosity, turbulent intensities and Reynolds shear stress were not reported.

Chilton and Stainsby [22] analysed different turbulent friction factor correlations and found the Wilson & Thomas correlation [103] the best available analytical correlation for HB liquids. They observed that due to poor rheometry, incorrect fitting, inappropriate use of rheological models or incomplete data sets, a large fraction of published data were of little worth in validating numerical results. Chilton and Stainsby further carried out RANS simulations of HB liquids using a Newtonian low Reynolds number $k - \epsilon$ model. Simulations were found to underestimate the turbulent friction factor by 15% compared to experiments and the Wilson & Thomas correlation. Using their definition of Reynolds number (see table 2.1) and their numerical results, Chilton and Stainsby proposed new turbulent friction factor correlations, one of them was based on the Blasius equation and another was based on Prandtl's equation for Newtonian liquids. The predictions of these correlations were in a good agreement with the available

experimental results, however, these correlation were very complex and have not been used in the literature thereafter.

Warsi [99] showed the capability of the Reynolds stress mixing length model for RANS simulations of PL liquids, however, similar to Malin [67, 68] no turbulence statistics was reported. Pinho [75] proposed a modified $k - \epsilon$ model for RANS simulations of GN liquids which was assessed in Cruz and Pinho [30] for PL liquids. The simulations underestimated the friction factor by 10% compared to the Dodge & Metzner correlation.

Compared to RANS, large eddy simulations (LES) capture a wider range of flow scales explicitly and therefore, can potentially provide a better insight into the flow. However, similar to RANS, LES also need special subgrid scale (SGS) models, to capture the behaviour of the small scales. LES was used by Ohta and Miyashita [73] and Gnambode et al. [42] for PL liquids, however, they ignored the effect of strain rate fluctuations in their formulation. Ohta and Miyashita [73] considered only slightly shear-thinning ($n = 0.85$) and shear-thickening liquids ($n = 1.15$) and therefore, the effects of non-Newtonian rheology were very small. Gnambode et al. [42] covered a wider range of n $(0.5 - 1.4)$ but their friction factor predictions were more than 20% away from the Dodge & Metzner correlation for strong shear-thinning liquids. Their profiles of the mean axial velocity and turbulence intensities also showed large deviation from the data available from well resolved direct numerical simulations, which are more accurate than LES.

Although advances have been made in developing RANS and LES techniques for GN liquids, still these are not mature and need further improvements. Unlike RANS and LES, direct numerical simulation (DNS) does not require any special model for capturing the small flow scales. DNS can resolve all turbulence scales and present a greater insight in fluid flow. When validated, DNS can be reliably used to disentangle the effect of rheology model parameters. However, due to the high computational cost, DNS studies have been limited to only weakly turbulent flows.

There are several techniques for discretising the domain for DNS such as finite difference, finite volume etc., but the spectral–Fourier technique is known for its higher accuracy and excellent convergence properties which are essential for accurate turbulent flow predictions. Rudman and Blackburn [83], Rudman et al. [84, 85] used this technique for DNS of PL and HB liquids and found the results qualitatively similar to those observed in earlier experimental and numerical studies. The transition to turbulence was delayed to a higher Re_G. The mean axial velocity and the axial turbulence intensity were higher but the radial and azimuthal turbulence intensities were lower for shear-thinning liquids compared to Newtonian liquids at similar Re_G. Mean viscosity was found to increase with increasing distance from the wall as expected for shear-thinning liquids. For HB liquids, the yield stress was found to enhance the shear-thinning effect. Although the DNS and experimental results agreed qualitatively, the numerical predictions of the bulk velocity were approximately 25% lower than the experimental value [84]. Rudman et al. suggested that this discrepancy could be a result of viscoelastic effects shown by the liquids (CMC solutions) in experiments, which were not modelled in numerical simulations. The agreement between simulations and experiments was better in Rudman and Blackburn [83] where a Carbopol fluid which shows negligible viscoelastic effects, was used, however, the discrepancies were still significant (of order 10-15%). Rudman and Blackburn suggested that a poor rheology characterisation could cause the observed discrepancies between simulations and experiments although had no data to back up this hypothesis. As mentioned earlier, the shear rate range used in a typical rheology characterisation is usually not wide enough to cover the high end of shear rates relevant to turbulent flows. In the absence of high shear rate data, rheology model extrapolates the viscosity to high shear rates, which can give unrealistic viscosity estimates and hence potentially lead to erroneous flow predictions.

Gavrilov and Rudyak [40] carried out DNS of PL liquids for Re_{MR} up to 20 000 using a finite element method. They found an increase in the turbulent anisotropy with shear thinning, which was also observed by Rudman et al. [84]. They suggested that the increased turbulent anisotropy with shear thinning modi-

fied the redistribution of turbulent energy between Reynolds stress components and resulted in increased fluctuations in the axial direction but decreased in the radial and the azimuthal directions. However, there was no data to support this hypothesis. The damping of wall-normal velocity fluctuations decreased the momentum transport via the Reynolds shear stress from the core towards the wall which resulted in drag reduction. Similar to the mean viscosity, viscosity fluctuations were also found to increase with increasing the distance from the wall.

Summary

Most numerical studies summarised above aimed at developing numerical techniques for GN liquids. RANS and LES are still not matured enough to confidently model turbulent flows of GN liquids. DNS provides a detailed description of turbulent flows, but studies by Gavrilov and Rudyak [40] and Rudman and Blackburn [83], Rudman et al. [84, 85] are the only DNS studies available. In these studies, the results of higher order turbulence statistics such as energy budgets (discussed in chapter 3) are lacking. Little is known about the effect of fluid yield stress on the turbulent pipe flow behaviour. The reason for discrepancies between numerical predictions and experiments has been hypothesised but the proof still forthcoming.

2.3   Flow through an open channel

Open channels as a medium of transport have the advantage of lower cost and simple design when compared to pipelines. An open channel can effectively transport liquids and slurries by taking the advantage of gravity and hence eliminating the need for expensive pumps. Pipe and open channel flows are quite similar to each other except one important aspect that in open channel flows, there is a free surface whose position and shape can vary in time and space. The depth of flow, discharge rate and the channel slope are all inter dependent in an open channel flow. The presence of the free surface also decreases the number of axes of symmetry in an open channel flow compared to a pipe flow. Together these make open channel flows more complex than pipe flows.

An additional non-dimensional number which is relevant to open channel flows is the Froude number

$$Fr = U_b/(gh). \tag{2.24}$$

Here, h is the flow depth and U_b is the bulk flow velocity. The Froude number defines the speed of the bulk velocity relative to the speed of a small wave at the free surface. Based on the value of the Froude number, open channel flows are characterised as subcritical ($Fr < 1$), critical ($Fr = 1$) and supercritical ($Fr > 1$) flows. For subcritical flows, little surface deformation is observed.

Another classification of open channel flows is based on the flow conditions [3, 46]. Steady-uniform open channel flow is the one which is treated in open channel flow hydraulics [93] and therefore, is important. In steady and uniform open channel flows, the flow depth is invariant with time and does not change in the streamwise direction. For these flows, an expression for the shear stress is obtained by considering the force balance (see figure 2.3) as:

$$\tau_{yx} = \rho g(h - y) \tag{2.25}$$

where g is the driving force per unit volume in the flow direction. Another expression for τ_{yx} can be obtained from the rheology model. However, due to multiple walls, the shear rate in an open channel flow contains terms including both $\partial u/\partial x$ and $\partial u/\partial y$. Only under the assumption of a sheet flow ($h << b$, where b is the channel width), can the velocity gradient $\partial u/\partial x$ be ignored. Consequently, the shear stress can be expressed as a function of $\partial u/\partial y$ alone and together with Eq. 2.25 it can be solved for the axial velocity under laminar conditions [see Burger [20] for the derivation]. For any other open channel flow, the governing equations have to be solved numerically. However, irrespective of the channel shape and the fluid rheology, an expression for the time and area averaged shear stress referred to as the mean wall shear stress τ_w is obtained as:

$$\tau_w = \rho g R_h \tag{2.26}$$

where

$$R_h = A/P_w \tag{2.27}$$

is the hydraulic radius of the channel, A is the channel cross-sectional area and P_w is the wetted perimeter. Thus the friction factor for an open channel flow is defined as:

$$f = 2gR_h/U_b^2 \tag{2.28}$$

Open channel flows of Newtonian liquids such as water have been very well
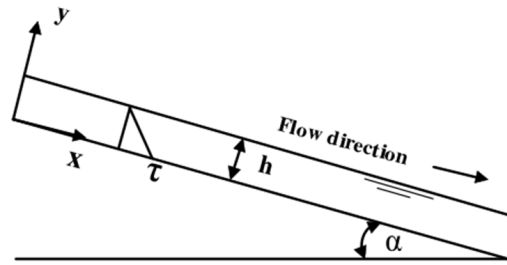
Fig. 2.3 Force balance for an open channel flow in the streamwise direction

studied for decades and since Te Chow [93] many books have been written on this topic. Reliable methods for analysis and design of open channels carrying Newtonian liquids are available in standard books [21, 93]. In contrast, the literature on open channel flows of non-Newtonian liquids is limited. Because non-Newtonian liquids show different flow behaviour to Newtonian liquids, the design methods developed for Newtonian liquids may not be appropriate for non-Newtonian liquids.

2.3.1   Reynolds number for open channel flows

For Newtonian liquids, pipe flow relationships can be used for open channel flows by using the channel hydraulic diameter D_h ($D_h = 4R_h$) for the length scale instead of the pipe diameter. This has theoretical and experimental support [59]. Thus, the Reynolds number for the open channel flow of a Newtonian fluid is defined as $Re = U_b D_h/\nu$. Although there have been experimental studies showing that the hydraulic diameter is an appropriate length scale for open channel flows of GN liquids under laminar conditions [4, 48], the same is yet to be shown for turbulent flows.

In the case of non-Newtonian liquids for which the choice of the viscosity scale is not clear, several Reynolds number definitions have been proposed for open channel flows of GN liquids. A few of these definitions are listed in table 2.2 but similar to pipe flow, none of the definition is universally accepted. It is worth noting that the pipe flow Reynolds number definitions are also possible choices for open channel flows of GN liquids, however, as mentioned earlier that the appropriateness of the hydraulic diameter as a length scale for GN liquids is yet to be shown.

Table 2.2 Different Reynolds numbers for open channel flows of GN liquids

Proposed by	Mathematical definition	comments
Kozicki and Tiu [61]	$Re = \dfrac{\rho V^{2-n} R_h{}^n}{2^{n-3} K (\frac{a+bn}{n})^n}$	Applicable for the power law rheology model, a and b depend on the shape of the channel
	$Re = \dfrac{4\rho V R_h}{K} \left[\dfrac{1}{a+b} - \dfrac{1}{b}\left(\dfrac{\tau_y}{\tau_w}\right) + \dfrac{a}{b(a+b)}\left(\dfrac{\tau_y}{\tau_w}\right)^{(1+b/a)} \right]$	Applicable for the Bingham rheology model, a and b depend on the shape of the channel
Hao and Zhenghai [53]	$Re = \dfrac{4R_h V}{K + \tau_y R_h/(2V)}$	Applicable for the Bingham rheology model
Haldenwang [46]	$Re_2 = \dfrac{8\rho V^2}{\tau_y + K(2V/R_h)^n}$	

2.3.2 Studies of open channel flows of GN liquids

The literature of open channel flows of GN liquids can be divided into three categories [49]:

24

1. Studies that aimed at evaluating the fluid rheological properties by postulating the laminar flow to be one-dimensional, steady and uniform on an inclined surface. Under these assumptions, the shear stress varies linearly from a maximum value at the wall to zero at the free surface and gives a shear stress distribution similar to a pipe flow. Studies in this category used this information to determine the rheology model parameters from the flow depth vs. inclination data.

2. Studies that were primarily motivated by engineering applications, which attempted to predict the flow rate for a given rheology model, shape and inclination of the channel. Different correlations for predicting the friction factor were proposed, which were empirical and for turbulent flows, many of them were developed from some pipe flow correlation. Similar to the studies from the first category, these studies also relied on the assumptions of uniform, steady and one dimensional flow.

3. Studies that relaxed one or more assumptions (uniform, one dimensional and steady flow) on which studies from the other two categories relied.

Out of these three categories only studies from the secondary category are relevant to the current work and are reviewed here.

Experimental studies

Kozicki and Tiu [61] analysed the flow of GN liquids through channels of different cross-sections. Correlations for predicting the average velocity in the laminar and turbulent regimes were proposed, which used geometric coefficients to capture the effect of channel shape (see table 2.2). The turbulent flow correlation was based on the Dodge and Metzner pipe flow correlation (Eq. 2.16). By using an analogy with flow through pipes, they defined a new Reynolds number for open channel flows of GN liquids (see Table 2.2). The critical Reynolds number for transition to turbulence was found to be a function of the channel shape and compared to pipe flows, the transition was found to occur at a higher Reynolds number for all geometries. From these observations, Kozicki and Tiu

suggested that the critical Reynolds numbers defined for pipe flows were not strictly applicable to open channel flows of GN liquids. No work was carried out to validate the proposed correlations.

Alternate correlations were proposed by Hao and Zhenghai [53] and Coussot [28] for laminar flows. The study by Hao and Zhenghai [53] was limited to only Bingham liquids and only one channel slope was considered whereas the flow index was fixed in Coussot [28]. Due to these limitations, the correlations proposed in these studies can not be generalised. Abulnaga [1] also studied the flow of Bingham liquids and proposed another definition for the Reynolds number. New correlations were proposed for laminar and turbulent flows, which have been used in designing the GN liquids systems [4]. Wilson [101] proposed that the Wilson and Thomas pipe flow correlations for HB liquids (Eq. 2.21) could be used for open channel flows with the pipe diameter replaced by the channel hydraulic diameter.

Haldenwang [46] carried out an extensive experimental investigation of laminar and turbulent flows of GN liquids, results of which were presented in Haldenwang and Slatter [47] and Haldenwang et al. [49]. The experiments covered a wide range of parameters including three different rheologies (PL, Bingham and HB), three different channel sizes and five inclinations. Using the channel hydraulic radius, the pipe flow Reynolds number definition proposed by Slatter and Lazarus [90] (see Re_2, table 2.1) was modified to give a new Reynolds number definition for GN liquids (see table 2.2). Using this Reynolds number definition, it was shown that all the experimental data of laminar flows collapses on the Newtonian curve $16/Re_2$.

Alderman and Haldenwang [4] compared various laminar and turbulent flow correlations for GN liquids using the experimental data of Haldenwang and Slatter [47]. They found that various correlations showed large discrepancies in predicting the bulk velocities compared to experiments despite giving good agreement with the measured friction factor. The laminar and turbulent correlations proposed by Haldenwang [46] were found in the best agreement with the experiments compared to other correlations.

Except Kozicki and Tiu [61], all of the studies mentioned above considered only rectangular open channel flows and a critical review of these studies is available in Alderman and Haldenwang [4]. The effect of the shape of the channel cross-section was studied by Burger [20] for four different geometries including a rectangular section. Because the Reynolds number definitions proposed by Kozicki and Tiu [61] is not applicable for HB fluids ($n \neq 1$ and $\tau_y \neq 0$), they preferred the Reynolds number definition of Haldenwang [46] (referred to as Re_2). For laminar flows, they found that the laminar friction factor correlation $f = 16/Re_2$ which was used for rectangular channels did not agree with the results of other channel shapes [16]. Therefore, they proposed to replace the constant 16 in the correlation with a coefficient K_1 where K_1 is a function of the channel shape. However later it was found that the modified correlation worked only for PL liquids and gave large errors for yield stress liquids (Bingham and HB) compared to experiments [17]. The turbulent friction factors were found to agree with the modified Blasius correlation $f = a\,Re_2^b$ where a and b are functions of the channel shape [18]. Additional correlations were proposed for the laminar and turbulent flows [19], which were found to be in a good agreement with experiments, however, only limited experimental data was used for validation.

Summary

Similar to pipe flow studies, open channel flow studies have been predominantly aimed at defining friction factor correlations for GN liquids. Several Reynolds number definitions and friction factor correlations have been proposed but none of them is universally accepted. Except Kozicki and Tiu [61] and Burger [20], none of the studies considered the effect of the shape of the channel cross section.

Numerical studies

Compared to experimental studies, numerical studies of open channel flow of GN liquids are limited. This is not surprising considering that computations of open channel flows are more challenging for GN liquids than Newtonian. The challenges arise due to very high viscosity at low shear rates which unlike pipe

flows, are common in an open channel flow because of the stress free boundary conditions at the free surface.

Ohta and Miyashita [73] performed DNS and LES computations for turbulent open channel flow of GN liquids but those were limited only for sheet flows ($h << b$). The only numerical study of open channel flow is by Guang et al. [43], which carried out DNS of Herschel-Bulkley liquids through semi-circular channels. When compared with experiments, DNS was found to over-predict the friction factor by approximately 40% compared to experiments. The reason for this was not explained and is not clear.

2.4   Chapter summary

Existing literature shows that there is no universally accepted Reynolds number definition for GN liquids and unlike Newtonian liquids, a pipe flow Reynolds number definition may not be appropriate for open channel flows of GN liquids. Several correlations for predicting the friction factor in laminar and turbulent flows of GN liquids have been proposed in which the Dodge and Metzner correlation is likely the best candidate for pipe flows of PL liquids. In contrast, there is no best suitable candidate for yield stress liquids. Turbulent flow correlations developed for pipe flows, have been shown to give erroneous predictions for yield stress liquids.

For pipe flows, it has been shown experimentally and numerically that shear thinning (decreasing n) delays transition to turbulence and decreases the turbulent friction factor for a given Reynolds number. An increase in the axial turbulent intensities but decrease in the radial and the azimuthal turbulent intensities has also been shown experimentally and via simulations. Turbulence statistics such as turbulence intensities, mean viscosity and Reynolds stress distributions have been studied only for weakly turbulent flows. The effect of yield stress on a turbulent pipe flow is not clear.

Compared to pipe flows, open channel flows of GN liquids have received scant attention and the literature is mostly limited to friction factor data. The appropriateness of the channel hydraulic diameter for open channel turbulent

flows of GN liquids is yet to be shown. Only a few studies have reported the effect of the shape of the channel cross-section. Secondary flows are known to be induced in open channel flows of Newtonian liquids, however, there is no study discussing the secondary flows for GN liquids. Similarly, the distribution of the mean shear stress at the wall has not been studied.

RANS and LES techniques are still not mature enough for simulations of GN liquids. DNS has been used to study turbulent pipe and open channel flows of GN liquids, however, large discrepancies have been found in predicting the friction factor using DNS compared to experiments, the reasons for which are not clear. The effect of shear rate range in rheology characterisation on turbulent flow predictions of GN liquids has been proposed as cause of the discrepancies, however, it is not proven.

3

Methodology

In this chapter, the governing equations as they are implemented in the code and the methodology behind the code are presented. The Reynolds averaged Navier–Stokes and energy budget equations for the mean and the fluctuating flows are derived. The procedure for determining the simulation parameters and domain-length and mesh-resolution independence of the current results is discussed. Because there is no reliable experimental data available for turbulent flow of GN liquids, the results of a Newtonian fluid are compared with those available in the literature for validating the underlying methodology.

3.1   Governing equations for non-Newtonian liquids

The flow solver used in the current study was developed by Blackburn & Rudman [83] which is based on the methodology presented in Blackburn and Sherwin [11] and discussed in Rudman and Blackburn [83]. Here, the simulation methodology is reviewed in brief. Since the instantaneous viscosity is spatially varying, the incompressible Navier–Stokes equations must be written in stress-divergence form:

$$D\boldsymbol{v}/Dt = \rho^{-1}\left(-\boldsymbol{\nabla}p + \boldsymbol{\nabla}\cdot\boldsymbol{\tau} + \boldsymbol{g}\right), \quad \text{with} \quad \boldsymbol{\nabla}\cdot\boldsymbol{v} = 0 \qquad (3.1)$$

where $\boldsymbol{v}$ is the velocity vector, p is the static pressure, $\boldsymbol{\tau}$ is the stress tensor and $\boldsymbol{g}$ is the body force. For ease of notation, p, $\boldsymbol{\tau}$ and $\boldsymbol{g}$ in Eq. 3.1 are divided by the constant fluid density ρ, but referred to as pressure, stress and body force respectively in subsequent discussion. The shear stress tensor $\boldsymbol{\tau}$ is modelled with the GN assumption as:

$$\boldsymbol{\tau} = 2\nu(\dot{\gamma})\boldsymbol{s} \tag{3.2}$$

where $\boldsymbol{s} = [\boldsymbol{\nabla v} + \boldsymbol{\nabla v}^T]/2$ is the instantaneous strain rate tensor and the kinematic viscosity ν is calculated using the rheology model. It is worth noting that although GN liquids such as mining slurries may show differences in normal stresses which may lead to viscoelastic behaviour, Eq. 3.2 does not model any normal stress differences. This is not of any concern for the current work, because it takes very high concentration of solids (with solid volume fraction of larger than 40%) to achieve significant normal stress differences [6, 64] and by that concentration the flow could only be laminar.

The Herschel–Bulkley (HB) rheology model and its subsets – power-law and Bingham rheology models, are used in the current study. All of these rheology models show a numerically singular viscosity at zero shear rate which is avoided in simulations by using a 'cut-off' shear rate ($\dot{\gamma}_c$) as:

$$\nu = \begin{cases} \nu(\dot{\gamma}) & \text{if } \dot{\gamma} > \dot{\gamma}_c \\ \nu(\dot{\gamma}_c) & \text{otherwise} \end{cases} \tag{3.3}$$

A very low value for the shear rate cut-off (of the order of 1×10^{-2} s^{-1}) is used to ensure that it does not affect the flow predictions. Except in a tiny region in open channel simulations, the shear rate is never found to reach such a low value. It is worth noting that the liquids of interest to this work (particle suspensions) can show second normal-stress differences at high concentration of solid particles [29], however, Eq. 3.2 does not model these stresses. Therefore, the current work is relevant only for fine particle suspensions with low solid concentrations.

For numerical robustness, the convective term in Eq. 3.1 is implemented in skew-symmetric form, i.e. $(\boldsymbol{v} \cdot \boldsymbol{\nabla v} + \boldsymbol{\nabla} \cdot \boldsymbol{vv})/2$. The body force term $\boldsymbol{g}$ in Eq. 3.1

is the force per unit volume driving the flow, which is the axial pressure gradient for a pipe flow and the gravity component in the streamwise direction for an open channel flow. The form of the Navier–Stokes equations implemented in the code is thus

$$\partial \boldsymbol{v}/\partial t + (\boldsymbol{v} \cdot \boldsymbol{\nabla}\boldsymbol{v} + \boldsymbol{\nabla} \cdot \boldsymbol{vv})/2 = -\boldsymbol{\nabla}p + \boldsymbol{\nabla} \cdot (2\nu\boldsymbol{s}) + \boldsymbol{g}. \tag{3.4}$$

In simulations, the spatial discretisation uses two-dimensional spectral elements to cover the flow cross-section (e.g. in figure 3.1 for a pipe) with the streamwise direction discretised using Fourier expansion. The spectral element representation uses standard tensor-product nodal basis with Gauss–Lobatto–Legendre collocation points. Since the body force is constant for both pipe and open channel flows, the pressure in Eq. 3.4 can be periodic as required by the Fourier expansion used in this direction. The code execution is parallel over planar Fourier modes; product terms are computed pseudo-spectrally and not de-aliased. Time integration is second-order and uses backwards-differencing for approximating temporal derivatives in the velocity-correction scheme [44, 57]. The time-integration method as originally proposed by Karniadakis et al. [57] requires a spatially constant viscosity which is accommodated here by adopting a technique introduced by Leslie and Gao [63] in the context of large-eddy simulation. The viscosity ν is split into a spatially constant component, ν_{ref}, with variable remainder $\nu - \nu_{\text{ref}}$ to give the momentum equation

$$\partial \boldsymbol{v}/\partial t + (\boldsymbol{v} \cdot \boldsymbol{\nabla}\boldsymbol{v} + \boldsymbol{\nabla} \cdot \boldsymbol{vv})/2 = -\boldsymbol{\nabla}p + \nu_{\text{ref}}\nabla^2\boldsymbol{v} + 2\boldsymbol{\nabla} \cdot \{(\nu - \nu_{\text{ref}})\boldsymbol{s}\} + \boldsymbol{g}. \tag{3.5}$$

Following this decomposition, the term $\nu_{\text{ref}}\nabla^2\boldsymbol{v}$ is handled implicitly in time while the remaining viscous term is dealt with explicitly and grouped with the nonlinear terms. One advantage of this method is that by appropriate choice of ν_{ref}, it is possible to integrate stably with time steps close to the Courant–Friedrichs–Lewy limit, rather than at smaller values which would be determined by a fully explicit treatment of viscous diffusion.

A no-slip boundary condition is used for walls and a zero shear boundary condition is used for the free surface. It is worth noting that a no-slip boundary
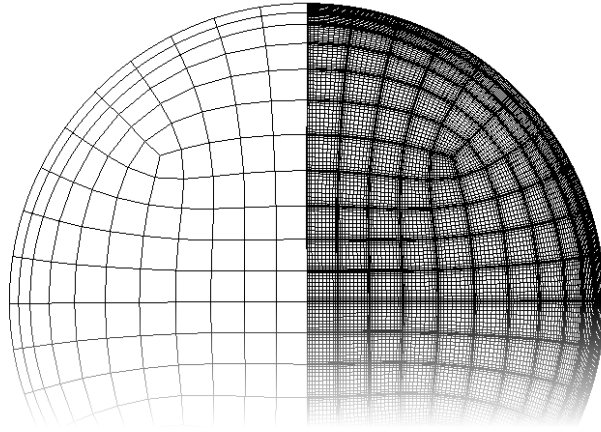
Fig. 3.1 Detail of a spectral element mesh used to discretise the pipe cross-section, illustrating the elements (left) and grid nodes for 12$^{\text{th}}$-order element interpolation functions, $N_p = 12$ (right).

condition is a result of the continuum hypothesis and is true for all practical single phase flows. However, wall slip (also called wall depletion effects or apparent slip) can occur in multiphase flows such as slurry flows because of the possibility of displacement of the solid particles away from the wall, leaving a lower-viscosity, depleted layer of the carrier liquid (lubrication layer) near the wall [81]. Wall slip has been known to cause discrepancies in measuring the viscosity of such fluids at low shear rates [9] (note that the viscosity is measured under laminar conditions). Shear rates are much larger in turbulent flows and the rapid mixing between the wall layer and core region in turbulent flow is unlikely to allow the formation of any lubrication layer near the wall. Thus, a no-slip boundary condition is appropriate for turbulent flows of slurries.

Mesh and domain-length independence of the results was ensured and is discussed in section 3.6. Simulations used initial conditions taken from earlier simulations on different meshes or from simulations with a different rheology model and were run until the calculated instantaneous shear stress integrated over the wall (wall shear stress) and the bulk velocity had reached a statistically steady value. In most cases the wall shear stress and the bulk velocity fluctuated by approximately 2% about the mean value. The time interval required to reach this state typically corresponded to around ten to twenty domain wash-through times. Once this state had been reached, time-averaged statistics were accumulated over

another ten to fifteen transit times for pipe flows and for thirty to forty domain wash-through times for open channel flows.

3.2 Reynolds-averaged Navier–Stokes equation for an incompressible GN fluid

Reynolds decomposition is used to separate variables into their ensemble mean and the fluctuating components. Here, velocity is decomposed as $\boldsymbol{v} = \boldsymbol{V} + \boldsymbol{v}'$; viscosity $\nu = \bar{\nu} + \nu'$ and the rate of strain tensor as $\boldsymbol{s} = \boldsymbol{S} + \boldsymbol{s}'$, where $\boldsymbol{V}$, $\bar{\nu}$ and $\boldsymbol{S}$ are the time-averaged quantities. Thus the Reynolds-averaged mean momentum equation for an incompressible non-Newtonian fluid is written as:

$$\boldsymbol{V} \cdot \boldsymbol{\nabla} \boldsymbol{V} = -\boldsymbol{\nabla} P + \boldsymbol{\nabla} \cdot \overline{\boldsymbol{\tau}} + \boldsymbol{g} \tag{3.6}$$

Here the mean stress tensor is the sum of three stress components.

$$\overline{\boldsymbol{\tau}} = 2\bar{\nu}\boldsymbol{S} - \overline{\boldsymbol{v}'\boldsymbol{v}'} + 2\overline{\nu'\boldsymbol{s}'} \tag{3.7}$$
$$= \boldsymbol{\tau}^v + \boldsymbol{\tau}^R + \boldsymbol{\tau}^{fv}.$$

As in the mean momentum equation for a Newtonian fluid, there is a mean viscous stress $\boldsymbol{\tau}^v$ and a Reynolds stress $\boldsymbol{\tau}^R$, however, unlike Newtonian liquids, here $\boldsymbol{\tau}^v$ is formed from a spatially varying viscosity $\bar{\nu}(r)$. For non-Newtonian liquids, a new stress term, $\boldsymbol{\tau}^{fv}$, arises which is referred to as the turbulent viscous stress $\boldsymbol{\tau}^{fv}$. Unlike other shear stress terms, $\boldsymbol{\tau}^{fv}$ can be positive or negative depending on the rheology of the fluid and unlike $\boldsymbol{\tau}^R$, it does not vanish at the wall. This is because it is a correlation between the fluctuations in viscosity $\nu' = \nu - \bar{\nu}$ and shear rate $\boldsymbol{s}' = \boldsymbol{s} - \boldsymbol{S}$. Because the shear rate involves both mean and fluctuating velocity gradients which do not vanish at the wall, this leads to non-zero viscosity fluctuations there. Together these allow non-zero turbulent viscous stress at the wall. Using an order of magnitude analysis, Pinho [75] showed that $\boldsymbol{\tau}^{fv}$ could only be neglected in the mean flow of a non- or weakly shear-thinning fluid and for strongly shear-thinning liquids, especially in the vicinity of the wall, this term can be large. It must be noted that in a pipe flow for which an expression for the

35

mean shear stress can be derived theoretically, the turbulent viscous stress $\boldsymbol{\tau}^{fv}$ can also be calculated as a mean shear stress deficit $\boldsymbol{\tau}^{fv+} = \bar{\boldsymbol{\tau}} - \boldsymbol{\tau}^v - \boldsymbol{\tau}^R$ (see Eq, 3.7) as done by Ptasinski et al. [79, 80] for viscoelastic liquids.

3.3 Energy budget equations

The total kinetic energy per unit mass is defined as $q = u_i u_i / 2$ and using the Reynolds decomposition, the mean kinetic energy is written as $\bar{q} = K + k$ where $K = U_i U_i / 2$ is the mean flow kinetic energy (MFKE) and $k = \overline{u_i' u_i'} / 2$ is the turbulent kinetic energy (TKE). Non-uniform viscosity and viscosity fluctuations modify the MFKE and TKE budget equations for a non-Newtonian fluid. The MFKE and TKE budget equations are derived in Cartesian coordinates for a non-Newtonian fluid in Appendix A. In the current work, the energy budgets are presented and discussed only for a pipe flow for which the results are transformed to polar coordinates to present them as a function of the radial distance (chapters 5-7).

3.3.1 Mean flow kinetic energy budget

An equation for the MFKE can be obtained by taking the divergence of Eq. 3.6 which produces

$$\overbrace{\frac{\partial K}{\partial t}}^{K_t} + \overbrace{U_j \frac{\partial K}{\partial x_j}}^{\mathcal{A}_m} = \overbrace{-U_j \frac{\partial P}{\partial x_j}}^{W_{dp/dz}} + \overbrace{\left(-\frac{\partial U_i \overline{u_i' u_j'}}{\partial x_j} \right)}^{\mathcal{T}^m} + \overbrace{2 \frac{\partial \bar{\nu} S_{ij} U_i}{\partial x_j}}^{\mathcal{D}^m} + \overbrace{\left(-2 \bar{\nu} S_{ij} S_{ij} \right)}^{\epsilon^m} + \overbrace{\overline{u_i' u_j'} S_{ij}}^{-\mathcal{P}}$$

$$+ \overbrace{2 \frac{\partial U_i \overline{\nu' s_{ij}'}}{\partial x_j}}^{\Upsilon^m_{nn}} + \overbrace{\left(-2 \overline{\nu' s_{ij}'} S_{ij} \right)}^{\chi_{nn}}. \tag{3.8}$$

The first two terms in Eq. 3.8 i.e. K_t and $\mathcal{A}^m$, are the rate of change and the mean advection of K both of which vanish for pipe flow as the mean flow is temporally stationary, one component and uniform in the axial direction. The mean flow energy production, $W_{dp/dz}$, is the only source of energy in Eq. 3.8. Mean flow stresses occur for both Newtonian and non-Newtonian liquids ($\tau^v = 2\bar{\nu} S_{ij}$ and $\tau^R = -\overline{u_i' u_j'}$) and appear in four places and play two roles; first, they appear in transport terms $\mathcal{D}^m$ and $\mathcal{T}^m$ that distribute the energy within the domain (Note the volume integral of each transport term is zero [78]). Second, they appear in

36

ϵ^m and $-\mathcal{P}$ which act as a sink. As shown later in section 3.3.2, $-\mathcal{P}$ also appears with opposite sign in TKE budget (see Eq. 3.9) and thus represents the energy transfer from the mean flow to turbulence.

The last two terms in Eq. 3.8, Υ_{nn}^m and χ_{nn}, appear only for non-Newtonian liquids as they arise from the interaction between the turbulent viscous stress $\tau^{fv} = 2\overline{\nu' s_{ij}'}$, and the mean flow. The turbulent viscous transport, Υ_{nn}^m, is a transport term and modifies the total MFKE transport whereas the mean shear turbulent viscous dissipation, χ_{nn}, modifies the total MFKE dissipation. The non-Newtonian dissipation term, χ_{nn}, also appears in the TKE budget (see Eq. 3.9), the implications of which are discussed in section 3.3.2. Note that χ_{nn} can be positive or negative depending on the rheology of the fluid, however, positive values of χ_{nn} do not imply MFKE production. The mean flow can receive energy only through the action of mean pressure gradient on the mean flow and positive values of χ_{nn} instead correspond to a reduced MFKE dissipation.

3.3.2 Turbulent kinetic energy budget

The equation for the ensemble-average turbulent kinetic energy ($k = \overline{u_i' u_i'}/2$) is

$$
\overbrace{\frac{\partial k}{\partial t}}^{k_t} + \overbrace{U_j \frac{\partial k}{\partial x_j}}^{\mathcal{A}} = \overbrace{-\overline{u_i' u_j'} S_{ij}}^{\mathcal{P}} + \left\{ \overbrace{-\frac{\partial \overline{u_i' u_i' u_j'}}{\partial x_j}}^{\mathcal{T}} \overbrace{-\frac{\partial \overline{p' u_j'}}{\partial x_j}}^{\Pi} + \overbrace{\frac{\partial (2\overline{\nu} \overline{s_{ij}' u_i'})}{\partial x_j}}^{\mathcal{D}} \right\} \overbrace{-2\overline{\nu} \overline{s_{ij}' s_{ij}'}}^{\epsilon}
$$

$$
+ \left\{ \overbrace{\frac{\partial (2\overline{\nu' u_i' S_{ij}})}{\partial x_j}}^{\xi_{nn}} + \overbrace{\frac{\partial (2\overline{\nu' s_{ij}' u_i'})}{\partial x_j}}^{\mathcal{D}_{nn}} \right\} \overbrace{-2\overline{\nu' s_{ij}'} S_{ij}}^{\chi_{nn}} \overbrace{-2\overline{\nu' s_{ij}' s_{ij}'}}^{\epsilon_{nn}}. \qquad (3.9)
$$

In Eq. 3.9, terms in the first row are common for both Newtonian and non-Newtonian liquids and are referred to as the Newtonian terms. As with the MFKE budget (Eq. 3.8), the first two terms in Eq. 3.9, k_t and $\mathcal{A}$, vanish for pipe flow. As mentioned in section 3.3.1, the turbulent kinetic energy production, $\mathcal{P}$, is the only source term in Eq. 3.9 and it couples the MFKE and the TKE budget equations. The mean viscous dissipation, ϵ, is negative definite and, as the name suggests, it is the dissipation of TKE due to the mean viscosity. The gradient terms, $\mathcal{T}$, Π, $\mathcal{D}$, distribute TKE, k, within the domain. Although they can not produce or dissipate TKE, they can be local sources or sinks in the TKE budget.

The remaining terms, ξ_{nn}, $\mathcal{D}_{nn}$, χ_{nn} and ϵ_{nn} are zero for a Newtonian fluid as they arise due to viscosity fluctuations and are referred to as the non-Newtonian TKE budget terms. In these, the gradient terms, the mean shear turbulent viscous transport, ξ_{nn}, and the turbulent viscous transport, $\mathcal{D}_{nn}$, either enhance or diminish transport by the Newtonian transport terms. In the non-Newtonian dissipation terms, the mean shear turbulent viscous dissipation, χ_{nn}, appears in both the MFKE and the TKE budget equations with the same sign, meaning that it affects both energy budgets in a similar manner. Both χ_{nn} and ϵ_{nn} appear as source/sink terms in TKE budget, although neither is obviously positive (or negative) definite for shear-thinning liquids. As mentioned in section 3.3.1 for χ_{nn}, positive values of either of these terms does not mean that they are true sources of turbulent kinetic energy. Turbulence can only source energy from the mean flow and although χ_{nn} involves the mean flow via S_{ij}, its genesis is in the total viscous dissipation and as such it is clearly part of the total turbulent dissipation. The turbulent viscous dissipation, ϵ_{nn}, has similar origins and is more clearly associated with dissipation. By summing the terms with similar nature, the TKE budget equation is written as:

$$\frac{Dk}{Dt} = \mathcal{P} + T^k - \epsilon^k \qquad (3.10)$$

where, $T^k = \mathcal{T} + \Pi + \mathcal{D} + \mathcal{D}_{nn} + \xi_{nn}$, is the total transport and $\epsilon^k = \epsilon + \chi_{nn} + \epsilon_{nn}$ is the total dissipation.

3.4 Non-dimensional variables

Wall units are defined in a similar manner to the Newtonian analysis using the nominal wall viscosity ν_w (Eq. 2.11), as the viscosity scale. The friction velocity $u^* = (\tau_w/\rho)^{1/2}$ is used for the velocity scale and ν_w/u^* for the length scale. Hence, the non-dimensional distance from the wall is expressed as $y^+ = y/(\nu_w/u^*)$, where $y = (R - r)$ for pipe flow. The mean axial velocity is normalised as $U_z^+ = U_z/u^*$, mean viscosity as $\nu^+ = \bar{\nu}/\nu_w$ and the root mean square viscosity fluctuations as $\nu'^+ = (\overline{\nu'^2})^{1/2}/\nu_w$. Turbulence intensities are expressed in wall units as $u_i'^+ = (\overline{u_i'^2})^{1/2}/u^*$. Shear rate is normalised by τ_w/ν_w, stress terms by τ_w

38

and the energy budget terms by $(u^*)^4/\nu_w$. The Fanning friction factor f which is the non-dimensional wall shear stress is defined as $f = 2\tau_w/(\rho U_b^2)$.

Although the nominal wall shear stress, τ_w, and the nominal wall viscosity, ν_w, are chosen here for scaling, it is shown later in section 5.1.2 that these scalings do not maintain the fundamental $U_z^+ = y^+$ relation near the wall. Later a scaling is developed that gives $U_z^+ = y^+$, however, ν_w and u^* are chosen in the majority of the analysis below because these can be determined *a priori* from the mean pressure gradient which is easily measured in experiments. This allows a direct comparison to DNS results. Except where dimensions are specified, all results are presented in non-dimensional units.

3.5   Simulation parameters

In later chapters, turbulent flows of HB liquids are investigated for pipes and open channels. The range of rheology parameters is $n = 0.4 - 1.2$ and yield stress $\tau_y = 0 - 20\%$ of the nominal wall shear stress τ_w . Open channels with a rectangular cross section are considered where the hydraulic radius R_h (Eq. 2.27) is fixed and the channel aspect ratio ($AR = 2b/h$ where $2b$ is the channel width and h is the fluid depth) is varied for $AR \in [1, 4]$. As seen later the fixed hydraulic radius implies a fixed flow rate for all AR for a given forcing (discussed in chapter 8).

The work in this study can be divided into two groups – first, where the friction Reynolds number is fixed and the effects of modifying rheology model parameters or changing the channel aspect ratio are studied. Second, where the effects of increasing Reynolds number are studied for a given rheology. For the simulations from the first group, a friction Reynolds number, $Re_\tau = 323$ was chosen for pipe flows and $Re_\tau = 146$ for open channel flows to give a similar generalised Reynolds number Re_G of approximately $10\,000$ for a shear-thinning fluid (PL, $n = 0.6$) in both flow configurations. The friction Reynolds number Re_τ was fixed by setting the nominal wall viscosity ν_w and the nominal wall shear stress τ_w. The flow index or the yield stress was varied and accordingly the consistency, K, was adjusted to give the desired nominal wall viscosity ν_w (see

Eq. 2.11). In case of open channel flows, τ_w in Eq. 2.11 was calculated using Eq. 2.26. The fixed τ_w in a pipe or an open channel implies a fixed forcing in those simulations. Although $Re_\tau = 146$ in an open channel flow may seem a bit low for a turbulent flow, contours plots of the instantaneous flow field showed that the flow was turbulent (figures 8.1 and 8.2). The turbulence intensities were also of the same order as in pipe flow at $Re_\tau = 323$ (see figure 5.12 and figures 8.14 - 8.16). The fact that the friction Reynolds number Re_τ is lower in open channel flow compared to a pipe flow at similar Re_G indicates that an open channel flow requires less forcing compared to a pipe flow to achieve a given flow rate. The results of the pipe flow are discussed in chapter 5 and of the open channel flows in chapter 8.

For the second group, simulations were run for Newtonian and shear-thinning (PL, $n = 0.6$) liquids for $Re_\tau = 323, 500$ and 750. The nominal wall viscosity was fixed for both liquids at a given Re_τ. The results from this study are presented in chapter 7.

3.6 Mesh, domain-length and time step independence

Mesh design for these flows is an iterative process, influenced by rules-of-thumb for the resolution and domain size established in Newtonian DNS [77]. Turbulent flow structures become finer with increasing n, therefore, DNS requires a higher mesh resolution as n is increased. Since axial domain periodicity is used, it is also important to ensure that the domain is sufficiently long to not unduly influence results. In the current study, the mesh-resolution, time step and the domain-length-independence are checked for a pipe flow at $Re_\tau = 323$. The mesh chosen for the rest of the simulations was one in which the statistics did not vary with either increased mesh-resolution or longer domain.

The domain length is verified for its adequacy via two point correlation of axial velocity fluctuations $\rho_{u'_z u'_z}$ defined as:

$$\rho_{u'_z u'_z}(\Delta z) = \langle u'_z(r, \theta, z, t) u'_z(r, \theta, z + \Delta z, t) \rangle / \langle u'_z(r, \theta, z)^2 \rangle \qquad (3.11)$$

Here, u_z' represents the axial velocity fluctuations at time t and $\langle \rangle$ denotes averaging in time and θ and z directions. Simulations were run for a domain length of $L_z = 4\pi D$ (approximately $12D$) and for $n = 0.4 - 1.2$. Since the velocity fluctuations are correlated for a longer distance in the flow of a more shear-thinning fluid [84], a slightly longer domain ($L_z \approx 16D$) was used for $n = 0.4$. A mesh with 300 spectral elements of a polynomial order of 10 and 288 axial planes was used, which was fine enough to resolve the flow scales with a sufficient accuracy (see the results of the mesh-resolution-independence study in Appendix B). As seen in figure 3.2, $\rho_{u_z' u_z'}$ decays to zero for all n. Close to the pipe centre, $\rho_{u_z' u_z'}$ remains positive for much of the domain, however, its value is small (less than 0.1). Overall, these results indicate an adequate domain length. Negative values of $\rho_{u_z' u_z'}$ in the profiles of $n = 0.4$ and $n = 0.6$ indicate intermittent turbulent regions as also seen in near wall streaks (shown later in figure 5.3). The larger negative values of $\rho_{u_z' u_z'}$ for $n = 0.4$ indicate the transitional nature of this flow at $Re_\tau = 323$. These results show that a minimum domain length of $11D$ is required in order that streamwise correlations are sufficiently small. This domain length is twice that used by Eggels et al. [36] in their DNS of a Newtonian fluid at $Re_\tau = 180$ and comparable to that suggested by Chin et al. [25] for DNS of a Newtonian fluid at $Re_\tau = 170 - 500$. In the current work, a domain length of $L_z = 4\pi D$ is used for the pipe and open channel flow simulations at $Re_\tau = 323$ and $Re_\tau = 146$ ($Re_G \approx 10\,000$) and is decreased slightly to $L_z \approx 10D$ for the pipe flow simulations at $Re_\tau = 500$ and 750 as the correlation length decreases with increasing Reynolds number.

Once the domain length is chosen, the adequacy of mesh resolution is checked by running simulations and comparing the results of different meshes with different mesh resolutions in the axial and the polynomial directions. The results of the mesh-resolution-independence study are reported in Appendix B. The final mesh had 300 spectral elements of 12th polynomial order and 384 axial planes (192 Fourier modes). This gave a mesh resolution of $\Delta y^+ = [0.8 - 4.0]$ in the wall normal direction, $\Delta(r\theta)^+ \approx 6$ in the azimuthal direction and $\Delta z^+ \approx 21$ in the axial direction. The mesh used for $n = 1.2$ had a slightly higher number of elements near the pipe centre (total 384 spectral elements) to ensure a better
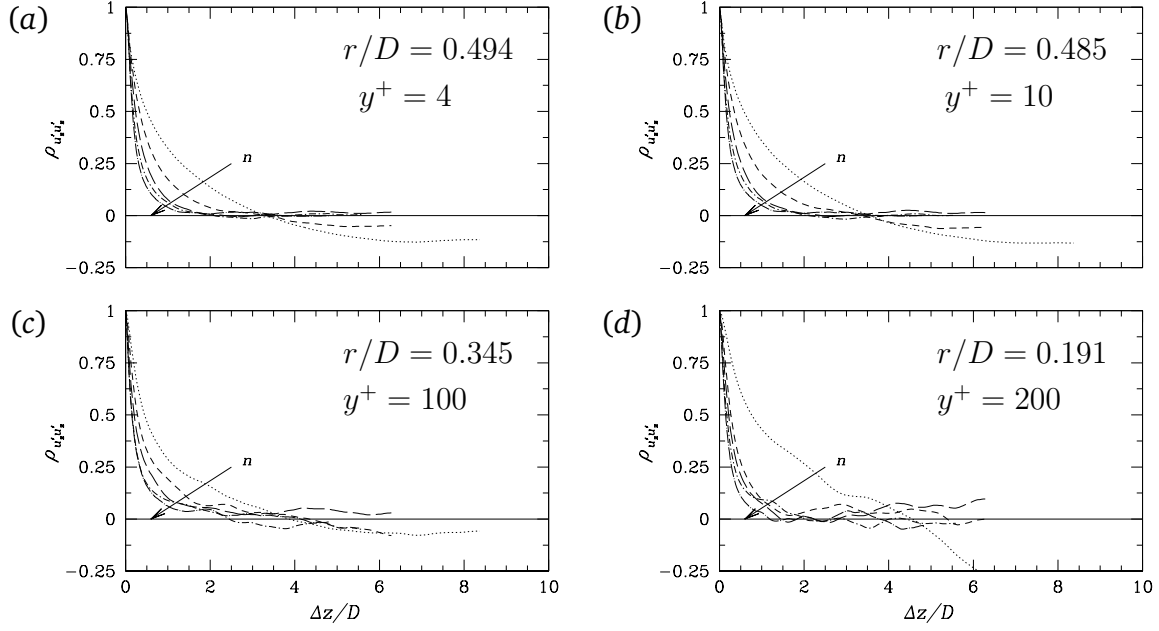
Fig. 3.2 Two point correlation coefficient of axial velocity fluctuations as a function of stream-wise separation $\Delta z/D$ plotted for $n = 0.4 - 1.2$ at $Re_\tau = 323$ (see table 5.1) at different y^+ locations. Arrows show the direction of increasing n.

mesh refinement there. This is because the viscosity of a shear-thickening fluid decreases with the distance from the wall and therefore, the viscous length scale for a shear-thickening fluid will be smaller near the pipe centre compared to a shear-thinning fluid.

A time-step independence study was carried out for a shear-thinning fluid ($n = 0.6$), results of which are also reported in Appendix B. The mesh resolution and the time step size as used for final simulations for different Reynolds number are presented in table 3.1. No mesh-resolution or time-step size independence study was carried out for $Re_\tau > 323$ and the mesh-resolution and the time-step size were chosen based on non-dimensional values for $Re_\tau = 323$ taking into account rules generally used for Newtonian liquids. The open channel meshes used a similar mesh resolution (in wall units) and domain length as in the acceptable pipe mesh at $Re_\tau = 323$.

Table 3.1 Mesh spacing and time step size in wall units used in pipe flow simulations at different Re_τ

$pipe/channel$	Re_τ	Δy^+	$\Delta r\theta^+$	Δz^+	$\Delta t/(\nu_w/u^{*2})$
Pipe	323	0.8–4.0	6	21	0.035
Pipe	500	0.8–4.0	6	12	0.023
Pipe	750	0.8–4.0	6	12	0.021
Open channel	146	0.8–5.0	6	21	0.017

3.7 Validation of numerical method

As mentioned in chapter 2, the experimental data available in the literature for GN liquids could not be used here due to a poor rheology characterisation in those studies. Therefore, to provide a baseline comparison of the underlying numerical method, statistical data from a Newtonian fluid are compared with the experimental results of den Toonder and Nieuwstadt [32] for $Re_\tau = 323$ and with the DNS data of El Khoury et al. [38] at $Re_\tau = 360$ and $Re_\tau = 500$ (figures 3.3 and 3.4). The DNS results of Chin [23] for $Re_\tau = 500$ are also included. As seen in figure 3.3, profiles of mean velocity, turbulence intensities, Reynolds shear stress and the turbulent kinetic energy production obtained from DNS agree well with the experimental results except very close to the wall, where some of the experimental results are acknowledged to be unreliable. The current results are in good agreement with the DNS results of El Khoury et al. [38] (figure 3.4). Although no reliable experimental data is available for comparison of GN liquids, in chapter 4, limited validation is provided for measurements in GN liquids.
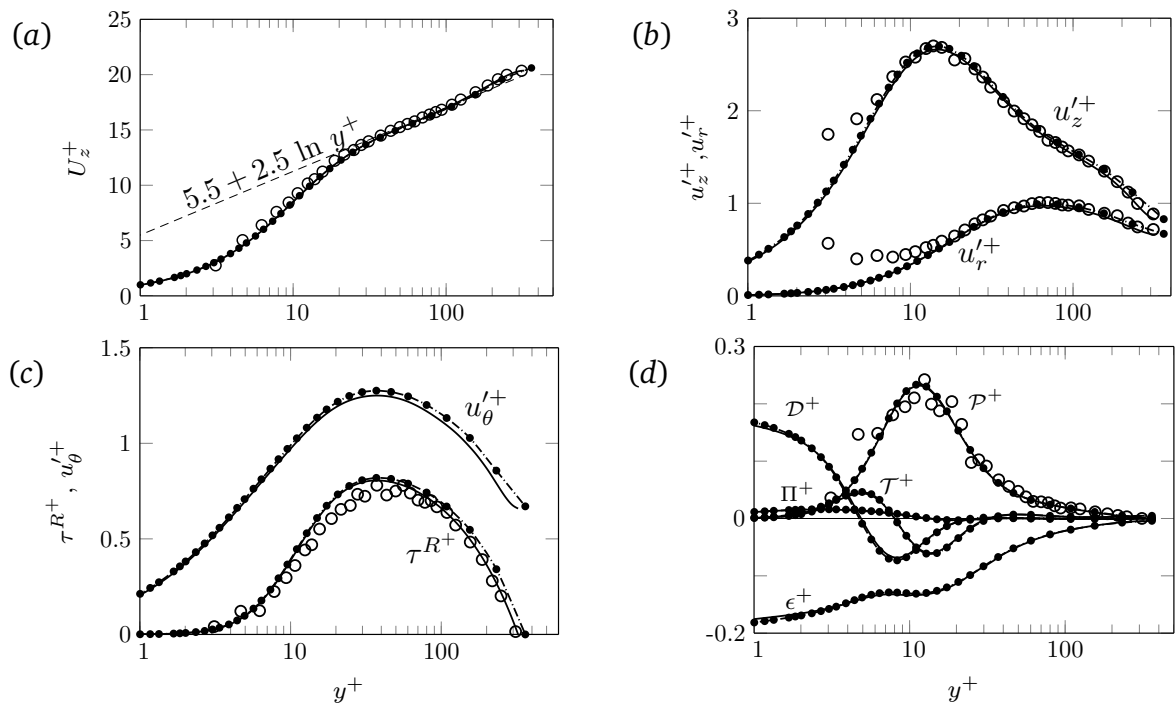
Fig. 3.3 Wall-scaled statistical profiles from DNS of Newtonian fluid at $Re_\tau = 323$ (solid line), compared to experimental results of den Toonder and Nieuwstadt [32, circles: $Re_\tau = 314$] and DNS results of El Khoury et al. [38, filled circles: $Re_\tau = 360$]. (*a*) mean axial velocity; (*b*) rms of axial and radial velocity fluctuations; (*c*) Reynolds shear stress and azimuthal velocity fluctuations (*d*) turbulent kinetic energy budget.
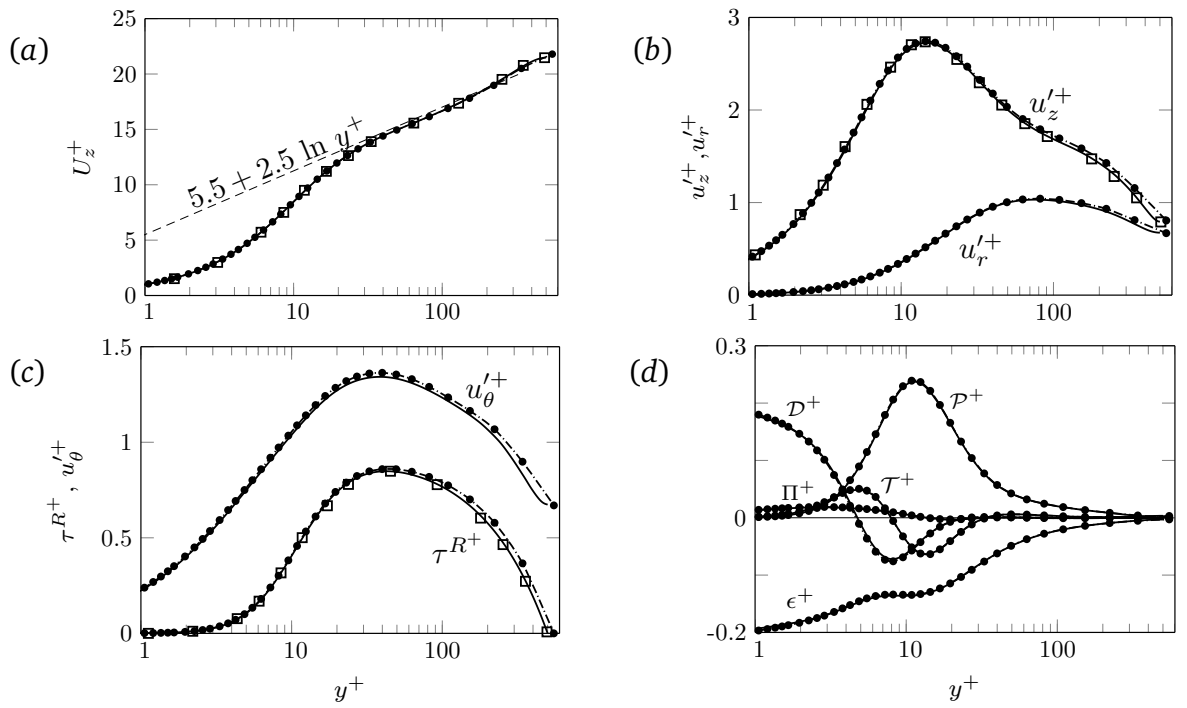
Fig. 3.4 Wall-scaled statistical profiles from DNS of Newtonian fluid at $Re_\tau = 500$ (solid line), compared to DNS results of El Khoury et al. [38, filled circles: $Re_\tau = 550$] and Chin [23, squares: $Re_\tau = 500$]. (*a*) mean axial velocity; (*b*) rms of axial and radial velocity fluctuations; (*c*) Reynolds shear stress and azimuthal velocity fluctuations (*d*) turbulent kinetic energy budget.

4

The importance of rheology characterisation for turbulent flow predictions

4.1 Chapter summary

In this chapter, the importance of high shear rate rheology on turbulent pipe flow predictions using DNS is discussed. This work has been published in the Journal of non-Newtonian fluid mechanics and the published article is attached here. A summary of the published work is as follows:

DNS of turbulent pipe flows of GN liquids have shown discrepancies in the past compared to experiments [83, 85]. The errors in predicting flow rate for a given pressure gradient were as large as 20% compared to the experimental value. Since these kind of discrepancies are not seen for Newtonian liquids, the errors are likely to be associated with rheology characterisation. Assuming DNS were well resolved and the rheology measurements were taken carefully, possible candidates leading to the inaccuracies in DNS are 1) Viscoelasticity shown by the liquids used in experiments which was not modelled in simulations. 2) lack of

high shear rate data in rheology characterisation, which is typical to turbulent flows. In the attached paper it is shown that the lack of high shear rate data in rheology characterisation is indeed responsible for the observed discrepancies. Rheology measurements usually cover shear rates which are much lower than the maximum shear rate in turbulent flows. In the absence of high shear rate data, DNS extrapolates the shear rheogram which leads to errors in viscosity estimates and thus in DNS predictions. Additionally, it is shown that errors in predicting friction factor using a turbulent flow correlations are also significantly decreased if high shear rate rheology data is used.

Shear rates in turbulent flows span several orders of magnitude and it is not possible to cover the entire shear rate range in rheology measurements. It is shown here that the errors introduced in rheology characterisation at very low shear rates do not affect the predictions of DNS and a turbulent friction factor correlation to any significant extent. By analysing the probability shear rate distribution in the flow, it is shown that it is the near wall region where DNS predictions are the most sensitive to the errors in viscosity estimates. The probability density curve of shear rate in the near wall region when expressed in wall units is found to be almost independent of the rheology and the Reynolds number. Using this observation, a criterion for the maximum shear rate required in rheology characterisation to get a good agreement between DNS and experiments is proposed.

4.2   Publication

The article J.Singh, M. Rudman, H.M. Blackburn, A. Chryss, L.Pullum and L.J.W. Graham. The importance of rheology characterization in predicting turbulent pipe flow of generalized Newtonian liquids. *J. non-Newt. fluid mech.* 232:11-21(2016) is reproduced with permission Elsvier Publishing, Copyright 2016.

4.3   Errata

There is a typo in Eq. 5 in the attached paper. The viscous stress terms should be $\nabla.\tau$ (it is written incorrectly as $\nabla\tau$.)

Monash University

Declaration for Thesis chapter 4

In the case of the publication in Chapter 4, the nature and extent of my contribution to the work was the following:

Nature of contribution	Extent of contribution
Writing, editing, performing simulations, and data analysis	85%

The following co-authors contributed to the work:

Name	Nature of contribution	Extent of contribution
Prof. M. Rudman	Project supervision and conception, manuscript writing, editing & revision.	NA
Prof. H.M. Blackburn	Project supervision and conception, manuscript writing, editing & revision.	NA
Dr. A. Chryss	Project supervision, rheology measurements & analysis, manuscript writing and editing.	NA
Dr. L. Pullum	Project conception, experiments and experimental analysis, paper revision.	NA
Dr. L.J.W. Graham	Experiments and paper review.	NA

The undersigned hereby certify that the above declaration correctly reflects the nature and extent of the candidate's and co-authors' contributions to this work.

Candidate's Signature: █████████   Date: 27/04/2017

The undersigned hereby certify that the above declaration correctly reflects th█████████████████████uthors contributions to this work.
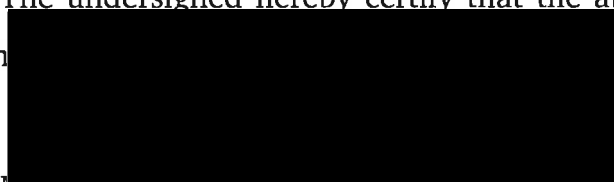
Main Supervisor's Signature.   Date: 27/04/2017
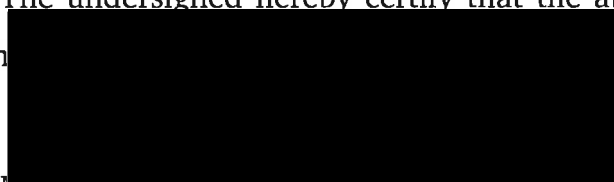
The importance of rheology characterization in predicting turbulent pipe flow of generalized Newtonian fluids

J. Singh[a], M. Rudman[a,*], H.M. Blackburn[a], A. Chryss[b], L. Pullum[c], L.J.W. Graham[b]

[a] Department of Mechanical and Aerospace Engineering, Monash University, Vic 3800, Australia
[b] CSIRO Minerals Resources Flagship, Clayton, Vic 3168, Australia
[c] Private consultant, Olinda, Vic 3788, Australia

ABSTRACT

Most Direct Numerical Simulation (DNS) of turbulent flow of generalized Newtonian (GN) fluids presented to date have shown significant discrepancy between experimental measurement and simulation. In addition to DNS, empirical correlations using different rheology models fitted to the same shear rheogram have also shown to give significantly different results. Important to note is that for turbulent flow predictions it is a common practice to use a shear rheogram which is measured at shear rates well below the values encountered in turbulent flows. This paper highlights the importance of obtaining high shear rate rheology in reducing these discrepancies. Further, it is shown that if high shear rate rheology is used in rheology characterisation, the choice of rheology model has little influence on the results. An important aside is that accurate prediction of laminar flow gives absolutely no confidence that a rheology model is acceptable in modelling the turbulent flow of the same fluid. From an analysis of instantaneous shear rates in the predicted turbulent flow field, the probability distribution of the non-dimensionlised shear rates in the near-wall region appears to collapse onto a universal curve. Based on this, we propose that the maximum shear rate required in rheology characterisation should be at least twice the shear rate corresponding to the mean wall shear stress.

© 2016 Elsevier B.V. All rights reserved.

1. Introduction

Many fluids in industrial applications and nature show non-Newtonian behaviour i.e. they do not show a uniform viscosity under isothermal conditions. Generalised Newtonian (GN) fluids are a class of non-Newtonian fluids for which the shear stress tensor $\boldsymbol{\tau}$ can be expressed as a product of a non-constant viscosity and the strain rate tensor:

$$\boldsymbol{\tau} = 2\mu(\dot{\gamma})\boldsymbol{S} \qquad (1)$$

Here, $\dot{\gamma}$ is the second invariant of the strain rate tensor $\boldsymbol{S} = \frac{1}{2}[\nabla\boldsymbol{v} + (\nabla\boldsymbol{v})^T]$ determined as $\dot{\gamma} = \sqrt{(2\boldsymbol{S}:\boldsymbol{S})}$ and μ is a scalar viscosity usually called an effective or apparent viscosity. The GN assumption assumes an instantaneous response of the fluid to the applied shear stress and therefore, the viscosity of a GN fluid can be expressed as a function of shear rate $\dot{\gamma}$ as in Eq. 1. Note that the effective viscosity of a GN fluid can also depend on temperature, but we do not consider the effect of temperature in the current study. In practice, the effective or apparent viscosity of a GN fluid

is determined by dividing the shear stress measured in a rheometer by the shear rate at which the stress is measured. These measurements are performed in a uni-directional flow in a rheometer. Fine particle suspensions, sewage sludges, molten lava, some polymer solutions, some bodily fluids and paints are examples of fluids that are well approximated by the GN assumption. Although the apparent viscosity of these fluids is often very high, industrially relevant flows can be turbulent at sufficiently high flow rates or in pipes with sufficiently large diameters. Despite their wide applications, there have been only a few studies dedicated to the fundamental understanding of turbulent flow of GN fluids, the majority of which have been experimental [1–6] with the primary objective often to derive a general correlation for the friction factor.

Unlike Newtonian fluids where the kinematic viscosity can be measured very accurately, non-Newtonian fluids are far more difficult to characterise. Despite this, the assumption of GN behaviour as a constitutive model appears to work well for a range of fluids. However, the constitutive equation relating the shear stress and shear rate is usually determined by fitting a particular mathematical rheology model to the experimental measured shear rheogram. There are many rheology models available for GN fluids [7,8], but the Herschel–Bulkley [9] and the Hallbom rheology models

[10] have been found to represent the rheology of fluids such as mining and waste water slurries quite well [10–12]. The Herschel–Bulkley model defines the effective viscosity as:

$$\mu = \tau_y/\dot{\gamma} + K(\dot{\gamma})^{n-1} \tag{2}$$

Here, the yield stress τ_y, consistency K and flow index n are the model parameters. This model reduces to the power-law rheology model giving $\mu = K(\dot{\gamma})^{n-1}$ when $\tau_y = 0$ and the Bingham model $\mu = \tau_y/\dot{\gamma} + K$ when $n = 1$, both of which are commonly used in application. Unlike the Herschel–Bulkley model which has no theoretical basis [10], the Hallbom rheology model (Eq. 3) is derived by considering the behaviour of solid particles in homogeneous shear-thinning mineral suspensions and relates the viscosity and shear rate via the following equation:

$$\mu^k = (\tau_0/\dot{\gamma})^k + (\mu_\infty)^k \tag{3}$$

In this equation the model parameters are known as the yield stress τ_0, the infinite shear viscosity μ_∞ and the scaling factor k. The benefit of the Hallbom model in approximating (for example) a fine particle suspension is that as $\dot{\gamma} \to \infty$, the carrier fluid rheology is recovered, unlike the Herschel–Bulkley model in which the predicted viscosity drops below that of the carrier fluid. This is not physically possible.

Rheograms used for determining rheology model parameters in industrial application are typically measured over shear rates that would rarely exceed 500 s^{-1} (and often significantly less). This range is well below the shear rates that could be encountered in turbulent flow. Another way of determining the model parameters for the rheology models discussed here is via the use of analytical expressions that relate the bulk velocity (volumetric flow rate per unit cross-sectional area) and pressure gradient under laminar flow conditions to the model parameters [7,8]. These relationships can be (and often are) used for determining rheology parameters from the measured laminar flow curve (i.e. flow rate versus pressure drop), often in a small scale laboratory pipe loop. The shear rate range over which laminar flow is appropriate will depend on the fluid and pipe diameter. For laboratory experiments it is typically less than 300 s^{-1} and sometimes much smaller. It has been shown that constitutive equations based on different rheology models determined from the same laminar pipe data when used with theoretical or empirical correlations for determining the friction factor give barely distinguishable results in the laminar region as expected. However, the discrepancy in the turbulent regime can be as large as 50% [12,13]. Regardless, it is a common practice in hydraulic conveying to use such measurements.

Numerical techniques such as Reynolds Averaged Navier–Stokes(RANS), large eddy simulation (LES) and direct numerical simulations (DNS) require a constitutive equation for estimating viscosity. Although simulation of turbulent flow of GN fluids using these numerical techniques, particularly DNS, show encouraging outcomes [14–16], the most fundamental flow prediction (flow rate versus pressure drop, or equivalently friction factor) is usually in error. In DNS of pseudo–plastic fluids, Rudman *et al.* [14] found that for a given pressure gradient the bulk velocity predicted by DNS was 25% lower than the experimental value. Given that the same code at a similar resolution was able to predict the turbulent flow of a Newtonian fluid to within a few percent, this level of error is unacceptable. The discrepancy between DNS and experiments could be due to the following factors:

1. Inaccurate experimental measurements;
2. Poor choice of simulation method and parameters in terms of method accuracy, simulation resolution, computational domain length and time duration over which results are averaged;
3. The rheology measurements and/or data fitting;
4. The assumption of a GN rheology model.

Given that the experimental techniques used for the pipe flow measurements reported in Rudman *et al.* are standard and were validated against well characterised water data, experimental error is believed to be far smaller than the observed discrepancy. Thus, the first point is unlikely to be the cause. A spectral element-Fourier method which is exponentially convergent [17] was used in that study and domain length and mesh convergence were ensured, therefore, the second point is also unlikely to be the cause. In their simulations, Rudman *et al.* observed that the instantaneous, local shear rates spanned many orders of magnitude and were predicted to be significantly higher than those values used in the rheological characterisation. They suggested that the extrapolation of the shear rheogram for estimating viscosity beyond the range of shear rate where it was measured lead to the observed discrepancy between simulation and experiment. Thus the third point remains a possibility. The assumption that a GN model is appropriate is a difficult one to demonstrate conclusively. Although it remains a possibility that the GN assumption is not valid, we do not consider this as an alternative here. We agree with the argument in Rudman *et al.*, and later demonstrate, that the majority of the discrepancy arises due to poor rheology characterisation at high shear rates. It is worth noting that for turbulent flow predictions using empirical correlations (for example Dodge & Metzner [2] and Wilson & Thomas [18]), the importance of high shear rate rheology has also been advocated by other researchers [2,7,19]. Shook & Roco [19] suggest that for turbulent flow predictions, the shear rheogram used in rheology characterisation should be measured to shear rates at least as high as those corresponding to the mean wall shear stress τ_w.

The objectives of the present study are three-fold. First we aim to show that shear rheograms determined using traditional approaches such as laminar pipe flow curves or rheometry measured at low shear rates, when extrapolated to shear rates relevant to turbulent flows can deviate significantly from the actual rheology. By including the high shear rate rheology of the fluid in rheological characterisation, discrepancies between experiments and predictions using DNS or empirical turbulent flow correlations can be significantly reduced. Second, if an appropriate range of shear rates is considered in the rheology characterisation, the choice of the rheology model has a very small effect on turbulent flow predictions of DNS or empirical correlations. The third objective of this study is to define a criterion for the maximum shear rate (and shear stress) to use in rheology characterisation in order for DNS to produce good results. In the process of determining this we analyse the shear rate distribution in turbulent pipe flow field for the first time. The results suggest that in the near-wall region, the probability distribution of non-dimensionlised instantaneous shear rate collapses to a universal distribution for different models, fluids and Reynolds numbers. Based on this observation we propose that for turbulent flow predictions of shear-thinning fluids, the rheology characterisation should use the rheogram measured at least up to twice the mean wall shear stress.

2. Pipe flow measurements

The pipe flow test apparatus is shown schematically in Fig. 1. It comprises a 14 m pipe loop ($\approx$300 diameters) with an internal diameter of 44.5 mm. A 400 litre agitated tank supplies a Warman $2 \times 1\frac{1}{2}$ AH variable speed pump for circulating fluids around the loop. The pressure gradients in both the upper and lower horizontal lines are measured using differential pressure (DP) cells spanning straight sections of pipe. The volumetric flow rate is monitored via a magnetic flow-meter. The rig instrumentation is data logged using a stand-alone LabVIEW application allowing the normal transport flow characteristics to be obtained in real time. In order to test the instrumentation a water-only flow curve was
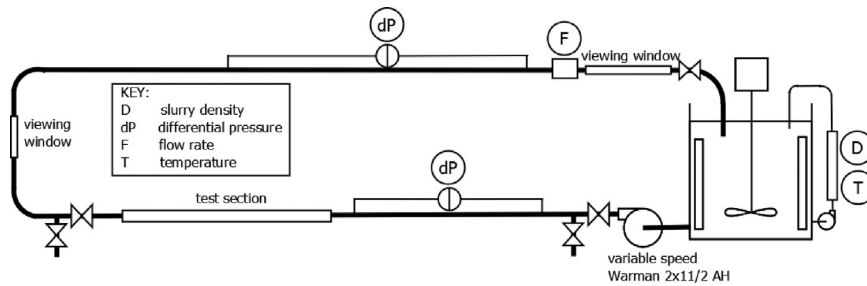
Fig. 1. Schematic of pipe rig.

obtained and compared against the established values for a hydraulically smooth pipe (based on pipe Reynolds number and Darcy–Weisbach friction factor). The agreement was within expected variations; $\pm$ 5% at a bulk velocity $U_b = 0.2$ m s^{-1} and $\pm$ 2% at $U_b = 3.0$ m s^{-1}. The majority of the measurement error arises from measuring at the low end of the pressure sensor. This implies that more accurate readings are probable for the Carbopol fluid under investigation, as the Carbopol fluid requires much higher pressure gradients than water.

For the data used in this study, 300 litres of Carbopol 980 solution was made and allowed to stabilise. The nominal concentration of the solution was 0.075 wt% and the solution was neutralised using sodium hydroxide to a pH between 6.5 and 7. The tests required a series of steady flow rate conditions to be established and pressure drop on both legs to be recorded and time-averaged. The pressure drop measurements were taken for flow rates from the laminar region to the turbulent. They were sampled at 0.5 Hz over a period of 300 s and time averaged. Spectral analysis was conducted on the data and no significant frequencies were detected, ensuring that the pressure readings are not affected by any unintended flow phenomena. The DP cells were 2 m apart and had an accuracy of 0.15% of full scale deflection, with a further allowance of 0.1% for ambient vibration effects. This equates to an uncertainty in pressure drop readings of $\pm$ 7.5 Pa m^{-1}. For a measured pressure gradient of 2500 Pa m^{-1} this corresponds to an error of 0.3%. The flow meter used had an accuracy of 0.25% which corresponds to an uncertainty of 0.007 m s^{-1} at a bulk velocity $U_b = 2.9$ m s^{-1}. The temperature of the fluid in the pipe loop could not be controlled but was monitored via a Platinum Resistance Thermometer (PRT) inserted in the stream outside of the pressure measurement zones and also in the tank. The PRT is able to measure reliably to $\pm$ 0.1 °C and a maximum variation of $\pm$ 0.2 °C was recorded in the course of a single run. Any inaccuracy in the measured fluid density is predominantly due to the temperature change. The fluid behaves similarly to water in this regard and the uncertainty in density is therefore less than 0.01%.

3. Rheology measurements and characterisation

3.1. Measurement

A wide range of shear rates is covered in the rheology measurements by using two different measurement geometries; a concentric cylinder and a parallel plate (see Table 1). Using different geometries also provides a mean of confirming data where the measurements overlap. A Haake Rheostress RS1 rheometer was used throughout and temperature control was maintained via a recirculating water bath, with test temperatures matched to those in the pipe flow measurements (see Section 2) within $\pm$ 0.1°C. The concentric cylinder geometry was used to measure the rheology in low to medium shear rate region (see Table 1). The larger surface area

Table 1
Details of the geometries used in the rheometry and corresponding shear rate range.

Geometry	Dimensions	Shear-rate range
Concentric cylinder	Inner-Cylinder dia.= 38 mm, Outer-Cylinder dia.= 41 mm	0.01 − 100 s^{-1}
Parallel plate	Plate-dia.= 60 mm, gap=0.2 mm	10 − 15000 s^{-1}

of this geometry provided shear stress measurements that were 2.9 times more sensitive than the parallel plate geometry. The upper range of the measurements in the concentric cylinder geometry was limited due to the inaccuracies caused by the onset of Taylor-Couette eddies, a secondary flow effect at high shear rates [20]. In the unaffected region the correct shear rate (allowing for the non-Newtonian fluid effect) was obtained by using an integration approach for the Couette inverse problem [21]. This method is generally more successful than a differential approach due to the inevitable noise present in real data. For the measurements in the medium to high shear rate region, a parallel plate geometry was used. As high shear rate rheometry necessitate small measurement gaps the alignment of our parallel plate geometry was tested using a camera with a macroscopic lens calibrated against a 0.1 mm graticule. The rheometer gap measurement consistently underestimated the distance in the order of 0.01 mm when compared to the optical technique. This would produce an error of the order of 5% with the 0.2 mm gap used and the shear rate was recalculated accordingly. In this geometry, the calculation of the rim shear stress corrected for non-Newtonian fluids required the differentiation of measured instrument torque as a function of shear rate at the rim [22]. Duplicate results from each geometry, after any necessary corrections, were combined and averaged in the overlapping shear rate regions.

3.2. Characterisation

To address the aims of the paper, a number of different rheology characterisations are performed on the measured data. The model parameters of these characterisations are shown in Table 2 and the corresponding shear rheograms for the full shear rate range (0.01 to 15 000 s^{-1}) are plotted in linear and log coordinates in Fig. 2. We use the term 'model' in two different contexts below. In the first, 'model' type refers to the mathematical form of the rheological model we fit to (power–law, Herschel–Bulkley etc.). In the second, 'model' means the mathematical form *plus* the fitted parameters that describe the best fit to the data. The meaning should be clear from the usage. The curve fitting exercise to determine the rheology parameters from the measured data is carried out using the `lsqcurvefit` function in MATLAB which determines a least-square fit to a non-linear data set.
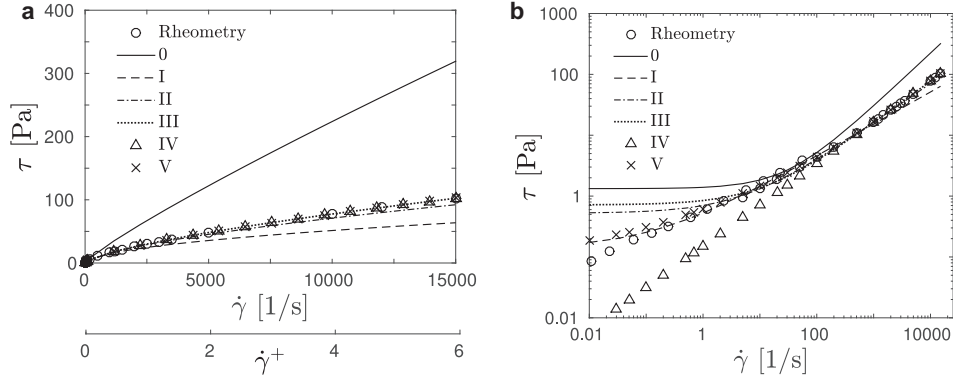
Fig. 2. Shear rheograms for different rheology models plotted in (a) linear and (b) log-log scales. Here $\dot{\gamma}^+ = \dot{\gamma}/(u_\tau^2/\nu_w)$ is the shear rate expressed in wall units. Low shear rate models *0* and *I* show large deviation from the measured rheology at high shear rates whereas high shear rate models *II–V* deviate from each other at very low shear rates.

Table 2

Rheology models determined using the laminar pipe flow curve and the measured shear rheogram with differing shear rate ranges. The first column is the rheology identifier, and the second column specifies what data was used in determining the model parameters.

Herschel–Bulkley		τ_y (Pa)	K (Pa.s$-n$)	n
0	laminar pipe flow data	1.33	0.067	0.88
I	[0.01, 500] s^{-1}	0.14	0.389	0.53
II	[0.01, 5 000] s^{-1}	0.52	0.177	0.65
III	[0.01, 15 000] s^{-1}	0.72	0.129	0.69
Power law			K(Pa.s^{-n})	n
IV	[0.01, 15 000] s^{-1}	–	0.15	0.68
Hallbom		τ_0(Pa)	μ_∞^k(Pa.s^{-k})	k
V	[0.01, 15 000] s^{-1}	0.0526	0.311	0.169

Model 0

In rheology model *0*, the Herschel–Bulkley model is fitted to the laminar pipe flow curve (see Section 2) using the analytical expression given in Eq. 4.

$$U_b = nR\left(\frac{\tau_w}{K}\right)^{1/n} (1-\phi)^{n+1/n} \left\{ \frac{(1-\phi)^2}{3n+1} + \frac{2\phi(1-\phi)}{2n+1} + \frac{\phi^2}{n+1} \right\}$$

(4)

Here, $\phi = \tau_y/\tau_w$ and τ_w is the mean wall shear stress calculated from the axial pressure gradient ($\tau_w = (D/4)dp/dz$). As seen in Fig. 2a and b, the shear rheogram of fit *0* deviates significantly from the measured data at both high and low shear rates. Worth noting in this regard is that the maximum shear rate (estimated from the analytical velocity profile) is ≈ 500 s^{-1}, however, rheology fit *0* fails to represent the rheology of the fluid accurately for shear rates $\dot{\gamma} > 100$ s^{-1}.

Models I–III

The rheogram obtained using the rheology measurement techniques described in Section 3.1 is used to fit the Herschel–Bulkley model over three different shear rate ranges to give models *I, II* and *III*, each with an increasing upper bound of maximum shear rate, (500 s^{-1}, 5000 s^{-1} and 15000 s^{-1}) and all with the lower bound of 0.01 s^{-1}.

The maximum shear rate considered in model *I* (500 s^{-1}) is typical of an industrial laboratory measurements and similar to the maximum implied in model *0*. As seen in Fig. 2a, model *I* clearly deviates below the measured rheology at shear rates $\dot{\gamma} > 1000$ s^{-1} indicating that the viscosity estimates using this rheology fit will be in error at high shear rates.

Rheology model *II* used the measured shear rheogram in the range of shear rate $\dot{\gamma} = 0.01 - 5000$ s^{-1}. This maximum shear rate is chosen based on an analysis of our DNS results where we observed that the instantaneous shear rates in the flow field were usually less than 5000 s^{-1} (see Section 5.3). This model deviates from the measured data for low shear ($\dot{\gamma} < 10$ s^{-1}) and a little for higher shear ($\dot{\gamma} > 5000$ s^{-1}).

Model *III* used the shear rheogram over the full range of measured shear rate data, i.e. $\dot{\gamma} = 0.01 - 15000$ s^{-1}.

Models IV and V

Model *IV* is based on the power–law model and model *V* is based on the Hallbom model. Both use data over the full range of measured shear rate, $\dot{\gamma} = 0.01 - 15000$ s^{-1}. We observed that the shear rheogram of the Hallbom model is very sensitive to the parameter μ_∞ (see Eq. 3) which is of order 10^{-5} Pa s^{-k}. Hence we choose μ_∞^k as the fitted parameter. As seen in Fig. 2a and b, the rheology predictions of models *IV* and *V* are good at high shear rates, although the power–law model deviates below the measurements for $\dot{\gamma} < 100$ s^{-1}. The Hallbom model agrees well for all shear rates $\dot{\gamma} > 1.0$ s^{-1}.

Summary

Except at very low shear rates (or 100 s^{-1} in the case of model *IV*), the rheograms of models *II–V* agree well with the measured data. Deviation, especially at quite low shear rates, highlights the difficulties associated with finding a universal model fit which can represent the rheology of a fluid over a very wide range of shear rates. The Hallbom model comes closest to fulfilling the condition of universality. For a given rheology model, the model parameters vary with the shear rate range used in rheology characterisation (see *I–III* in Table 2 for the Herschel-Bulkley fits). This highlights the fact that while a rheology model aims to capture the essence of the fluid rheology, the parameters determined from the curve fitting exercise usually have no direct physical basis in themselves.

It is worth noting that at lower shear rates, model fits to the rheometric data (models *I–V*) deviate significantly below model 0 (the rheology fit determined from the laminar pipe flow curve). Given that model 0 predicts the laminar flow behaviour very well, it is clear that laminar flow rate predictions using any of models *I–V* will likely be in error. An important corollary of this is that accurate prediction of laminar flow behaviour is no indicator of model performance in the turbulent flow through the same pipe and that such agreement cannot be used as validation data for turbulent flow prediction. Indeed, poor prediction in laminar flow does not automatically invalidate the accuracy of a model in turbulent flow, in direct contradiction to usually accepted practice with Newtonian fluids. As a final comment, rheology measurements at

low shear rates are difficult and most likely to be error-prone in normal measurement situations. We will later demonstrate that inadequacy of low shear rate rheology does not affect turbulent flow predictions significantly.

A note on visco-elasticity

Peixinho *et al.* (2005) [23] measured the rheology of a 0.2 wt% Carbopol solution and observed visco-elastic effects for shear stresses greater than approximately 110 Pa. The shear stress value for which visco-elasticity becomes important will increase with decreasing Carbopol concentration. Because the concentration used here is approximately 0.075 wt%, visco-elastic effects will not become noticeable for us until the shear stresses becomes significantly higher than 110 Pa. Even at the highest shear rates we measure (15 000 s^{-1}), the shear stress does not exceed 90 Pa. Thus our 0.075 wt% Carbopol solution can be confidently modelled as an inelastic fluid.

4. Computational methodology

4.1. Numerical method

A nodal spectral element-Fourier DNS code [15,17] is used to solve the following governing equations written for the flow of an incompressible GN fluid.

$$\partial \boldsymbol{v}/\partial t + \boldsymbol{v} \cdot \nabla \boldsymbol{v} = -\nabla p + \nabla \boldsymbol{\tau} + \boldsymbol{f}, \quad \text{with} \quad \nabla \cdot \boldsymbol{v} = 0. \tag{5}$$

Here $\boldsymbol{v}$ is the velocity vector, p is the modified or kinematic pressure i.e. pressure divided by a constant density, $\boldsymbol{\tau}$ is the shear stress tensor given by Eq. 1 where the viscosity μ is calculated using the rheology model. In Eq. 5, f is the constant body force per unit mass. which is set equal to the pressure gradient divided by density. The code uses Fourier expansions in the axial direction and thus strictly enforces axial periodicity. Simulations were run until the calculated total wall shear stress is statistically converged, usually it fluctuates a little about a mean value. Once this dynamic steady state is reached, mean fields and turbulence statistics are collected for approximately twenty domain wash-through times.

4.2. Non-dimensional units

Results are non-dimensionalised in the standard manner. The mean wall shear stress is related to the pressure gradient via

$$\tau_w = \frac{D}{4} \frac{\partial P}{\partial z}. \tag{6}$$

Here, D is the diameter of the pipe. The mean axial velocity U is expressed in wall units as $U^+ = U/u_\tau$ where $u_\tau^2 = \tau_w/\rho$. Distance from the wall is expressed in wall units as $y^+ = (R - r)u_\tau/\nu_w$ where ν_w is the mean wall viscosity, r is the radial distance from the centre of the pipe and R is the radius of the pipe. The mean wall viscosity is calculated directly from the pressure gradient via Eq. 6 and the rheology model. For the Herschel–Bulkley model ν_w is determined from the mean wall shear stress as:

$$\nu_w = \frac{K^{1/n}}{\rho} \frac{\tau_w}{(\tau_w - \tau_y)^{1/n}}. \tag{7}$$

For the power–law rheology model ν_w is easily recovered by setting $\tau_y = 0$ in Eq. 7. For the Hallbom rheology model, ν_w is calculated using the following expression [8]:

$$\nu_w = \frac{\mu_\infty}{\rho(1 - Z^k)^{1/k}}, \quad \text{with} \quad Z = \frac{\tau_0}{\tau_w} \tag{8}$$

The non-dimensional shear rate is expressed in wall units as $\dot{\gamma}^+ = \dot{\gamma}/(u_\tau^2/\nu_w)$.

Because viscosity is not uniform in GN fluids, the definition of a suitable Reynolds number is not immediately clear. Here we will use the mean wall viscosity ν_w as the viscosity scale and define a generalized Reynolds number Re_G and a friction Reynolds number Re_τ using the bulk velocity U_b and friction velocity u_τ. These Reynolds numbers are:

$$Re_G = \frac{U_b D}{\nu_w}, \quad \text{and} \quad Re_\tau = \frac{u_\tau D}{\nu_w}. \tag{9}$$

4.3. Resolution and domain independence

A grid resolution and domain independence study using rheology model *III* was performed to ensure that the mean flow profiles and turbulence statistics do not change with mesh refinement or domain length. The final mesh had 16,500 grid points in the pipe cross-section with 288 Fourier planes in the axial direction giving 5.6 M node points. The near-wall mesh spacings expressed in wall units (defined above) are $\Delta r^+ = 1.3$, $r\Delta\theta^+ = 7$ and $\Delta z^+ = 25$ which correspond well to typical rules-of-thumb for wall resolving DNS [24].

4.4. Wilson–Thomas correlation for friction factor

There are several empirical correlations commonly used for predicting the friction factor in turbulent flow of GN fluids [18,25–27]. Our aim here is to understand if the predictive capability of such correlations is also improved by the use of high shear rate rheometry. We choose one correlation, the Wilson–Thomas correlation [18], because it is easily expressed for the three rheology models we consider. This correlation relates the bulk velocity U_b and friction velocity $u_\tau = \tau_w/\rho$ via:

$$U_b = 2.5u_\tau \ln\left(\frac{Du_\tau}{\nu_w}\right) + u_\tau(11.6(\alpha - 1) - 2.5 \ln(\alpha)). \tag{10}$$

Here α is the ratio of the area of rheograms of the non-Newtonian and Newtonian fluids up to the mean wall shear rate $\dot{\gamma}_w$. For a given rheology model, the area under the rheogram is given by

$$A = \int_{\dot{\gamma}=0}^{\dot{\gamma}_w} \mu(\dot{\gamma})\dot{\gamma} d\dot{\gamma} \tag{11}$$

Solving the above integration for a Newtonian fluid gives $A = \frac{1}{2}\dot{\gamma}_w\tau_w$ and with the Herschel–Bulkley rheology model this gives $A = \dot{\gamma}_w(\tau_w + n\tau_y)/(n + 1)$. Hence, the area ratio for a Herschel–Bulkley fluid can be written as $\alpha = (2/(n + 1))(1 + n\tau_y/\tau_w)$. For the Hallbom rheology model a general expression for calculating α is written as [8]:

$$\alpha = \frac{2}{\dot{\gamma}_w} \int_{\dot{\gamma}=0}^{\dot{\gamma}_w} \left[\left(\frac{\tau_0}{\tau_w}\right)^k + \left\{1 - \left(\frac{\tau_0}{\tau_w}\right)^k\right\}\left(\frac{\dot{\gamma}}{\dot{\gamma}_w}\right)^k\right]^{1/k} d\dot{\gamma} \tag{12}$$

For integer values of $1/k$ the above integration can be solved directly, however, for non-integer values of $1/k$, this integration must be carried out numerically.

5. Results and discussion

We split the comparison of DNS and experimental results into two main parts. First is the effect that shear rate range used in the rheology characterisation has on the turbulent flow predictions. In the second, the effect that the rheology model type has on the comparison is considered, given the models are based on identical shear rate data.

The measured experimental flow data is shown in Fig. 3. There are two points in the transitional regime and two in the turbulent, and below we consider results primarily at the highest flow velocity, 2.90($\pm$ 0.01) m s^{-1}, with some additional comparisons at the next highest velocity, 2.70($\pm$ 0.01) m s^{-1}.
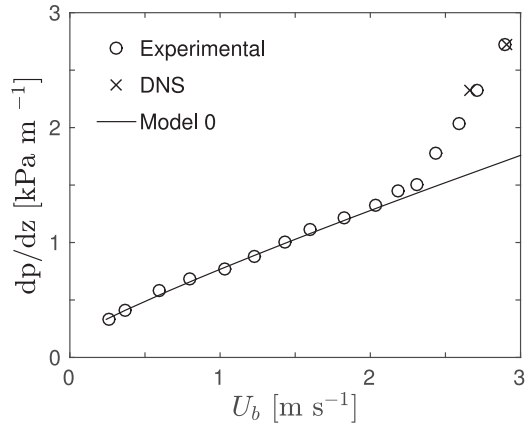
Fig. 3. Pressure gradient versus bulk velocity measured in (o) experiments and (x) predicted by DNS with rheology model *III*. The solid line is the laminar flow curve of model 0. The critical velocity of transition of flow from laminar to turbulent (identified as the point where the laminar flow curve deviates from the experimental data) is ≈ 2.3 m s^{-1}. DNS are run for the two highest bulk velocities measured in experiments i.e. $V = 2.70$ m s^{-1} and $V = 2.90$ m s^{-1}.

Table 3
Flow Reynolds number Re_G, Re_τ and the error in bulk velocity predictions using DNS and the Wilson–Thomas correlation (Eq. 10) at $dp/dz = 2.72$ kPa m^{-1}.

Rheology	Re_τ	Re_G	Error in DNS (%)	Error in Wilson–Thomas (Eq. 10) (%)
0	241	3500	−13	−12
I	887	16,000	8.3	19
II	666	11,300	1.2	10
III	633	10,600	0.3	7
IV	627	10,516	0.4	7.3
V	638	10,844	1.6	9.4

els for an axial pressure gradient $dp/dz = 2.72(\pm 7)$ kPa m^{-1}. The measured bulk velocity in experiments at this pressure gradient was $2.90(\pm 0.01)$ m s^{-1}. Predictions of the bulk velocity U_b using DNS and the Wilson–Thomas correlation are compared against the experimental value in Table 3. Given that rheology models 0 and *I* showed poor agreement with the measured rheology data, the large errors in predicted U_b with these models is expected (see Table 3). DNS underpredicts the bulk velocity U_b by 13% using model *0* whereas it overpredicts it by approximately 8% using model *I*. With high shear models *II* and *III*, DNS prediction of U_b comes very close to the experimental value (within 2%). Similar trends (although different magnitudes) are also seen in the prediction of U_b using the Wilson–Thomas correlation (Eq. 10) with the error decreasing to 7% with fit *III* compared to 19% with fit *I*.

Mean flow profiles are presented in Fig. 4a and b. For ease of discussion, we divide the flow into a wall-region ($y^+ < 10$), buffer-layer ($10 < y^+ < 30$), log-layer ($30 < y^+ < 200$) and core ($y^+ >$

5.1. Effect of the shear rate range in rheology characterisation

To consider the effect of shear rate range, we use models 0–*III* which are based on the Herschel–Bulkley rheology model but use different shear rate ranges. DNS are run using these mod-
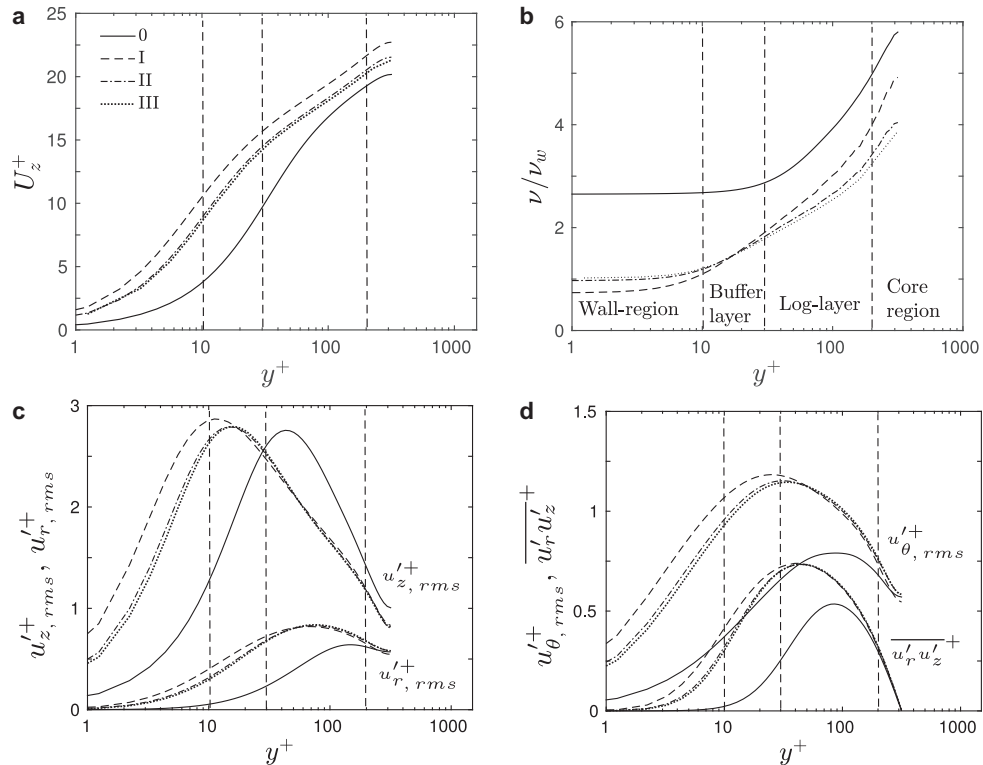
Fig. 4. The effect of shear rate range used in rheology characterisation in predicting flow at $dp/dz = 2.72$ kPa m^{-1}. All are Herschel–Bulkley models, with model 0 determined from the laminar pipe flow data and models *I*–*III* determined from increasing range of shear rate. Profiles of (a) mean axial velocity (b) mean viscosity and (c,d) the turbulence statistics. Division of the flow region based on the distance from the wall y^+ is shown in (b). The mean wall viscosity ν_w of fit *III* is used in calculating y^+. Profiles of low shear rate models *0* and *I* can be seen deviating from those of high shear rate models *II* and *III* which agree well with each other except the mean viscosity profiles where a small offset between the profiles of models *II* and *III* can be seen in log-layer and core-region.
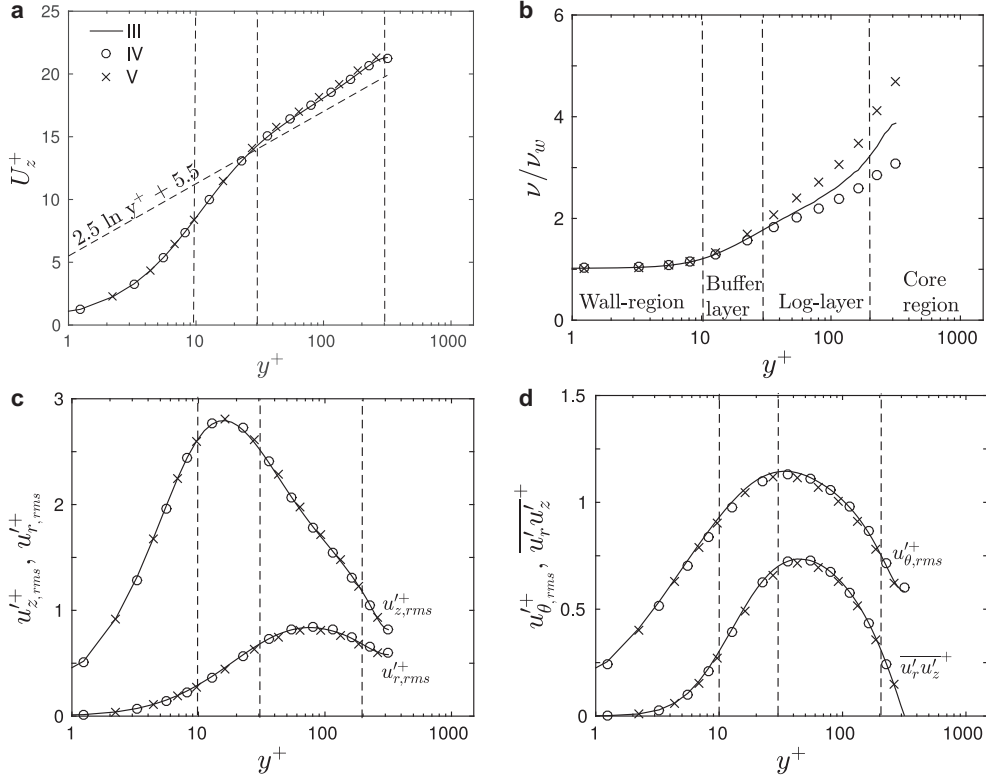
Fig. 5. The effect of rheology model type on mean flow profiles. Model *III* is Herschel–Bulkley, model *IV* is power–law and model *V* is a Hallbom model. Profiles of (a) mean axial velocity (b) mean viscosity and (c,d) turbulence statistics of different high shear rate models *III–V* at $dp/dz = 2.72$ kPa m^{-1}. The dashed line in (a) shows the classical Newtonian log law $U_z^+ = 2.5 \ln y^+ + 5.5$. The mean wall viscosity ν_w of model *III* is used to calculate y^+. Except mean viscosity, profiles of all rheology models agree very closely with each other.

200). Note that at such low Reynolds number ($Re_G \approx 10\,000$) splitting the flow into regions based on these numbers is somewhat arbitrary, however the results will later vindicate this choice. The general picture for models *I–III* is similar with a linear near-wall layer, a small log-like region and core that lifts very slightly above the log profile, not easily seen in the figure.

Results from model 0 have the hallmark of being a transitional flow without an obvious log-like region in the profile. This is in agreement with the higher viscosity predicted by this model at high shear rates. Consistent with the predictions of U_b, the mean axial velocity profiles of models *II* and *III* are close to each other and the profile of model *I* deviates (Fig. 4a). Note that ν_w of model *III* is used in non-dimensionalisation which ensures that if the profiles collapse in wall units, they will collapse in the physical units too. Hence, the results of different rheology models can be compared directly. If we scale the profiles, particularly of the mean axial velocity and viscosity, of different rheology models with their respective ν_w, the profiles would collapse in the wall region making it difficult to interpret the results.

The mean viscosity profile for each case is nearly uniform in the wall layer and appears to have a log-like region in part of the y^+ region corresponding to the velocity log-region, but then increases significantly toward the core of the flow. Rheograms of models *II* and *III* deviated from each other at low shear rates ($\dot{\gamma} < 50$ s^{-1}) (Fig. 2b) and this is reflected in the mean viscosity profiles in the log-layer and core. Note that this difference in mean viscosity does not affect the mean axial velocity profile to any notable extent.

Understanding the relationship between different rheology models and the resulting predicted velocity profile (and value of U_b) is straightforward. In a pipe flow, the total mean shear stress τ at any radial location r is given by

$$\tau = \tau_w \left(\frac{r}{R} \right). \tag{13}$$

In the wall region specifically, where the velocity fluctuations decay to zero, almost all of the stress is due to the mean viscosity. As seen from Fig. 4b the mean viscosity is nearly uniform in the wall layer. Together these two considerations allow us to write,

$$\tau_w \left(\frac{r}{R} \right) \approx \rho \nu_w \frac{\partial U_z}{\partial r} \tag{14}$$

or

$$\frac{\partial U_z}{\partial r} \approx \frac{\tau_w}{\rho \nu_w} \left(\frac{r}{R} \right) = \dot{\gamma}_w \left(\frac{r}{R} \right). \tag{15}$$

For a given τ_w, the viscosity profile that predicts a higher viscosity at a given shear will also result in a lower wall shear rate. From Eq. 15, lower shear rate equates to a lower increase in velocity with distance from the wall, at least within the wall region. Beyond the wall layer, the mean viscous shear stress decreases (and the viscosity increases) and differences in mean shear play less of a role in influencing the velocity profile and bulk velocity. The key influence occurs in the near-wall region. Thus overestimation of the viscosity by the rheology model will result in underestimation of the mean axial velocity, as seen for model 0 in Fig. 4a. Similarly, underestimation of viscosity will result in overestimation of
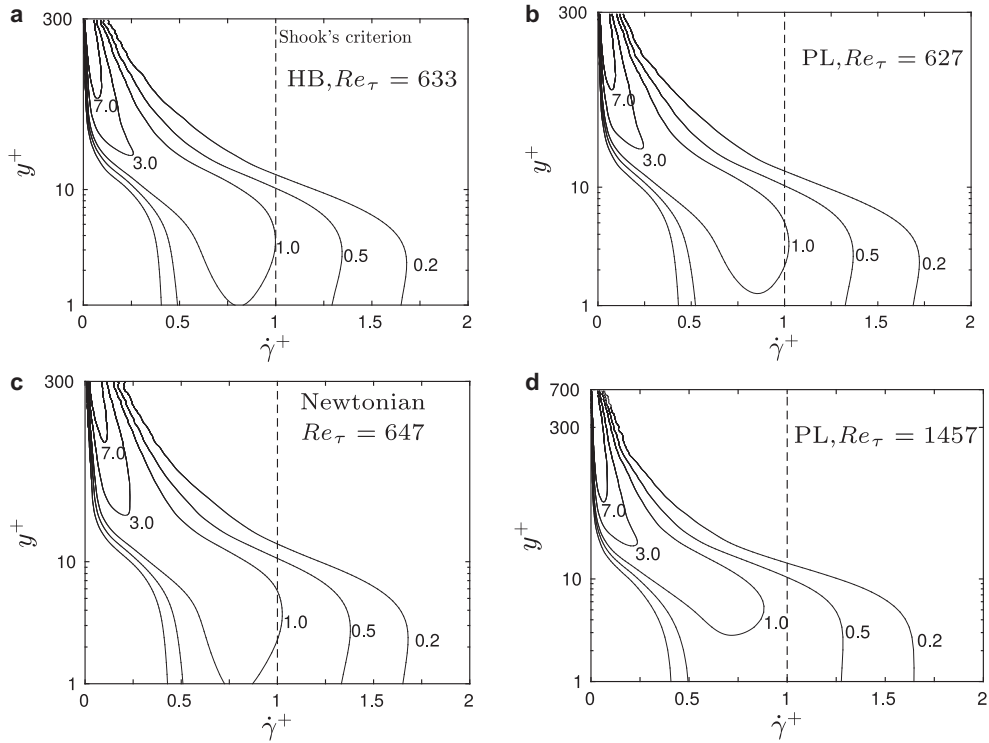
Fig. 6. Distribution of the conditional probability $p(\dot{\gamma}^+|y^+)$ of a fluid with (a) Herschel–Bulkley rheology *III* at $Re_\tau = 633$ (b) power–law rheology *IV* at $Re_\tau = 627$ (c) Newtonian rheology at $Re_\tau = 647$ and (d) the power–law rheology at $Re_\tau = 1457$. Contours are of % probability. The spread of the probability distribution of instantaneous shear rate near the wall when plotted in wall units is almost independent of the rheology and Re_τ.

the mean axial velocity, as seen for model *I*. This explains why the difference in rheograms for models *II* and *III* at low shear rates is reflected only in the mean viscosity profiles (Fig. 4b) and not in the mean axial velocity profiles (Fig. 4a). Profiles of the rms velocity fluctuations and Reynolds stress predicted using rheology models *II* and *III* are shown in Fig. 4c and d. They also agree well with each other and deviate only slightly in the wall-region and the buffer-layer. Again, the near-wall, high shear rheology of these two models is similar and results in similar turbulence statistics, despite the differences in predicted viscosity at low shear rates that are typical of the core region.

Additional DNS were run using models *II* and *III* at a lower pressure gradient of $dp/dz = 2.33$ kPa m^{-1}. The flow at this pressure gradient is closer to transition. Similar results were observed to the case of 2.72 kPa m^{-1}, with the error in DNS predictions of U_b being -1% with model *II* and -1.77% with model *III*. The corresponding errors obtained using the Wilson–Thomas correlation were 5% and 6.5%.

Summary

These results show that the error introduced in the rheology characterisation by neglecting high shear rate data, can lead to large discrepancies between experiments and predictions using either DNS or the Wilson–Thomas correlation. Discrepancies between the results from DNS and experiments are largely due to incorrect viscosity estimates in the wall-region.

5.2. Effect of rheology model type

As seen in Section 3 and Fig. 2, it is possible to obtain constitutive equations based on different rheology model types (models *III–V*) which agree closely with each other over most of the shear

rate range. These models only deviate from each other significantly at shear rates $\dot{\gamma} < 100$ s^{-1}. Based on the results in Section 5.1, we hypothesise that provided high shear rate rheology is used in rheology characterisation, the choice of rheology model type will have a negligible effect on turbulent flow predictions using either DNS or the Wilson–Thomas correlation. In order to test this hypothesis, additional DNS are run using rheology models *IV* (power–law) and *V* (Hallbom) for a pressure gradient $dp/dz = 2.72$ kPa m^{-1}.

As seen in Table 3 the bulk velocity predictions using DNS or the Wilson–Thomas correlation with rheology fits *III–V* are close to each other, validating our hypothesis. Similar agreement is seen for the mean axial velocity profile and turbulence statistics where the profiles of models *III–V* overlap each other (Fig. 5). Again the effect of the deviation in the model rheograms is limited to the predicted mean viscosity profiles in the log-layer and the core-region. The reason, also explained in Section 5.1, is that the shear rates are very low in the log-layer and the core-region. Therefore, the shear stress tensor and hence the predictions of the mean axial velocity and the turbulence statistics are affected notably by the deviation in viscosity estimates in the log-layer and the core-region.

5.3. A criterion for the maximum shear rate needed in rheology characterisation

Results presented in Section 5.1 and 5.2 show that high shear rate data is required in rheology characterisation in order to obtain good agreement between the results from experiments and DNS. It has also been shown that it is relevant in obtaining better agreement in the use of empirical correlations, in particular the
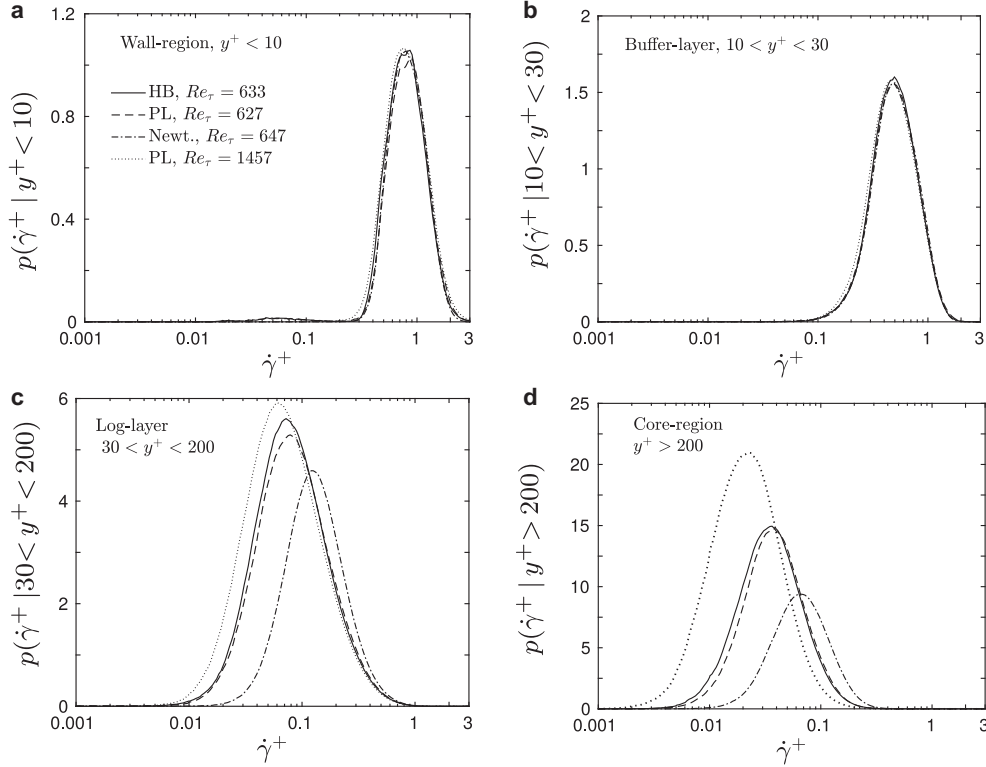
Fig. 7. Profiles of $p(\dot{\gamma}^+|y^+)$ plotted as a function of $\dot{\gamma}^+$ in (a) wall-region (b) buffer-layer (c) log-layer and (d) the core-region for the cases from Fig. 6. Profiles of the probability distribution of different rheology and Re_τ overlap each other in the wall-region and buffer-layer. In wall units, the profiles show rheology and Re_τ dependence only in the log-layer and core-region.

Wilson–Thomas correlation. However, the obvious question is yet to be answered, "How high is high enough?".

To provide some rigour in developing an answer to this question, instantaneous shear rate distributions in the turbulent flow DNS are analysed using conditional probability densities. This approach identifies the range of shear rates in different parts of the flow volume. The conditional probability density function (pdf) $p(\dot{\gamma}^+|y^+)$ is defined as the probability that the shear rate is equal to $\dot{\gamma}^+$ given that the distance from the wall is given by y^+. It is normalised such that

$$\int_{y^+=0}^{R^+} \int_{\dot{\gamma}=0}^{\infty} p(\dot{\gamma}^+|y^+) d\dot{\gamma}^+ dy^+ = 1. \tag{16}$$

This definition then allows the marginal pdf to be written as a constant

$$p(y^+) = \int_{\dot{\gamma}=0}^{\infty} p(\dot{\gamma}^+|y^+) d\dot{\gamma}^+ = 1/R^+ \tag{17}$$

Thus the probability density is weighted by distance (not by area). This is not the only way to normalise the distribution, however it allows more direct comparison with channel flow results by removing the effect of the radial coordinate from the definition.

The full conditional probability density function is calculated in the current simulations for rheology models *III* and *IV* in which $Re_\tau \approx 630$ (results for model *V*, the Hallbom model, are almost indistinguishable and are not shown). The pdf's are compared with those from our unpublished DNS results of a Newtonian fluid at $Re_\tau = 647$ and a pseudo–plastic fluid modelled with the power–law rheology model at $Re_\tau = 1457$ in Fig. 6. The qualitative picture is very similar for all cases. Decrease in the shear rate magnitude with distance from the wall can be seen clearly in the con-

tour plots of $p(\dot{\gamma}^+|y^+)$. The distribution of shear rate is wider near the wall and much narrower (and at lower shear rate) towards the centre of the pipe where the probabilities are also significantly higher. Considering the near-wall shear rates in particular, a large region of non-negligible probability exists for shear rates $\dot{\gamma}^+ > 1$. This suggests that Shook's criterion, (expressed here as $\dot{\gamma}^+_{max} = 1$), underestimates the shear rates that bracket the relevant near-wall values, and is not high enough to capture around half of the range that is important.

An alternative way of presenting the same information is to average the conditional pdf's over ranges of y^+ corresponding to the wall, buffer, log and core regions of the flow. This more clearly highlights similarities and differences between the cases. Averaged pdf's are presented in Fig. 7. In the wall region, profiles of $p(\dot{\gamma}^+|y^+)$ collapse quite well onto the same profile for different rheologies and at two different Re_τ. The same is observed in the buffer layer, although the profile is different to near-wall, with higher probability and a lower value at which the probability peak occurs. Moving away from the wall, the distributions begin to separate in the log layer and become significantly different in the core. Most notable in the core is that the probability peak for the Newtonian fluid is at a higher shear rate than the two non-Newtonian fluids at similar Re_τ. This behaviour is expected. Although the mean viscosities of the non-Newtonian cases match the Newtonian case at the wall, viscosites are higher in the core for shear-thinning fluids. Consequently shear rates will be lower. The profile for the higher Re_τ power–law case is shifted to lower non-dimensional shear rate and demonstrates that shear rates in the core do not increase linearly with increasing mean wall shear (i.e. increasing Re_τ).

In the near-wall region the profiles of the probability distribution in Fig. 7a (i.e. $p(\dot{\gamma}^+|y^+ < 10)$) spread as high as $\dot{\gamma}^+ \approx 3$ but the value of the probability for $\dot{\gamma}^+ > 2$ is less than 0.1, indicating that the total flow volume with shear rates higher than this is very small. The condition $\dot{\gamma}^+ > 2$ corresponds to $\dot{\gamma} > 5000 \text{ s}^{-1}$ for $Re_\tau \approx 630$. The collapse of these probability profiles in the near-wall are suggestive of a universal near-wall shear rate distribution, although further simulation are required to confirm this collapse for a broader range of the rheologies (in particular with higher yield stress) and for other values of Re_τ. Based on these observations we propose that the maximum shear rate $\dot{\gamma}^+_{max}$ in the rheology characterisation should be 2. This criterion can further be expressed in terms of shear stress using the constitutive equation of rheology model. For the Herschel–Bulkley model it is straight forward to show:

$$\tau/\tau_w = \tau_y/\tau_w + \frac{K}{\rho U_\tau^{2(1-n)} \nu_w^n}(\dot{\gamma}^+)^n \qquad (18)$$

With $\dot{\gamma}^+_{max} = 2$ this equation can be rewritten to give τ_{max} as

$$\tau_{max}/\tau_w = 2^n - (2^n - 1)\tau_y/\tau_w \qquad (19)$$

For shear thinning Herschel–Bulkley fluids, Eq. 19 is a maximum when n approaches one and the yield stress approaches zero, i.e. the maximum value it can take is 2. Hence, in terms of all shear thinning Herschel–Bulkley fluids, using rheology characterisation at shear stresses given by $\tau_{max} = 2\tau_w$ will provide a margin of safety in the measurements.

6. Conclusions

This study shows that choosing an appropriate shear rate range in rheology characterisation is crucial in obtaining good turbulent flow predictions using DNS and influences in a positive way the results obtained from the Wilson–Thomas correlation. Standard methods of determining rheology model parameters such as using the laminar pipe flow curve or from low shear rate rheograms, can result in large error in turbulent flow predictions. Fundamentally, this study shows the familiar dangers associated with extrapolation of data. It serves as a reminder to practitioners that extrapolating rheology outside the range where it was measured can result in unreliable predictions using DNS or empirical correlation.

Results obtained with three simple rheology models namely the power–law, Herschel–Bulkleyand the Hallbom models, which are commonly used in applications, show that if an appropriate range of shear rate is considered in the rheology characterisation, the model type has a little effect on turbulent flow predictions. This means that using a more complex rheology model or using a piece-wise fit to the rheology data to improve the accuracy of the model at lower shear rates will not have a significant effect on the turbulent flow predictions using DNS or the Wilson–Thomas correlation. The effect of errors introduced at low shear rates due to poor rheology measurements or poor fitting were found to be limited to the mean viscosity predictions in the log-layer and core-region. They do not affect the profiles of the mean axial velocity or the turbulence statistics to any notable extent.

In the near-wall region and the buffer-layer where shear rates are highest, the conditional probability distributions of non-dimensionalised, instantaneous shear rates are found to be essentially independent of rheology and Reynolds number. Based on this observation we propose that the maximum shear rate in rheology characterisation should be at least twice the mean wall shear rate. When expressed in terms of shear stress, Eq. 19 provides the same criteria, although using the simpler value of twice the mean wall shear stress will provide a margin of safety.

The comparison between DNS and experiments presented in the current study is based entirely on bulk velocity because velocity profiles and turbulence statistics could not be measured in the current experimental facility. However, the previous comparisons [14] to experimental mean flow profiles showed the DNS was able to predict the correct form (but not magnitude) of the profiles. When coupled to a demonstration of the correct integrated velocity, demonstrated in this paper, the results collectively suggest the complete picture is likely to be correct. However, only consistent measurement will prove this conclusively.

We note that Peixinho *et al.* [23] carried out pipe flow measurements in the turbulent regime using a 0.2 wt% Carbopol solution and measured the rheology at high shear rates. However, the Carbopol fluid used in their study was acknowledged to show viscoelastic effects at Reynolds numbers they considered i.e. the fluid showed a partial recovery when the applied shear stress is removed. Therefore, their experimental measurements could not be used in the current study for validation purposes as visco-elastic effects are likely to be influencing the measurements.

As a final point, although we advocate the use of high shear rate rheology in rheological characterisation, in practice it could be very difficult to measure such rheology in fine particle mineral suspensions such as the mining and waste slurries that have motivated this study. In these fluids centrifugal effects in most rheometric methodologies will tend to separate the solids-even for very small particles. Accurate rheology measurement of these fluids at high shear rates therefore remains an open problem.

References

[1] A.B. Metzner, J.C. Reed, Flow of non-newtonian fluids – correlations for laminar, transition and turbulent flow regimes, A. I. Ch. E. J. 1 (1955) 434–444.
[2] D.W. Dodge, A.B. Metzner, Turbulent flow of non-Newtonian systems, A. I. Ch. E. J. 5 (1959) 189–204.
[3] R.M. Clapp, Turbulent heat transfer in pseudoplastic non-Newtonian fluids, in: International Development in Heat Transfer, 1961, pp. 652–661.A. S. M. E., Part 111, Sec. A.
[4] D.C. Bogue, A.B. Metzner, Velocity profiles in turbulent pipe flow. Newtonian and non-Newtonian fluids, Ind. Eng. Chem. Fundam. 2 (2) (1963) 143–149.
[5] J. Park, T. Mannheimer, T. Grimley, Pipe flow measurements of transparent non-Newtonian slurry, J. Fluids Eng. 111 (3) (1989) 331–336.
[6] F.T. Pinho, J.H. Whitelaw, Flow of non-Newtonian fluids in a pipe, J. non-Newtonian Fluid Mech. 34 (1990) 129–144.
[7] R. Chhabra, J. Richardson, Non-Newtonian Flow and Applied Rheology, second ed., Elsevier, 2008.
[8] D.J. Hallbom, Pipe flow of homogeneous slurry, Citeseer, 2008 Ph.D. thesis.
[9] W.H. Herschel, R. Bulkley, Measurement of consistency as applied to rubber-benzene solutions, Proc. Annu. Meet. Am. Soc. Test Mater. 26 (1926) 621–633.
[10] D. Hallbom, B. Klein, A physical model for yield plastic fluids, Particul. Sci. Technol. 27 (1) (2009) 1–15.
[11] R. de Kretser, P.J. Scales, D.V. Boger, Improving clay-based tailings disposal: case study on coal tailings, AIChE J. 43 (7) (1997) 1894–1903.
[12] N. Heywood, D.-H. Cheng, Comparison of methods for predicting head loss in turbulent pipe flow of non-Newtonian fluids, Trans. Inst. of Meas. Control 6 (1) (1984) 33–45.
[13] E.V.d. Heever, A. Sutherland, R. Haldenwang, Influence of the rheological model used in pipe-flow prediction techniques for homogeneous non-newtonian fluids, J. Hydraulic Eng. 140 (12) (2014) 04014059.
[14] M. Rudman, H.M. Blackburn, L.J.W. Graham, L. Pullum, Turbulent pipe flow of shear–thinning fluids, J. Non-Newt. Fluid Mech. 118 (1) (2004) 33–48.
[15] M. Rudman, H.M. Blackburn, Direct numerical simulation of turbulent non-Newtonian flow using a spectral element method, Appl. Math. Mod. 30 (2006) 1229–1248.

[16] S. Guillou, R. Makhloufi, Effect of a shear-thickening rheological behaviour on the friction coefficient in a plane channel flow: a study by Direct Numerical Simulation, J. Non-Newt. Fluid Mech. 144 (2007) 73–86.

[17] H.M. Blackburn, S.J. Sherwin, Formulation of a galerkin spectral element—fourier method for three-dimensional incompressible flows in cylindrical geometries, J. Comput. Phys. 197 (2) (2004) 759–778.

[18] K.C. Wilson, A.D. Thomas, A new analysis of the turbulent flow of non-newtonian fluids, Can. J. Chem. Eng. 63 (4) (1985) 539–546.

[19] C. Shook, M. Roco, Slurry Flow, Butterworth-Heinemann, 1991.

[20] G.I. Taylor, Stability of a viscous liquid contained between two rotating cylinders, Philos. Trans. R. Soc. Lond. series a 223 (1923) 289–343.Containing Papers of a Mathematical or Physical Character

[21] W.C. MacSporran, Direct numérical evaluation of shear rates in concentric cylinder viscometry, J. Rheology (1978-present) 30 (1) (1986) 125–132.

[22] K. Walters, Rheometry/K.Walters, Vol. 1, Chapman and Hall, New York, London, 1975.distributed by Halstead Press

[23] J. Peixinho, C. Nouar, C. Desaubry, B. Thron, Laminar transitional and turbulent flow of yield stress fluid in a pipe, J. Non-Newtonian Fluid Mech. 128 (23) (2005) 172–184.

[24] U. Piomelli, Large-eddy simulations: where we stand, in: C. Liu, Z. Liu (Eds.), Advances in DNS/LES, AFOSR, Greyden Press, 1997, pp. 93–104. Louisiana

[25] E.J. Garcia, J.F. Steffe, Comparison of friction factor equations for non-newtonian fluids in pipe flow, J. Food Process Eng. 9 (2) (1986) 93–120.

[26] J. Hartnett, M. Kostic, Turbulent friction factor correlations for power law fluids in circular and non-circular channels, Int. Commun. in Heat Mass Transf. 17 (1) (1990) 59–65.

[27] P. Gao, J.-J. Zhang, New assessment of friction factor correlations for power law fluids in turbulent pipe flow: a statistical approach, J. Cent. S. Univ. Technol. 14 (2007) 77–81.

<div style="text-align: right; font-size: 3em;">5</div>

The effect of yield stress and shear thinning on turbulent pipe flow

The work presented in the previous chapter identified the cause of discrepancies between DNS and experiments in earlier studies [83, 85] and thus gives confidence in modelling turbulent flow of GN liquids using DNS. In this chapter, DNS is used to study the effects of modifying flow index and yield stress on a turbulent pipe flow. The generalised Reynolds number in the current study is approximately $10\,000$ which is higher than earlier DNS studies of GN liquids [83, 84] and therefore, presents a wider range of length and time scales in the flow. The findings of power-law liquids reported in this chapter have been accepted for publication in the Journal of Fluid Mechanics.

5.1   The effect of shear thinning

The effect of shear thinning (decreasing n) is studied via simulations of power-law (PL) liquids with the flow index $n \in [0.4, 1.2]$. The friction Reynolds number is fixed at $Re_\tau = 323$ by fixing the axial forcing g and the nominal wall viscosity ν_w (see Eq. 2.11 and Eq 3.4). For this Re_τ, the generalised Reynolds number Re_G slightly varies from $10\,000 - 12\,000$ and the Metzner–Reed Reynolds number

varies from approximately $4\,000$ to $15\,000$. The simulation parameters are given in table 5.1 and the fluid viscosity for these cases is plotted against the shear rate in figure 5.1. It can be seen that decreasing the flow index (shear thinning) affects the viscosity at all shear rates except at the wall value ($\dot{\gamma}^+ = 1$) where a fixed value is forced for all n.

Table 5.1 Simulation parameters for pipe flow at $Re_\tau = 323$ for different n. The non-dimensional body force gR/u^{*2} and the nominal wall viscosity $\nu_w/(u^*R)$ are 2 and $1/323$ respectively.

n	$K/(\rho u^{*2-n} R^n)$	Re_G	Re_{MR}
0.4	9.9080×10^{-2}	11862	4291
0.6	3.1181×10^{-2}	11189	5498
0.8	9.8128×10^{-3}	10681	7401
1.0	3.0870×10^{-3}	10322	10322
1.2	9.7179×10^{-4}	10106	14784
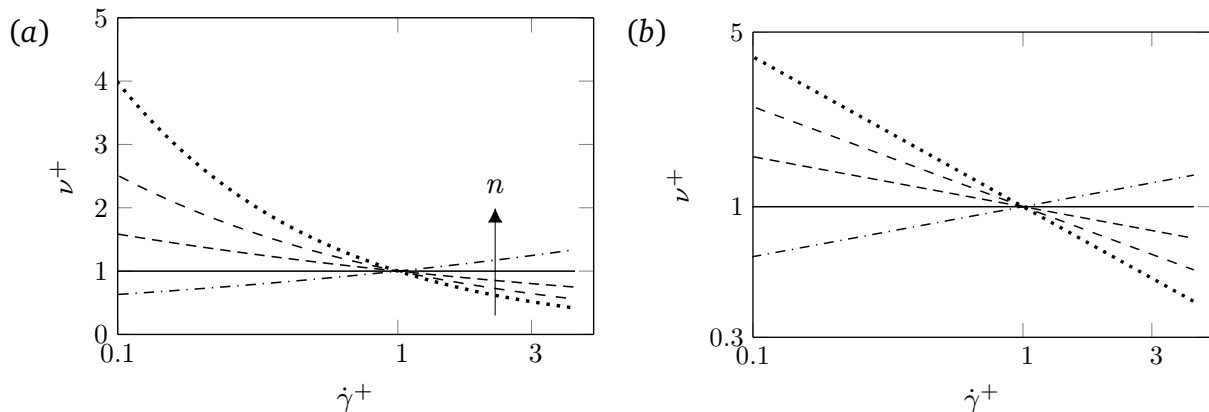
Fig. 5.1 Non-dimensionalised viscosity plotted as a function of non-dimensional shear rate for different n (see table 5.1 for the values of rheology parameters) plotted on (*a*) linear-log axes and (*b*) on log-log axes. In this and subsequent figures, arrows labelled n indicate the direction of increasing flow index.

5.1.1 Observations of instantaneous flow

The effect of flow index n on instantaneous flow structures is shown in figures 5.2 and 5.3. Finer scale structures are observed with increasing n, which is seen clearly in the contours of axial velocity and viscosity plotted on a pipe cross section in figure 5.2 and in the near wall streaks shown in figure 5.3 (*a*) and (*f*).

The finer scales also correspond to higher frequency motions, although later it will be seen that they are also associated with lower turbulent kinetic energy. The longer, wider low-speed streaks seen in figure 5.3 for lower n are associated with reduced wall normal turbulence intensities by shear thinning which will be discussed in section 5.1.2. There are qualitative correlations evident between the surface contours on adjacent surfaces indicating the radial extent of these structures demonstrating the imprint of the outer flow on near wall fluctuations [56].
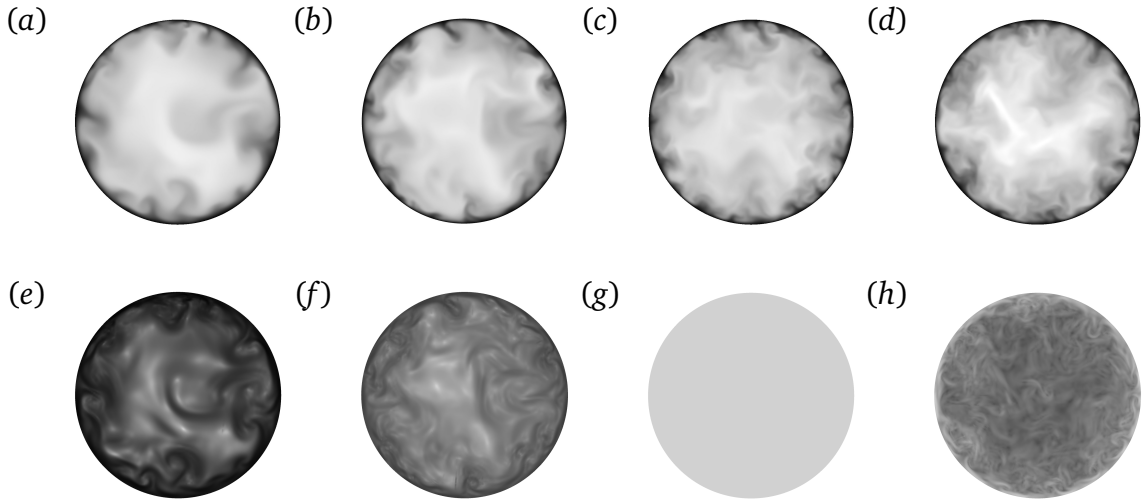
Fig. 5.2 Top row: contours of instantaneous axial velocity normalised by the bulk velocity U_b (0 is black, 1.4 is white). Bottom row: contours of instantaneous viscosity normalised by the maximum viscosity (0.1 is black, 1.0 is light grey). From left to right, flow indices are (a,e) $n = 0.6$ (b,f) $n = 0.8$, (c,g) $n = 1.0$ and (d,h) $n = 1.2$. Velocity and viscosity contours are plotted for the same time instant for each n.

The information presented in figure 5.3 can be quantified using the velocity integral length scale which is a measure of the characteristic correlation distance between velocity fluctuations at two points in the flow field. Here, the streamwise velocity integral length scale, l_z, is calculated by integrating the two point autocorrelation function (Eq. 3.11) to the point where it first crosses zero. As expected from the qualitative information in figure 5.3, l_z increases with decreasing n at all y^+ (figures 5.4a, b). At $y^+ = 10$ it decreases from approximately 60 for $n = 1$ to around 100 for $n = 0.6$. This suggests that axial velocity fluctuations are correlated for a longer distance for lower n. For all flow
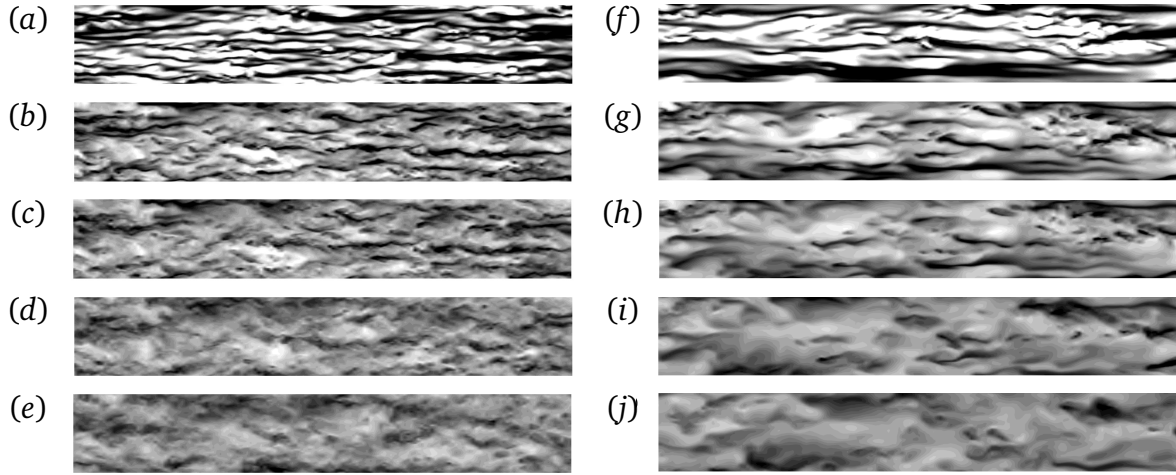
Fig. 5.3 Contours of instantaneous axial velocity fluctuations normalised by the local mean axial velocity at $y^+ = 10, 30, 45, 70, 100$ (from top to bottom) for (*a-e*) Newtonian and (*f-j*) $n = 0.6$ plotted on surfaces of constant y^+. White represents positive fluctuation and black negative. Contours have been stretched azimuthally to maintain the same vertical extent.
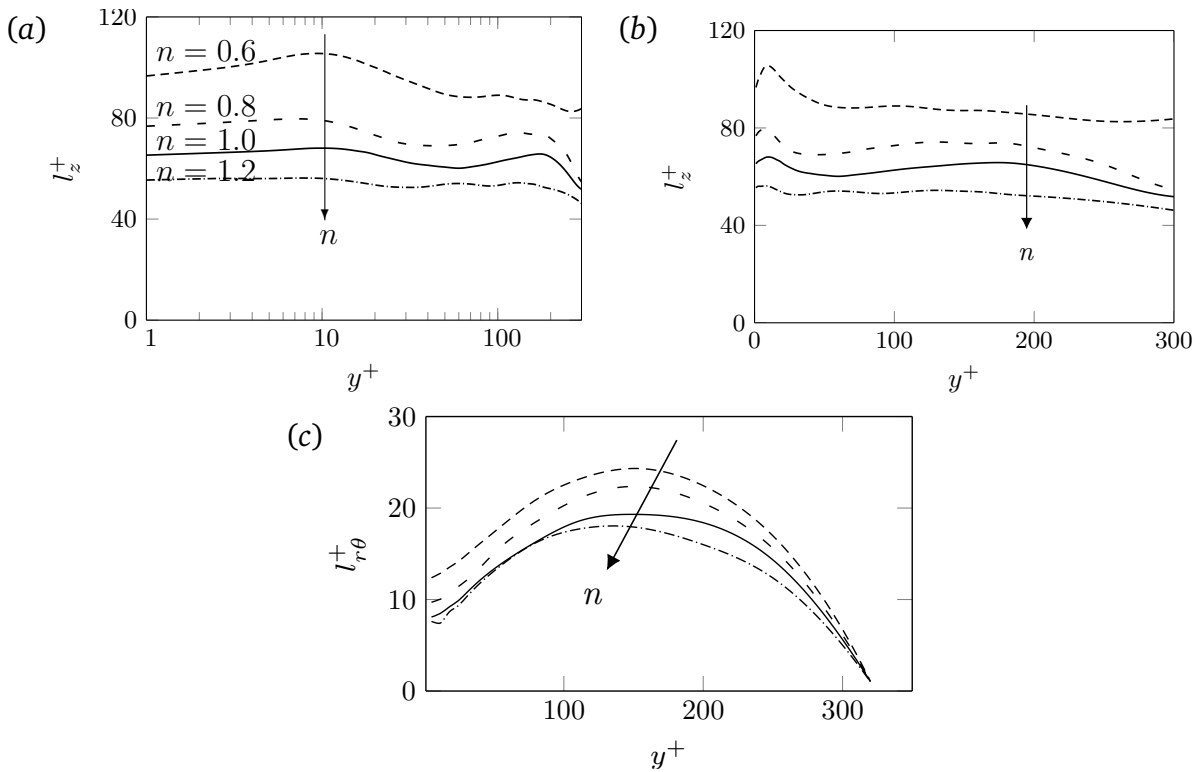
Fig. 5.4 (*a,b*) Streamwise integral length scales (*c*) azimuthal integral length scale plotted as functions of y^+.

indices, the maximum l_z occurs at $y^+ \approx 10$ with the exact location slightly shifting

away from the wall with decreasing n (figure 5.4b). Azimuthal length scales near the pipe wall follow a similar trend with n (figure 5.4c).

5.1.2 Mean flow and turbulence statistics

Mean axial velocity and viscosity

The mean axial velocity (U_z^+) profiles of different n show little variation when plotted in outer variables (not shown) and the differences are seen when they are plotted in wall coordinates (figure 5.5a). For ease of discussion, the flow domain is nominally divided into four regions – the viscous sublayer ($y^+ < 5$), buffer layer ($5 < y^+ < 30$), log layer ($30 < y^+ < 200$) and core region ($y^+ > 200$). Although this flow domain subdivision is common for Newtonian liquids [78], it will be seen later that the delineation is not as obvious for GN liquids.

In Newtonian liquids, it is well known that the mean axial velocity profile in the viscous sublayer follows $U_z^+ = y^+$ which is the near-wall form of the law of the wall [78]. A similar viscous sublayer was anticipated in the analyses of Dodge and Metzner [35] and Clapp [27] for PL liquids. A viscous sublayer appears in the mean axial velocity profiles for $n \neq 1$ in figure 5.5a, however, a close examination shows that the profiles for different n deviate slightly from the Newtonian case. This is more clearly seen in figure 5.5 (b) where the difference (ΔU_z^+) between U_z^+ of the PL and Newtonian liquids is plotted against y^+. For all y^+, the ΔU_z^+ profiles for shear thinning GN liquids lie above the Newtonian profile (and *vice versa* for shear-thickening). In all subsequent discussion, when a trend is described as occurring with shear thinning ($n < 1$), it should be taken as read that the opposite trend occurs with shear thickening ($n > 1$) unless otherwise explicitly mentioned.

Although the effect of flow index is seen at all y^+, ΔU_z^+ profiles deviate significantly only beyond $y^+ \approx 10$. The maximum ΔU_z^+ occurs somewhere in the log layer with the exact location depending on the value of n. Note that the area integral of ΔU_z^+ at a cross section represents the excess bulk flow rate. Higher values of ΔU_z^+ indicate higher bulk flow (hence higher U_b) for lower n indicating drag reduction as also reported in previous studies [35, 83, 84].
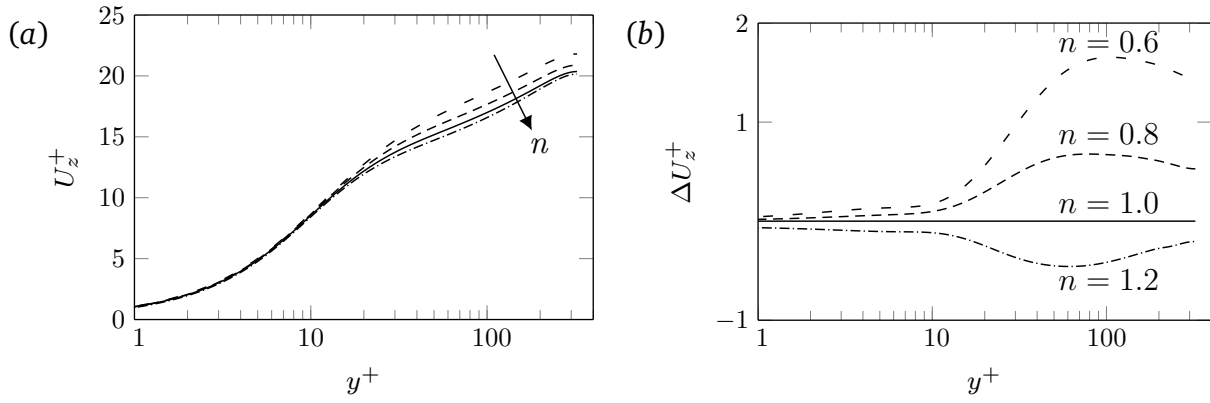
Fig. 5.5 Profiles of (a) mean axial velocity U_z^+, and (b) difference between U_z^+ for a non-Newtonian and Newtonian fluid plotted against y^+.
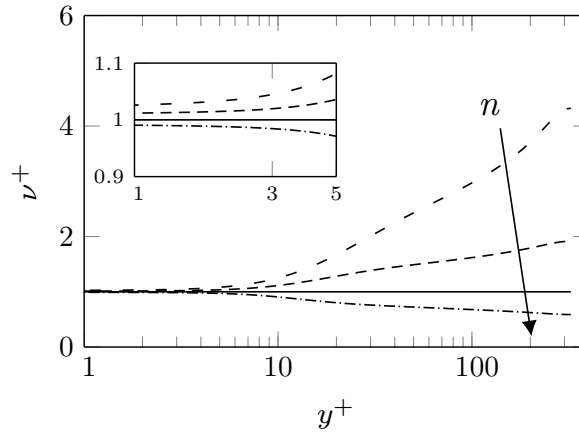
Fig. 5.6 Profiles of the normalised mean viscosity $\nu^+ = \bar{\nu}/\nu_w$, plotted as a function of y^+. Detail in the viscous sublayer is shown in the inset figure.

Profiles of the normalised mean viscosity, $\nu^+ = \bar{\nu}/\nu_w$, show only minor dependence on n for $y^+ < 10$ with values slightly higher for lower n (figure 5.6). At $y^+ = 10$, the mean viscosity $\bar{\nu}$ is 25% higher than the nominal wall viscosity ν_w for $n = 0.6$ and 10% lower for $n = 1.2$. As viscosity of a shear-thinning fluid increases with decreasing shear rate, we expect the mean viscosity ν^+, to increase monotonically towards the centre of the pipe for a shear-thinning fluid as observed. For all $n \neq 1$, mean viscosity profiles deviate rapidly from the wall value beyond $y^+ = 10$. The profiles of ν^+ appear to display a log like region over the range $20 \lesssim y^+ \lesssim 200$, although the reasons for this are not yet understood.

Mean shear stress budget

Noting that the mean shear stress is zero at the pipe centre and reaches a maximum τ_w at the wall, integration of the Reynolds-averaged Navier–Stokes equation, Eq. 3.6, leads to the following expression for the (r, z) component of the mean non-dimensional shear stress:

$$\tau_{rz}^{+} = \tau_{rz}^{v+} + \tau_{rz}^{R+} + \tau_{rz}^{fv+} = \frac{r}{R} = \left(1 - \frac{y^+}{R^+}\right). \tag{5.1}$$

In a fully developed pipe flow, only the (r, z) component of the mean shear stress component remains, therefore, subscript rz is dropped in the following discussion for clarity.

The effect of flow index n on the mean shear stress budget is shown in figure 5.7 where similar profiles of τ^{v+} and τ^{R+} are seen for all n. As required, the profile of the total mean shear stress is the same for all n and is a straight line in linear coordinates with a maximum at the wall and zero at the pipe centre.
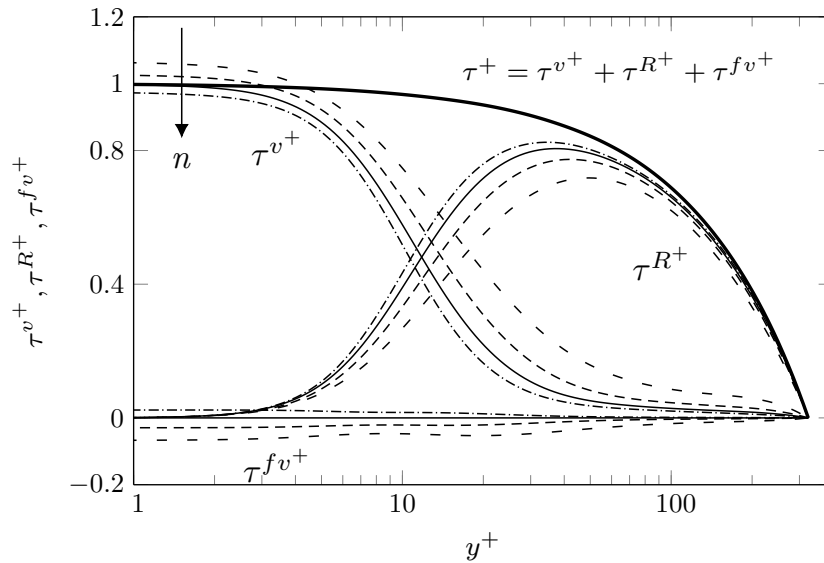
Fig. 5.7 Profiles of the (r, z) component of the mean viscous stress τ^{v+}, Reynolds shear stress τ^{R+}, and the turbulent viscous stress τ^{fv+}, plotted for different n. The profile of the total mean stress τ^+ is linear and the same for all n and is given by Eq. 5.1.

The mean viscous stress, τ^{v+}, is maximum at the wall and remains nearly constant until $y^+ \approx 3$ and then decreases towards the centre of the pipe. For

shear-thinning liquids, τ^{v^+} is higher than the Newtonian fluid across the entire radius. For the Newtonian fluid, the mean viscous stress τ^v drops to 5% of the nominal shear stress τ_w by $y^+ = 50$, however, for $n = 0.6$ it is still $\approx 15\%$ of τ_w at $y^+ = 50$. It does not drop to 5% of τ_w until $y^+ \approx 200$, which indicates a significant thickening of the region over which the viscous stress plays a role as first suggested by Wilson and Thomas [103]. Note that $\tau^{v^+} = 2\nu^+ S_{rz}^+$, thus the increase could be a result of either increased ν^+ (see figure 5.6) or increased $S_{rz}^+ = (\partial U_z^+/\partial y^+)/2$ (see figure 5.8). From these figures, the increase in τ^{v^+} in the viscous sub-layer is seen to be due to small increases in both ν^+ and S_{rz}^+. Beyond $y^+ > 10$, the increase in τ^{v^+} with decreasing n is primarily due to an increase in ν^+.
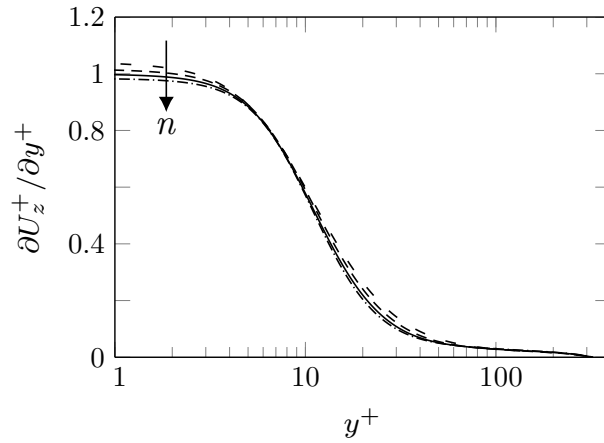
Fig. 5.8 Profiles of the mean velocity gradient plotted as a function of y^+ for different n.

Outside the viscous sublayer, the increase in τ^{v^+} with shear thinning is compensated for primarily by a decrease in the Reynolds shear stress τ^{R^+}. For the Newtonian fluid, the maximum value of the Reynolds shear stress τ^R is approximately 80% of τ_w which occurs at $y^+ \approx 40$. In contrast, for $n = 0.6$, the maximum τ^R is approximately 70% of τ_w with the location of maximum τ^R moving away from the wall, $y^+ \approx 50$. These results are discussed further in section 5.1.2.

Since the Reynolds shear stress is almost zero in the viscous sublayer, higher mean viscous stress, τ^{v^+}, here with shear thinning is compensated for by a decrease in the turbulent viscous stress τ^{fv^+}. Because $\tau^{fv^+} = 0$ for a Newtonian

fluid, this results in increasingly negative values for $n < 1$ as seen in figure 5.7. However, the contribution of τ^{fv} to the mean shear stress budget is overall small (approximately 5% of τ_w at the wall for $n = 0.6$).

Overall, the effect of increased shear thinning (decreasing n) on the mean shear stress budget is to increase the mean viscous stress and decrease the Reynolds stress. The turbulent viscous stress which is zero for a Newtonian fluid becomes more negative with shear thinning but is small compared to other components. It must be noted that the turbulent viscous stress is determined using the fluctuations in viscosity and shear rate, however, it can also be determined as a deficit in the time-averaged shear stress i.e. $\tau^{fv+} = r/R - \tau^{v+} - \tau^{R+}$ (see Eq. 5.1) from the measurements of the turbulent viscous stress and the Reynolds stress as done by Ptasinski et al. [79, 80] for viscoelastic liquids.

Mean axial velocity gradient and a new scaling for wall coordinates

A higher mean axial velocity in the viscous sublayer was observed for a more shear-thinning fluid in figure 5.5. This can be explained by considering the mean viscosity and the turbulent viscous stress. Using $\tau^{v+} = \nu^+(\partial U_z^+/\partial y^+)$, Eq. 5.1 can be rearranged to write the mean axial velocity gradient as:

$$\frac{\partial U_z^+}{\partial y^+} = \frac{1}{\nu^+}\left(1 - \frac{y^+}{R^+} - \tau_{rz}^{R+} - \tau_{rz}^{fv+}\right). \tag{5.2}$$

In the viscous sublayer, the Reynolds shear stress τ^{R+} is almost zero and $y^+/R^+ \approx 0$. Thus using (5.2), $\partial U_z^+/\partial y^+$ in the viscous sublayer can be approximated as

$$\frac{\partial U_z^+}{\partial y^+} \approx \frac{1}{\nu^+}\left(1 - \tau_{rz}^{fv+}\right). \tag{5.3}$$

For a Newtonian fluid $\tau^{fv+} = 0$, and hence Eq. 5.3 gives $\partial U_z^+/\partial y^+ = 1$ which reduces to the classical near wall form of the law of wall $U_z^+ = y^+$. However, τ^{fv+} is negative for a shear-thinning fluid and its magnitude increases with shear thinning. Although the mean viscosity, ν^+, also increases slightly with shear thinning (see figure 5.6), it does not compensate for the effect of τ^{fv+} in Eq. 5.3

and thus, an increase in $\partial U_z^+/\partial y^+$ with decreasing n is expected. Indeed from Eq. 5.2, the effect of negative τ^{fv+} is to increase $\partial U_z^+/\partial y^+$ at all y^+, however, its influence diminishes with increasing y^+.

In order to collapse the mean axial velocity profiles in the viscous sublayer for different n, velocity and viscosity scales should include the turbulent viscous stress and the mean wall viscosity $\bar{\nu}_w$ which is different from the nominal wall viscosity ν_w (figure 5.6). In order to define the new velocity and viscosity scales to give such collapse, the mean shear stress equation, Eq. 3.7, is used here at the wall in the (r, z) direction which gives

$$\rho\bar{\nu}_w\partial U_z/\partial y = \tau_w - \tau^{fv}. \tag{5.4}$$

Here, $\tau^v = \rho\bar{\nu}_w\partial U_z/\partial y$ is used. If Eq. 5.4 is non-dimensionalised using a velocity scale $u^\# = ((\tau_w - \tau^{fv})/\rho)^{1/2}$ and a viscosity scale $\bar{\nu}_w$, $U_z^\oplus = y^\oplus$ (a superscript $\oplus$ is used for the non-dimensionalisation using the new scales) is immediately recovered. These new velocity and viscosity scales are used for normalisation in figures 5.9 and 5.10. As expected profiles of the mean axial velocity gradient and therefore, the mean axial velocity collapse for different n in the viscous sublayer. Note that using the effective mean wall viscosity $\bar{\nu}_w$ only is not enough to give such collapse of the mean axial velocity as seen in figure 5.9 (b). This is also expected from Eq. 5.4.
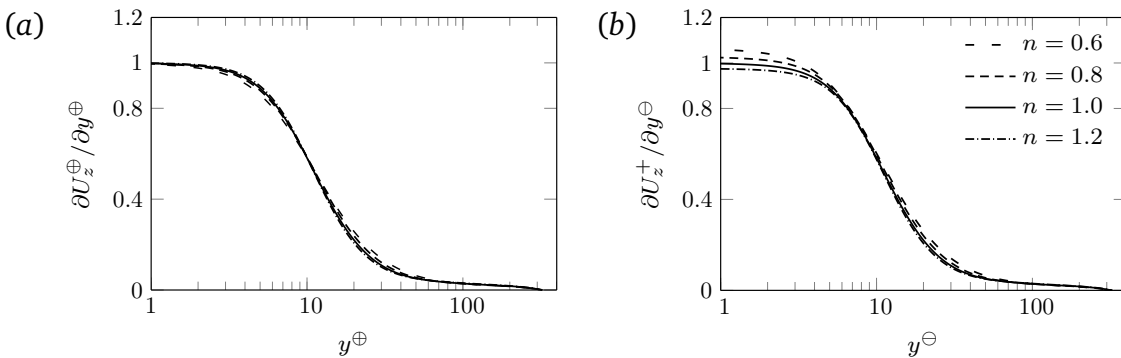
Fig. 5.9 Profiles of the mean axial velocity gradient for different n where the non-dimensionalistion used (a) $u^\#$ for the velocity scale and the mean wall viscosity $\bar{\nu}_w$ for the viscosity scale (b) u^* for the velocity scale and the mean wall viscosity $\bar{\nu}_w$ for the viscosity scale.
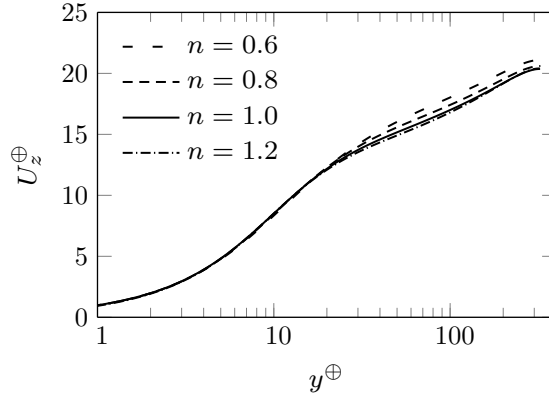
Fig. 5.10 Mean axial velocity profiles plotted for different n using $u^{\#}$ for the velocity scale and $\bar{\nu}_w$ for the viscosity scale in non-dimensionalisation.

A mitigating factor against using these new scales is that they are less practical. Neither $u^{\#}$ or $\bar{\nu}_w$ can be determined *a priori* in experiment or simulation. The mean shear rate and axial velocity gradient required at the wall are difficult to measure accurately in experiment. Although the new scaling collapses near wall profiles of the mean axial velocity, its gradient and the mean viscous stress, profiles of other mean flow variables and correlations do not collapse for different n in the viscous sublayer (not shown). Finally, profiles of the total mean shear stress for different n no longer lie on top of each other because the shear stress scale $\rho u^{\#^2}$ varies with n (figure 5.11). Thus in the process of recovering one fundamental Newtonian relation, another fundamental relation is lost. As a consequence of these facts u^* and ν_w as mentioned in section 3.4 are used in the non-dimensionalisation.

Turbulence intensities

The results presented in section 5.1.2 show that the mean axial velocity U_z^+, and the mean viscosity ν^+, are only weakly dependent on n in the viscous sublayer. However, this is not the case for the axial turbulence intensity, $u_z'^+$, as shown in figure 5.12 (*a*). Here $u_z'^+$ increases with decreasing n at all y^+ and its peak moves further from the wall. For $n = 0.6$, the increase in the viscous sublayer is of order 25%.
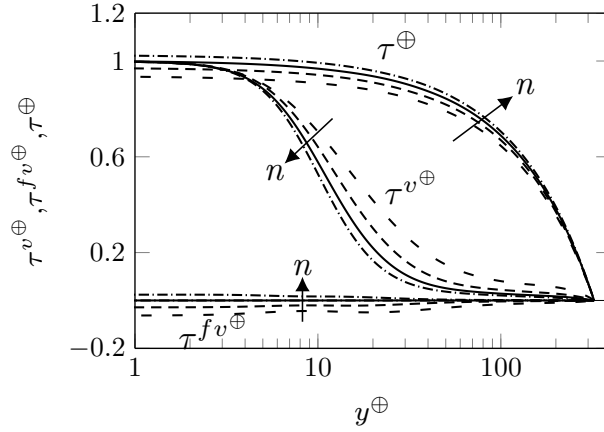
Fig. 5.11 Profiles of the viscous stresses, τ^v and τ^{fv}, plotted for different n using $u^{\#}$ for the velocity scale and $\bar{\nu}_w$ for the viscosity scale in non-dimensionalisation.

Unlike $u_z'^+$ which showed a flow-index-dependence for all y^+, the radial and the azimuthal turbulence intensities ($u_r'^+$, $u_\theta'^+$) show dependence on n mainly outside the viscous sublayer, where they decrease with decreasing n (figures 5.12 *b,c*). The location where $u_r'^+$, $u_\theta'^+$ profiles deviate significantly from each other coincides with the location where the mean viscosity ν^+ also deviates from the Newtonian value. This suggests that $u_r'^+$, $u_\theta'^+$ strongly depend on the mean fluid viscosity and that higher viscosity for lower n damps the velocity fluctuations normal to the mean flow direction. Note that the turbulence intensity profiles plotted in outer units (normalised by the bulk velocity U_b) also show similar trends (figures 5.12 *d-f*). Both of these trends have been noted previously [40, 83, 84] and have been suggested as being due to decreased energy transfer from axial velocity fluctuations to transverse velocity fluctuations via pressure fluctuations [40]. However, this has not been demonstrated to date.

For a power-law fluid, root mean square (rms) viscosity fluctuations $\nu'^+ = \nu'_{rms}/\nu_w$ are non-zero at all y^+ and increase with shear thinning (figure 5.13 *a*). Similar to the mean viscosity, ν'^+ remains uniform in the viscous sublayer and increases with y^+ outside the viscous sublayer. Except for $n = 0.6$ and presumably $n < 0.6$, however, the increase in ν'^+ with y^+ is small. Profiles of ν'^+ normalised by the local mean viscosity show that ν'^+/ν^+ increases only up to a certain y^+ (the value of which increases with shear thinning) and then starts decreasing (figure 5.13 *b*). Higher ν'^+ suggests higher instantaneous viscosities
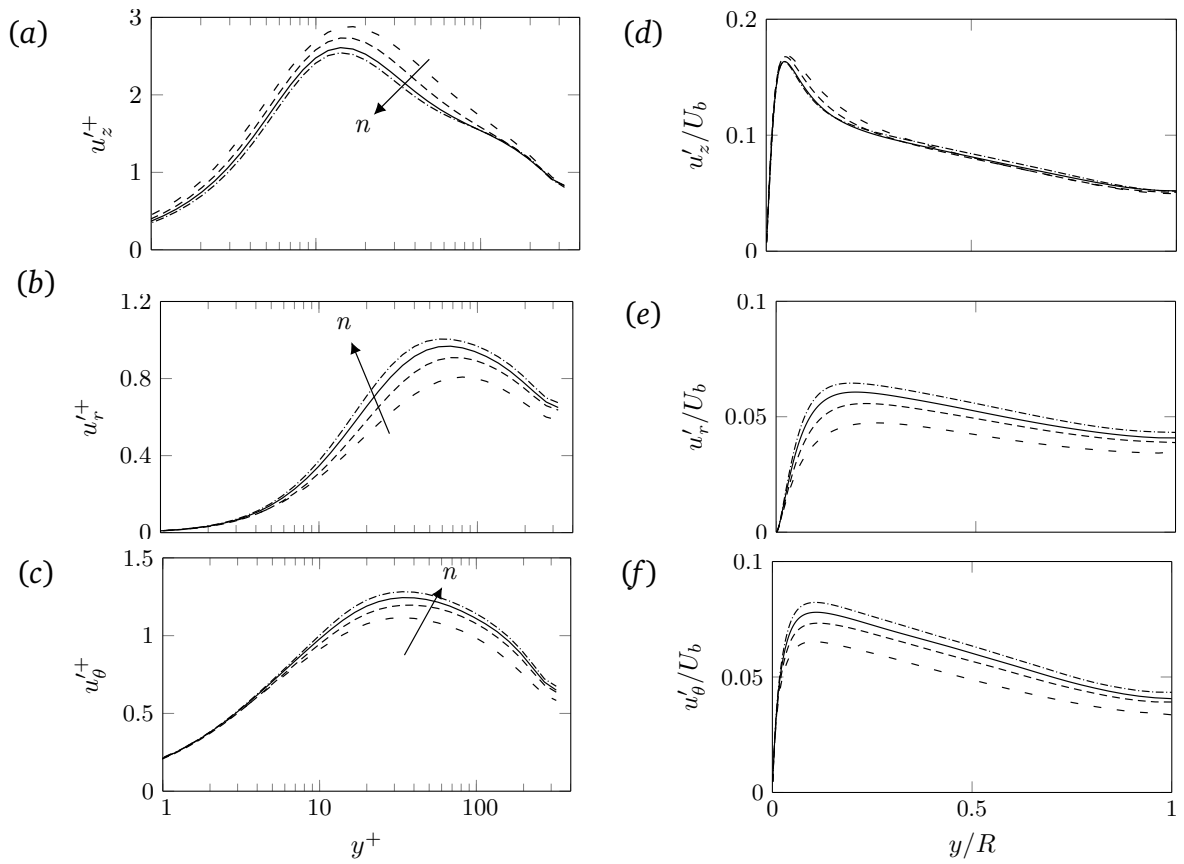
Fig. 5.12 Profiles of turbulence intensities plotted in wall units (*a-c*) and in outer units (*d-f*) for different flow indices n.
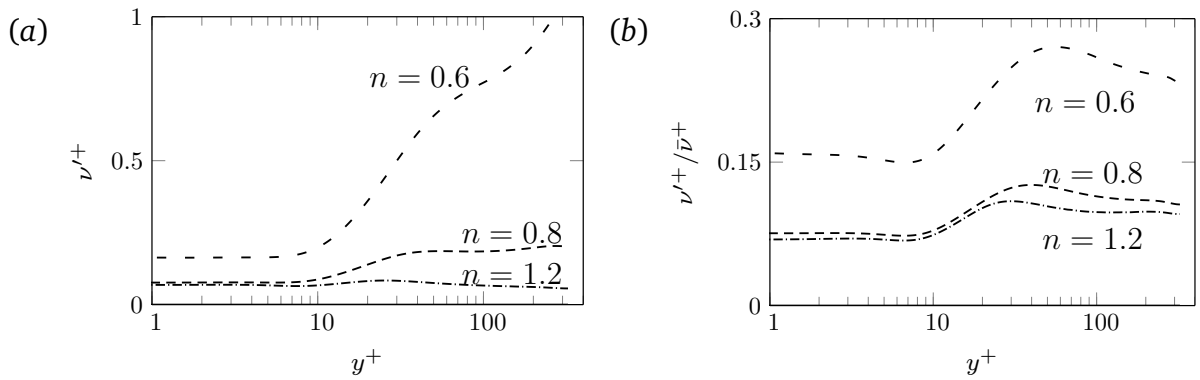
Fig. 5.13 Profiles of rms viscosity fluctuations normalised by (*a*) the mean wall viscosity ν_w and (*b*) mean viscosity, $\bar{\nu}(y^+)$ plotted for different n.

for a more shear-thinning fluid, which is also seen by comparing figure 5.2 (*e*) and (*f*).

Quadrant analysis of Reynolds stresses

The quadrant analysis of Reynolds stress as proposed by Wallace et al. [98] is considered here to show the effect of shear thinning in different Reynolds stress quadrants. The instantaneous wall normal velocity fluctuations are defined as $\tilde{v}_r' = -v_r'$ where v_r' has a different sign here from Wallace et al. because of the coordinate system employed. The analysis classifies the $v_z'\tilde{v}_r'$ signal into four different categories: $Q1(+v_z', +\tilde{v}_r')$, $Q2(-v_z', +\tilde{v}_r')$, $Q3(-v_z', -\tilde{v}_r')$ and $Q4(+v_z', -\tilde{v}_r')$. These quadrants are associated with different physical events. For channel flows of Newtonian liquids, it has been found that most of the Reynolds stress production is associated with the ejection (Q2) and sweep (Q4) of low-speed fluid near the wall. Consequently they are also termed the ejection and sweep quadrants (see Wallace [97]).

Figure 5.14 compares the joint probability distribution $P(-v_r'/u^*, v_z'/u^*)$ for $n = 1.0$ and $n = 0.6$ for values of y^+=10, 30, 70 and 100. In the near wall region, the major axis of $P(-v_r', v_z')$ is less inclined in the direction of Q2–Q4 for $n = 0.6$ (figure 5.14e) compared to the Newtonian fluid (figure 5.14a), which suggests that shear-thinning rheology suppresses the contribution of ejection and sweep events to Reynolds stress generation. Compared to a Newtonian fluid, a narrower spread of the marginal probability distribution $P(-v_r')$ for $n = 0.6$ in the near wall region (seen clearly for $y^+ = 10$ and 30) suggest that with shear thinning, axial velocity fluctuations become larger than wall normal fluctuations (as known from figure 5.12). Therefore, there is a less momentum exchange via the Reynolds shear stress in the wall normal direction.

Summary of the mean flow and turbulence intensity results

The key results in this section are that the effect of shear thinning is to increase the mean axial velocity, mean viscosity and axial turbulence intensity but, to decrease the radial and azimuthal turbulence intensities. The mean viscous stress is increased slightly in the very near wall region and quite significantly in the buffer layer, and the distance from the wall where it drops to order 5% of the
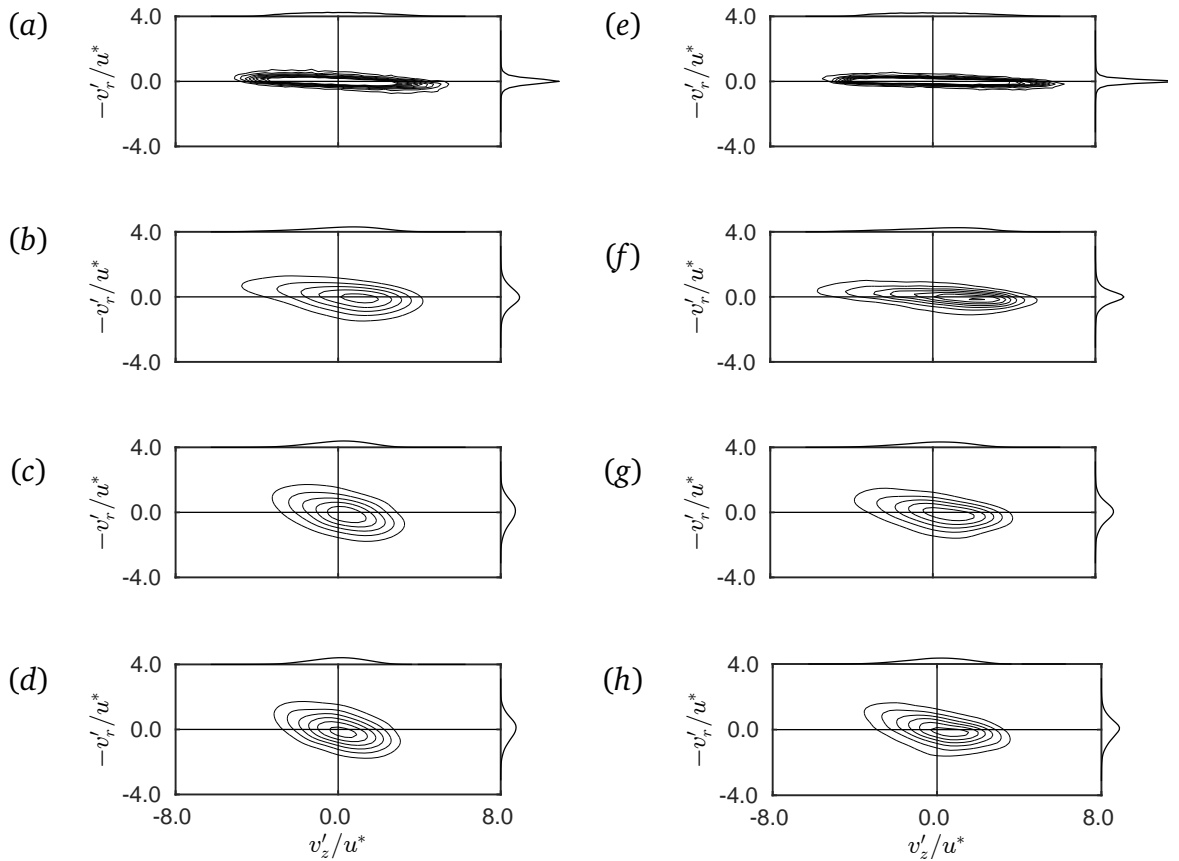
Fig. 5.14 Joint and marginal probability distributions of the axial and wall normal velocity fluctuations (v'_z and $-v'_r$) plotted at $y^+ = 10, 30, 70, 100$ (from top to bottom) for (*a-d*) Newtonian and (*e-h*) $n = 0.6$.

total stress is significantly increased. With shear thinning, the Reynolds stress decreases across the pipe and the new term in the mean shear stress balance, the turbulent viscous stress, is always negative, offsetting the increased mean viscous stress very near the wall. This results in an increase in the mean axial velocity gradient and the bulk velocity (hence, the flow rate) with shear thinning.

5.1.3 Energy budgets

Non-uniform viscosity and viscosity fluctuations modify the mean flow kinetic energy (MFKE) and turbulent kinetic energy (TKE) budget equations for a non-Newtonian fluid as shown in section 3.3. Here, the effects of modifying flow index on these energy budget equations are discussed.

Mean flow kinetic energy budget

To set the scene for subsequent discussion, the MFKE budget for a Newtonian fluid is described first and the profiles of different terms (see Eq. 3.8) are plotted in figure 5.15. Because the mean axial pressure gradient dP/dz, is independent of r, profiles of the mean flow energy production, $W^+_{dp/dz}$, follow a similar trend as seen for U^+_z in figure 5.5 (a) and $W^+_{dp/dz}$ increases towards the wall (seen more clearly in figure 5.16 a). Very near the wall ($y^+ < 3$), the MFKE budget is purely a balance between the two viscous terms, $\mathcal{D}^{m^+}$ and ϵ^{m^+}, because the Reynolds shear stress, τ^{R^+}, is almost zero here, as do the two terms that contain it (i.e. the Reynolds stress transport, $\mathcal{T}^{m^+}$, and the turbulent kinetic energy production, $-\mathcal{P}^+$).

Over the range $3 < y^+ < 60$, there is a more complex balance between the Newtonian transport and dissipation terms, $\mathcal{T}^{m^+}$, $\mathcal{D}^{m^+}$, ϵ^{m^+} and $-\mathcal{P}^+$. For $y^+ > 3$, both $\mathcal{T}^{m^+}$ and $-\mathcal{P}^+$ grow in magnitude with $\mathcal{T}^{m^+}$ adding energy in this region and $-\mathcal{P}^+$ dissipating it , with both terms reaching a maximum at $y^+ \approx 10$. The mean viscous transport, $\mathcal{D}^{m^+}$, is a sink for $y^+ > 8$ and source for $y^+ < 8$, which means that it transports energy to the viscous sublayer because its volume integral is zero. The turbulent kinetic energy production, $-\mathcal{P}^+$, is significant only for $3 \lesssim y^+ \lesssim 40$ and it reaches a maximum approximately at the same location where $\mathcal{D}^{m^+}$ and ϵ^{m^+} cross each other as also noted in Thais et al. [94] for viscoelastic liquids.

The Reynolds stress transport, $\mathcal{T}^{m^+}$, acts as a source up to $y^+ \approx 40$ where it changes sign due to the change in the slope of the Reynolds shear stress (see figure 5.7). It then acts as a sink, which shows that the Reynolds shear stress transports energy from $y^+ > 40$ towards the wall. For $y^+ > 60$, the MFKE budget is mainly a balance between $\mathcal{T}^{m^+}$ and $W^+_{dP/dz}$ because the turbulent energy transfer term, $-\mathcal{P}^+$, is very small and approaches zero at the pipe centre.

The effect of changing the flow index on individual mean flow energy budget terms is shown in figures 5.15 and 5.16. First the effect of shear thinning on those terms that also appear for a Newtonian fluid are discussed before examining the modifications resulting to the non-Newtonian terms. As mentioned

76
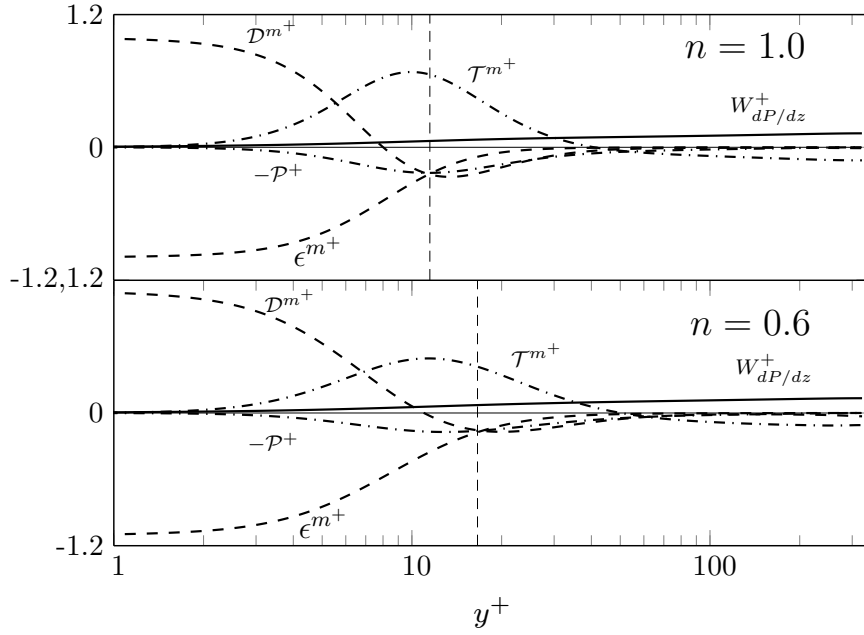
Fig. 5.15 Profiles of the mean flow kinetic energy terms from Eq. 3.8 plotted in wall coordinates for a Newtonian fluid (top) and $n = 0.6$ (bottom). Vertical grey lines show the location where $\mathcal{D}^{m^+}$, $-\mathcal{P}^+$ and ϵ^{m^+} intersect.

earlier also, when a trend is described as occurring with shear thinning, it should be taken as reading that the opposite trend occurs with shear thickening.

As already noted in section 5.1.2, the mean axial velocity profile for a shear-thinning fluid lies above the Newtonian profile and consequently, the mean flow energy production, $W^+_{dP/dz}$, must increase with shear thinning as seen in figure 5.16(a). However, with the exception of $W^+_{dP/dz}$, most terms show little variation with n beyond $y^+ \approx 60$ although there are sufficient differences to balance the increased production. The radial location where the two viscous terms, $\mathcal{D}^{m^+}$ and ϵ^{m^+}, cross each other is also shifted by shear thinning as observed in figure 5.15.

The mean axial velocity gradient, $\partial U_z^+/\partial y^+$, and hence the mean viscous stress, τ^{v^+}, increases with shear thinning (figure 5.7), therefore, more negative $\epsilon_m^{v^+}$ is observed with shear thinning in figure 5.16(d). Since the gradient of τ^{v^+} is also less negative for a more shear-thinning fluid further from the wall, higher values of $\mathcal{D}^{m^+}$ result until $y^+ \approx 15-20$ where this term becomes slightly less negative for a more shear-thinning fluid (figure 5.16c). Similarly, lower Reynolds stress with decreasing n (figure 5.7) results in less negative turbulent energy

(a)

0.15

0.1

0.05

0

$W_{dP/dz}^+$

$n = 0.6$
$n = 0.8$
$n = 1.0$
$n = 1.2$

n

(b)

0.8

0.4

0

−0.2

$\mathcal{T}^{m+}$

(c)

1.2

0.8

0.4

0

−0.4

$\mathcal{D}^{m+}$

(d)

0

−0.4

−0.8

−1.2

ϵ^{m+}

(e)

0

−0.1

−0.2

−0.3

$-\mathcal{P}^+$

(f)

0.09

0.03

−0.03

χ_{nn}^+

(g)

0.03

0

−0.09

Υ_{nn}^{m+}

1   10   100

y^+

(h)

0.03

0

−0.03

$\Upsilon_{nn}^{m+} + \chi_{nn}^+$

1   10   100

y^+
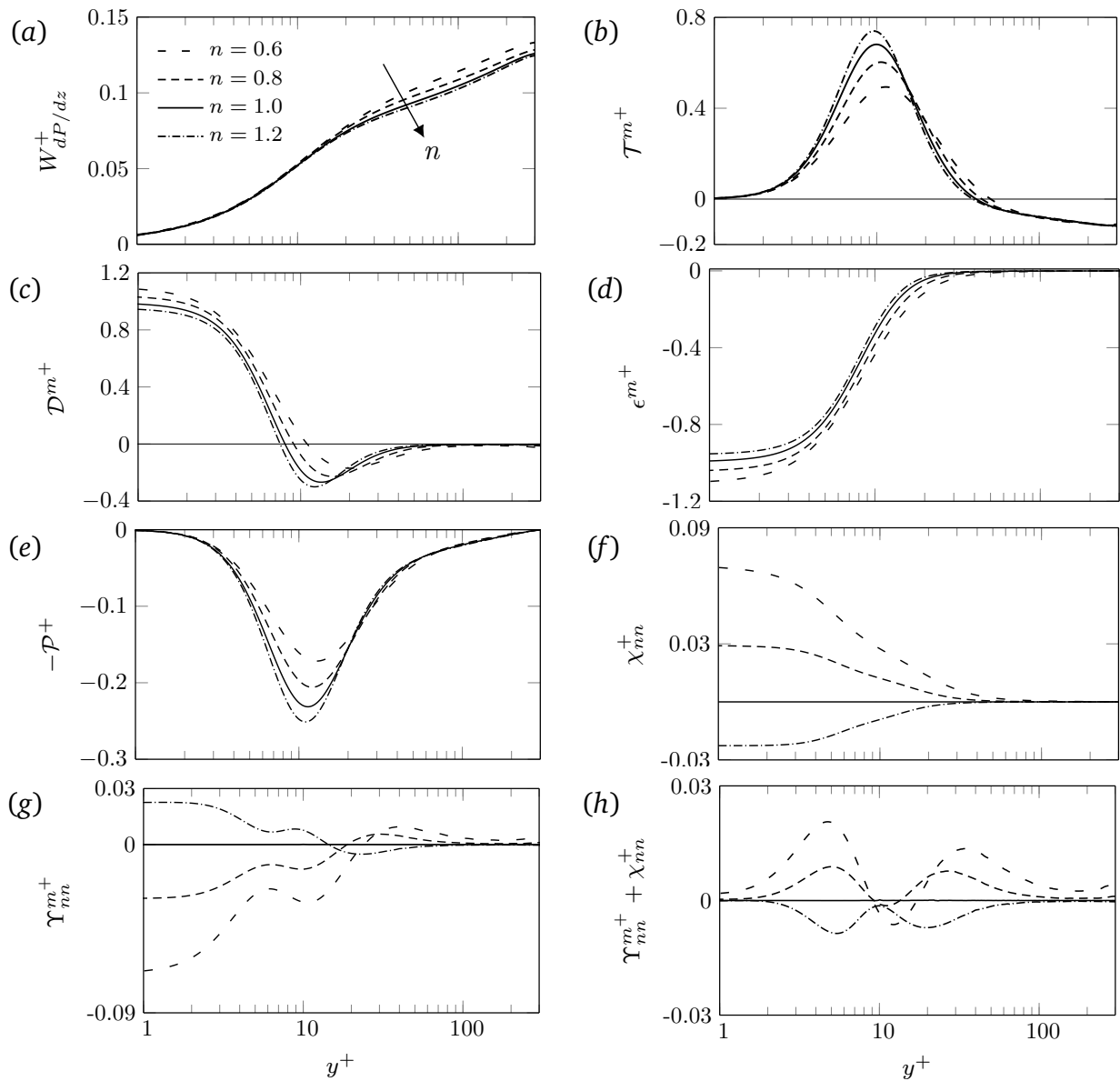
Fig. 5.16 Profiles of the mean flow kinetic energy energy budget terms from (Eq. 3.8) plotted for different flow indices n in wall variables. Note that the vertical scale changes in each plot.

transfer, $-\mathcal{P}^+$, (figure 5.16 e) and lower values of the Reynolds stress transport, $\mathcal{T}^{m^+}$, up to approx $y^+ \approx 20$ at which point the latter term becomes a little higher with shear thinning (figure 5.16 b). As discussed in section 3.3.2, $-\mathcal{P}^+$ appears with opposite sign in the turbulent kinetic energy budget as a production term. Thus the decrease in magnitude of $-\mathcal{P}^+$ observed here with shear thinning means there is a less energy transferred via this mechanism into turbulence for lower n. The combination of higher MFKE production, $W^+_{dP/dz}$, and less energy transfer to turbulence via $-\mathcal{P}^+$ suggests that there will be higher dissipation by the mean viscous stress (ϵ^{m^+}) in case of lower n — this may be observed in figure 5.16 (d).

The two non-Newtonian terms, $\Upsilon^{m^+}_{nn}$ and χ^+_{nn}, vary most significantly with n for $y^+ < 60$, similarly to the Newtonian transport and dissipation terms. However, their magnitude is approximately one order less than the $\mathcal{D}^{m^+}$ and ϵ^{m^+} and they play a smaller role in the MFKE balance. The non-Newtonian dissipation, χ^+_{nn}, is negatively related to τ^{fv^+} which was seen to be negative for shear-thinning liquids (figure 5.7). Thus χ^+_{nn} is expected to be positive for shear-thinning liquids (as seen in figure 5.16 f) and this reduces dissipation. However, the sum of ϵ^{m^+} and χ^+_{nn} (figure 5.17 a) shows that the net effect of these two viscous dissipation terms only slightly increases the magnitude of total dissipation in the very near wall and buffer layer. The non-Newtonian transport term, $\Upsilon^{m^+}_{nn}$, changes sign in $y^+ \approx 15 - 20$ (depending on n) and for shear thinning acts as a sink of the mean flow energy for $y^+ \lesssim 15$ and a source further away from the wall. Overall, except in a narrow region near $y^+ \approx 10$, the non-Newtonian terms act as a source for shear-thinning liquids and as a sink for the shear-thickening fluid ($n = 1.2$) in the MFKE budget at all y^+ (figure 5.16 h).

In summary, the mean flow energy production increases with shear thinning outside the buffer layer. For all other terms, the overall effect of shear thinning is to modify the MFKE budget terms most significantly in the near wall region $y^+ \lesssim 60$. The total viscous dissipation is increased with shear thinning but the turbulent energy transfer (which peaks at $y^+ \approx 10$) becomes less negative. The magnitude of the total viscous transport is also increased with shear thinning. The turbulent transport which is the mean flow energy transfer via the Reynolds stress and also peaks at $y^+ \approx 10$, decreases with shear thinning. The non-
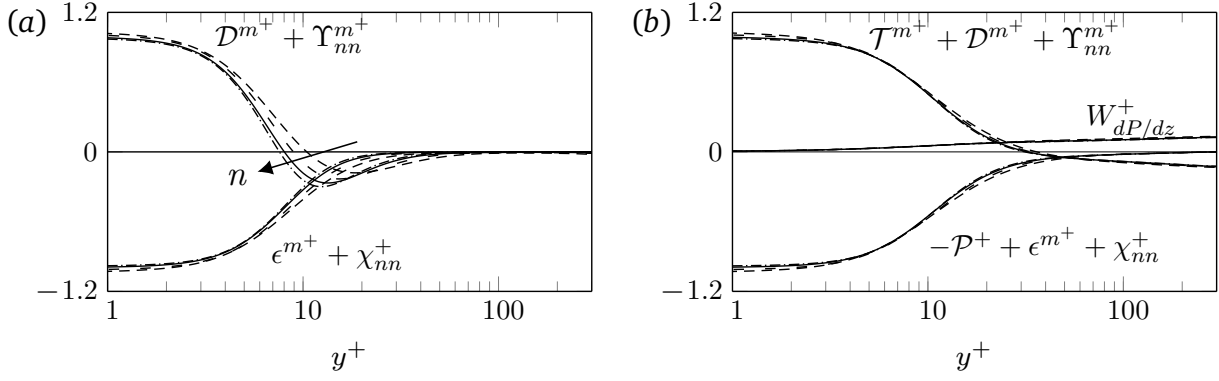
Fig. 5.17 Profiles of the sum of Newtonian and non-Newtonian (*a*) viscous transport and dissipation terms (*b*) total transport and dissipation in (3.8) plotted for different flow indices n.

Newtonian terms largely act as a source in the MFKE budget for shear-thinning liquids. In the total transport and dissipation profiles the shear-thinning effect almost disappears in $4 \lesssim y^+ \lesssim 10$ (figure 5.17*b*).

Turbulent kinetic energy budget

The effect of modifying flow index n on the individual TKE budget terms (Eq. 3.9) is shown in figure 5.18. Turbulent kinetic energy production, $\mathcal{P}^+$, decreases with shear thinning over $3 < y^+ < 20$ with the peak shifting slightly away from the wall (figure 5.18*a*). Turbulent kinetic energy production is the product $-\overline{u_i' u_j'} S_{ij}$ and for a pipe flow, only the S_{rz} component survives, which gives $\mathcal{P}^+ = \tau^{R+}(\partial U_z^+/\partial y^+)/2$. Since S_{rz}^+ is little affected by shear thinning for $3 < y^+ < 20$ (figure 5.8), the observed decrease in $\mathcal{P}^+$ with shear thinning is primarily due to the decrease in Reynolds stress (figure 5.7).

As n decreases, turbulent dissipation, $\epsilon^+ = 2\nu^+ \overline{s_{ij}' s_{ij}'}^+$, increases in magnitude for all y^+, although most noticeably for $y^+ < 5$ and then less so over $20 < y^+ < 100$ (figure 5.18*a*). The increase over $20 < y^+ < 100$ is due to the increase in the mean viscosity with shear thinning (figure 5.6) because $\overline{s_{ij}' s_{ij}'}^+$ decreases here for all n (figure 5.19*a*). However, the increase in ϵ^+ with decreasing n close to the wall is due to increased strain rate fluctuations $\overline{s_{ij}' s_{ij}'}$ with decreasing n as the mean viscosity is only weakly dependant on n (figure 5.6).
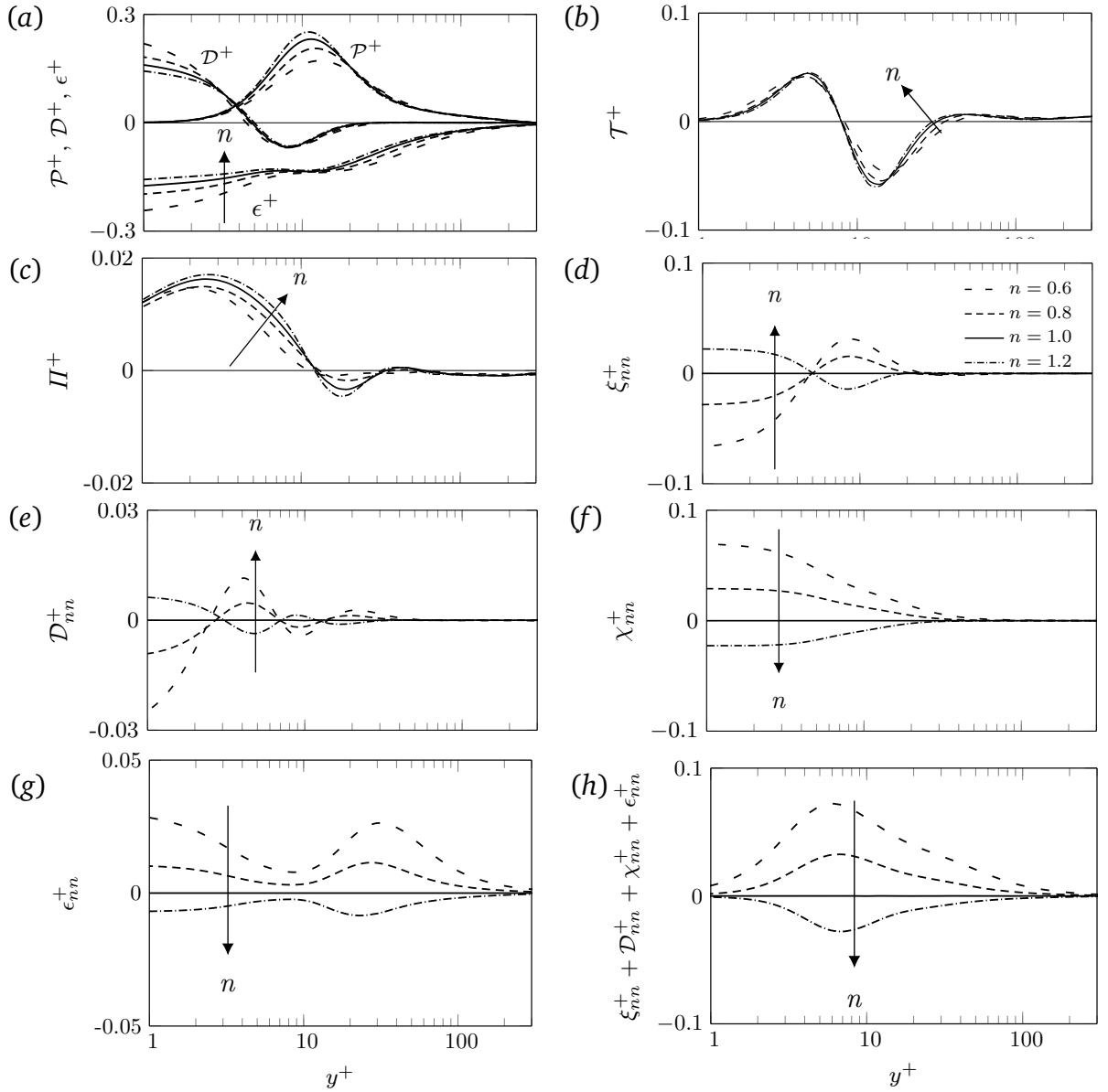
Fig. 5.18 Profiles of the turbulent kinetic energy budget terms (see Eq. 3.9) plotted for different flow indices n in wall variables. Note that the vertical scale changes in each plot.

Profiles of the three Newtonian transport terms, $\mathcal{D}^+$, $\mathcal{T}^+$ and Π^+, are shown in figures 5.18(*a-c*). The mean viscous transport, $\mathcal{D}^+$, is the largest in magnitude and shows flow-index-dependence mostly in the viscous sublayer where it increases with shear thinning (figure 5.18 *a*), partly countering the more negative dissipation for lower n. Recalling that i) $\mathcal{D}$ is the gradient of $2\nu^+ \overline{s_{ij}'^+ u_i'^+}$ (see Eq. 3.9) ii) that only the radial derivative survives and iii) that the mean viscosity, ν^+, is almost constant in the viscous sublayer (figure 5.6), it can be

concluded that larger $\mathcal{D}^+$ for smaller n is due to more rapid increase with radius in $\overline{s'_{ri}u'_i}^+$ in the viscous sublayer with shear thinning.

The main effect of decreasing n on the turbulent velocity transport, $\mathcal{T}^+$, is flattening and broadening of the profile in $8 < y^+ < 50$ (figure 5.18b). The contribution of the pressure related transport, Π^+, is small compared to the other transport terms (figure 5.18c) and although its magnitude is reduced in the viscous sublayer and buffer layer with shear thinning, this has a little effect on the total turbulent energy transport.

Overall, the effect of reducing flow index on the Newtonian terms in TKE budget is to elevate the mean viscous transport, $\mathcal{D}^+$ and turbulent dissipation, ϵ^+, close to the wall ($y^+ < 3$), and to decrease turbulent production, $\mathcal{P}^+$, near $y^+ = 10$.

The non-Newtonian transport terms, the mean shear turbulent viscous transport, ξ_{nn}^+, and the turbulent viscous transport, $\mathcal{D}_{nn}^+$, are significant only for $y^+ \lesssim 40$ and the magnitude of both increases with shear thinning (figures 5.18d and e). The contribution of ξ_{nn}^+ to the turbulent kinetic energy budget at the wall is significant where it is approximately 25% of the total Newtonian transport ($\mathcal{T}^+ + \Pi^+ + \mathcal{D}^+$) for $n = 0.6$ and approximately 13% for $n = 0.8$. ξ_{nn}^+ acts opposite to the Newtonian viscous transport, $\mathcal{D}^+$ for $0 \lesssim y^+ \lesssim 30$. Since $\mathcal{D}^+$ is due to the mean viscous stress τ^{v^+} and ξ_{nn}^+ is due to the turbulent viscous stress τ^{fv^+}, this opposition is expected from the opposite signs of the two viscous stresses (see figure 5.7). The contribution of $\mathcal{D}_{nn}^+$ to the turbulent kinetic energy budget is small (less than 10% of the Newtonian transport $\mathcal{T}^+ + \Pi^+ + \mathcal{D}^+$ for $n = 0.8$). The sum of all transport terms ($\mathcal{T}^+ + \Pi^+ + \mathcal{D}^+ + \mathcal{D}_{nn}^+ + \xi_{nn}^+$) is shown in figure 5.19b where it is seen that the effect of shear thinning is to reduce the transport by the Newtonian terms for $0 \lesssim y^+ \lesssim 20$ and to increase it marginally over $20 \lesssim y^+ \lesssim 70$.

The other two non-Newtonian terms, the mean shear turbulent viscous dissipation, χ_{nn}^+, and the turbulent viscous dissipation, ϵ_{nn}^+, are positive for shear-thinning liquids (figures 5.18f, g). As previously mentioned, they are identified as dissipation terms that act to reduce the mean flow dissipation ϵ^+ over the entire

pipe radius, but particularly for $y^+ < 40$. For $n = 0.6$, they reduce the dissipation in the viscous sublayer close to the wall by approximately 40%. Their net effect is most clearly seen in figure 5.19 (a) where the total dissipation is seen to reduce with shear thinning for $y^+ \lesssim 30$ with the reduction balancing the reduction in net transport for $y^+ < 5$ and partially balancing the reduction in production observed around $y^+ \approx 10$.

In the very near wall region, ξ_{nn}^+ and χ_{nn}^+ almost cancel each other, as do $\mathcal{D}_{nn}^+$ and ϵ_{nn}^+, resulting in no net effect of the non-Newtonian TKE budget terms at the wall. The net effect of these terms increases through the viscous sublayer reaching a maximum near $y^+ \approx 7$ before slowly decreasing again out to $y^+ > 100$ (figure 5.18 h). They thus provide an additional source of energy in the TKE budget for shear-thinning liquids.

A summary of the effects of flow index modification is shown in figure 5.19 (b) where the total turbulent production, transport and dissipation are compared for different n. They show flow-index-dependence only for $y^+ \lesssim 70$ and shear thinning is seen to reduce the magnitude of each, albeit over different ranges of y^+.
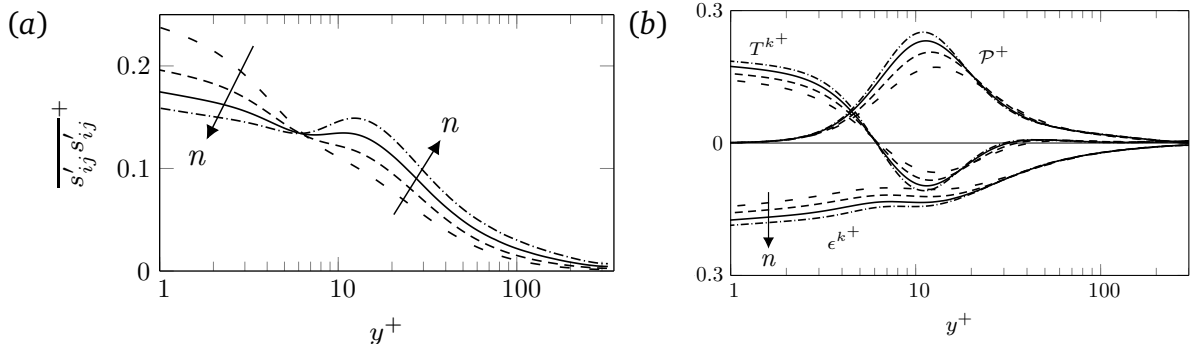
Fig. 5.19 Profiles of (a) $\overline{s'_{ij}s'_{ij}}^+$ (b) turbulent kinetic energy production ($\mathcal{P}^+$), total dissipation ($\epsilon^{k+} = \epsilon^+ + \chi_{nn}^+ + \epsilon_{nn}^+$) and transport ($T^{k+} = \mathcal{T}^+ + \Pi^+ + \mathcal{D}^+ + \mathcal{D}_{nn}^+ + \xi_{nn}^+$) plotted for in wall units for different n.

Shear thinning widens the production region (where production exceeds the total dissipation) by increasing its upper bound (figure 5.20) whereas the lower bound remains fixed at $y^+ \approx 6$. In this region, the total transport becomes negative and thus carries the excess energy ($\mathcal{P}^+ - \epsilon^{k+}$) away from the production
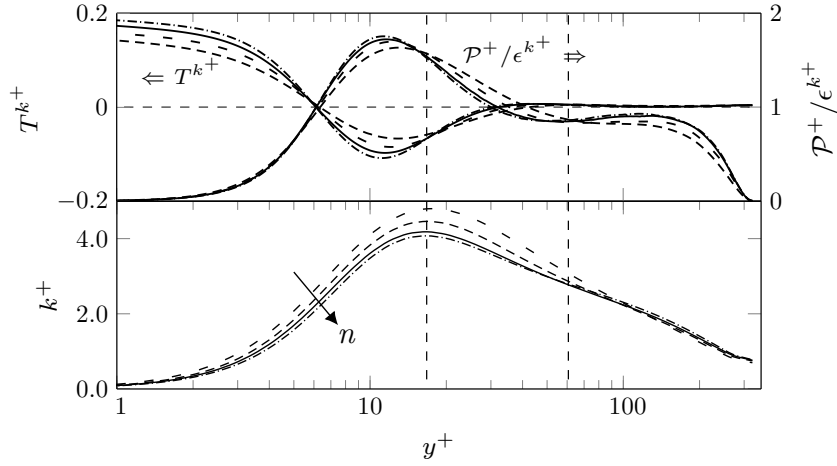
Fig. 5.20 Profiles of the ratio of turbulent kinetic energy production to total dissipation ($\mathcal{P}^+/\epsilon^{k^+}$), total transport ($T^{k^+}$) and the turbulent kinetic energy k^+ plotted in wall units.
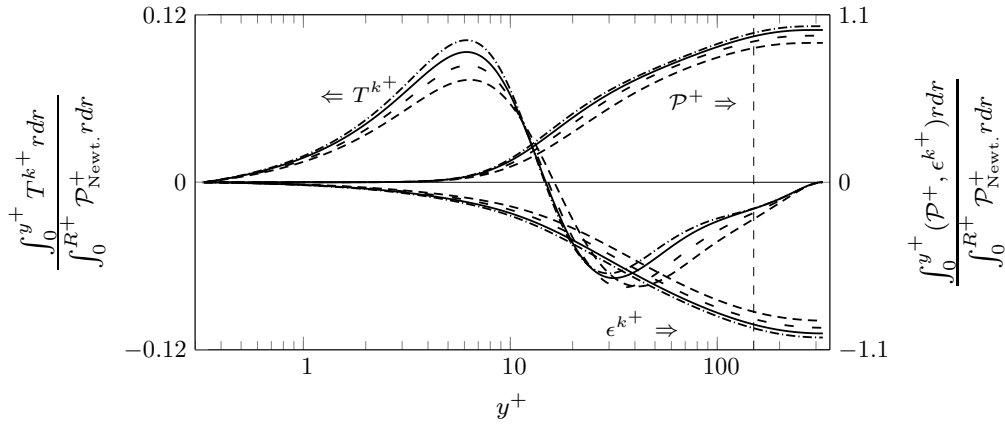
Fig. 5.21 Integrated budget of turbulent kinetic energy production ($\mathcal{P}^+$), transport ($\mathcal{T}^+ + \Pi^+ + \mathcal{D}^+ + \mathcal{D}_{nn}^+ + \xi_{nn}^+$) and dissipation ($\epsilon^+ + \chi_{nn}^+ + \epsilon_{nn}^+$), normalised by the total Newtonian turbulent production (volume integral of $\mathcal{P}^+$ for $n = 1$) plotted for different n. The primary axis on the left is for the turbulent transport budget and the secondary axis on the right is for the turbulent production and dissipation.

region. The ratio of the TKE production to total dissipation ($\mathcal{P}^+/\epsilon^{k^+}$) is higher for $15 \lesssim y^+ \lesssim 60$ but lower for $6 \lesssim y^+ \lesssim 15$ and beyond $y^+ \approx 60$ with shear thinning.

Profiles of the TKE production, total dissipation and transport integrated over the pipe cross section from wall to y^+ show that shear thinning globally reduces the overall turbulent kinetic energy production and hence the total dissipation (figure 5.21). Beyond $y^+ = 150$, profiles of the integrated production and total dissipation for all n are almost flat showing that most of the turbulent kinetic energy production and dissipation occurs for $y^+ < 150$. Profiles of the

integrated total turbulent transport there (also negative of the extra energy available for turbulence i.e. $-(\mathcal{P}^+ - \epsilon^{k^+})$) show that there is more energy available (T^{k^+} is more negative for $y^+ \gtrsim 25$) for turbulence for a more shear-thinning fluid. This suggests that shear thinning decreases dissipation more than it decreases the production.

Using the results of $\mathcal{P}^+/\epsilon^{k^+}$ shown in figure 5.20, the TKE profiles for different n can be explained. For $y^+ < 15$, there is a narrow region ($y^+ \approx 6 - 15$) where $\mathcal{P}^+/\epsilon^{k^+}$ is clearly lower for a more shear-thinning fluid and therefore, the turbulent kinetic energy profiles slowly converge to a single curve towards the wall. The turbulent kinetic energy k^+ peaks at $y^+ \approx 15$ which is slightly higher than the location where $\mathcal{P}^+/\epsilon^{k^+}$ attains a maximum and approximately the same location where $\mathcal{P}^+/\epsilon^{k^+}$ profiles for different n cross each other. Over the region $15 \lesssim y^+ \lesssim 60$, higher TKE production than dissipation results in higher k^+ in the case of more shear-thinning liquids. A part of this higher k^+ is transported away from the wall and part towards the wall. For $y^+ > 60$, there is more dissipation for lower n which dissipates the extra energy and the k^+ profiles of different n collapse on top of each other for $y^+ \gtrsim 90$.

Summary of the energy budget

Results of the MFKE budget show that except the MFKE production, all other terms show flow-index-dependence only near the wall for $y^+ \lesssim 60$. Shear thinning increases the MFKE production and hence dissipation. The non-Newtonian terms are a source in the MFKE budget for a shear-thinning fluid and sink for the shear-thickening. Similar to the MFKE budget terms, TKE budget terms are also dependent on n only near the wall. Shear thinning decreases the turbulence production in the buffer layer whereas it increases the turbulent transport and the Newtonian dissipation primarily in the viscous sublayer. The non-Newtonian terms act as a local source in the TKE budget. The non-Newtonian dissipation terms in both MFKE and TKE are positive for a shear-thinning fluid and therefore decrease the total viscous dissipation.

5.1.4 Summary

The results presented in this section show that the flow structures becomes wider and the low speed streaks run longer in the flow of a more shear-thinning fluid. The mean axial velocity profiles of a power-law fluid do not strictly follow $U_z^+ = y^+$ in the viscous sublayer and the mean velocity gradient increases with shear thinning. Mean axial velocity profiles at different n show large deviation in the log layer and lie above the Newtonian profile for shear-thinning liquids. The mean viscosity increases with shear thinning with the effect being most noticeable only outside the viscous sublayer. Turbulence intensities when expressed in wall units are found to increase in the axial direction but decrease in the radial and the azimuthal direction with shear thinning.

The Reynolds shear stress is also found to decrease with decreasing n. The turbulent viscous stress is negative for a shear-thinning fluid and its magnitude of the turbulent viscous stress is maximum at the wall. Due to increased viscosity and mean shear rate, the mean viscous stress increases with shear thinning. Except for the mean flow energy production, the effect of shear thinning is seen in the mean flow and the turbulent energy budgets mostly for $y^+ < 60$. The new terms introduced in the turbulent kinetic energy budget due to the non-Newtonian rheology are found to add a source for a shear-thinning fluid and sink for a shear-thickening fluid.

5.2 The effect of yield stress

Apart from decreasing flow index, a fluid can also give lower viscosity at higher shear rates if it has a yield stress τ_y. Both shear thinning and yield stress also have a similar effect on a laminar pipe flow (see section 2.2.1). Here, the effect of τ_y is studied on a turbulent pipe flow at $Re_\tau = 323$ via simulations with the Bingham rheology model. The yield stress is varied from 0 to 20% of the nominal wall shear stress τ_w. The simulations parameters are given in table 5.2 and the fluid viscosity is plotted in figure 5.22. It can be seen that modifying τ_y modifies the fluid viscosity ν, for all shear rates except at the wall $\dot\gamma^+ = 1$ where a fixed

mean wall viscosity is forced. Compared to shear thinning (figure 5.1), the effect of modifying τ_y is smaller for shear rates larger than the wall value, $\dot{\gamma}^+ > 1$.

Table 5.2 Simulation parameters for pipe flow of different n and τ_y at $Re_\tau = 323$. Non-dimensional body force gR/u^{*2}, the nominal wall viscosity $\nu_w/(u^*R_h)/$ are fixed at 323, 2 and $1/323$ respectively.

Identifier	n	$K/(\rho u^{*2-n}R^n)$	τ_y^+ (%)	Re_G	Re_{MR}
Bi5		2.9399×10^{-3}	5	10463	
Bi10	1.0	1.3927×10^{-3}	10	10635	-
Bi20		1.2379×10^{-3}	20	11103	
HB10	0.8	2.8352×10^{-3}	10	11036	
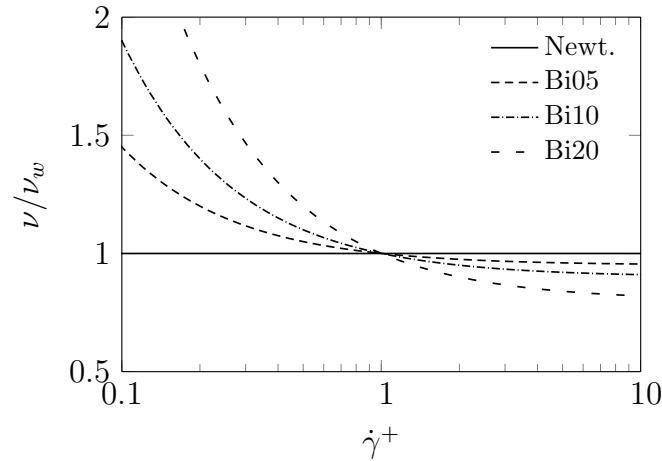
Fig. 5.22 Viscosity rheograms plotted for Bingham liquids with different τ_y but the same ν_w at $Re_\tau = 323$. The effect of modifying yield stress is seen mainly at shear rates lower than $\dot{\gamma}_w^+$.

Figure 5.23 shows contours of instantaneous axial velocity near the wall (in the buffer layer at $y^+ = 10$) and at a cross section for Newtonian and Bingham liquids. Despite having the same mean wall viscosity, differences in the flow of these liquids are clear even very close to the wall. Similar to shear thinning, increasing τ_y reduces the fluctuations in the flow and low speed streaks run longer in the streamwise direction for a higher τ_y. When the information in figure 5.23 is quantified using the integral length scales (see section 5.1.1), it is found that the integral length scale of the axial velocity fluctuations is large in both streamwise and azimuthal directions near the wall with increasing τ_y (figure 5.24). This is similar to the effect of shear thinning in PL liquids as seen in figure

5.4, however, unlike PL liquids, here the profiles of Bi5 and Newtonian cross each other away from the wall seen clearly in figure 5.24 (a). Similar behaviour is seen for Bi10 and Bi20, however, the reason for which is not clear.
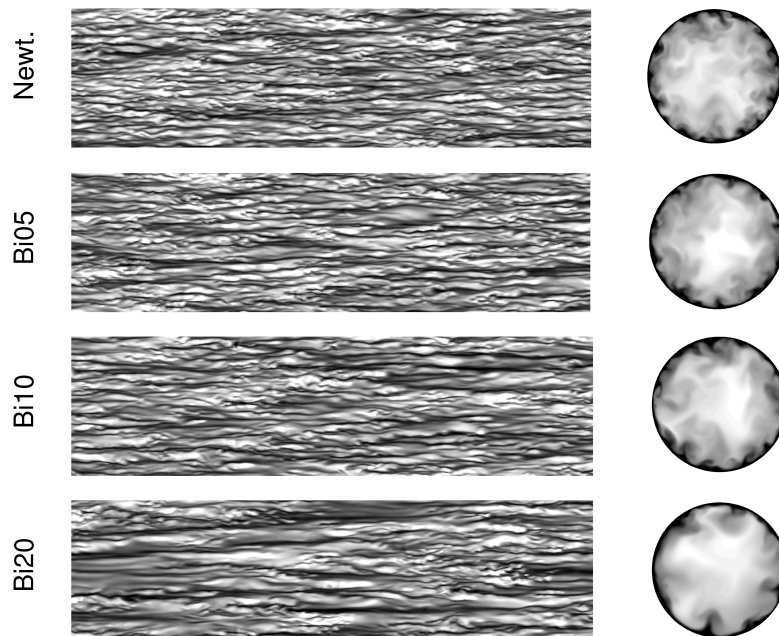
Fig. 5.23 Instantaneous axial velocity contours (left) at $y^+ = 10$ shown on developed cylindrical surfaces and (right) at a cross section plotted for (from top) Newtonian fluid and Bingham liquids Bi5, Bi10 and Bi20. Flow is from left to right, and lighter grey represents higher speed. Flow becomes more transitional as the yield stress is increased.
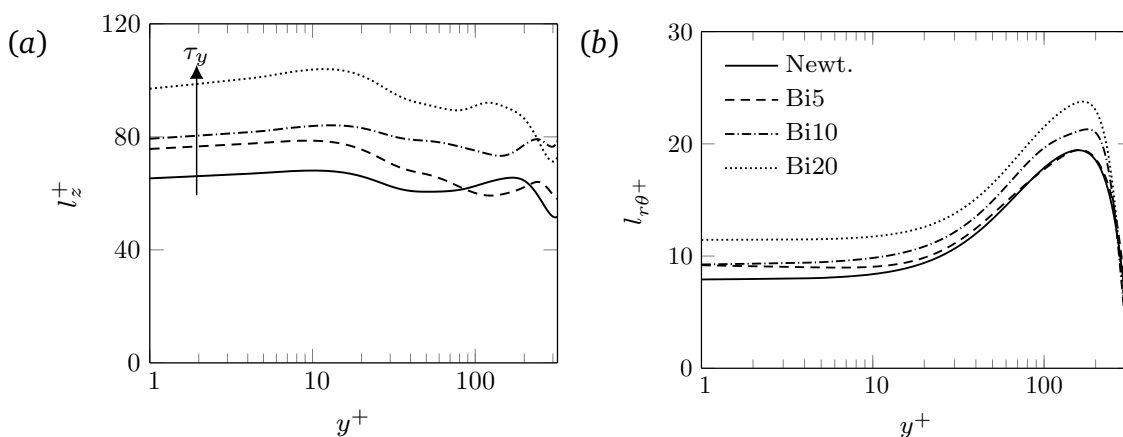
Fig. 5.24 Profiles of the (a) streamwise integral length scale and (b) azimuthal integral length scale plotted as a function of y^+ for different τ_y.

5.2.1 Mean flow and low order turbulence statistics

Mean axial velocity and viscosity

Profiles of the mean axial velocity U_z^+ for Newtonian and Bingham liquids are shown in figure 5.25 (a) and compared to the Newtonian profile. The flow domain is divided into viscous sublayer, buffer layer, log layer and core region for ease of discussion. The mean axial velocity profiles show a yield-stress-dependence only outside the viscous sublayer seen clearly in figure 5.25 (b) where the difference between U_z^+ for Bingham and Newtonian liquids is plotted. Outside the viscous sublayer, the mean axial velocity U_z^+ is larger for higher τ_y for $y^+ \gtrsim 15$, which corresponds to an higher flow rate. In the log layer, U_z^+ profiles for all liquids show a log region where the profiles shift above the Newtonian profile with increasing τ_y. The effect of increasing τ_y is marginal on the mean velocity gradient (figure 5.26) and it appears primarily for the range of $y^+ \in [8-80]$. These results are in contrast to those of the power-law liquids where shear-thinning increased U_z^+ at all y^+ (figure 5.5 a) and increased the mean velocity gradient noticeably in the log layer (figure 5.8).
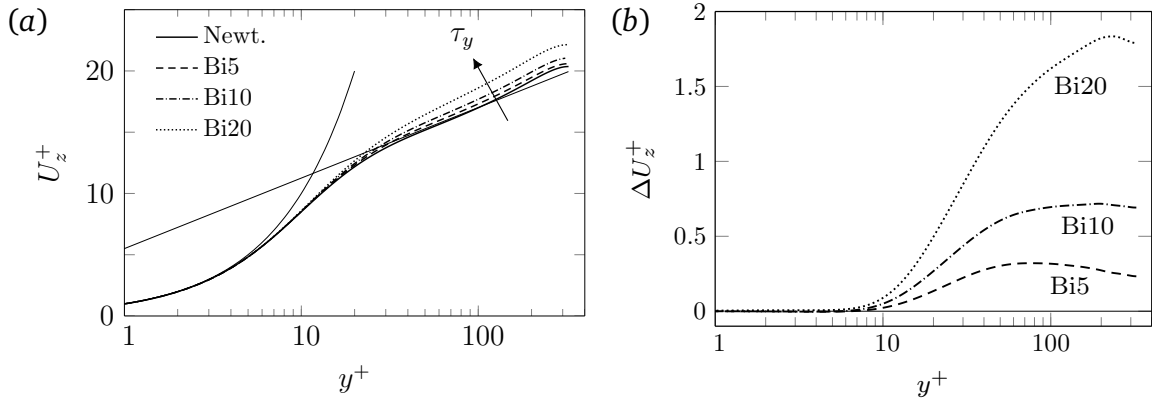
Fig. 5.25 Profiles of the (a) mean axial velocity U_z^+ and (b) difference between U_z^+ for a non-Newtonian and Newtonian liquids plotted against y^+ for Bingham liquids at $Re_\tau = 323$.

Increasing yield stress affects the mean viscosity ν^+ in a similar way to shear thinning. For a given fluid, the mean viscosity ν^+ is almost uniform in the viscous sublayer, but increases rapidly with y^+ beyond $y^+ \approx 10$ (figure 5.27). For Bi20, it is almost fifteen times larger than the mean wall viscosity ν_w.
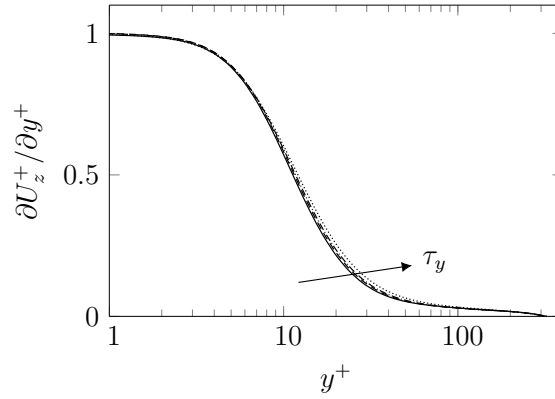
Fig. 5.26 Profiles of the mean axial velocity gradient plotted for Bingham liquids at $Re_\tau = 323$.
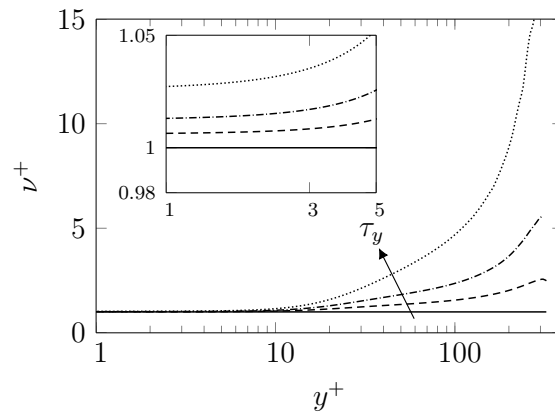
Fig. 5.27 Profiles of the mean viscosity plotted for different τ_y. The inset figure shows a closer look of the mean viscosity profiles in the viscous sub-layer. Mean viscosity is increased with increasing τ_y outside the viscous sublayer.

Similar to the mean axial velocity, ν^+ is also affected by increasing τ_y mainly outside the viscous sublayer. This is expected because $\dot{\gamma}$ decreases with y^+ and the viscosity of a Bingham fluid increases with increasing τ_y for $\dot{\gamma} < \dot{\gamma}_w$ (see figure 5.22). The effect of increasing τ_y on ν^+ is very small (approximately 3%) in the viscous sublayer. Similar to the mean viscosity profiles for shear-thinning liquids (figure 5.6), here also a log alike region is seen for Bingham liquids the reason for which is not obvious.

Mean shear stress budget

For a given fluid, the mean viscous stress $\tau^{v^+} = \nu^+ \partial U_z^+ / \partial y^+$ decreases monotonically with y^+ and for a given y^+, τ^{v^+} is higher for higher τ_y (figure 5.28). The latter is mainly due to higher ν^+ for higher τ_y because the profiles of $\partial U_z^+ / \partial y^+$

are only slightly affected by τ_y (see figure 5.25 b). This increase in τ^{v^+} with τ_y is mostly compensated for by a decrease in Reynolds shear stress τ^{R^+}. Similar to a shear-thinning fluid, the turbulent viscous stress, τ^{fv^+}, is negative for a Bingham fluid and increases in magnitude with increasing τ_y and decreases with y^+ vanishing at the pipe centre. The turbulent viscous stress only marginally (less than 5%) contributes in the total mean shear stress budget and as expected from Eq. 5.2, it only slightly modifies the mean axial velocity profiles. Overall, these results are similar to those of shear-thinning PL liquids except for τ^{fv^+}. It is less near the wall and bigger near the centre which is opposite to that seen for shear-thinning liquids (see figure 5.7 and 5.28).
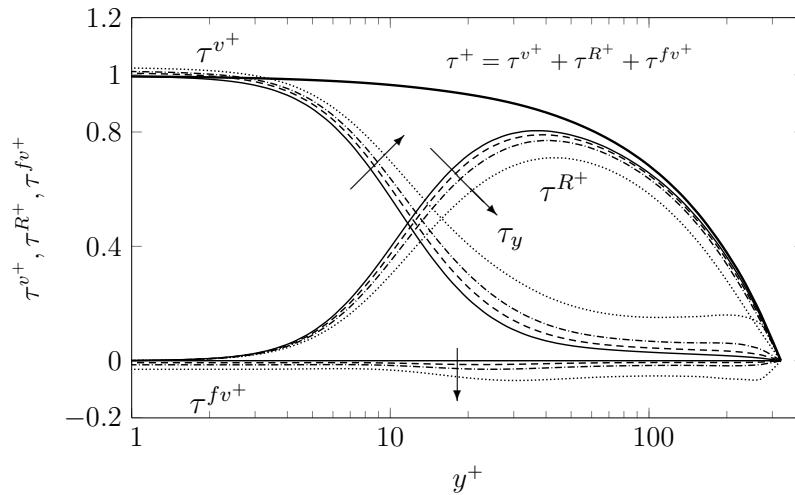
Fig. 5.28 Profiles of the mean viscous stress τ^{v^+}, Reynolds shear stress τ^{R^+} and the turbulence viscous stress τ^{fv^+} plotted for Bingham liquids. The thick line shows the profiles of the total mean shear stress which is the same for all cases and plotted here only for the Newtonian fluid. Line legend is the same as used in previous figures. Yield stress increases τ^{v^+} and τ^{fv^+} (in magnitude) but decreases τ^{R^+}.

Turbulence intensities

Turbulence intensities are also affected by increasing τ_y similar to as shear thinning. The axial turbulence intensity $u_z'^+$ is higher but the radial and the azimuthal turbulence intensities, $u_r'^+$ and $u_\theta'^+$ are lower for higher τ_y (figure 5.29). The net effect is seen in the turbulent kinetic energy (k^+) profiles (figure 5.29 b). The turbulent kinetic energy k^+ is higher for higher τ_y in the buffer layer and inner log layer for $y^+ \lesssim 80$ which is dominated by the increase in $u_z'^+$ rather than

the decrease in $u_r'^+$ and $u_\theta'^+$ with increasing τ_y. However, the trend reverses for $y^+ \gtrsim 100$ and k^+ is lower for higher τ_y because the effect of τ_y on $u_z'^+$ diminishes there whereas $u_r'^+$ and $u_\theta'^+$ continue decreasing. A noticeable difference in k^+ profiles compared to power-law liquids is that k^+ profiles of different n collapse in the core (figure 5.20) but the profiles of different τ_y do not.
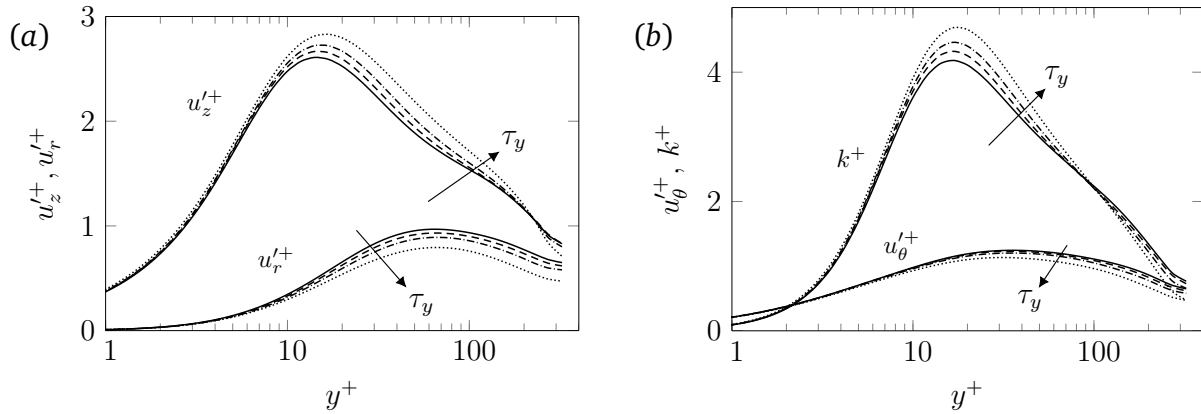
Fig. 5.29 Profiles of turbulence intensities (a) in the axial and the radial direction (b) in the azimuthal direction and turbulent kinetic energy plotted in wall coordinates for Bingham liquids. Turbulence intensities increase in the axial direction but decrease in the radial and the azimuthal direction with increasing yield stress.

5.2.2 Turbulent kinetic energy budget

Profiles of the TKE budget terms (see Eq. 3.9) are shown in figure 5.30, which except for a few differences (discussed here) are similar to those of shear-thinning PL liquids (figure 5.18). Turbulent kinetic energy (TKE) production, $\mathcal{P}^+$, is lower for higher τ_y (figure 5.30 a). Since $\mathcal{P}^+ = \tau^{R+}(\partial U_z^+/\partial y^+)$, lower $\mathcal{P}^+$ is mainly due to lower τ^{R+} for higher τ_y (figure 5.28) (the mean velocity gradient $\partial U_z^+/\partial y^+$ is negligibly affected by τ_y, figure 5.25 b). In the y^+ range where $\mathcal{P}^+$ shows a strong yield-stress-dependence, the mean viscous dissipation, ϵ^+, is independent of τ_y. A similar trend was observed for shear-thinning PL liquids (see figure 5.18), the reason of which is not yet clear. At all other y^+, increasing τ_y increases mean viscous dissipation ϵ^+. The effect of increasing τ_y on ϵ^+ is the greatest outside the viscous sublayer and is in contrast to shear thinning which increased ϵ^+ (in magnitude) more in the viscous sublayer.

The total turbulent transport in the viscous sublayer is dominated by the mean viscous transport $\mathcal{D}^+$. It balances the mean viscous dissipation ϵ^+
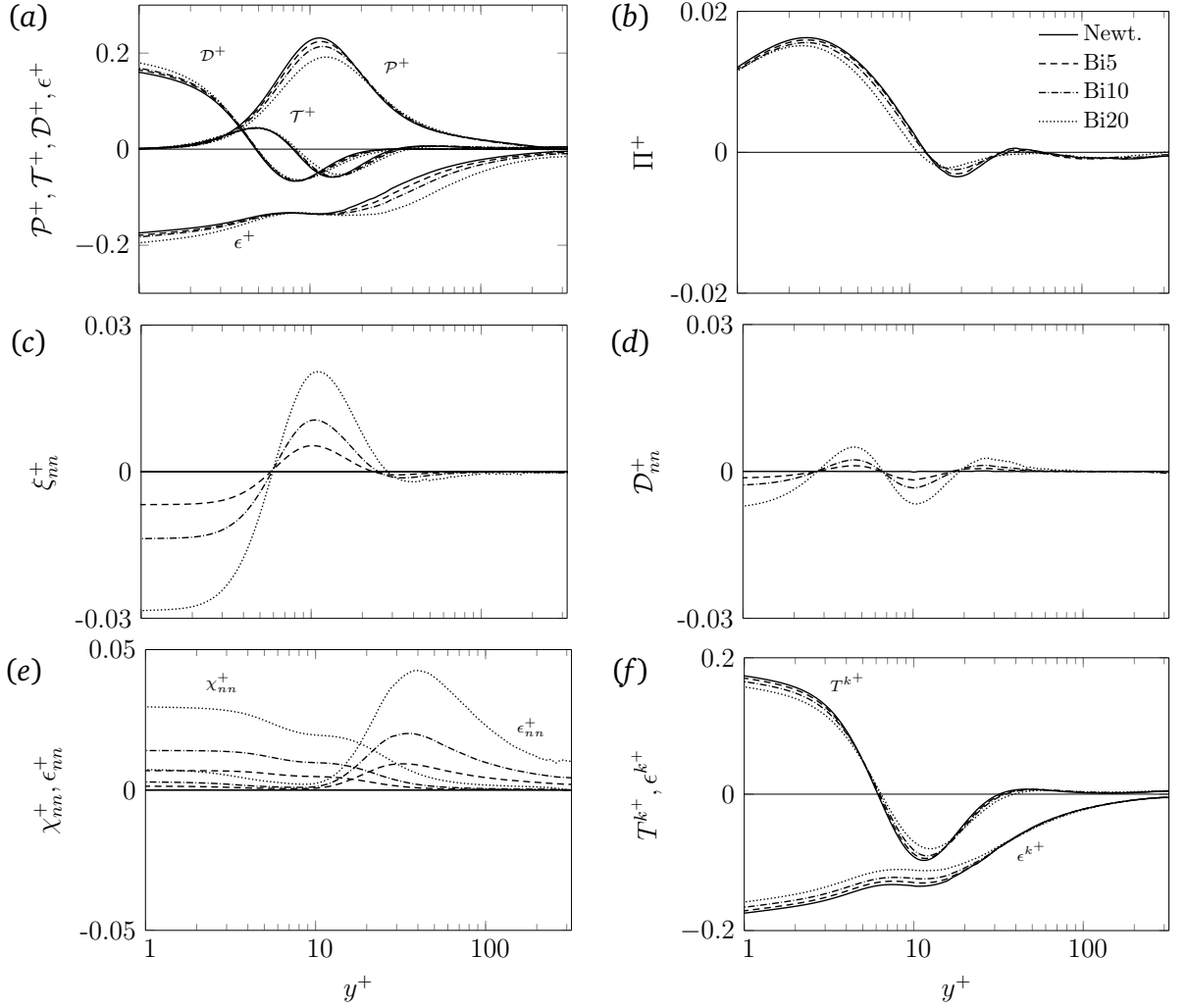
Fig. 5.30 Profiles of (*a,b*) Newtonian kinetic energy budget terms (*c–e*) non-Newtonian terms (f) sum of the Newtonian and non-Newtonian transport and dissipation terms plotted in wall units for the Newtonian fluid and Bingham liquids with different τ_y.

(figure 5.30 *a*). It increases in magnitude with increasing τ_y, however, the effect is marginal beyond $y^+ \approx 2$. The remaining Newtonian transport terms, the turbulent transport, $\mathcal{T}^+$, and the pressure-gradient work, Π^+, show a yield-stress-dependence only in the buffer layer ($y^+ \approx 7 - 30$, see figures 5.30 *a* and *b*). The pressure-gradient work, Π^+, is small compared to other Newtonian transport terms and it decreases in magnitude with increasing τ_y whereas the effect of increasing τ_y is marginal on $\mathcal{T}^+$.

The non-Newtonian terms which arise from viscosity fluctuations, are plotted in figures 5.18 *c–e*. The transport terms, ξ_{nn}^+ and $\mathcal{D}_{nn}^+$, are significant
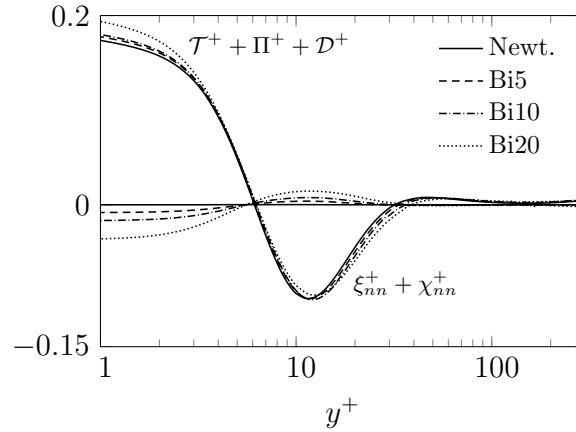
Fig. 5.31 Profiles of the sum of the Newtonian and non-Newtonian transport terms. The non-Newtonian transport usually opposes the Newtonian transport.

only for $y^+ \lesssim 50$. Although they change sign with y^+, their magnitude increases with increasing τ_y for a given y^+. The mean shear turbulence viscous transport, ξ_{nn}^+, usually has a sign opposite to the mean viscous transport, $\mathcal{D}^+$, and therefore, reduces the Newtonian transport for all y^+ (figure 5.18 c). The other non-Newtonian transport term, $\mathcal{D}_{nn}^+$, is three to four times smaller than ξ_{nn}^+. The overall effect of the non-Newtonian transport terms is to decrease the magnitude of total transport with increasing τ_y (figure 5.31), which is similar to the shear-thinning effect (figures 5.18 d,e).

The yield-stress-dependence of the non-Newtonian dissipation terms is also similar to that of shear thinning alone. Both non-Newtonian dissipation terms, χ_{nn}^+ and ϵ_{nn}^+, are positive for Bingham liquids (figure 5.18 e) and increase in magnitude with increasing τ_y. The mean shear turbulent viscous dissipation, χ_{nn}, is maximum near the wall and decreases with y^+ vanishing somewhere in the log-layer depending on the value of τ_y. The turbulent viscous dissipation, ϵ_{nn}^+, is small (about $1/3^{rd}$ of χ_{nn}^+) in the viscous sublayer, it reaches a minimum at $y^+ \approx 10$ and then starts increasing. The location where ϵ_{nn}^+ peaks shifts away from the wall with increasing τ_y.

In the viscous sublayer, the total dissipation, $\epsilon^{k+} = \epsilon^+ + \chi_{nn}^+ + \epsilon_{nn}^+$, decreases with increasing τ_y due to positive χ_{nn}^+ and ϵ_{nn}^+ (figure 5.18f). Decreased dissipation persists until the start of the log layer ($y^+ \approx 30$). Total transport, $T^{k+} = \mathcal{T}^+ + \Pi^+ + \mathcal{D}^+ + \xi_{nn}^+ + \epsilon_{nn}^+$, also decreases (in magnitude) in wall layer ($y^+ < 60$) with increasing τ_y except near the edge of the viscous sublayer ($y^+ = 5$)

94

where the profiles for different τ_y cross. Overall, the effect of increasing τ_y is seen for $y^+ \lesssim 60$ which was also seen for PL liquids (figure 5.18).

5.2.3 Summary

The effect of τ_y is the greatest outside the viscous sublayer and seen more clearly for the viscosity dependent terms, τ^{fv^+}, ϵ^+, χ^+_{nn} and ϵ^+_{nn}. The mean axial velocity is also independent of τ_y in the viscous sublayer. This is in contrast to shear thinning which showed the greatest effect inside the viscous sublayer. Differences are also seen for the turbulent kinetic energy profiles which deviate slightly for different τ_y but were independent of n there.

5.3 Modification of the yield stress effect by shear thinning

Many liquids in applications show both yield stress and shear-thinning behaviour and can be modelled with the HB rheology model. In order to see the joint effect of shear thinning and τ_y, the results of a shear-thinning PL fluid with $n = 0.8$ (referred to as PL) and a Bingham fluid Bi10 are compared with those of a HB fluid with the same flow index as the shear-thinning fluid and τ_y as the Bingham fluid ($\tau^+_y = 0.10$) at $Re_\tau = 323$. The HB fluid is referred to as HB10 in the following discussion.

The fluid viscosity for the three liquids PL ($n = 0.8$), Bi10 and HB10 are plotted in figure 5.32. Since ν_w is fixed, all rheograms cross each other at the wall shear rate, $\dot{\gamma}^+ = 1$. Except in a range $\dot{\gamma}^+ \in [0.2, 1]$, the PL viscosity is lower than Bi10. In contrast, HB10 consistently shows higher viscosities than Bi10 for $\dot{\gamma}^+ < 1$ and lower for $\dot{\gamma}^+ > 1$. Contours of the instantaneous axial velocity near the wall show qualitatively similar flow for PL and Bi10. As expected, less disordered motion and low speed streaks running longer are seen in HB10 compared to other cases, which suggests that the flow of HB10 is the closer transition than the other cases. Since the flow of PL and Bi10 are qualitatively very similar, the results of these two liquids are compared first before considering the joint effect of τ_y and n in HB10.
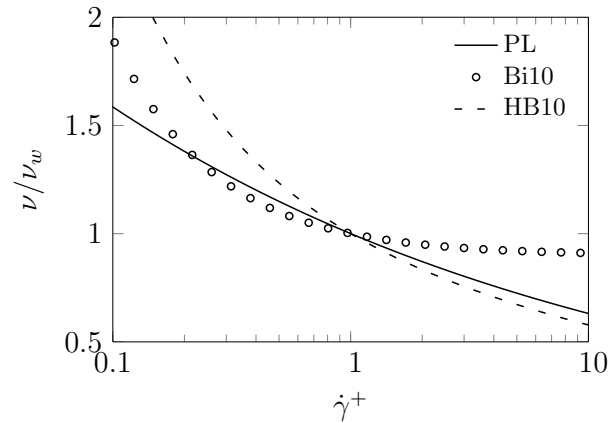
Fig. 5.32 Viscosity rheograms plotted for power-law (PL, $n = 0.8$), Bingham (Bi10, $\tau_y^+ = 10\%$) and Herschel–Bulkley (HB, $n = 0.8$ and $\tau_y^+ = 10\%$) liquids.
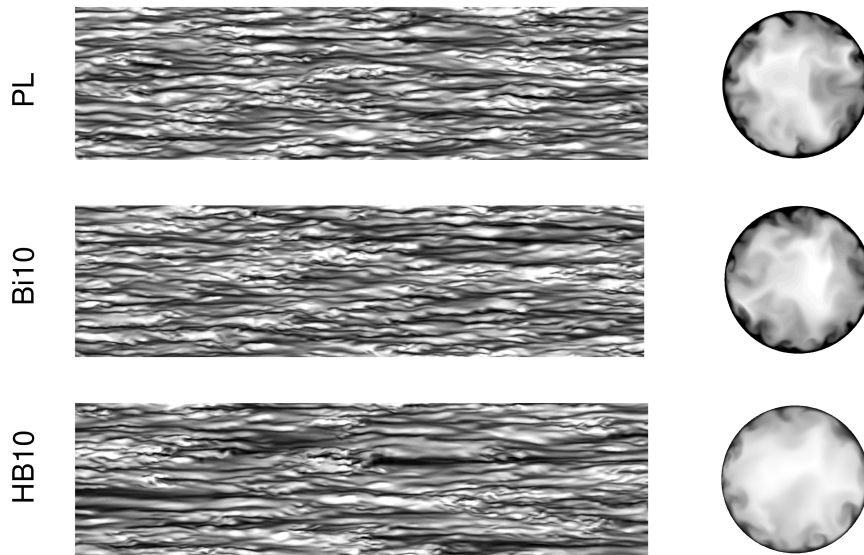
Fig. 5.33 Instantaneous axial velocity contours (left) at $y^+ = 10$ shown on developed cylindrical surfaces and (right) at a cross section in the middle of the domain plotted for (from top) HB liquids and Bi10. Flow is from left to right, and lighter grey represents higher speed. Flow becomes more transitional as the yield stress is increased or the fluid becomes more shear-thinning.

5.3.1 Comparison of power-law and Bingham rheologies

The mean axial velocity (U_z^+) profiles of PL and Bi10 almost overlap at all y^+ (figure 5.34 a), however, a close look via the mean velocity gradient $\partial U_z^+/\partial y^+$ shows that U_z^+ is slightly higher (approximately 2%) for the PL fluid than Bi10 in the viscous sublayer (figure 5.34 b). Outside the viscous sublayer, the profiles of $\partial U_z^+/\partial y^+$ for PL and Bi10 overlap (marker and solid line). In contrast, profiles of the mean viscosity ν^+ overlap for PL and Bi10 only very near the wall (figure

5.35 a). For $y^+ > 10$, Bi10 clearly shows significantly higher mean viscosity than PL because of its higher viscosity at low shear rates compared to PL.

(a)

(b)
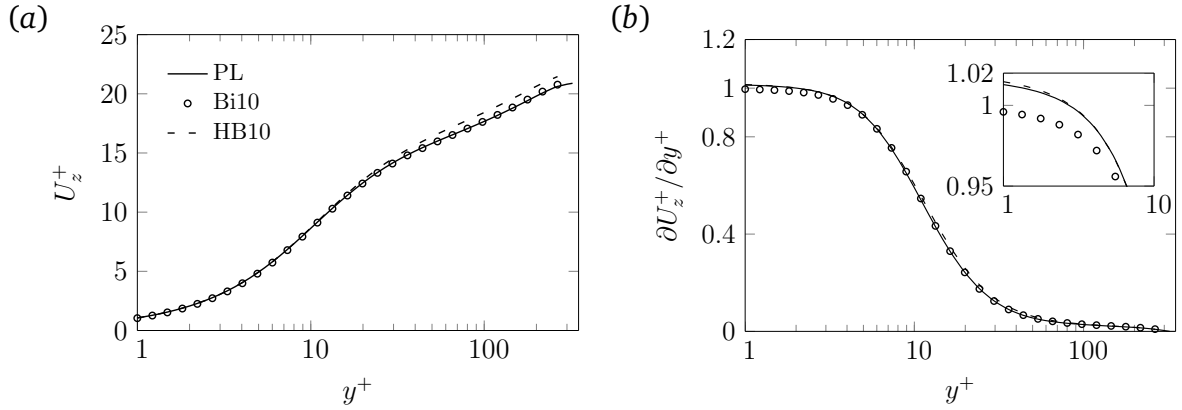
Fig. 5.34 Profiles of the (a) mean axial velocity, U_z^+ (b) and the mean axial velocity gradient, $\partial U_z^+/\partial y^+$ plotted for PL, Bi10 and HB10.

Similar to the mean axial velocity, profiles of the axial turbulence intensity, $u_z'^+$, and Reynolds stress, τ^{R+}, also overlap for PL and Bi10 (figure 5.35 b) whereas profiles of radial and azimuthal turbulence intensities ($u_r'^+$ and $u_\theta'^+$) deviate from each other outside the viscous sublayer (figure 5.35 c). The location where these profiles and ν^+ profiles start to deviate is at approximately the same location which indicates a direct influence of ν^+ on $u_r'^+$ and $u_\theta'^+$.

The turbulent viscous stress, τ^{fv+}, is slightly lower (in magnitude) for Bi10 than PL in the viscous sublayer and the trend reverses for $y^+ > 10$ (figure 5.35 d). Since the Reynolds stress profiles overlap for these two cases (figure 5.35 b) and the total mean shear stress is independent of rheology (see section 5.1.2), the reduced τ^{fv+} in the viscous sublayer in Bi10 is balanced by a corresponding decrease in the mean viscous stress τ^{v+} as seen in figure 5.35 (d). In the TKE budget, the viscosity dependent terms, $\mathcal{D}^+$, ϵ^+, ξ_{nn}^+, $\mathcal{D}_{nn}^+$, χ_{nn}^+ and ϵ_{nn}^+, are larger in magnitude for PL than Bi10 near the wall ($y^+ \lesssim 15$) but, the trend changes away from the wall (figure 5.36).

Overall the results of PL and Bi10 are mostly similar qualitatively and quantitatively except for a few differences seen for the mean viscosity and the non-Newtonian TKE budget terms.

97
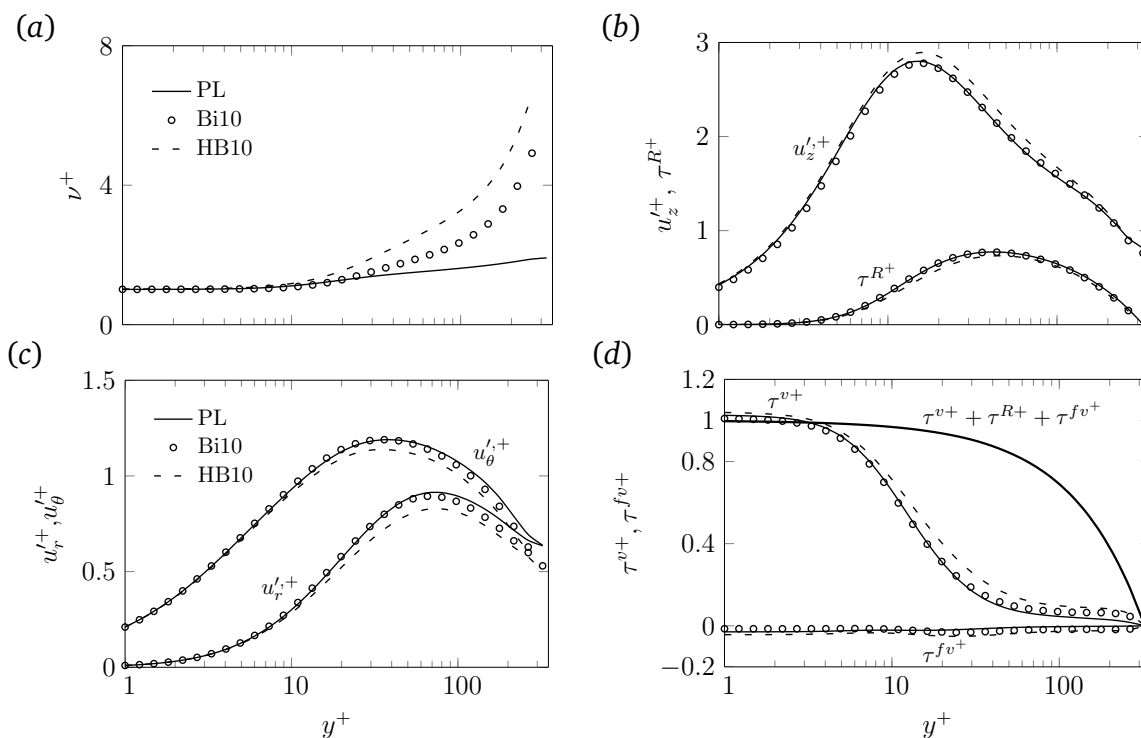
Fig. 5.35 Profiles of (*a*) axial and radial turbulence intensities (*b*) azimuthal turbulence intensities (*c*) mean viscosity and (*d*) the mean viscous stress τ^{v+} and the turbulence viscous stress τ^{fv+} plotted for HB liquids (lines) and Bi10 (markers).

5.3.2 Joint effect of shear thinning and the yield stress

HB10 includes both yield stress and shear thinning behaviour, therefore, as expected the mean axial velocity profiles of HB10 deviate above both PL and Bi10 (figure 5.34 *a*). In the viscous sublayer, profiles of the mean axial velocity gradient of HB10 and PL overlap (figure 5.34 *b*), which supports our argument presented for Bingham liquids in section 5.2 that yield stress does not have a significant effect on the mean axial velocity in the viscous sublayer.

Since the mean viscosity, ν^+, in the viscous sublayer is negligibly affected by modifying τ_y or n (see figure 5.6 and 5.35 *a*), ν^+ profiles of HB10 overlap PL and Bi10 in the viscous sublayer. Outside the viscous sublayer, ν^+ profiles of HB10 deviate above the others (figure 5.35 *a*), which shows that modifying τ_y affects ν^+ in core significantly.

The joint effect of shear thinning and τ_y is to increase the anisotropy of turbulent fluctuations, with increased $u_z'^+$ and decreased $u_r'^+$ and $u_\theta'^+$ outside
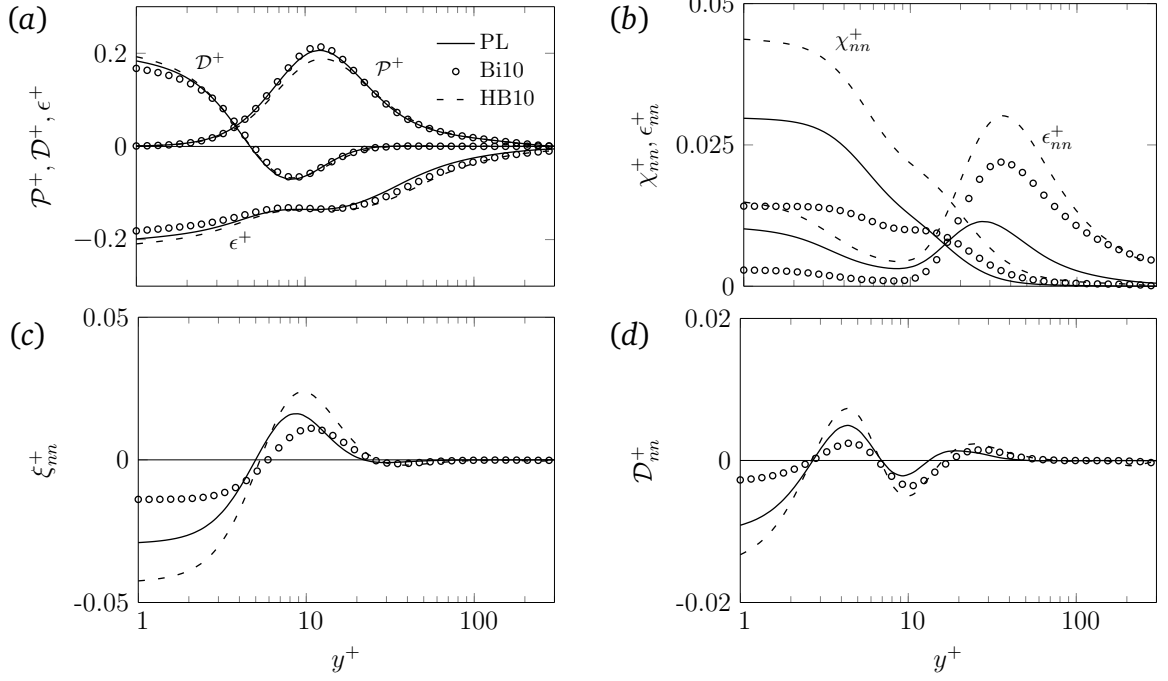
Fig. 5.36 Profiles of turbulence kinetic energy budget terms plotted in wall units for PL (solid line), Bi10 (markers) and HB10 (dashed line).

the viscous sublayer (figures 5.35 b, c). Larger values of the turbulent viscous stress, τ^{fv^+}, are also seen for HB10 compared to other cases due to both shear thinning in the viscous sublayer and higher τ_y for $y^+ \gtrsim 10$ (figure 5.35 d). The larger values of τ^{fv^+} for HB10 lead to a higher mean viscous stress τ^{v^+} at all y^+ compared to other cases.

In the TKE budget, profiles of the transport and the production terms for HB10 deviate from others only near the wall ($y^+ \lesssim 60$) (figure 5.36). As expected, for a given y^+, the turbulence kinetic energy production, $\mathcal{P}^+$, is minimum for HB10. In contrast, the mean viscous transport, $\mathcal{D}^+$, and the mean viscous dissipation, ϵ^+, are maximum for HB10 (figure 5.36 a). The mean viscous dissipation (ϵ^+) profile of HB10 closely follows the profile of PL in the viscous sublayer and the profiles of Bi10 outside the viscous sublayer. Profiles of the non-Newtonian terms for HB10 closely follow the profiles of the their sum for PL and Bi10 (figures 5.36 b-d). These are more influenced by shear thinning in the viscous sublayer and by τ_y outside it.

5.3.3 Summary

In summary, the combined effect of shear thinning and yield stress is that all deviations observed for τ_y are increased in effect. The effects are additive but not linear. Shear thinning in the HB rheology modifies the flow primarily in the near wall region.

5.4 Empirical correlations

There are several correlation available for PL and HB liquids for predicting the mean velocity and the turbulent friction factor (see chapter 2), however, for GN liquids, particularly for PL liquids, the Dodge and Metzner correlation (Eq. 2.16) has been found to give the best agreement with experiments. In this section, the DNS results of PL liquids are compared with the Dodge & Metzner correlations for the friction factor (Eq. 2.16) and the mean axial velocity (Eq. 2.15). The results are also compared with alternate correlations (Eq. 2.18 and 2.23) which are either widely used or have a theoretical support. Since the Wilson–Thomas correlation (Eq. 2.21) is widely used for HB liquids [50], the friction factor predictions using DNS and the Wilson–Thomas correlation are also compared.

Figure 5.37 (a) compares the DNS predictions of U_z^+ against the Dodge & Metzner correlation (Eq. 2.15). In this figure, the Dodge & Metzner scaling $\hat{y} = \left[(\rho^n \tau_w^{2-n})^{1/2}/K \right] y^n$ is used to scale distance from the wall. As seen in the figure, the agreement is poor and given a degree of confidence in the accuracy of the DNS results as discussed in chapter 4, this suggests that Eq. 2.15 is not appropriate, at least for $Re_\tau = 323$. Similarly, the predictions of Clapp's correlation (Eq. 2.18) and DNS do not agree (figure 5.37b), although the discrepancies are less obvious in this case. The deviation between the predictions of these correlations and DNS decreases when Reynolds number is increased as discussed in chapter 7.

DNS friction factor ($f = 2\tau_w/\rho U_b^2$) predictions are compared with the Dodge & Metzner correlation (Eq. 2.16) in figure 5.38 and table 5.3 where a good agreement between DNS predictions and Eq. 2.16 can be seen with the largest error (approximately 5%) occurring for the shear-thickening fluid. Since the
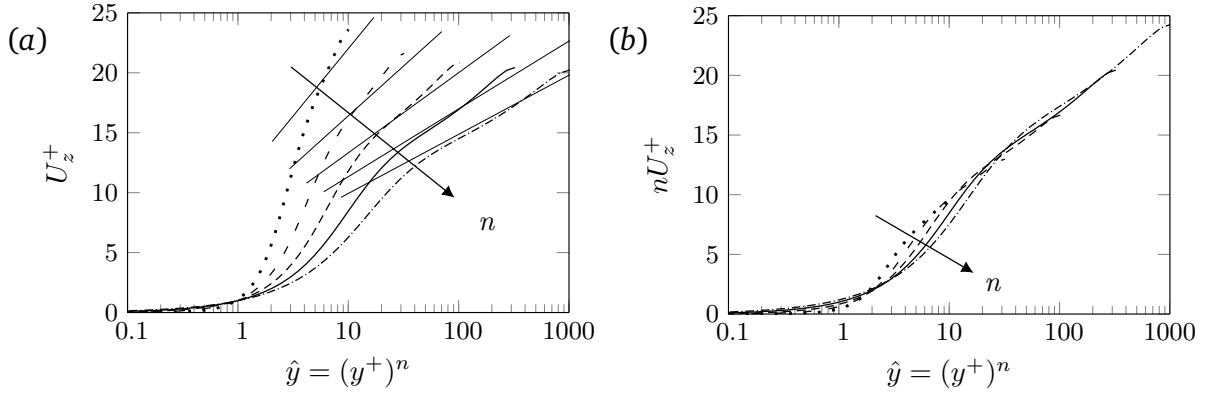
Fig. 5.37 DNS mean velocity predictions compared with (a) Dodge & Metzner velocity profile, Eq. 2.15 and (b) Clapp's profile, Eq. 2.18.

Dodge and Metzner correlation is a semi-empirical correlation whose parameters were derived from the experimental data of shear-thinning liquids, it is expected to give relatively large errors for shear-thickening liquids. For $n = 0.6$, prediction of Anbarlooei & Cruz correlation (Eq. 2.23) agree with the Dodge & Metzner correlation and DNS, however, for for $n \geq 0.8$, the agreement between DNS and Anbarlooei's correlation is better than the Dodge & Metzner correlation. Since Anbarlooei & Cruz correlation is based on the Blasius correlation for Newtonian fluid and the Dodge & Metzner correlation is based on Nikuradse's correlation and for lower turbulent Reynolds number, the Blasius correlation agrees better with experiments and DNS for Newtonian fluid. Therefore, a better agreement between the DNS predictions and Anbarlooei & Cruz correlation is expected than the Dodge & Metzner correlation. This assessment is revisited in section **??** for higher Reynolds numbers. Unlike the Dodge & Metzner and Anbarlooei

Table 5.3 Comparison of DNS predictions of friction factor f against the Dodge & Metzner correlation for different n at $Re_\tau = 323$.

n	$f \times 10^3$	$f_{DM} \times 10^3$	Error(%)
0.6	6.7	6.6	0.9
0.8	7.3	7.3	0.6
1.0	7.8	7.7	1.3
1.2	8.2	7.8	4.8

& Cruz correlations, the Wilson–Thomas correlation defines the bulk velocity in terms of the mean pressure gradient and the rheology parameters. It is used to
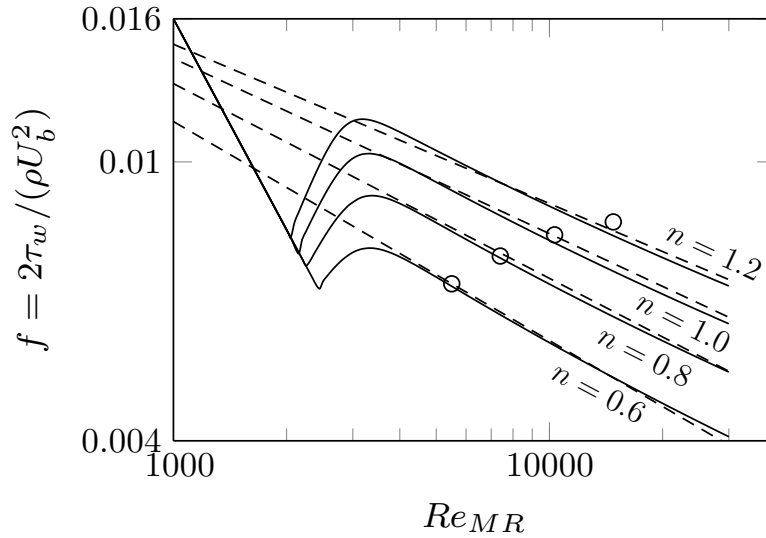
Fig. 5.38 Moody diagram, plotting Fanning friction factor as a function of Metzner–Reed Reynolds number Re_{MR}. DNS results (circles) are compared to the predictions of Dodge & Metzner correlation, Eq. 2.16 (solid lines) and Anbarlooei's correlation, Eq. 2.23 (dashed lines).

Table 5.4 DNS turbulent friction factor predictions compared with the Wilson–Thomas correlation, Eq. 2.21.

Case	$f \times 10^3$	$f_{WT} \times 10^3$	Error(%)
power-law liquids			
$n = 0.6$	6.7	5.8	13.0
$n = 0.8$	7.3	6.7	8.0
$n = 1.0$	7.8	7.6	3.0
$n = 1.2$	8.2	8.4	3.0
Yield stress liquids			
Bi5	7.63	7.22	5.0
Bi10	7.3	6.8	6.7
Bi20	6.7	6.1	8.1
HB10	6.8	6.1	10

determine the friction factor f_{WT} in table 5.4. Since this correlation can also be easily used for PL liquids, the predictions of DNS and the Wilson–Thomas correlation are compared for all liquids in table 5.4. It can be seen that the deviation between the prediction of DNS and the correlation is of the order of 10% which is larger than seen with the Dodge & Metzner correlation. Although the Wilson–Thomas correlation is backed by a theoretical analysis, the parameters

used in the correlation are empirical. The current results suggest that there is a need to revisit the correlation parameter to improve its accuracy.

Overall, Anbarlooei & Cruz correlation gives the best agreement with DNS for power-law liquids. For yield stress liquids, the Wilson–Thomas correlation's predictions are 5–10% in error compared to DNS.

5.5   Chapter summary

Simulations carried out for Herschel–Bulkley liquids with varying flow index and yield stress at a fixed friction Reynolds number of 323 show that shear thinning and increasing yield stress modify a turbulent pipe flow similarly. Fluctuations in the instantaneous flow decrease with shear thinning or increasing yield stress. The mean axial velocity profiles scaled with the nominal wall viscosity ν_w and the traditional friction velocity u^*, do not strictly follow the law of wall $U_z^+ = y^+$ for shear-thinning liquids. This is due to non-zero turbulent viscous stress which gives a higher U_z^+ for shear-thinning liquids compared to Newtonian liquids. New velocity and viscosity scales are derived, which collapse the mean axial velocity profiles in the viscous sublayer for different n. However, these new scales are difficult to determine from experiments. The effect of the yield stress on the mean axial velocity is very small in the viscous sublayer. Outside the viscous sublayer, the mean axial velocity profiles deviate above the Newtonian profile with shear thinning or increasing the yield stress.

The mean viscosity shows shear-thinning or yield-stress dependence mainly outside the viscous sublayer where it increases with shear thinning or increasing τ_y. The mean viscosity profiles show a log alike region the reason for which is not clear. For power-law liquids, the turbulent friction factor predictions using DNS were found to agree within 5% of the Dodge & Metzner correlation. This is much lower than the error found in Rudman et al. [84] (approximately 20%). Compared to the Dodge & Metzner, Anbarlooei & Cruz correlation is found to agree better with DNS of power-law liquids. Errors in the friction factor predictions using Wilson & Thomas correlation are found to be higher for lower n and higher τ_y compared to DNS. However, the discrepancies were less than 10%.

Turbulence intensities are found to increase in the axial direction but decrease in the radial and the azimuthal direction with shear thinning or increasing τ_y. This is likely due to the decrease in the turbulent energy transfer from the axial component to others as suggested by Gavrilov and Rudyak [40] for PL liquids. The Reynolds stress is also found to decrease with shear thinning or increasing τ_y. Due to viscosity fluctuations a new term is introduced in the mean momentum balance: the turbulent viscous stress which is negative for both shear-thinning and Bingham liquids. The magnitude of the turbulent viscous stress is maximum at the wall and displays a minimum in the buffer layer with the exact location depending on n. Due to increased viscosity and mean shear rate, the mean viscous stress increase with shear-thinning or increasing τ_y.

Except for the mean flow energy production, the effect of shear-thinning or increasing τ_y is seen on the mean flow energy budgets mostly for $y^+ < 60$. The mean flow energy production and dissipation are increased with shear thinning or increasing τ_y. The non-Newtonian terms act as a local source in the mean flow kinetic energy budget for both shear-thinning and Bingham liquids. Similar to the mean flow kinetic energy, the turbulent kinetic energy budget also shows flow-index or yield-stress dependence mainly for $y^+ < 60$. Shear thinning and the yield stress are found to have a notable effect on turbulence kinetic energy production in the buffer layer. The new terms introduced in the turbulent kinetic energy budget from the non-Newtonian rheology are found to add a local source for both shear-thinning and Bingham liquids.

Although, shear-thinning and yield stress effects are very similar, there are a few differences. Shear thinning increased the mean axial velocity in the viscous sublayer whereas the effect of the yield stress was negligible in the current simulations. Profiles of the axial turbulence intensity, mean viscous stress, turbulent viscous stress, mean viscous dissipation and the non-Newtonian transport and the dissipation terms also showed a larger shear-thinning dependence in the viscous sublayer for pure shear-thinning liquids whereas outside the viscous sublayer, the effect of τ_y was more than the shear-thinning effect.

A key result observed here is that both shear-thinning and yield stress affected the turbulent kinetic energy budget mainly in the near wall region, $y^+ < 60$, which suggests that the GN rheology is most important near the wall. This is further investigated and discussed in chapter 6. The shift in the mean axial velocity profiles with shear thinning or increasing yield stress is similar to the effect of decreasing Reynolds number in Newtonian liquids [24]. The Reynolds-number and shear-thinning effects are further analysed for Newtonian and shear-thinning liquids at higher Re_τ in chapter 7. These simulations will also show if log layer in the mean viscosity profiles is real or not.

<div align="right">

6

</div>

The rheology dependent region

For Newtonian liquids, the fluid viscosity is known to be important largely in the viscous wall region $y^+ < 50$ [78]. The same is not obvious for GN liquids since these liquids show non-uniform viscosity. Viscosity approximately four times larger than the nominal wall viscosity ν_w for a shear-thinning PL fluid ($n = 0.6$) and six times larger than ν_w for a HB fluid ($n = 0.8$, $\tau_y/\tau_w = 10\%$) were observed at the pipe centre in figures 5.6 and 5.27. The viscosity will increase further as the fluid becomes more shear-thinning or yield stress is increased. However, it was also observed that the effect of both shear thinning and yield stress on the turbulent kinetic energy budget was confined mainly to the near wall region (figures 5.18 and 5.30). Errors introduced in the rheology characterisation at shear rates typical of the outer log layer and of core region were also found not to affect the DNS predictions to any significant extent (see chapter 4). Together these observations suggest that the GN rheology is important mainly in the near wall region, although exactly how far this extends from the wall is unclear.

DNS is capable of modelling unreal physics i.e., it is possible to specify fluid properties and boundary conditions which actually do not exist in reality [71]. In the current study, this feature of DNS is used to investigate the effect of modifying viscosity in the log layer and core region for a shear-thinning

PL fluid. As both shear thinning and increasing yield stress similarly affect a turbulent pipe flow, (discussed in chapter 4 and 5), the outcomes of this study can be extended to any GN fluid at least qualitatively or possibly quantitatively. The method used here is slightly different from the one used in earlier chapters, therefore, it is described first before discussing the results.

6.1 Methodology

The solver used here is the same as used earlier and the difference in methodology comes via the rheology model. Earlier a single rheology model was used in the whole domain, whereas the current simulations use a hybrid rheology model over y^+. A power-law (PL) rheology model is used up to a certain y^+ from the wall and is then smoothly blended to transition to a uniform viscosity (Newtonian rheology) over small y^+ range of 30. A notation y_u^+ is used for the centre of the blended zone. Higher values of y_u^+ imply a wider PL rheology domain and hence, a narrower uniform viscosity region. The uniform viscosity is set equal to the mean PL viscosity at y_u^+ in a standard simulation.

6.2 GN rheology dependent region for a shear-thinning fluid

A moderately shear-thinning ($n = 0.6$) fluid is considered and the width of the PL rheology domain (y_u^+) is varied from 35 to 70. The results are compared with those from a standard simulation (i.e. $y_u^+ \approx 323$). These simulations are named as I (standard simulation), II, III in the order of decreasing y_u^+. Simulations are run for $Re_\tau = 323$. The consistency, forcing and the mesh are the same as for $n = 0.6$ in chapter 5 and the values of the uniform viscosity for different y_u^+ are given in table 6.1.

Mean Flow and turbulence intensities

Profiles of the mean viscosity are shown in figure 6.1a, and as set, a uniform viscosity is observed in simulations II and III for $y^+ > y_u^+$. Viscosity profiles below y_u^+ are indistinguishable from each other. It appears that the mean axial velocity

Case	y_u^+	ν_N/ν_w
I	323	–
II	70	2.6
III	35	2.0

Table 6.1 The values of y_u^+, which signifies the width of the PL rheology domain, for different simulations. The pipe radius is $R^+ = 323$ and ν_N is the uniform viscosity used beyond y_u^+ in simulations II and III. The simulation I refers to the standard simulation where a PL rheology with $n = 0.6$ is used in the whole domain.

profiles for all three simulations collapse on a single curve (figure 6.1b). However, a closer look shows that the profile of III deviate above the others for $y^+ < 30$ and below them beyond that. The same is observed in the profiles of the mean axial velocity gradient (figure 6.1c) where the profiles of III deviate from others largely in the viscous sublayer ($y^+ < 5$).
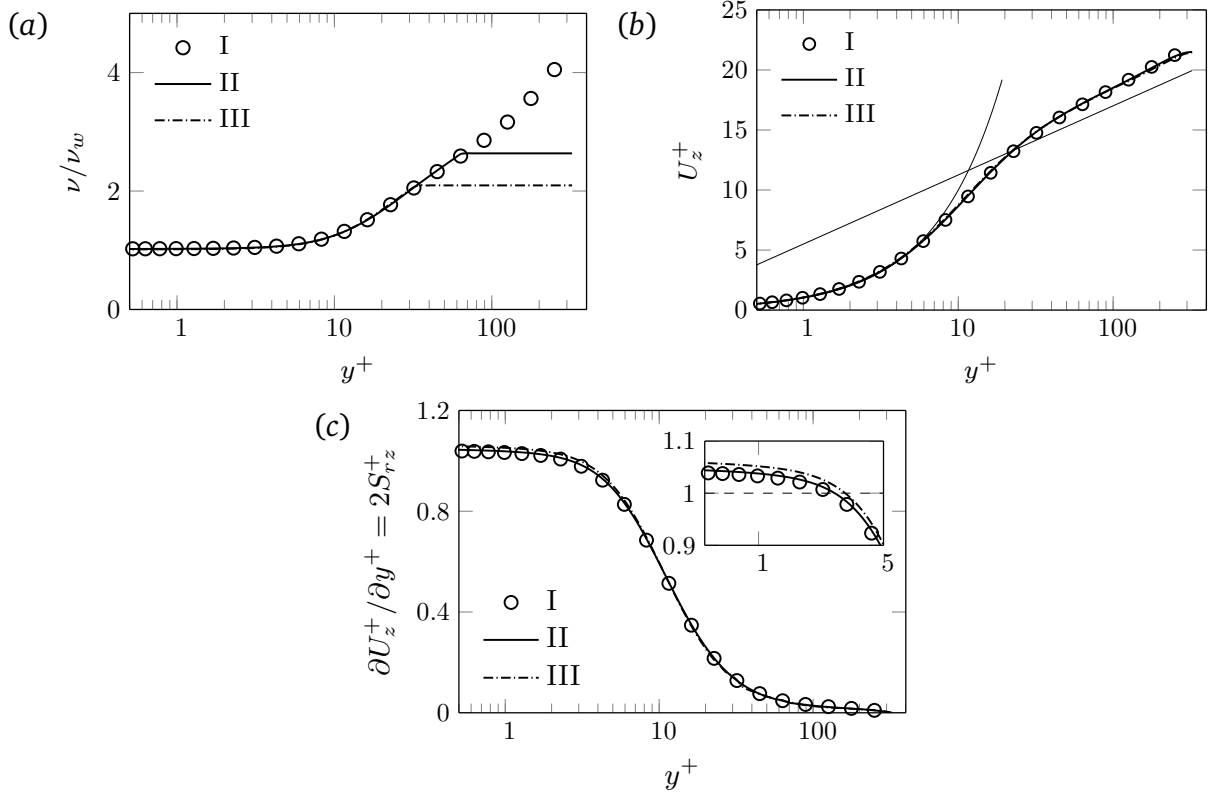
Fig. 6.1 Profiles of (a) the mean viscosity and (b) the mean axial velocity plotted in wall units. Dotted lines in (b) show the classical Newtonian law of wall $U_z^+ = y^+$, $U_z^+ = 2.5 \ln y^+ + 5.5$. The effect of switching the rheology model is negligible on the mean axial velocity profiles.
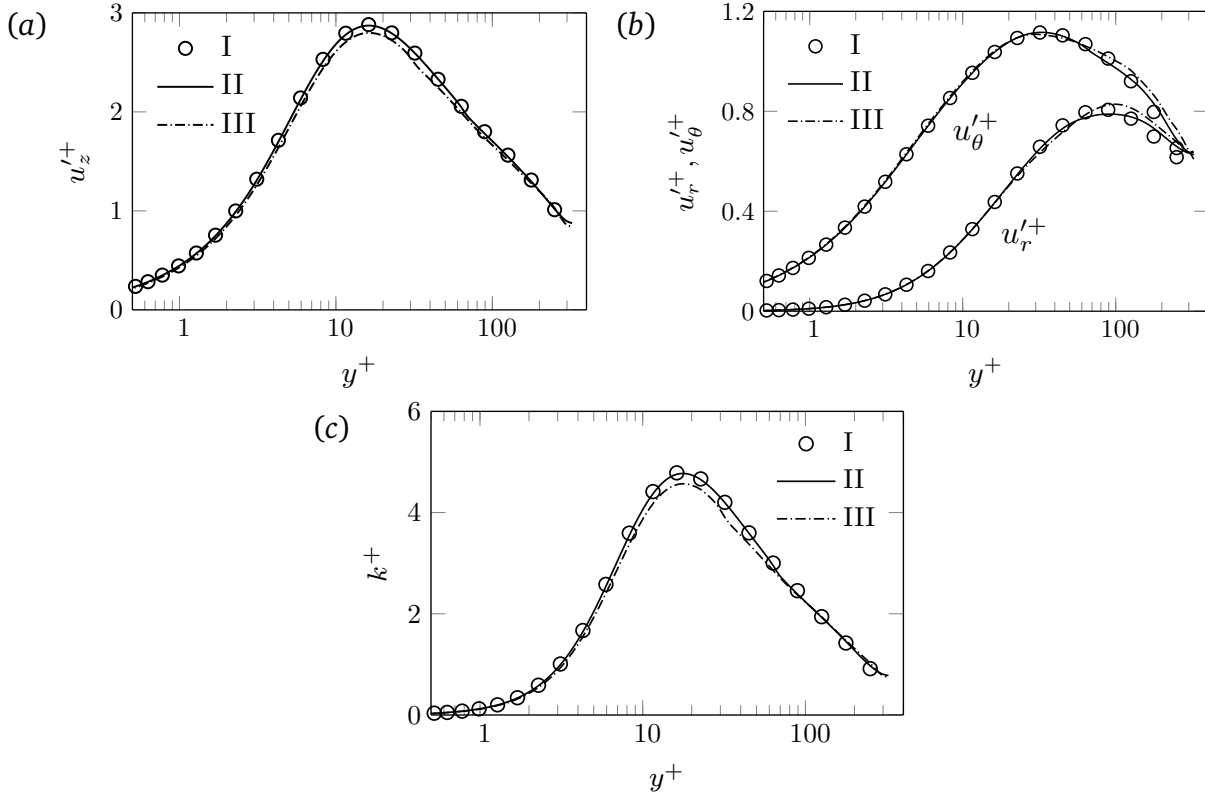
Fig. 6.2 Profiles of turbulence intensities in the (a) axial direction (b) radial and the azimuthal direction (c) turbulence kinetic energy k. Profiles of I and II almost overlap each other but deviate from those of III.

The effect of confining PL rheology to the near wall region has more effect on the turbulence intensities than the mean axial velocity as shown in figure 6.2. Similar to the mean axial velocity profiles, the differences between I and II are very small and seen mainly in the profiles of the radial and the azimuthal turbulent intensities for $y^+ > 70$. In contrast, all turbulence intensity profiles of III deviate from those of the standard simulation. The axial turbulence intensity profile starts to deviate in the viscous sublayer itself but profiles of the other components show deviation only for $y^+ > 20$.

These results suggest that PL rheology has an effect for $35 \lesssim y^+ \lesssim 70$ and, for $y^+ \gtrsim 70$, it has small effect on the overall profiles of mean axial velocity and turbulence intensities.

Mean Shear Stress

The total mean shear stress $\tau^+ = r/R$ is independent of the rheology for pipe flow. Because viscosity directly affects the mean viscous stress (τ^v) and the turbulent viscous stress (τ^{fv}), the effect of confining the PL rheology can be seen in the mean shear stress profiles (figure 6.3). As discussed in sections 3.2 and 5.1.2, only the (r, z) component of the total mean shear stress tensor $\boldsymbol{\tau}^+ = \boldsymbol{\tau}^{v+} + \boldsymbol{\tau}^{fv+} + \boldsymbol{\tau}^{R+}$ survives for a pipe flow. Therefore, only the (r, z) component of the mean shear stress budget is discussed here and the subscript rz is dropped for clarity.

By using a uniform viscosity for $y^+ > y_u^+$, viscosity fluctuation $\nu' = 0$ is forced in these simulations. This causes the turbulent viscous stress τ^{fv^+} to vanish for $y^+ > y_u^+$ (figure 6.3). Consequently, to maintain the total stress profile at correct level, $\tau^{v^+} + \tau^{R^+}$ must decrease. The difference in the mean viscous stress profiles between I and II is small because τ^{fv^+} has already decayed to less than 10% by $y^+ = 70$. This also leads to the Reynolds stress (τ^{R^+}) profiles of I and II overlapping each other. In contrast to II ($y_u^+ = 70$), there is a clear difference in the profiles of τ^{v^+} and τ^{R^+} between I and III ($y_u^+ = 35$). This is because the mean viscous stress τ^{v^+} is still large (approximately 30%) at $y^+ = 35$.

Overall these results suggest that the effect of modifying viscosity on the mean shear stresses is small for $y_u^+ = 70$ but large for $y_u^+ = 35$. Decreasing y_u^+ further will increase the deviation between the predictions of the standard and hypothetical simulations.

Summary

The results show that for $n = 0.6$, the non-uniform viscosity and viscosity fluctuations in $y^+ > 70$ have a little influence on the mean axial velocity and turbulence intensities. This is because viscosity affects the flow largely via the mean viscous stress which has already decayed to a very low value (less than 10% of its maximum) by $y^+ = 70$.
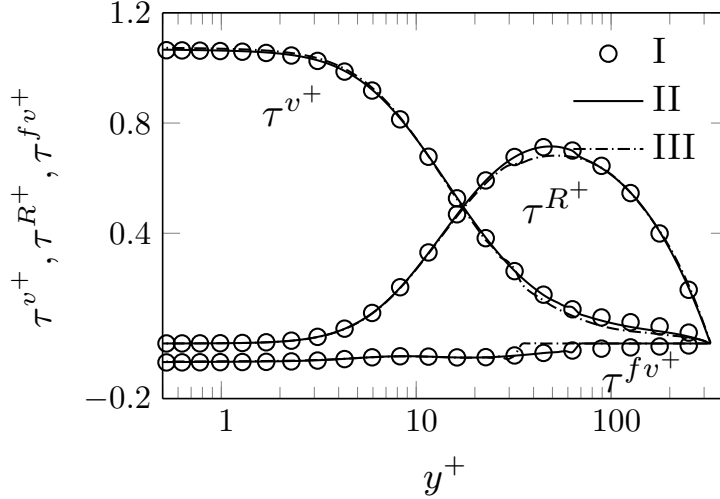
Fig. 6.3 Profiles of the rz component of the mean viscous stress τ^{v^+}, Reynolds stress τ^{R^+} and the turbulent viscous stress τ^{fv^+} plotted in wall units for different cases (see table 6.1).

6.3 The effect of shear thinning

Wilson and Thomas [103] argued that the region where viscous effects are important, thickens with shear thinning. This is also expected from figure 5.28 where increase in the near wall mean viscous stress was observed with shear thinning. To confirm the hypothesis of Wilson and Thomas, simulations are run for $y_u^+ = 50$ for $n = 0.6, 0.8$. If the hypothesis is correct, there will be larger differences between the standard and confined rheology simulations for $n = 0.6$ than $n = 0.8$. A notation "IV" is used for the simulations with $y_u^+ = 50$ in the following discussion.

The results of the simulations with $y_u^+ = 50$ are compared with their standard versions (simulation I) for both liquids in figure 6.4. As set, a uniform viscosity is seen for $y^+ > 50$ for both liquids (figure 6.4 a). Confining PL rheology to $y^+ < 50$ has a negligible effect on the mean axial velocity, turbulence intensities and Reynolds shear stress predictions for $n = 0.8$, whereas the differences between the confined rheology and standard simulations are clear for $n = 0.6$. However, a reasonable agreement between the standard and confined rheology simulations for $n = 0.6$ was obtained for $y_u^+ = 70$, which indicates the widening of the rheology (or viscosity) dependent region.
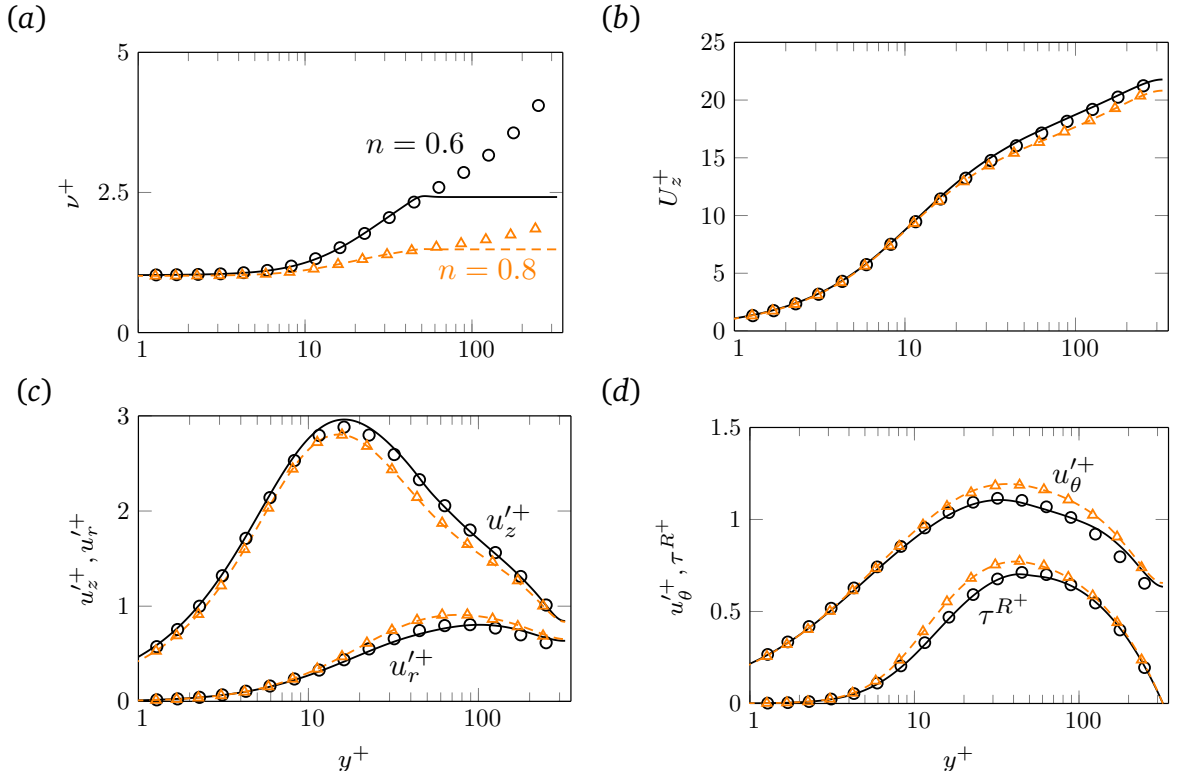
Fig. 6.4 Profiles of (*a*) mean viscosity (*b*) mean axial velocity (*c*) axial and radial turbulence intensities and (*d*) azimuthal turbulence intensity and Reynolds stress plotted for the full (lines) and restricted rheology (markers) simulations. Black lines are for $n = 0.6$ and orange lines are for $n = 0.8$.

6.4 Chapter summary

The current study identifies the GN rheology dependent region via a power-law rheology model by exploiting the ability of DNS to model physically impossible situations. The results from the confined rheology simulations show that modifying the fluid rheology beyond $y^+ = 70$ has no significant effect on the mean flow and first-order turbulence statistics for $n = 0.6$. By considering shear-thinning liquids with different flow indices, it is shown that the thickness of the rheology dependent region increases with shear thinning, which supports the argument of Wilson and Thomas [103].

The current findings are inline with the results reported in chapter 4 where the DNS predictions were found to be most sensitive to errors introduced at high shear rates such as those occur in the near wall region. Errors at low shear rates typical of the outer log-layer and core region negligibly affect the DNS

predictions. These results suggest that in RANS and LES numerical techniques, it could be possible to capture the effect of GN rheology by only modifying the turbulence models in the near wall region, for example, by modifying the wall functions.

The friction Reynolds number was fixed in the current study, however as shown in the next chapter that for $n = 0.6$, the overall effect of increasing Reynolds number on the energy budgets is negligible beyond $y^+ \approx 70$. This suggests that the extent of GN rheology dependent region will not vary with increasing Reynolds number, however, this needs to be confirmed in future.

7

The effect of increasing Reynolds number on turbulent pipe flow

The results in chapter 6 showed that GN rheology is important mostly in the near wall region and the non-uniform viscosity of a GN fluid in the core region has a little effect in a turbulent pipe flow. Shear rate increases with increasing Reynolds number, however as shear rate increases, viscosity becomes less sensitive to changes in shear rate as shown in figure 7.1 for a PL fluid. This suggests that the effect of GN rheology in a turbulent pipe flow might become negligible at very high Reynolds number and Newtonian profiles might be recovered.

The effect of increasing Reynolds number is studied here via simulations of Newtonian and shear-thinning ($n = 0.6$) liquids for $Re_\tau = 323 - 750$. The simulations parameters and mesh spacing for these simulations are presented in table 7.1. The mesh spacing is $y^+ = 0.8 - 4.0$ in wall normal direction, $\Delta(r\theta)^+ \approx 6$ in the azimuthal direction and $\Delta z^+ \approx 12$ in the streamwise direction. These mesh spacings are in a good agreement with the values used for Newtonian liquids at similar Re_τ [23]. The error in the sum of the energy budget terms is also less than 1% of the smallest term (not shown) which confirms an adequate mesh resolution and sufficiently long time averaging.
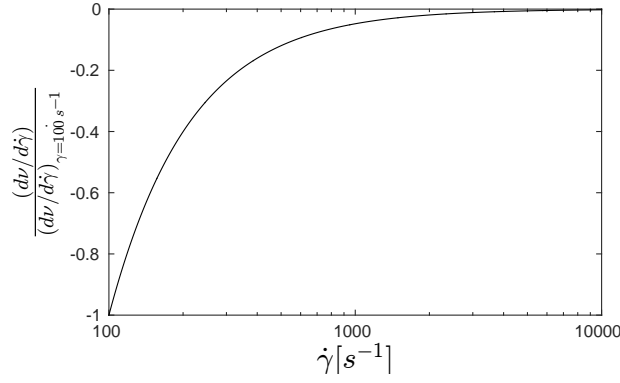
Fig. 7.1 Profiles of the rate of change in the viscosity with shear rate for a power-law fluid with $n = 0.6$. The shear rate dependence of the viscosity decreases with increase in shear rate.

Table 7.1 Simulation parameters for Newtonian and PL ($n = 0.6$) liquids for different Re_τ. The non-dimensional body force gR/u^{*2} is 2 and the nominal wall viscosity is $1/Re_\tau$.

Re_τ	n	$K/(\rho u^{*2-n} R^n)$	Re_G	Re_{MR}
323	0.6	3.1181×10^{-2}	11189	5498
	1.0	3.0870×10^{-3}	10322	10322
500	0.6	24.0201×10^{-3}	18471	7836
	1.0	1.9996×10^{-3}	17260	17260
750	0.6	18.8348×10^{-3}	28600	10450
	1.0	1.3333×10^{-3}	27000	27000

Contours of instantaneous axial velocity are plotted in figure 7.2 for a Newtonian fluid and in figure 7.3 for the shear-thinning fluid at $y^+ \approx 10$ in (a)-(c) and at a cross-section in (d)-(f) for different Re_τ. There are more small scale structures for higher Re_τ and less for the shear-thinning fluid compared to the Newtonian fluid. From these results, the integral length scales for the streamwise velocity fluctuations are expected to be larger for the shear thinning fluid than the Newtonian fluid for all Re_τ as seen in figure 5.4 for $Re_\tau = 323$.
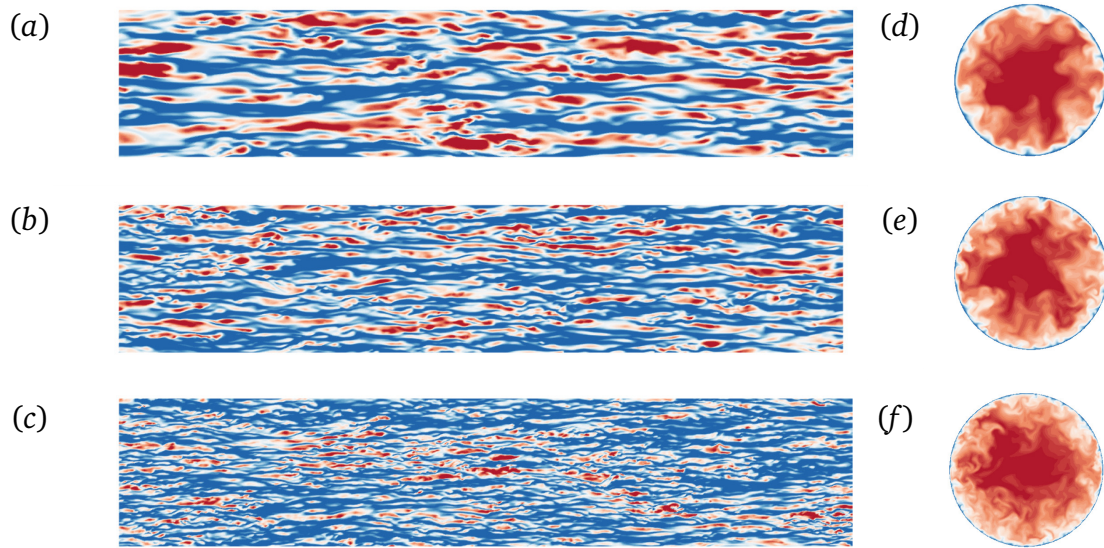
Fig. 7.2 Contours of the instantaneous axial velocity normalised by the bulk velocity plotted on (*a-c*) the developed cylindrical surface at $y^+ = 10$ and (*d-f*) a cross-section for a Newtonian fluid at (from top to bottom) $Re_\tau = 323, 500$ and 750. For *a-c,* the flow is from left to right. The contours levels vary from blue to red with the values 0.4 to 0.8 for *a-c* and 0.1 to 1.2 for *d-f*.
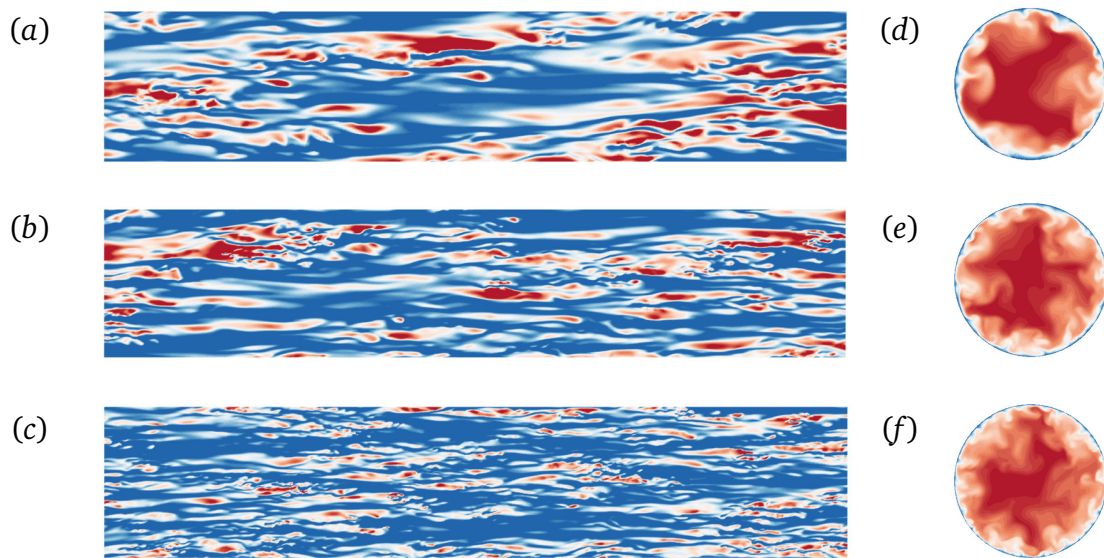
Fig. 7.3 Contours of the instantaneous axial velocity normalised by the bulk velocity plotted on (*a-c*) the developed cylindrical surface at $y^+ = 10$ and (*d-f*) a cross-section for the shear-thinning fluid at (from top to bottom) $Re_\tau = 323, 500$ and 750. For *a-c,* the flow is from left to right. The contours levels vary from blue to red with the values 0.4 to 0.8 for *a-c* and 0.1 to 1.2 for *d-f*.

7.1 Mean flow and turbulence intensities

Mean axial velocity

Profiles of the mean axial velocity (U_z^+) and its gradient in wall coordinates for different Re_τ are presented in figure 7.4 (a) and (b). The profiles are almost independent of Re_τ in the viscous sublayer for each fluid. The mean axial velocity there slightly increases with shear thinning (seen more clearly via the gradient $\partial U_z^+/\partial y^+$ in figure 7.4b). As discussed in section 5.1.2, this is a result of non-zero turbulent viscous stress there in shear-thinning liquids. Outside the viscous sublayer, the U_z^+ profiles deviate below with increasing Re_τ. Shear thinning slightly increases the mean axial velocity gradient in the viscous sublayer and for $y^+ \in [10 - 80]$ (figure 7.4b). The slope of the mean axial velocity profiles in the log layer is almost same (at highest Re_τ) for both the liquids.
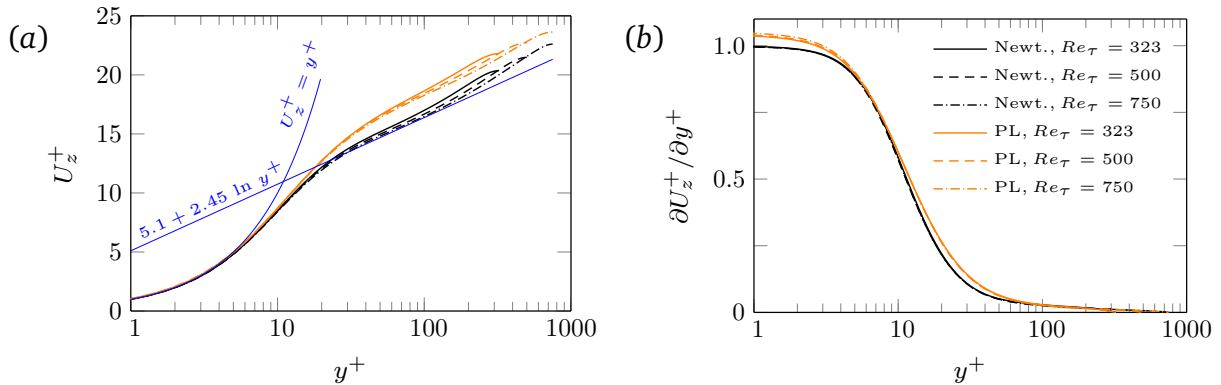
Fig. 7.4 Profiles of the (a) mean axial velocity and (b) mean axial velocity gradient plotted in wall coordinates for Newtonian (black lines) and shear-thinning liquids (orange lines). The solid lines are for $Re_\tau = 323$, dashed lines are for $Re_\tau = 500$ and the dash-dotted lines are for $Re_\tau = 750$. Blue lines in (a) show the classical law of wall.

The mean axial velocity profiles appear to follow a log-law $A \ln y^+ + B$ in the log layer for both liquids. This is further checked via the log-law indicator function, $\Xi = y^+ \partial U_z^+/\partial y^+$, that is constant in where the U_z^+ profiles follow a log-law (log region). Figure 7.5 (a) shows that for both liquids, the mean axial velocity profiles follow a log-law scaling only in a narrow region which widens with increasing Re_τ. This is consistent with the findings of Ahn et al. [2], Chin

et al. [24] and Zagarola et al. [107] for Newtonian liquids. The crest in the Ξ profile is usually taken as the slope parameter A in the log-law [24]. As seen in figure 7.5 (a), the slope parameter, A, slightly decreases with increasing Re_τ for both the liquids and slightly increases with shear thinning ($A = 2.52$ vs. 2.41). The location where a minimum Ξ is reached shifts away from the wall with shear thinning.

Although a log-law scaling is used more frequently, a power-law scaling also has been proposed [7]. It is worth noting that theoretically a power-law scaling is obtained in general and a log-law scaling is recovered only for an infinite Reynolds number [7]. However, Zagarola and Smits [108] suggested the existence of both the scalings, but in different ranges of y^+. The validity of a power-law scaling for the current results is checked via its indicator function $\Gamma = (y^+/U_z^+)\partial U_z^+/\partial y^+$ plotted in figure 7.5 (b). The figure shows that the mean axial velocity profiles follow a power-law scaling over a wider range of y^+ than a log-law scaling. The power-law coefficient Γ is almost independent of the Reynolds number and slightly decreases with shear thinning ($\Gamma = 0.15$ vs. 0.14).
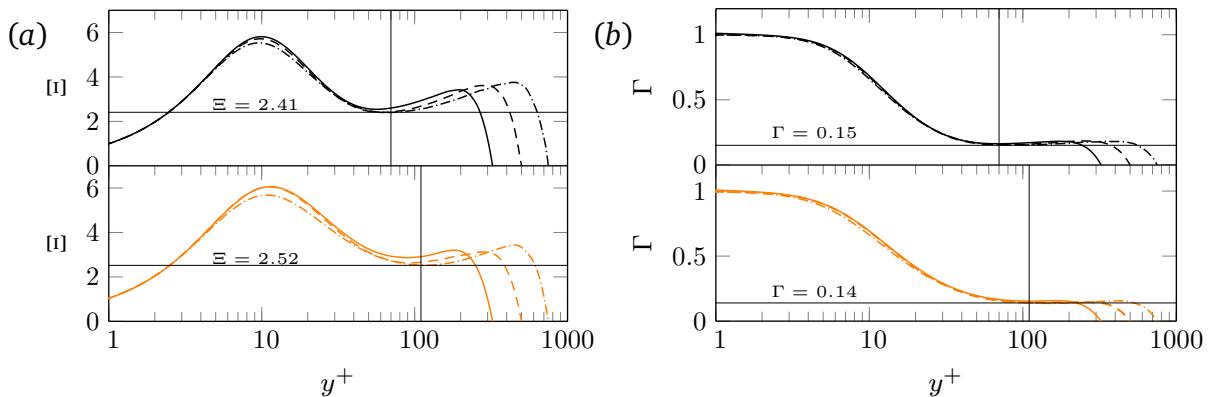
Fig. 7.5 (a) log-law and (b) power-law indicator functions for Newtonian and shear-thinning liquids. Vertical lines show the location where the labelled values are read.

Mean viscosity

Similar to the mean axial velocity, mean viscosity is also independent of the Reynolds number in the viscous sublayer but slightly increases there with shear-thinning (figure 7.6). The mean viscosity profiles show a log-like region and

collapse for different Re_τ up to $y^+ \approx 100$, the reason for which is not obvious. The extent of log-like region increases with increasing Re_τ.
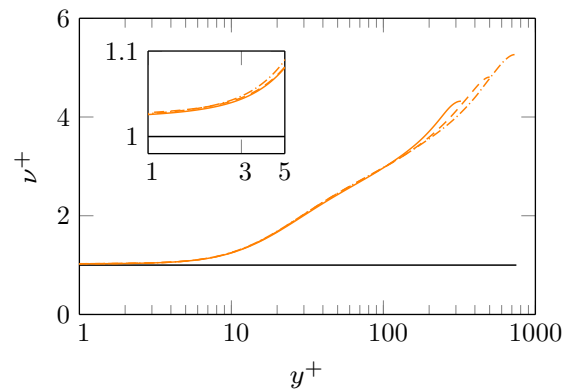
Fig. 7.6 Profiles of the normalised mean viscosity plotted for a shear-thinning fluid at different Re_τ. For line legend see figure 7.4.

Mean shear stress budget

The profiles of different mean shear stress components in the (r, z) direction (subscript rz is dropped for clarity) are plotted in wall coordinates in figure 7.7 for both liquids at different Re_τ. Except in the viscous sublayer, the mean viscous stress, τ^{v^+}, is independent of Re_τ for both the liquids and the profiles for different Re_τ deviate from each other only close to the pipe centre, which is because of the different extent of y^+ for different Re_τ. In the viscous sublayer, τ^{v^+} slightly increases with increasing Re_τ for the shear-thinning fluid, which is due to an increase in the magnitude of the turbulent viscous stress τ^{fv^+} (figure 7.7 c). In contrast to τ^{v^+} and τ^{fv^+}, the Reynolds shear stress, τ^{R^+}, significantly increases with increasing Re_τ and decreases with shear thinning outside the viscous sublayer. The ratio of peak τ^{R^+} and the ratio of the location where the peak τ^{R^+} is reached for shear-thinning and Newtonian liquids do not change with increasing Re_τ. This suggests that the extent of the shear-thinning effect on the Reynolds shear stress does not change with increasing Re_τ. Overall, the Re_τ-dependence of the mean shear stresses is similar for both liquids.
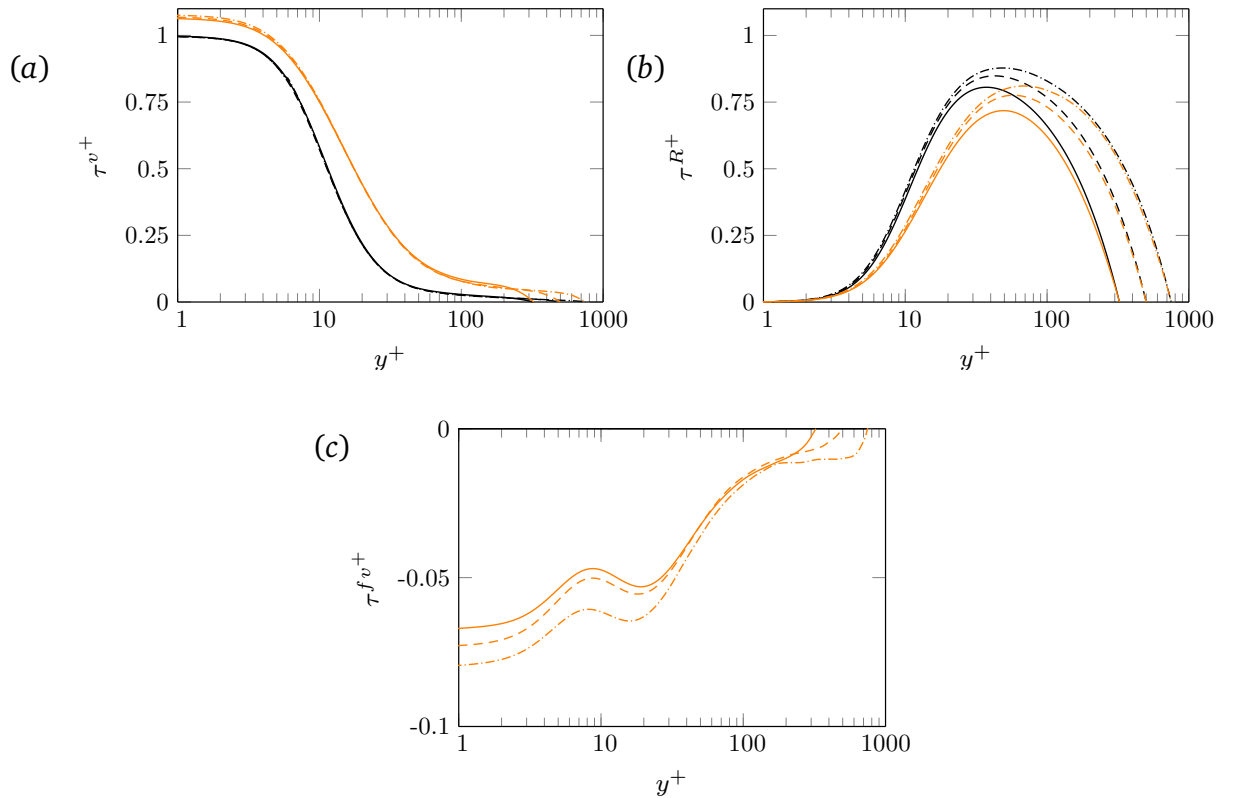
Fig. 7.7 Profiles of the (*a*) mean viscous stress τ^{v^+} (*b*) Reynolds shear stress τ^{R^+} and (*c*) the turbulent viscous stress τ^{fv^+} plotted for Newtonian and shear-thinning liquids for different Re_τ.

Turbulence intensities and viscosity fluctuations

Profiles of the turbulence intensities are also affected similarly for each fluid with increasing Re_τ and each component increases with increasing Re_τ (figure 7.8). The axial turbulence intensity ($u_z'^+$) profiles for different Re_τ are very close to each other near the wall but show a large Re_τ-dependence outside the buffer layer for $y^+ \gtrsim 30$. The location where $u_z'^+$ reaches a maximum is independent of Reynolds number for each fluid although is slightly further away from the wall for the shear-thinning fluid. The axial turbulence intensity for $y^+ \lesssim 200$ is higher for the shear-thinning fluid compared to the Newtonian fluid, but close to the pipe centre for $y^+ \gtrsim 200$, the $u_z'^+$ profiles of both liquids almost overlap each other, the reason for which is unknown. The radial and azimuthal turbulence intensity ($u_r'^+$ and $u_\theta'^+$) profiles of different Re_τ deviate from each other outside the viscous sublayer for both the liquids with the deviation being larger for higher Re_τ. Shear thinning decreases $u_r'^+$ and $u_\theta'^+$.

121
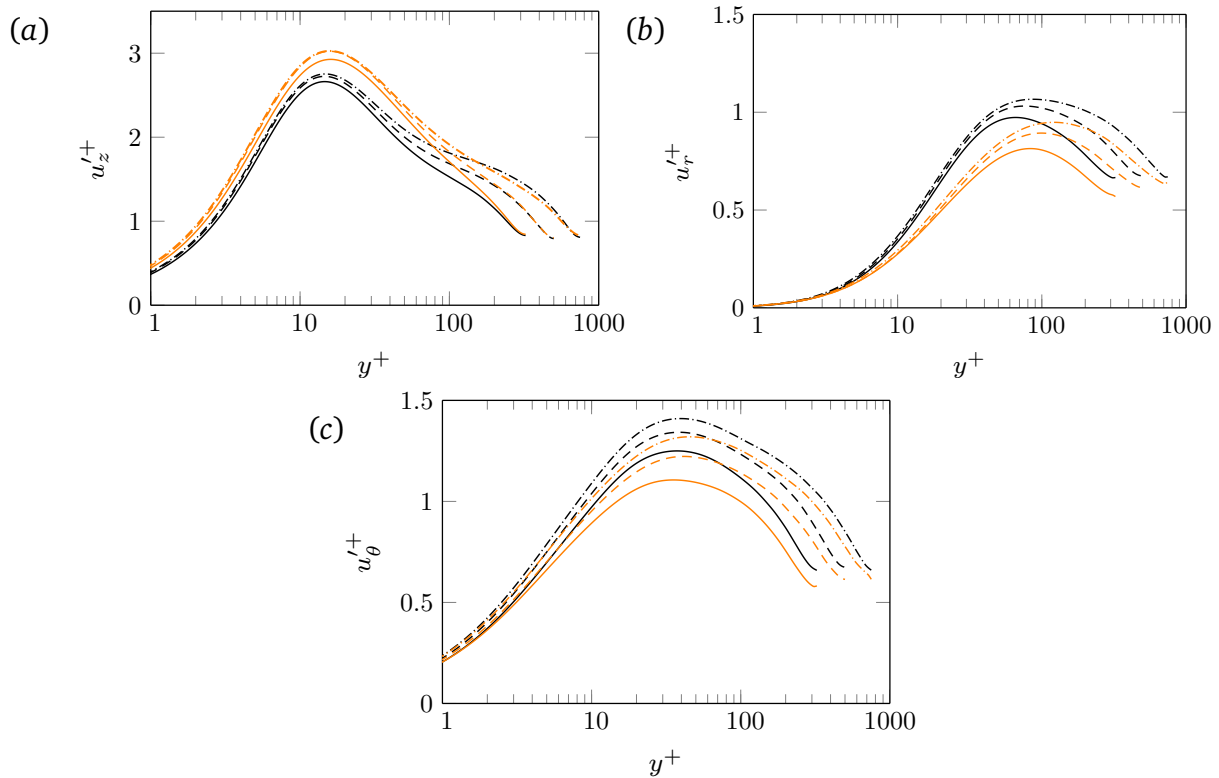
Fig. 7.8 Profiles of Reynolds shear stress and rms velocity fluctuations plotted in wall coordinates for Newtonian and shear-thinning ($n = 0.6$) liquids for different Re_τ.

As seen in figure 7.9 (a), the root mean square viscosity fluctuations normalised by the nominal wall viscosity (ν'^+) increase with the distance from the wall, and similar to the mean viscosity profiles, they are only marginally affected by increasing Re_τ. The differences between the profiles for different Re_τ are more clearly seen when the profiles are normalised by the local mean viscosity $\bar{\nu}^+$ (figure 7.9b). The locally normalised viscosity fluctuations, $\nu'^+/\bar{\nu}^+$, reach a maximum at $y^+ \approx 60$ which is approximately the same location up to which shear thinning rheology has the most prominent effect on the mean flow and the energy budgets as discussed in chapter 6 and in section 5.1.3.

7.2 Energy budgets

In section 5.1.3, an increase in the mean flow kinetic energy (MFKE) production and dissipation with shear thinning was observed for $Re_\tau = 323$, although it was accompanied by a decrease in the turbulence production and total turbulence
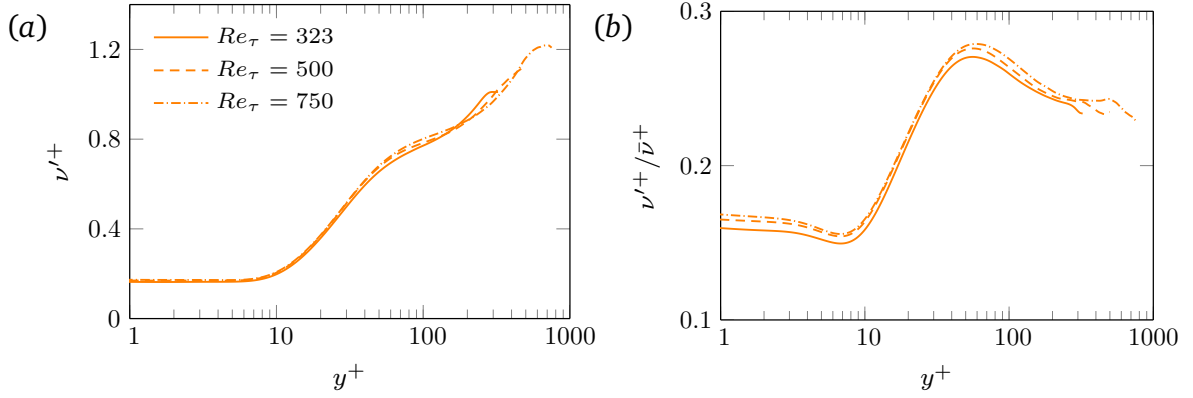
Fig. 7.9 Profiles of the rms viscosity fluctuations normalised by (*a*) the nominal wall viscosity and (*b*) the local mean viscosity.

dissipation. The new terms introduced due to viscosity fluctuations were found to act as a local source in the turbulent kinetic energy budget. Here, the energy budgets are analysed for different Re_τ to see whether the effect of shear thinning on the mean flow and the turbulent kinetic energy budgets is enhanced or diminished with increasing Re_τ.

7.2.1 Mean flow kinetic energy budget

The mean flow kinetic energy (MFKE) budget equation is given in Eq. 3.8 and the significance of each term was explained in section 3.3.1. There are two terms, $\mathcal{P}^+$ and χ_{nn}^+, common in both MFKE and turbulent kinetic energy (TKE) budget equations. These two terms are discussed later with the TKE budget in section 7.2.2 and the remaining MFKE budget terms are plotted in figure 7.10 and the main points are discussed below.

Since the Newtonian MFKE budget terms, $W_{dp/dz}^+$, $\mathcal{T}^{m+}$, $\mathcal{D}^{m+}$ and ϵ^{m+}, depend on the mean shear stress and mean axial velocity, as expected they show a similar Re_τ-dependence for each fluid. The effect of increasing Re_τ and shear thinning on the MFKE production, $W_{dp/dz}^+ = (U_z^+ \partial P^+/\partial z^+)$, is similar to that seen in the mean axial velocity (U_z^+) profiles because the mean pressure gradient $\partial P^+/\partial z^+$ is uniform. The MFKE production $W_{dp/dz}^+$ is lower for higher Re_τ.

The turbulent transport of MFKE, $\mathcal{T}^{m+}$, is a sink of MFKE near the pipe centre where it balances the MFKE production (other MFKE budget terms vanish
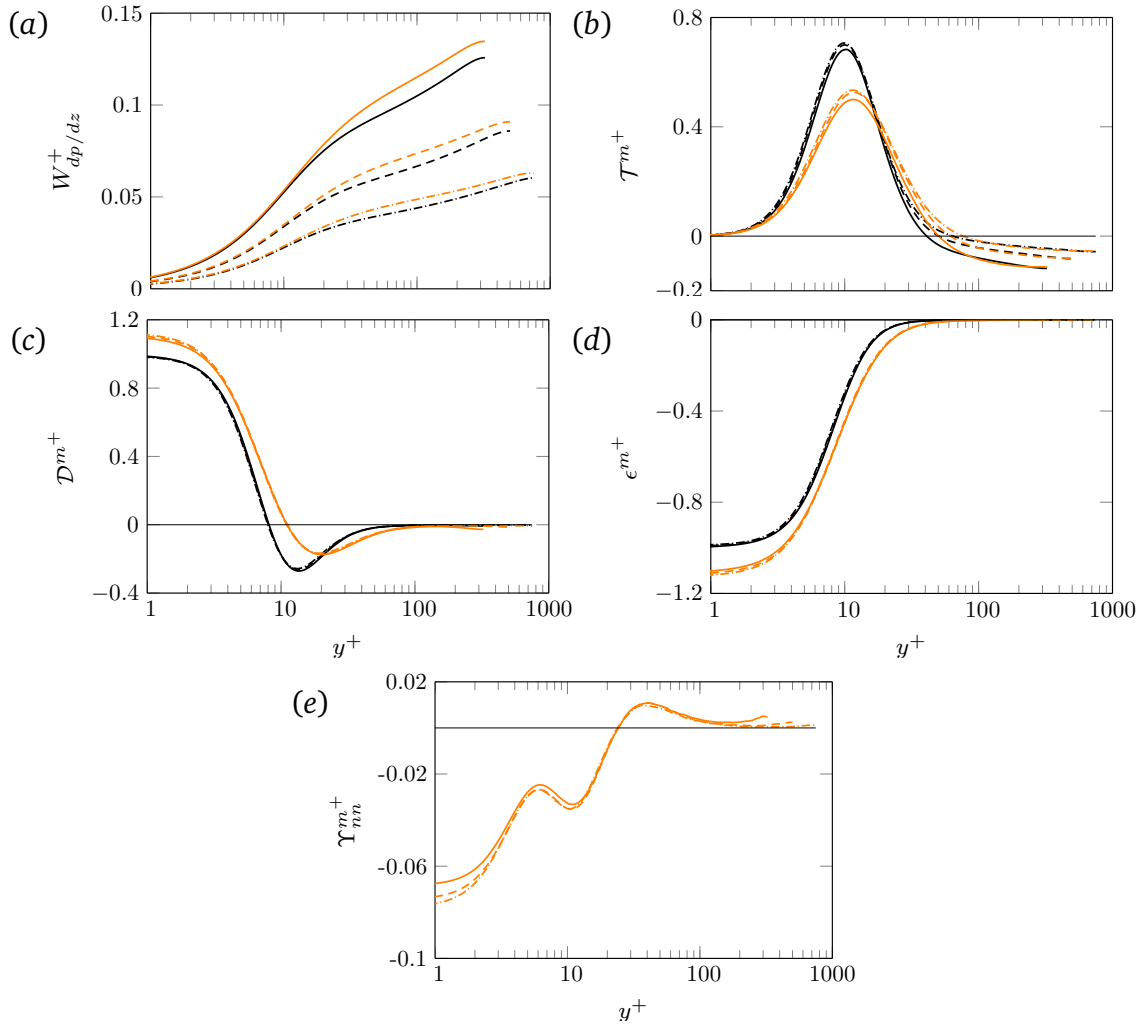
Fig. 7.10 Profiles of the terms which appear only in the mean flow kinetic energy budget (Eq. 3.8) plotted for Newtonian (black lines) and shear-thinning liquids (orange lines). Solid lines are for $Re_\tau = 323$, dashed lines for $Re_\tau = 500$ and the dashdotted lines are for $Re_\tau = 750$.

there). The turbulent transport $\mathcal{T}^{m^+}$ changes sign close to the wall and thus transports energy from the core region towards the wall (the volume integral of $\mathcal{T}^{m^+}$ is zero). The magnitude of $\mathcal{T}^{m^+}$ in the core region is lower for higher Re_τ which is due to the lower MFKE production there for higher Re_τ. Similar to the axial turbulence intensity ($u_z'^+$) profiles, the profiles of $\mathcal{T}^{m^+}$ of Newtonian and the shear-thinning liquids overlap each other in the core region, however, there is no obvious relation between $\mathcal{T}^{m^+}$ and $u_z'^+$. The location where $\mathcal{T}^{m^+}$ reaches a maximum slightly shifts towards the wall with increasing Re_τ for both liquids.

The remaining terms are the viscosity dependent terms ($\mathcal{D}^{m^+}$, ϵ^{m^+} and Υ_{nn}^+) which are significant only near the wall for $y^+ < 100$ (figure 7.10 c–e). In these terms, the mean viscosity dependent terms i.e. the mean viscous transport, $\mathcal{D}^{m^+}$, and the mean viscous dissipation, ϵ^{m^+}, dominate the MFKE budget near the wall and similar to the mean viscous stress, τ^{v^+}, both of these terms show a marginal dependence on Re_τ. Due to the higher τ^{v^+} in the shear-thinning fluid, the magnitude of $\mathcal{D}^{m^+}$ and ϵ_{m^+} is higher for the shear-thinning fluid compared to the Newtonian fluid. The turbulent viscous stress transport, Υ_{nn}^+, which is due to the turbulent viscous stress τ^{fv^+}, show a similar Re_τ-dependence as seen for τ^{fv^+} in figure 7.7 (c) and slightly increases with increasing Re_τ. However, the magnitude of Υ_{nn}^+ is very small compared to the mean viscous dissipation ϵ^{m^+}. The negative values Υ_{nn}^+ close to the wall suggest that it decreases the total viscous dissipation there.

Overall, the Reynolds number dependence of the MFKE budget terms is similar for both the liquids and the contribution of the non-Newtonian dissipation term, Υ_{nn}^+, is small in the total MFKE dissipation.

7.2.2 Turbulent kinetic energy budget

Similar to the MFKE budget, Newtonian terms in the turbulent kinetic energy (TKE) budget are also similarly affected with increasing Re_τ for each fluid (figure 7.11 a-e). The TKE production, $\mathcal{P}^+ = \tau^{R^+}(\partial U_z^+/\partial y^+)$, is higher for higher Re_τ for each fluid (figure 7.11 a), which is due to the higher Reynolds shear stress τ^{R^+} for higher Re_τ as seen in figure 7.7 (c). Shear thinning decreases τ^{R^+}, therefore, the TKE production $\mathcal{P}^+$ is lower for the shear-thinning fluid compared to the Newtonian fluid. The location of the maximum $\mathcal{P}^+$ slightly shifts away from the wall with shear thinning but is almost independent of Re_τ.

The increase in the TKE production with increasing Re_τ is accompanied by an increase in the mean viscous dissipation, ϵ^+ (figure 7.11 b). The mean viscous dissipation ϵ^+ shows Re_τ-dependence mainly for $y^+ \lesssim 30$. Higher ϵ^+ near the wall for higher Re_τ indicates larger shear rate fluctuations $\overline{s'_{ij}s'_{ij}}^+$ ($\epsilon^+ = 2\nu^+\overline{s'_{ij}s'_{ij}}^+$) for higher Re_τ because the mean viscosity is constant for a Newtonian fluid and is independent of Re_τ there for the shear-thinning fluid (figure 7.6).
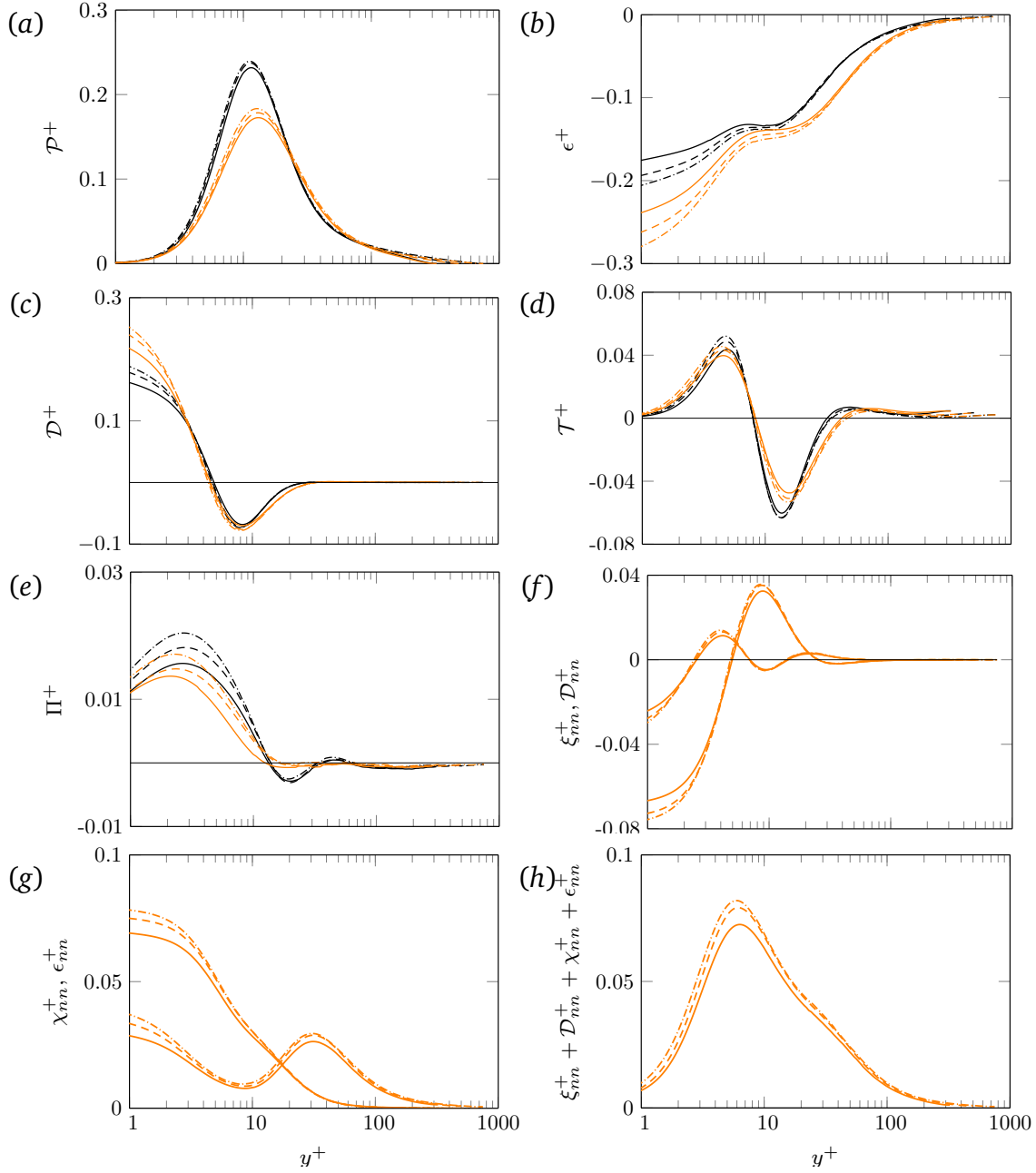
Fig. 7.11 Profiles of the turbulent kinetic energy budget terms (see Eq. 3.9) plotted for Newtonian (black lines) and shear-thinning liquids (orange lines) at different Re_τ.

The mean viscous dissipation near the wall is mainly balanced by the mean viscous transport, $\mathcal{D}^+$, there. Therefore, the profiles of $\mathcal{D}^+$ show a similar Re_τ-dependence as ϵ^+ for $y^+ < 3$, and $\mathcal{D}^+$ there is higher for higher Re_τ (figure 7.11c). The mean viscous transport $\mathcal{D}^+$ vanishes beyond $y^+ \gtrsim 30$. Profiles of the other Newtonian transport terms, $\mathcal{T}^+$ and Π^+, which are small compared to $\mathcal{D}^+$ (approximately five and ten times smaller), also show a similar Re_τ-dependence

for each fluid as seen for the mean viscous transport $\mathcal{D}^+$ (figures 7.11d and e). However unlike $\mathcal{D}^+$, $\mathcal{T}^+$ and Π^+ do not vanish until $y^+ \approx 100$. The non-Newtonian terms arising due to viscosity fluctuations are significant only for $y^+ \lesssim 30$ where they increase in magnitude with increasing Re_τ (figures 7.11f and g).

Profiles of the total transport $T^{k^+} = \mathcal{T}^+ + \Pi^+ + \mathcal{D}^+ + \xi_{nn}^+ + \mathcal{D}_{nn}^+$ and the total dissipation $\epsilon^{k^+} = \epsilon^+ + \chi_{nn}^+ + \epsilon_{nn}^+$ are affected similarly with increasing Re_τ for each fluid (figure 7.12). Both T^{k^+} and ϵ_{k^+} are higher for higher Re_τ. The total TKE transport, T^{k^+}, shows a Re_τ-dependence only in the viscous sublayer whereas the total turbulence dissipation ϵ^{k^+} is affected by increasing Re_τ until the outer edge of the buffer layer ($y^+ \lesssim 30$).
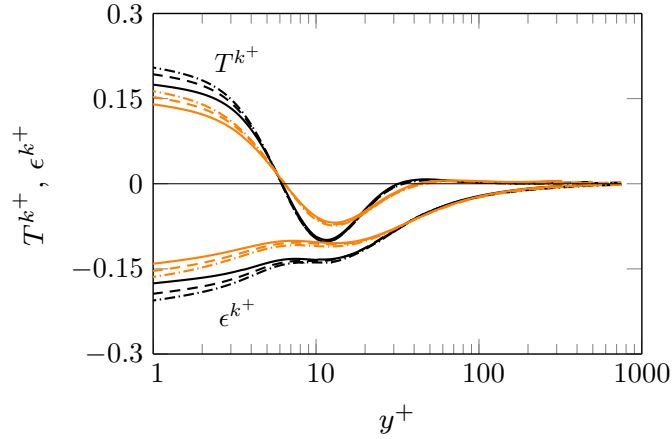
Fig. 7.12 Profiles of the sum of the Newtonian and non-Newtonian transport and the dissipation terms plotted for the Newtonian (black lines) and the shear-thinning fluid (orange lines).

The overall effect of increasing Re_τ on the TKE budget is qualitatively similar for each fluid. The non-Newtonian terms act as a sink in the TKE budget and their contribution increases with increasing Re_τ. The Reynolds number effect is mainly confined near the wall for $y^+ \lesssim 30$ whereas the shear-thinning effect is seen until $y^+ \approx 100$.

7.3   Comparison of the effect of shear thinning and increasing Reynolds number

It was noted in figures 7.2 and 7.3 that the velocity streaks become wider and longer with shear-thinning or decreasing Re_τ which suggests that the effect of shear thinning and increasing Re_τ are opposite to each other. However, this hypothesis does not hold for other results such as the axial turbulence intensity which increased with both shear thinning and increasing Re_τ (figure 7.8 a). In this section, the results of increasing Re_τ and shear thinning are compared to highlight the similarities and the differences between the two effects.

Shear thinning and increasing Re_τ affect the mean axial velocity profiles in an opposite manner. The effect of increasing Re_τ on the mean viscous stress, τ^{v^+}, and the turbulent viscous stress, τ^{fv^+}, is although similar but is very small compared to the shear-thinning effect. Both shear thinning and increasing Re_τ increase the axial turbulence intensity, $u_z'^+$, for all y^+. In contrast, the radial and the azimuthal turbulence intensities ($u_r'^+$ and $u_\theta'^+$) are affected oppositely by the two effects.

In the Newtonian mean flow kinetic energy (MFKE) budget terms, the mean viscosity dependent terms, $\mathcal{D}^{m^+}$ and ϵ^{m^+}, are only marginally affected by increasing Re_τ, therefore, a clear comparison between the shear-thinning and the Reynolds number effects can be made only for the remaining terms $W_{dp/dz}^+$, $-\mathcal{P}^+$ and $\mathcal{T}^{m^+}$. All of these terms are affected with shear thinning and increasing Re_τ in an opposite manner.

The Newtonian terms in the turbulent kinetic energy (TKE) budget show a mixed trend with the two effects. The mean viscosity dependent terms, ϵ^+ and $\mathcal{D}^+$, increase in magnitude with both shear thinning and increasing Re_τ, which suggests that the fluctuations in velocity gradients are similarly affected by both shear thinning and increasing Re_τ. In contrast, the turbulence production $\mathcal{P}^+$ (also discussed in the MFKE budget) and the pressure gradient work, Π^+, are affected oppositely with increasing Re_τ or shear thinning. The turbulent transport

of TKE, $\mathcal{T}^+$, is affected similarly with both shear thinning and increasing Re_τ in the viscous sublayer but the trend is reversed in the buffer layer.

All non-Newtonian terms in the MFKE and TKE budget are affected similarly with shear thinning or increasing Re_τ. The overall effect of shear thinning and increasing Re_τ is opposite to each other on the total TKE transport and dissipation (figure 7.12). A key result shown by this comparison is that the effect of shear thinning is not to decrease the effective Reynolds number as it appears in the near wall streaks. The gap between the profiles of the shear-thinning fluid and the Newtonian fluid also does not decrease with increasing Re_τ. Therefore, the shear-thinning effect is expected to persist even at higher Reynolds number, although it could be small.

7.4   Empirical correlations

In section 5.4, the mean axial velocity profiles predicted by DNS were found to deviate significantly from the profile proposed by Dodge and Metzner [35] (Eq. 2.15) for shear-thinning liquids. The DNS predictions of the friction factor for shear-thinning liquids were in a better agreement with Anbarlooei & Cruz correlation (Eq. 2.23) compared to the Dodge & Metzner correlation (Eq. 2.16), however, the maximum disagreement between the DNS predictions and Dodge & Metzner correlation was less than 5%. Here, this comparison is made at higher Reynolds number.

As seen in figure 7.13 (a), the mean axial velocity profiles of the shear-thinning fluid predicted by DNS deviate from the Dodge & Metzner profile (Eq. 2.15) for all Re_τ, however, the disagreement is less for higher Re_τ. This suggests that a good agreement between DNS and Dodge & Metzner correlation might be possible at very high Reynolds number.

Clapp's scaling [27] suggests that the profiles of nU_z^+ of different flow indices will collapse when plotted against the non-dimensional distance from the wall $\hat{y}$. This non-dimensionalisation is used in figure 7.13 (b) where it can be seen that the current values of Re_{MR} (the non-dimensional pipe radius $\hat{R}$ is higher for higher Re_{MR}) for the shear-thinning fluid are not high enough to compare

with the Newtonian fluid. This also means that Clapp's scaling is not applicable at the current Reynolds number for $n = 0.6$.
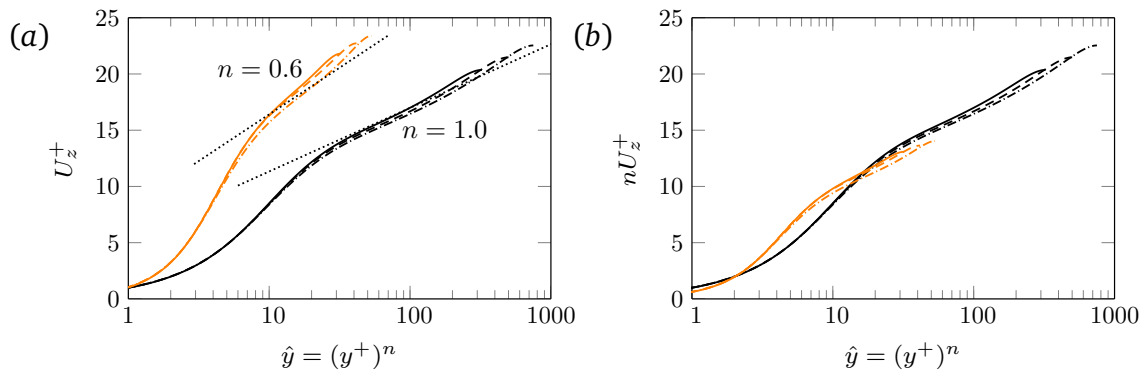

Fig. 7.13 Profiles of the mean axial velocity plotted using (*a*) Dodge & Metzner scaling [35] and (*b*) Clapp's scaling [27]. In (*a*) the prediction of Eq. 2.15 are shown using dotted lines. The same line patterns and colours are used as in previous figures.

The DNS predictions of the friction factor are compared with Dodge & Metzner and Anbarlooei & Cruz correlation in figure 7.14. Dodge & Metzner correlation reduces to Nikuradse correlation and Anbarlooei & Cruz correlation reduces to Blasius correlation for $n = 1.0$. Both correlations agree well with each other for $Re_{\mathrm{MR}} \lesssim 100\,000$ for the shear-thinning fluid. For the Newtonian fluid, the predictions of the Blasius correlation are slightly higher than Nikuradse's correlation. For the Newtonian fluid, the DNS predictions are in a better agreement with the Blasius correlation compared to Nikuradse's correlation. For the shear-thinning fluid, DNS slightly under-predicts the friction factor for higher Re_τ. The disagreement between DNS and the correlations might increase with further increasing Re_τ, however, this needs to be confirmed.

7.5   Chapter summary

Simulations carried out for Newtonian and shear-thinning PL fluid ($n = 0.6$) for $Re_\tau = 323, 500$ and 750 show that the effect of increasing Re_τ is similar for each fluid. Fluctuations in the flow are higher for higher Re_τ. The mean axial velocity profiles shift slightly below with increasing Re_τ, however, the effect of increasing Re_τ is almost negligible on the mean axial velocity gradient. The mean viscosity
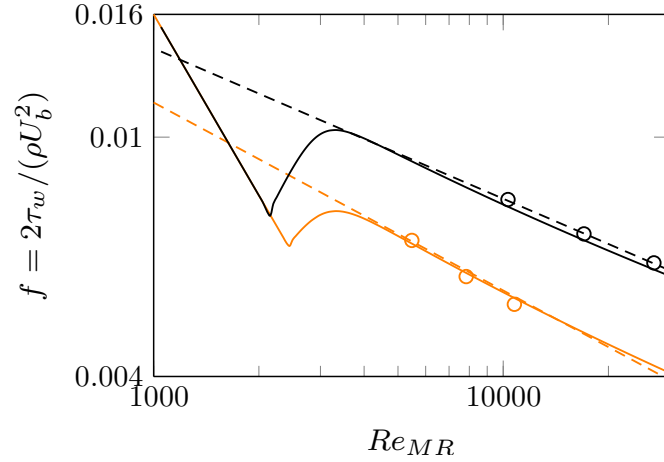
Fig. 7.14 Comparison of the friction factor predicted using DNS against Dodge & Metzner correlation (solid lines) and the Anbarlooei & Cruz correlation (dashed lines) for Newtonian (black lines) and the shear-thinning liquids (orange lines).

profiles for a shear-thinning fluid are almost independent of the Reynolds number until the inner log-layer ($y^+ \approx 100$). The effect of increasing Re_τ on the mean viscous stress and the turbulent viscous stress is small. In contrast, the Reynolds shear stress increase significantly with increasing Re_τ outside the viscous sublayer. All components of the turbulence intensities also increase with increasing Re_τ for each fluid.

The effect of increasing Re_τ on the mean flow and the turbulent kinetic energy is similar for each fluid and most terms are higher for higher Re_τ. A key result is that except for the mean flow kinetic energy production and the turbulence transport of the mean flow kinetic energy, all other terms in the energy budgets show a Reynolds number-dependence only near the wall for $y^+ \lesssim 100$. A comparison of the effect of shear thinning and increasing Re_τ showed that the effect of shear thinning is not to reduce the effective Reynolds number as it appeared in the near wall velocity streaks. The two effects mostly oppose each other.

The DNS prediction of the mean axial velocity profiles come closer to Dodge & Metzner profile for higher Re_τ which suggests that a good agreement between DNS and Dodge & Metzner profile is possible for very high Re_τ, however, this needs to be confirmed. In contrast, DNS slightly under-predicts the friction factor for higher Re_τ compared to Dodge & Metzner and Anbarlooei & Cruz

131

correlation with the deviation expected to increase with further increasing Re_τ. This also needs to be confirmed in future.

8

Flow through an open channel

Open channels are also common in applications. Indeed, the flow through a pipe also becomes an open channel flow when the pipe is not running full. Despite their wide applications, fundamental studies of open channel flow have not received the same level of attention as pipe flow. Compared to Newtonian fluids, the studies of non-Newtonian fluids in open channels are rare.

An open channel can have different cross-sections, however, channels with a rectangular cross-section are the most common because they are simple to design and easy to maintain. In this chapter, DNS results of a rectangular open channel flow with different aspect ratio AR ($AR = 2b/h$ where b is the half channel width and h is the fluid depth) are presented for Newtonian and shear-thinning (PL, $n = 0.6$) fluids to highlight the differences arising from shear-thinning rheology. The channel aspect ratio is varied from 1 to 4 while keeping the hydraulic radius (ratio of the channel cross-sectional area to the channel perimeter) fixed. The nominal wall shear stress τ_w (Eq. 2.26) and the nominal wall viscosity ν_w (Eq. 2.11) are also fixed in simulations to give a fixed Re_τ of 146. The channel dimensions are given in table 8.1 and the simulation parameters are given in table 8.2. The Froude number in the current simulations is much lower than one (subcrticial flow), therefore, a significant deformation of the free surface

is not expected in real flow for these parameters and a deformation-free boundary conditions such as used here (see chapter 3) is adequate. Note that the fluid depth is used for the length scale in defining the Froude number ($Fr = U_b/(gh)^{1/2}$) to be consistent with its traditional definition. Since the fluid depth decreases with increasing AR, this leads to an increase in the Froude number.

Table 8.1 Geometric parameters and Froude number in the current open channel simulations. The hydraulic radius is fixed. Simulations are run for Newtonian and shear-thinning (PL, $n = 0.6$) fluids. The nominal wall viscosity is fixed in simulations which is the same as the viscosity of the Newtonian fluid. The nominal wall shear stress is also fixed by fixing the forcing. The simulation parameters are given in table 8.2. The Froude number is calculated as $U_b/(gh)^{1/2}$ where g is the gravitational acceleration and h is fluid depth.

AR	$2b/R_h$	h/R_h	Fr_{Newt}	Fr_{nn}
1.0	3.0	3.0	0.24	0.27
2.0	4.0	2.0	0.30	0.33
4.0	6.0	1.5	0.34	0.38

Table 8.2 Simulation parameters for the current open channel simulations for Newtonian and shear-thinning liquids. The nominal wall viscosity and the nominal wall shear stress are fixed in simulations by fixing the forcing $g/(u^{*2}/R_h) = 1.0$ and the hydraulic radius for different channels. The Metzner–Reed Reynolds number is calculated using Eq. 2.7 with $D = 4R_h$.

n	$K/(\rho u^{*2-n} R_h^n)$	Re_G	Re_{MR}
0.6	1.7605×10^{-5}	10400	5400
1.0	2.332×10^{-5}	9300	9300

8.1 Instantaneous flow

By their nature, DNS simulations are unsteady and details of the flow change with time, although for the flume flows here, the flow statistics (e.g. mean, standard deviations, etc.) do not. A qualitative view of the unsteady flow is presented in figure 8.1 which shows contours of streamwise velocity on one cross section of the flume at a given time. The faster bulk velocity for the shear-thinning case is evidenced by the larger area covered by the dark red colours (velocity 1.3 and

above). As was also seen for a pipe flow, low and high speed streaks are wider and run longer for the shear-thinning fluid compared to the Newtonian fluid. Shear rates are the largest close to the wall therefore, the viscosity is lowest there and increases towards the centre which is expected for a shear-thinning fluid (figure 8.2).
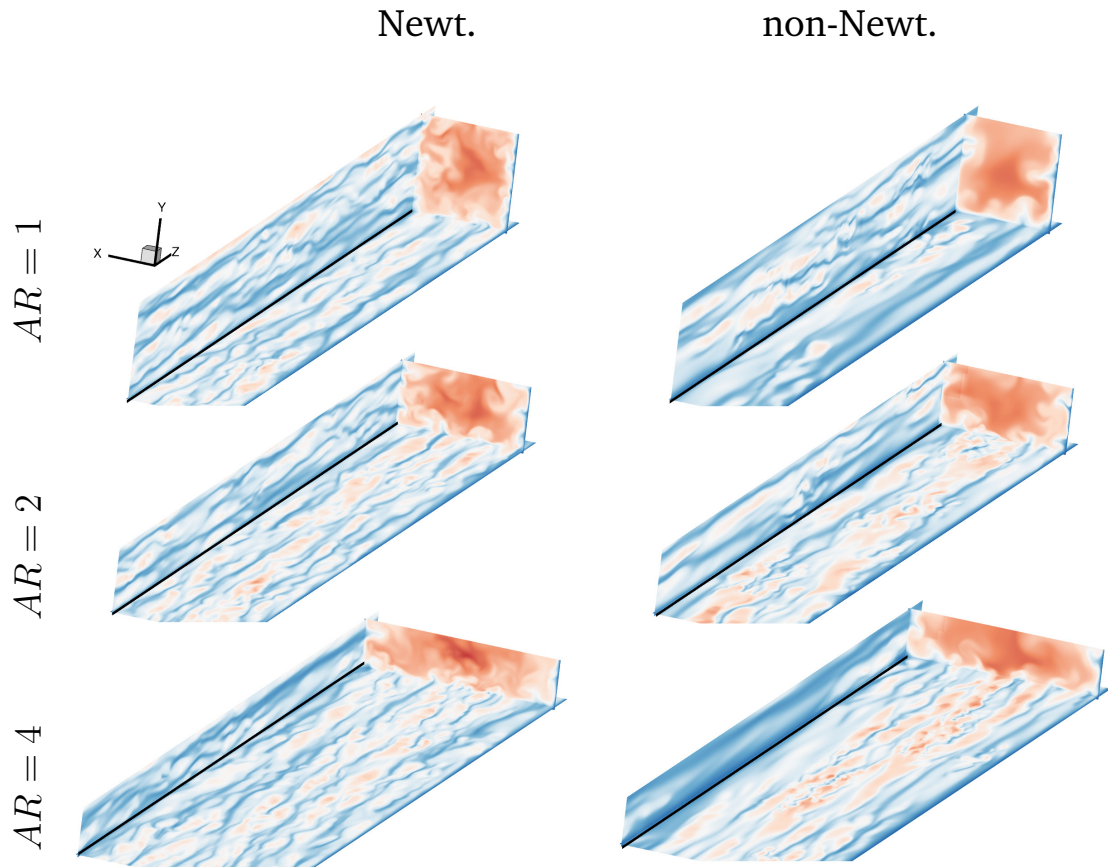
Fig. 8.1 Contours of the instantaneous axial ($z-$) velocity normalised by the bulk velocity plotted for Newtonian and shear-thinning liquids at a cross-section and close to the bottom and a side wall ($y^+ \approx 10$). Contour levels vary from 0(blue) to 1.3(red).

8.2   Bulk velocity and friction factor

Despite different aspect ratios, the predicted bulk velocity, U_b, does not vary with AR and the simulations give $U_b/u^* = 15.95$ for the Newtonian fluid and $U_b/u^* = 17.84$ for the shear-thinning fluid for all AR. The fact that the predicted bulk velocity (and hence the flow rate) does not change with aspect ratio for either fluid suggests that the hydraulic radius is an appropriate length scale to
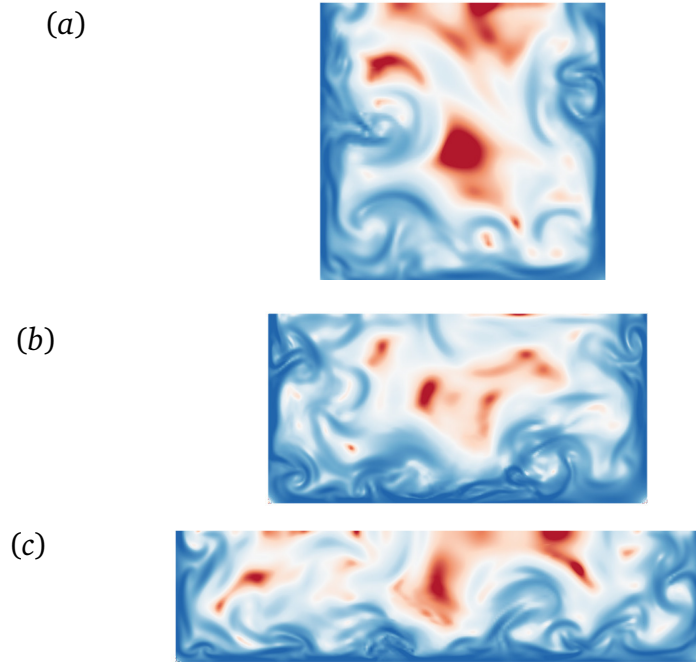
Fig. 8.2 Contours of the instantaneous viscosity normalised by the nominal wall viscosity plotted for the shear-thinning fluid at the same cross-section and time instant as in figure 8.1. Contour levels vary from 1(blue) to 6(red).

use in turbulent open channel flows of both Newtonian and GN liquids. However, this assessment might change when the shape of the channel cross-section is changed.

The nominal wall shear stress τ_w is fixed, therefore, the increased U_b with shear thinning leads to a decrease in the friction factor $f = 2\tau_w/\rho U_b^2$ (figure 8.3) which was also observed for a pipe flow (see chapters 5 and 7). The DNS friction factor predictions are in excellent agreement with the Dodge & Metzner correlation (Eq. 2.16 with pipe diameter D replaced by the channel hydraulic diameter D_h) for the Newtonian fluid whereas the agreement for $n = 0.6$ is within 5%. This agreement is only slightly worse than the agreement seen for a pipe flow. As noted earlier (see sections 5.4 and 7.4) the Dodge & Metzner and Anbarlooei & Cruz correlations (Eq. 2.23) agree closely with each other for $Re_G \lesssim 10\,000$. These results suggest that either of these correlations can be used for predicting turbulent friction factor in open channel flows of GN liquids at the considered Reynolds number ($Re_G \approx 10\,000$).
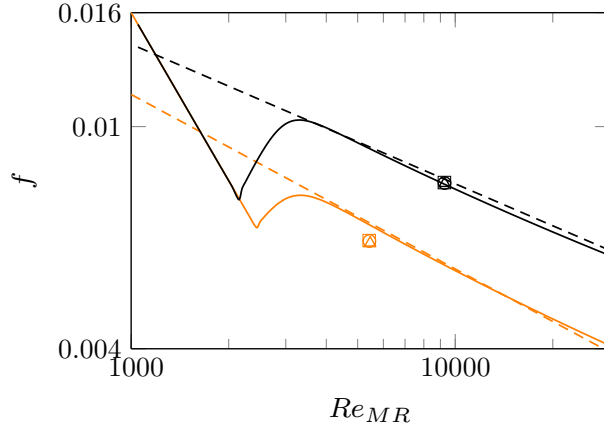
Fig. 8.3 Comparison of the friction factor predictions using DNS (markers) with Dodge & Metzner correlation (lines) and Abarlooei & Cruz correlation (dashed lines).

8.3   Mean wall shear stress

Unlike pipe flows, the mean wall shear stress, $\bar{\tau}_w$, is not uniform in an open channel and it is modified by the secondary flows [60]. Since Reynolds shear stress vanishes at the wall, only the viscous stresses, the mean viscous stress, τ_w^v, and the turbulent viscous stress, τ_w^{fv}, contribute to $\bar{\tau}_w$. The axially averaged mean shear stress components at the wall, τ_w^v and τ_w^{fv}, starting at A, traversing anticlockwise to D (see figure 8.4) are plotted in figure 8.5 for Newtonian and shear-thinning liquids and for different AR of the channel. In this figure, the mean wall shear stresses are normalised by the nominal wall shear stress τ_w (Eq. 2.26) and the distance s along the perimeter from A normalised by the wetted perimeter P_w is chosen for the $x-$axis. The line integral of the mean wall shear stress $\bar{\tau}_w^+$ divided by the wetted perimeter P_w is one for all cases which confirms that the simulations are converged and the data has been averaged for sufficient time.

General trends in the mean wall shear stress profiles are broadly similar for all AR and for both liquids with some "important" differences. A zero shear stress occurs at the bottom two corners B and C, which is because the fluid is almost stationary there. For the Newtonian fluid, the mean wall shear stress, $\bar{\tau}_w^+$, is maximum at the top two corners A and D. This is also true for the shear-

137
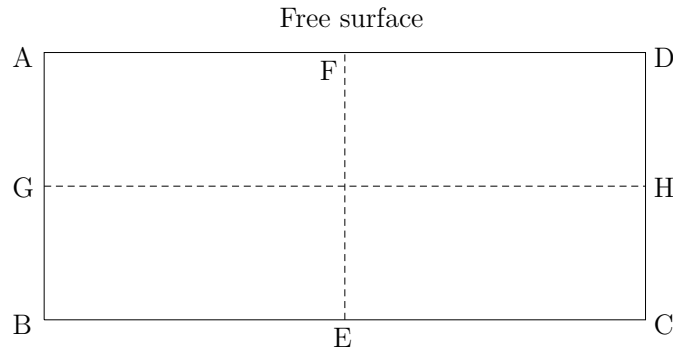
Fig. 8.4 Naming of corners and the horizontal and the vertical centre lines for an open channel.

thinning fluid for $AR = 1$ and 2, however, for $AR = 4$, $\bar{\tau}_w^+$ is maximum in the middle of the base BC (point E).

The mean wall shear stress distribution along the base BC is similar for all AR for the Newtonian fluid; it reaches a maximum in the middle and its magnitude increases with increasing AR. The trend is similar for the shear-thinning fluid except for $AR = 1$ for which $\bar{\tau}_w$ reaches a minimum in the middle. This will be seen later to be a secondary flow effect (discussed in section 8.7).

As mentioned, the mean wall shear stress for non-Newtonian liquids is the sum of the mean viscous stress $\tau_w^{v^+}$ and the turbulent viscous stress $\tau_w^{fv^+}$. As seen in figure 8.5, $\tau_w^{v^+}$ is higher than the mean wall shear stress $\bar{\tau}_w$ for most of the wall which is due to the negative turbulent viscous stress $\tau_w^{fv^+}$. The turbulent viscous stress is lower along the side walls but is higher along the base for higher AR. For pipe flow also the turbulent viscous stress was negative for a shear-thinning fluid (figure 5.7), however, there is no known theoretical analysis available to show this to be true.

The average $\bar{\tau}_w$ on side wall, τ_{w_s}, is lower for higher AR for both liquids (table 8.3) which is due to a proportional decrease in the surface area of the side walls with increasing AR. This is compensated for by an increase in the average $\bar{\tau}_w$ on the base, τ_{w_b}. Except for $AR = 1$, shear-thinning rheology decreases τ_{w_s} and increases τ_{w_b}. The contribution of the turbulent viscous stress in τ_w follows the same trend as seen for τ_{w_s} and τ_{w_b} and increases with increasing AR. For
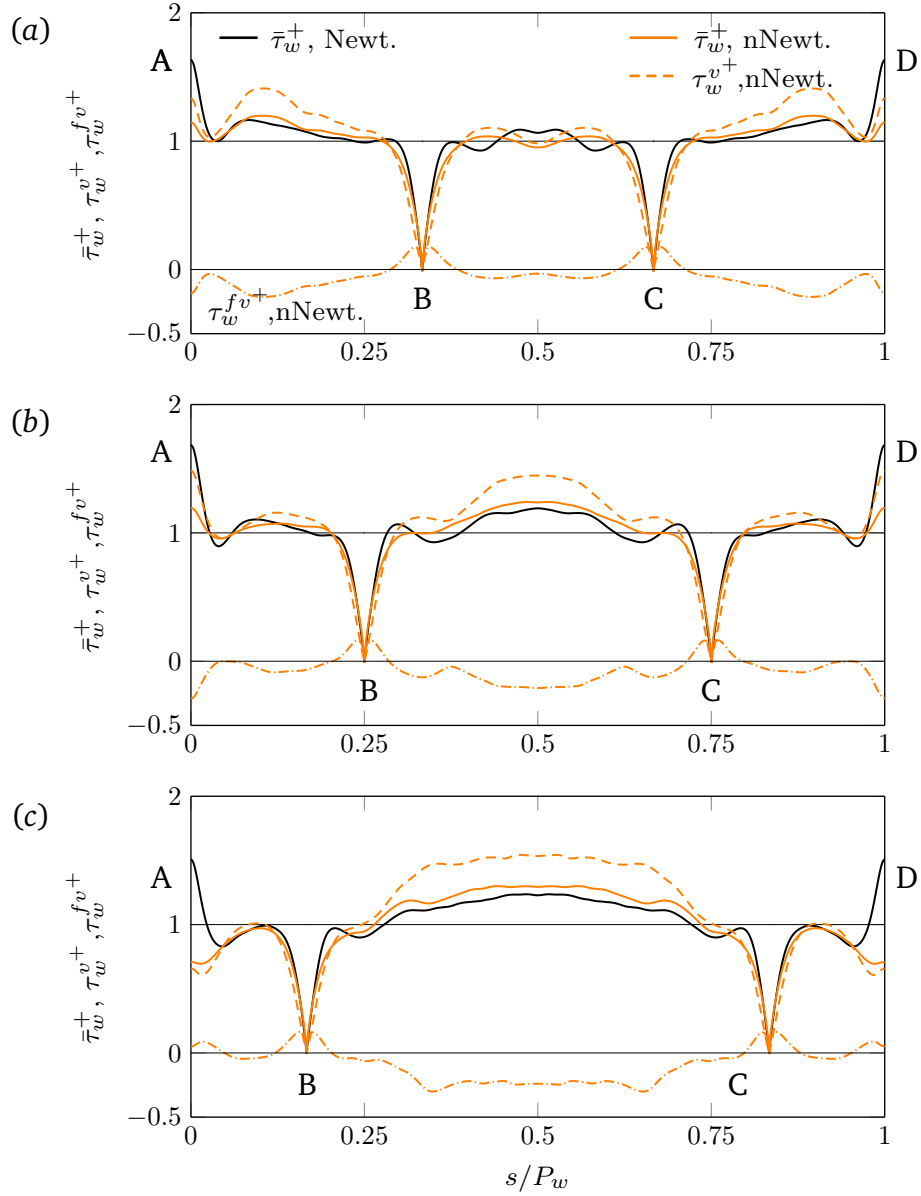
Fig. 8.5 Profiles of the mean shear stress components plotted for Newtonian (black lines) and shear-thinning (orange lines) liquids for (*a*) $AR = 1$ (*b*) $AR = 2$ and (*c*) $AR = 4$.

$AR = 4$, the average turbulent viscous stress at the base is almost 10% of τ_w but is negative.

In summary, shear-thinning rheology modifies the distribution of the mean wall shear stress at the base and at the side walls. The turbulent viscous stress in the shear-thinning fluid becomes more negative with increasing AR. For higher AR, the average mean wall shear stress is larger on the base and lower on the side walls for the shear-thinning fluid compared to Newtonian fluid.

Table 8.3 The average mean wall shear stress on the side walls and on the base expressed as a percentage of nominal wall shear stress τ_w for Newtonian and shear-thinning liquids. The average turbulent viscous stress at the wall in the shear-thinning fluid is given in brackets.

AR	$\tau_{w_s}^+$ (%)		$\tau_{w_b}^+$ (%)	
	Newt.	non-Newt.	Newt.	non-Newt.
1	69	69 (-5.8)	31	31 (-0.2)
2	50	49 (-1.5)	50	51 (-4.2)
4	30	27 (-1.0)	70	73 (-9.8)

8.4   Mean streamwise velocity

Contours of the mean streamwise velocity normalised by the bulk velocity are shown in figure 8.6 where a larger flow area with $U_z/U_b \geq 1.2$ (in red) can be seen for the shear-thinning fluid than the Newtonian fluid for all AR. This indicates that the flow moves faster in the core and slower near the wall for the shear thinning fluid than Newtonian. The shape of the contours indicates the presence of secondary flow which is discussed in section 8.7.

Unlike in pipe and sheet flows, the time-averaged data for an open channel flow can be spatially averaged only in the streamwise direction. Therefore, it is not possible to show a single profile for the mean flow quantities for an open channel flow. Here, the mean flow profiles along two lines, EF and GH, (see figure 8.4), which pass through the centre of the domain and run in the vertical and the horizontal directions are presented. The profiles of the normalised mean streamwise velocity (U_z/U_b) are plotted along these lines in figure 8.7 (*a*) for the vertical line EF and in figure 8.7 (*b*) for the horizontal line GH. Along the vertical line EF, U_z/U_b increases with the distance from the wall and reaches a maximum below the free surface for $AR = 1, 2$ (figure 8.7 *a*). This is known as velocity-dip phenomenon and is caused by secondary flows [72]. This velocity-dip disappears for $AR = 4$ for both liquids indicating very weak secondary currents in $AR = 4$. The magnitude of the maximum U_z/U_b increases with increasing AR. The profiles of U_z/U_b are also similar for both liquids along the horizontal centre line GH and
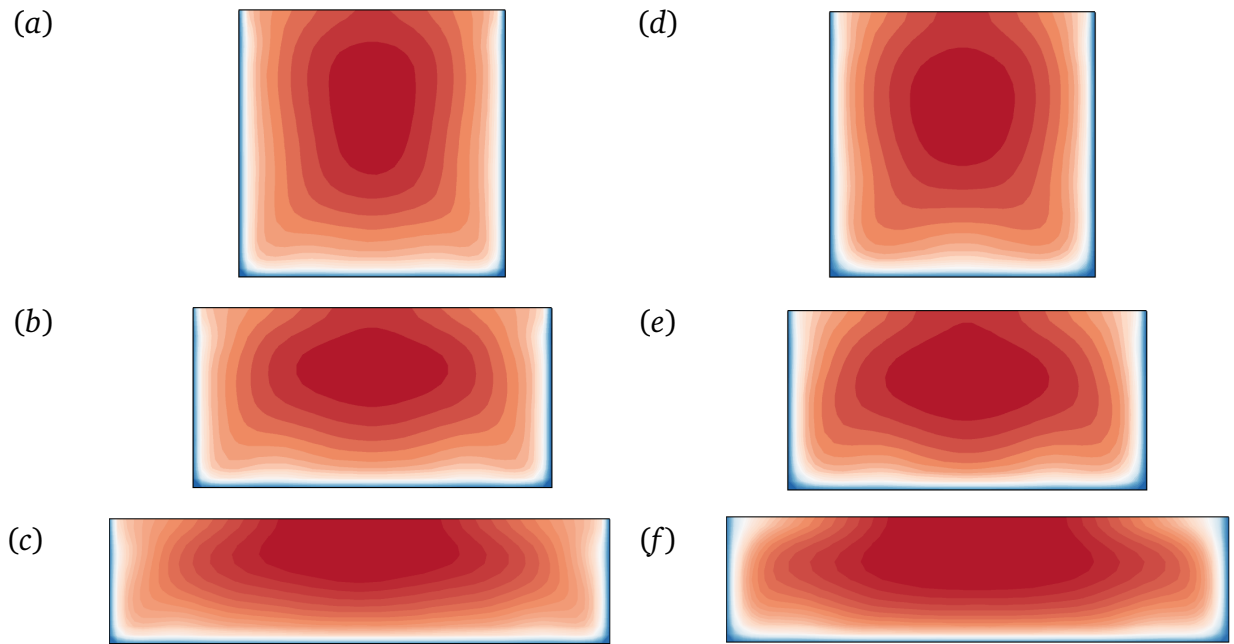
Fig. 8.6 Contours of the time-averaged streamwise velocity normalised by the bulk velocity shown for (a–c) Newtonian and (d–f) shear-thinning liquids for $AR = 1 - 4$ (from top to bottom). The contour levels vary from zero (blue) to 1.2 (red).

the shear-thinning fluid shows slightly higher values of U_z/U_b than the Newtonian fluid for most of the region (seen more clearly for $AR = 2$ and 4 in figure 8.7 b).
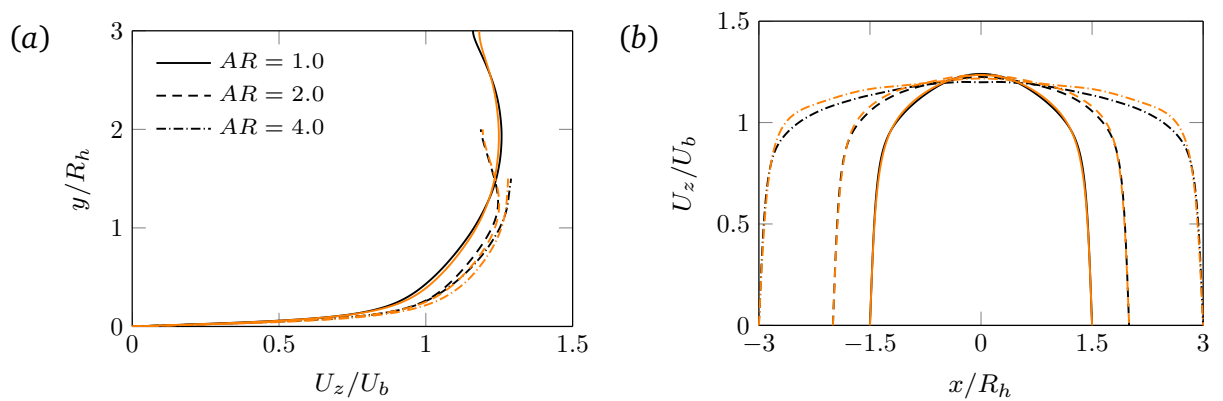
Fig. 8.7 Profiles of mean streamwise velocity for Newtonian (black lines) and shear-thinning liquids (orange lines) plotted as a function of the distance from the wall along (a) the vertical centre line EF and (b) the horizontal centre line GH.

The effects of the channel aspect ratio AR and shear thinning on the mean streamwise velocity become more clear when the profiles are plotted in wall coordinates (figure 8.8). For the Newtonian fluid, the mean streamwise velocity (U_z^+) profiles for $AR = 2$ and 4 overlap except very near the surface and lie significantly above the profile of $AR = 1$. The U_z^+ profiles of the shear-thinning fluid also show a similar trend with increasing AR, however, unlike the Newtonian fluid, the profile of $AR = 4$ lies slightly above the profile of $AR = 2$ for entire depth of flow. For both liquids, the velocity-dip phenomenon becomes weak with increasing AR and almost disappears for $AR = 4$, which was also seen in figure 8.7 (a). For $AR = 1$ and 2, the y^+ location where U_z^+ reaches a maximum and the velocity-dip (the difference between the maximum U_z^+ and its value at the free surface) is almost the same for both liquids. Also seen in figure 8.8 (b) is that in the viscous sublayer, the usual scaling $U_z^+ = y^+$ does not appear to be obeyed for either liquids. This is discussed further in section 8.6.
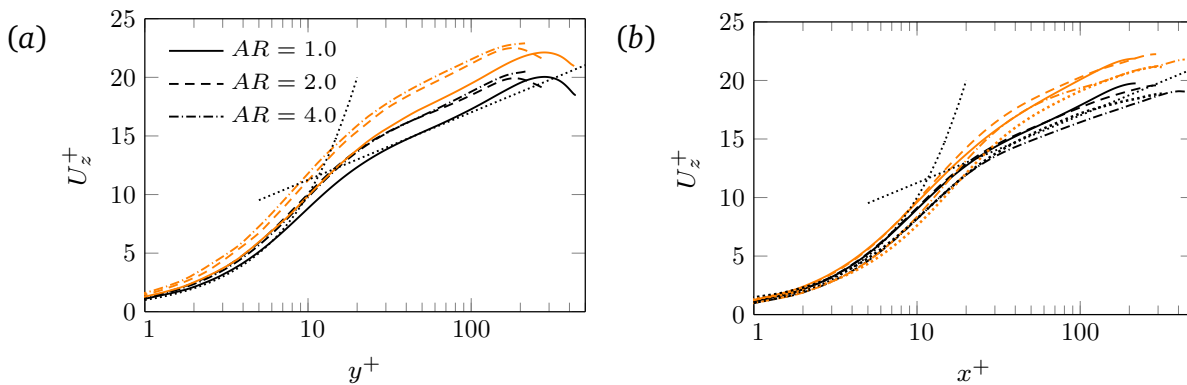
Fig. 8.8 Profiles of mean streamwise velocity for Newtonian (black lines) and shear-thinning liquids (orange lines) plotted in wall coordinates along (a) the vertical centre line EF and (b) the horizontal centre line GH. Dotted lines show the traditional law of wall $U_z^+ = \phi^+$, $U_z^+ = 2.5 \ln \phi^+ + 5.5$ where ϕ is the wall normal direction (x or y).

8.5 Mean viscosity

As expected, the mean viscosity of the shear-thinning fluid increases with the distance from the wall towards the centre or the free surface (figure 8.9). The maximum mean viscosity occurs close to the free surface and its location is pushed further closer to the wall with increasing AR. Very high viscosity in a tiny

region close to the bottom two corners is due to very low shear rates in those regions. Indeed, the shear rate there reaches a value less than the cut-off shear rate and thus, the viscosity in these regions is set to the maximum allowable viscosity (see chapter 3). However, it is unlikely that this could have affected the overall predictions as it happens only in a tiny region.
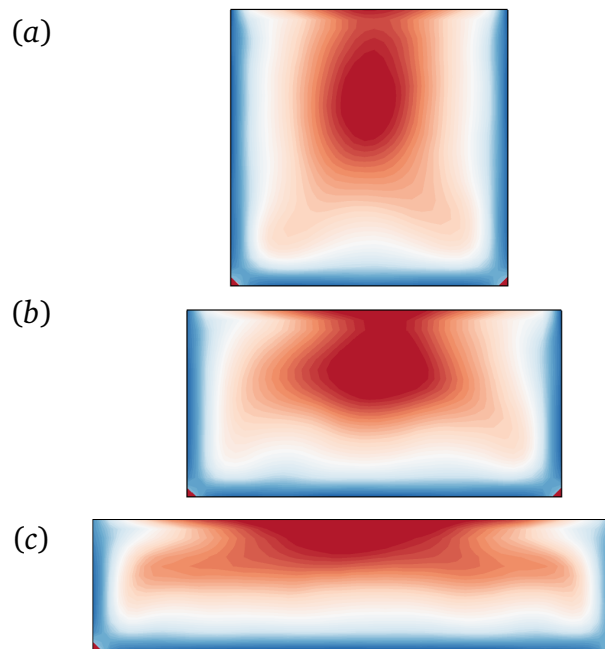
Fig. 8.9 Contours of the mean viscosity normalised by the mean wall viscosity for a shear-thinning fluid for (*a*) $AR = 1$, (*b*) $AR = 2\,2$ and (*c*) $AR = 4$. Contour levels vary from 1 (blue) to 4 (red).

Profiles of the mean viscosity normalised by the nominal wall viscosity ν_w are plotted along the vertical and horizontal centre lines, EF and GH, in figure 8.10. The mean viscosity increases with the distance from the wall but only significantly for $y^+(\text{or}\,x^+) \gtrsim 10$. This is similar to that seen for pipe flows (figure 5.6). Near wall viscosity ($y^+ \lesssim 10$) is slightly lower for higher AR, but away from lower wall (especially for $y^+ \gtrsim 60$) viscosity increases with AR (figure 8.10 *a*). In contrast, the profiles of all AR deviate from each other along the horizontal line GH for $y^+ \gtrsim 30$. The difference between the behaviour of the mean viscosity profiles along the vertical and the horizontal centre lines is likely to be a result of secondary currents which modify the velocity gradient and hence shear rate in the flow. Since the effect of secondary currents is expected to be

minimum and nearly uniform along the vertical line EF whereas the horizontal centre line passes through the secondary vortices, different behaviour of the shear rate and hence of the mean viscosity profiles along EF and GH is expected.
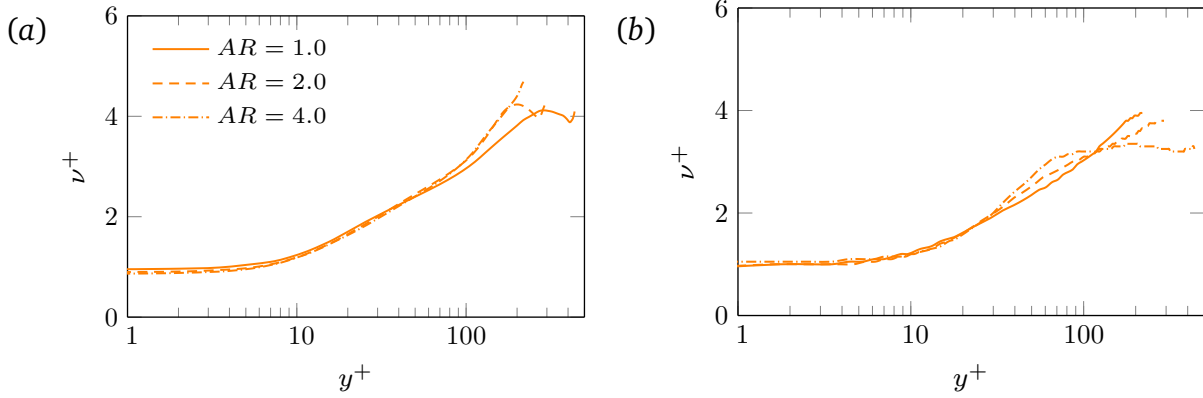

Fig. 8.10 Profiles of mean viscosity of the shear-thinning fluid plotted in wall units along (*a*) the vertical centre line EF and (*b*) the horizontal centre line GH.

8.6 Alternative scaling for the mean streamwise velocity

Since the mean wall shear stress varies along the wall, using the nominal wall shear stress is not a robust method of calculating the friction velocity [72]. For PL liquids, where the mean wall shear stress and the mean wall viscous stress are different from each other, using a friction velocity calculated from the mean wall viscous stress and the mean wall viscosity in non-dimensionalisation collapsed the near wall mean axial velocity profiles for Newtonian and shear-thinning liquids in a pipe flow (section 5.1.2). This scaling is used in figure 8.11 for open channel flows where the mean wall viscosity, $\bar{\nu}_w$, at point E or G (see figure 8.4) is used for the viscosity scale and $u^{\#} = (\bar{\nu}_w |\partial U_z / \partial \phi|_w)^{1/2}$ is used for the velocity scale (ϕ is the wall normal direction x or y). This gives $x^{\oplus} = \tilde{x} u^{\#} / \bar{\nu}_w$ and $y^{\oplus} = \tilde{y} u^{\#} / \bar{\nu}_w$, where $\tilde{x}$ and $\tilde{y}$ are the distances from the wall. As seen in figure 8.11, using this scaling collapses the near wall mean streamwise velocity profiles of different AR for both Newtonian and shear-thinning liquids. This indicates the universality of this scaling for wall bounded flows in the near wall region. Away from the wall, the $U_z^{\oplus}$ profiles of different AR are in a good agreement with the log profile

$U_z^{\oplus} = 2.5 \ln y^{\oplus} + 5.5$ for both liquids along the vertical line EF, however, similar agreement is seen only for the Newtonian fluid along the horizontal line GH. The profiles of the shear-thinning fluid deviate significantly from each other away from the wall along GH (figure 8.11 b).
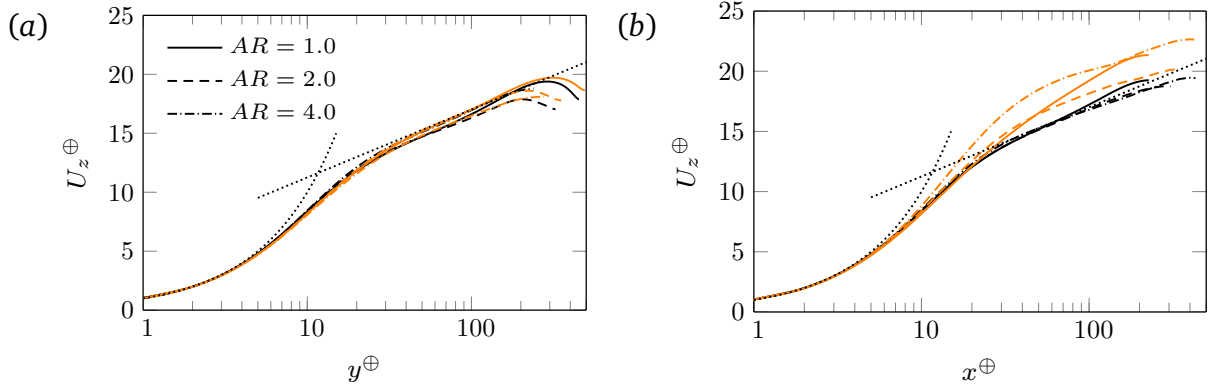

Fig. 8.11 Profiles of mean streamwise velocity for Newtonian (black lines) and shear-thinning liquids (orange lines) plotted in wall units along (a) the vertical centre line EF and (b) the horizontal centre line GH.

It must be noted that although the new scaling collapsed the near wall mean streamwise velocity profiles of different liquids and AR, this scaling is not practical for reasons mentioned in section 5.1.2.

8.7 Secondary flows

Secondary flows are known to occur in non-circular ducts for Newtonian fluids [14, 69] and for viscoelastic fluids [41, 100] even under laminar conditions. However, the effect of pure shear-dependent viscosity on secondary flows is still unknown. The profiles of the mean wall shear stress (figure 8.5) and contours of the mean streamwise velocity (figure 8.6) indicated the presence of the secondary currents normal to the streamwise direction. This is shown using mean velocity vectors, contours of the normalised mean in-plane velocity magnitude ($U_s = (U_x^2 + U_y^2)^{1/2}/U_b$), and contours of the mean streamwise vorticity in figures 8.12 and 8.13. The maximum in-plane velocity $U_{s_{max}}$ occurs close to the free surface where it is more than three percent of the bulk velocity for all AR and for both liquids. It is maximum for $AR = 2$ for both liquids. Contours of the streamwise vorticity show that for both liquids, the number of vortices along

the base are higher for higher AR. Although the in-plane velocity U_s is higher for the Newtonian fluid than the shear-thinning fluid close to the free surface and at side walls, the secondary currents penetrate from the boundary more deeply into the flow for the shear-thinning fluid. unlike other cases where the secondary currents are almost zero in the middle of the base, they do not vanish there in the shear-thinning fluid for $AR = 1$ and push the fluid away from the wall. This is responsible for a minimum in the mean wall shear stress in the middle of the base BC seen in figure 8.5 (a) for the shear-thinning fluid for $AR = 1$.
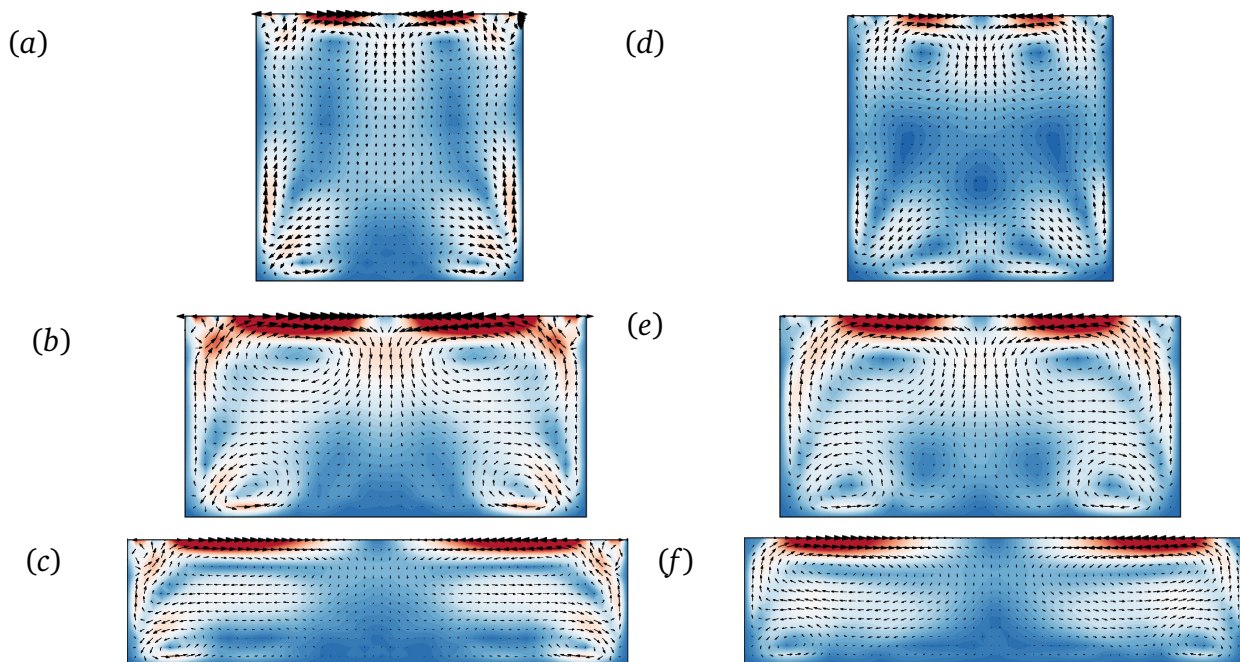
Fig. 8.12 Contours of in-plane velocity expressed as a percentage of the bulk velocity and cross-sectional velocity vectors for (a–c) Newtonian and (d–f) shear-thinning liquids. Contour levels vary from 0 (blue) to 3 (red).

Secondary flows in open channels are known to affect the solid particle suspensions in particle laden flows [105]. Slightly weaker, but a wider, region of secondary currents in the shear-thinning fluid compared to the Newtonian fluid suggests that the secondary currents will likely contribute more in lifting particles from a bed for a shear-thinning fluid, however, further investigation is needed to confirm this. The current results also suggest that the secondary flow effects will persist up to a higher AR for the shear-thinning fluid than the Newtonian fluid, however, this also needs to be confirmed via a further investigation.
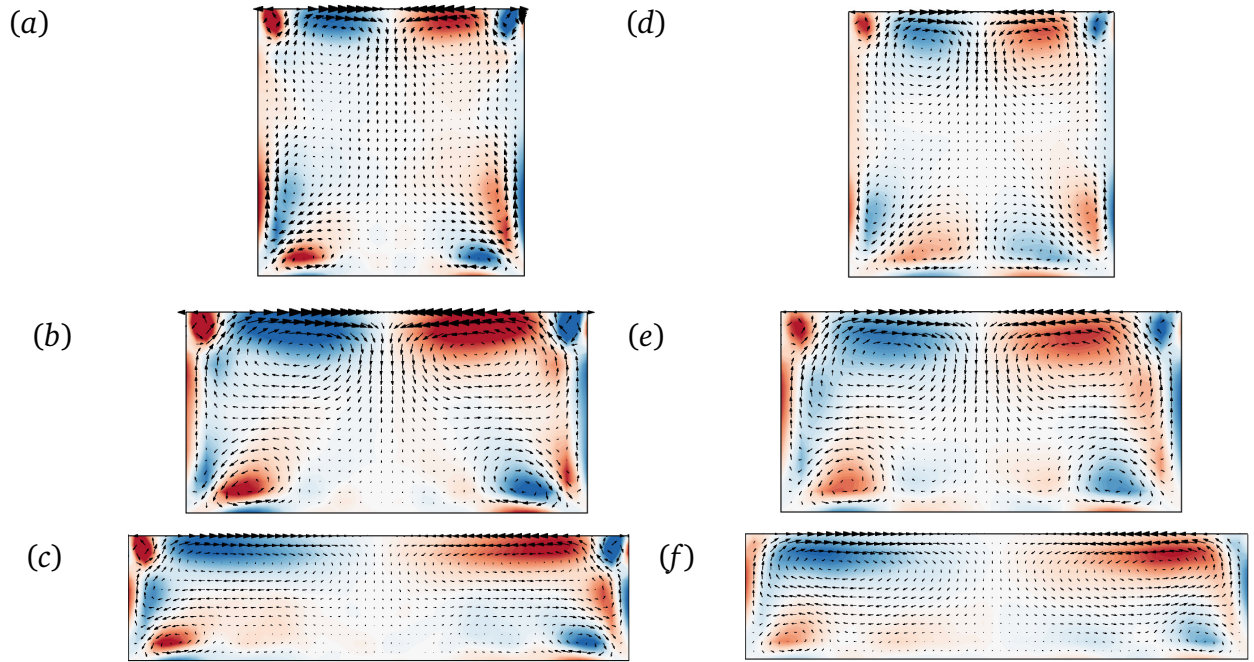
Fig. 8.13 Contours of the mean streamwise vorticity overlayed with cross-sectional mean velocity vectors for (*a–c*) Newtonian and (*d–f*) PL liquids. Contour levels vary from -0.3 (blue) to 0.3 (red).

8.8 Turbulence intensities

Compared to secondary flows, turbulence intensities are likely to contribute more in keeping the solid particles in suspension, therefore, the effect of varying AR and the fluid rheology on the turbulence intensities is studied here. Profiles of turbulence intensities are plotted in wall coordinates along the vertical and the horizontal centre lines, EF and GH, in figures 8.14 – 8.16. Along the vertical line EF, these profiles are similar to those in a pipe flow except close to the free surface. The maximum of each turbulence intensity component occurs close to the wall (at $y^+ \approx 10$) and then each decreases towards the free surface. Since the velocity normal to the free surface, u_y, is zero (as specified in simulations), $u_y'^+$ decays to zero at the free surface (figure 8.16 *a* and *c*), however, the other components, $u_x'^+$ and $u_z'^+$, increase again close to the free surface with the increase being significant for $u_x'^+$ (figure 8.15 *a* and *c*). Near the wall for $y^+ \lesssim 100$, all turbulence intensities increase with increasing AR along the vertical centre line EF for both liquids but the trend is reversed away from the wall. The location where the streamwise

turbulence intensity, $u_z'^+$ reaches a maximum is shifted away from the wall with increasing AR. The shear-thinning effect is similar to that as seen for a pipe flow; it increases the turbulence intensity in the streamwise direction but decreases it in the transverse directions for most of the flow. The effect of shear-thinning along the line GH is similar as seen for the vertical line and it increases the $u_z'^+$ but decreases $u_x'^+$ and $u_y'^+$. The most striking difference occurs in $u_x'^+$ which increases away from the wall and shows slightly higher peak values for $AR = 1$ and 2, but for $AR = 4$ there appears to be no obvious maxima near the free surface for either the Newtonian or shear-thinning fluid (figure 8.15 b).
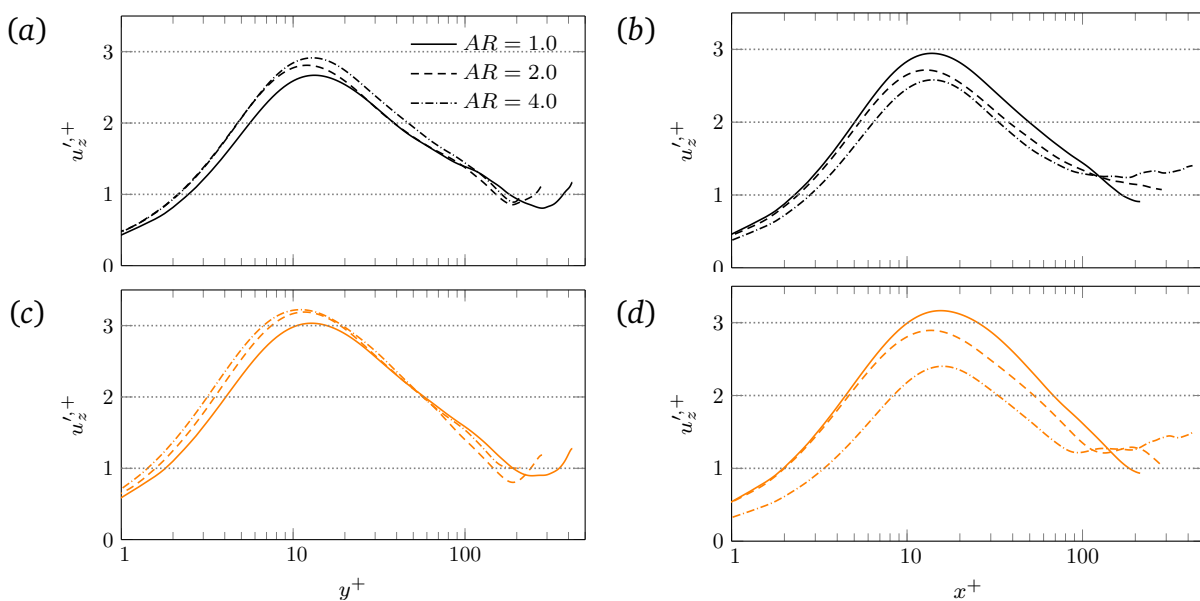
Fig. 8.14 Profiles of the streamwise turbulence intensity plotted in wall coordinates for Newtonian (black lines) and shear-thinning (orange lines) liquids along the (a,c) the vertical centre line EF and the (b,d) the horizontal centre line GH.

8.9   Chapter summary

In this part of the study, DNS is used to investigate the effect of varying channel aspect ratio and shear thinning on the turbulent flow of a rectangular open channel flow. Simulations are run for Newtonian and shear-thinning (power-law index $n = 0.6$) liquids at a fixed friction Reynolds number of 146 which is equivalent to a generalised Reynolds number of $10\,000$ for the shear-thinning fluid and slightly less, 9300, for the Newtonian fluid. The key finding is that
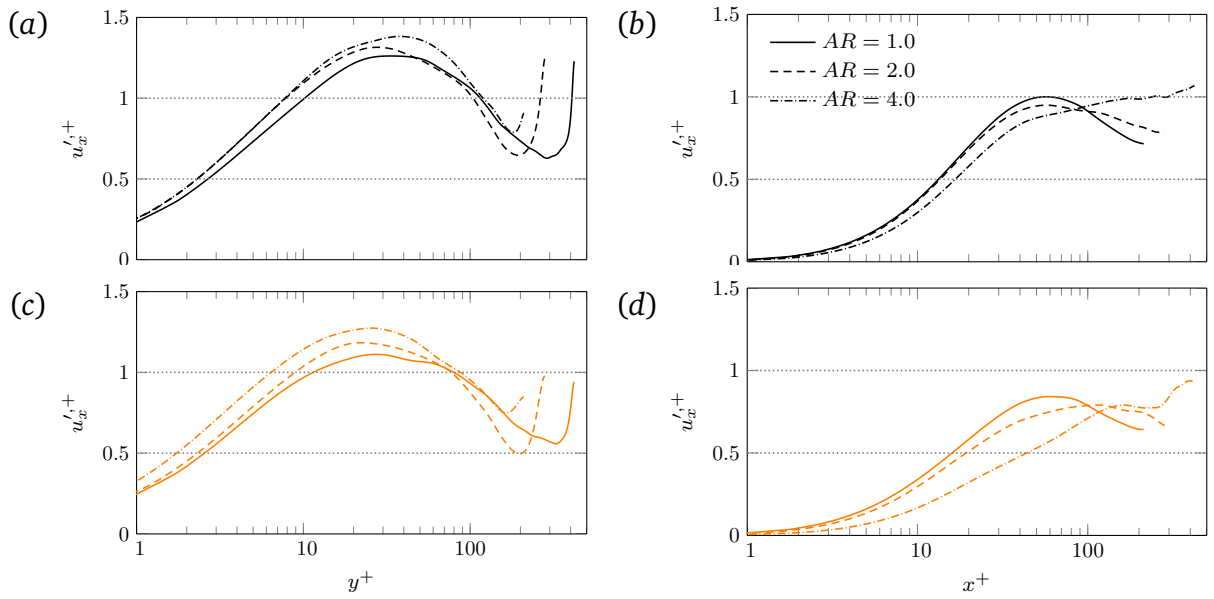
Fig. 8.15 Profiles of turbulence intensity in the $x-$direction (normal to the side walls) plotted in wall coordinates for Newtonian (black lines) and shear-thinning (orange lines) liquids along the (*a,c*) the vertical centre line EF and the (*b,d*) the horizontal centre line GH.
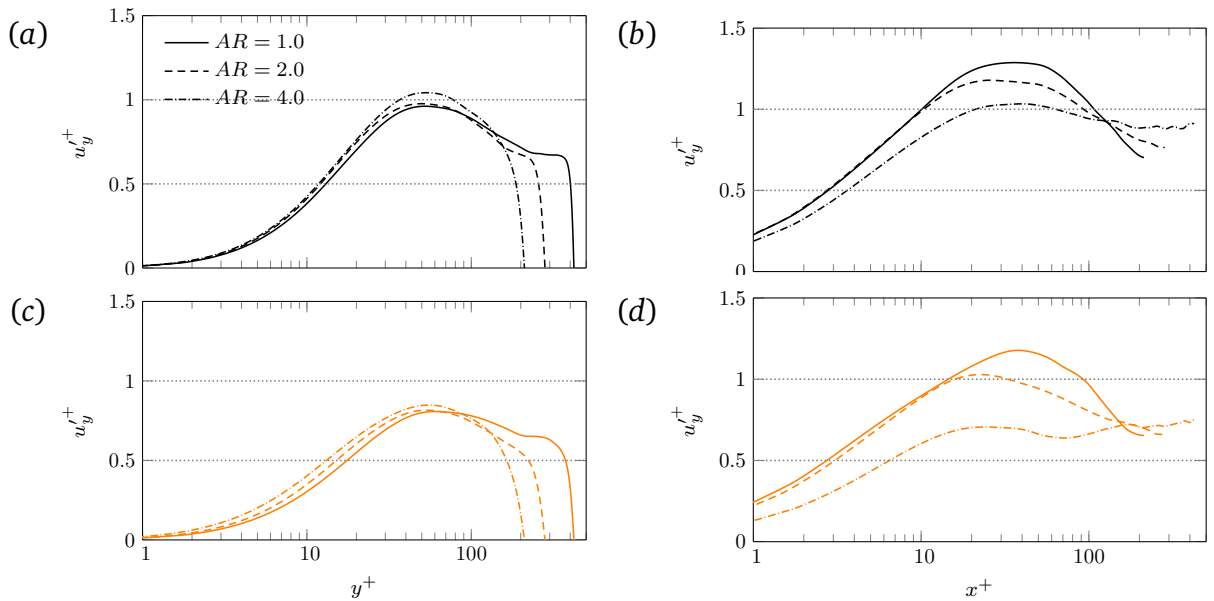
Fig. 8.16 Profiles of turbulence intensity in the $y-$direction (normal to the base) plotted in wall coordinates for Newtonian (black lines) and shear-thinning (orange lines) liquids along the (*a,c*) the vertical centre line EF and the (*b,d*) the horizontal centre line GH.

similar to a Newtonian fluid, the bulk velocity and hence the flow rate is almost independent of the channel aspect ratio for a shear-thinning fluid for a fixed

hydraulic radius. In general, the effect of varying aspect ratio is similar for both Newtonian and shear-thinning liquids and the effect of shear thinning is similar to that seen in a pipe flow. An asymmetry in the boundary conditions because of the free surface and corners induces secondary flows. These secondary flows are slightly weaker in the shear-thinning fluid compared to the Newtonian fluid, but they penetrate more deeply into the flow with shear thinning. This lead to a non-uniform distribution of the mean wall shear stress and lead to differences in the profiles of the mean streamwise velocity, mean viscosity and turbulence intensities along the vertical and the horizontal centre lines.

Similar to a pipe flow, the flow becomes less fluctuating with shear thinning. Mean velocity and the turbulence intensity in the streamwise direction increase but the turbulence intensity in the transverse direction decrease with shear thinning. Shear thinning increases the mean wall shear stress at the base but decreases it at the side walls. The mean streamwise velocity profiles of Newtonian and shear-thinning liquids are found to collapse near the wall if the mean viscosity and the mean viscous stress at the base of the profile are used in non-dimensionalisation. The log-law of the mean streamwise velocity profile is found valid only for the Newtonian fluid. The DNS predictions of the friction factor are in a reasonable agreement with the Dodge & Metzner correlation for a pipe flow.

The current study shows that it is possible to study open channel flows of GN liquids using DNS. Only channels with a rectangular cross-section are considered here and the effect of the channel shape remains to be investigated in future. The free-surface of the channel is modelled as a deformation-free boundary in the current simulations which is a reasonable assumption for subcritical flows such as considered here. However, it will not be a good approximation for nearly critical or supercritical flow. How shear thinning affects open channel flows of GN liquids at higher Froude numbers also remains to be investigated in future.

<div align="right">

9

</div>

Conclusions and way forward

While turbulence in Newtonian liquids is well studied, studies of non-Newtonian liquids are rare. Many studies of non-Newtonian liquids considered viscoelastic liquids which due to their drag reducing properties are very attractive for engineering applications. Only a few studies have appeared for GN liquids which are also very common in applications and in nature.

9.1 Conclusions

This thesis is a step forward towards understanding turbulence in flows of GN liquids. Flows through pipes and open channels are investigated using DNS. Significant discrepancies were observed in the past between DNS and experiments of turbulent pipe flows of GN liquids which are shown here to be caused by the lack of high shear rate data in rheology characterisation. Using Wilson & Thomas correlation for bulk velocity it is shown that the errors in the predictions of a turbulence flow correlation also decrease if high shear rate data is used. It is shown that that the maximum shear rate in rheology characterisation must be at least twice of the nominal wall shear stress to get a good agreement between DNS and experiments.

Simulations of turbulent pipe flow of power-law liquids at $Re_\tau = 323$ showed that the turbulent length scale of axial velocity fluctuations increase in the axial and azimuthal directions with shear thinning. The mean axial velocity profiles when normalised by traditional wall scaling do not follow the Newtonian law of wall $U_z^+ = y^+$ in the viscous sublayer. This is caused by an additional mean shear stress - the turbulent viscous stress which arises in the mean momentum equation due to viscosity fluctuations. $U_z^+ \neq y^+$ for power-law liquids has a direct implication on Reynolds-averaged Navier–Stokes simulations and large-eddy simulations and suggests that the wall functions in those numerical techniques require modifications for PL liquids. An alternate scaling (see section 5.1.2) which uses the mean viscosity and the mean axial velocity gradient at the wall is proposed to recover the law of wall for power-law liquids. However, this scaling is not possible to determine *a priori* in DNS and in experiments. Outside the viscous sublayer, the mean axial velocity profiles are found to deviate above the Newtonian profile with shear thinning. Higher mean axial velocity for a shear-thinning fluid leads to higher bulk velocity and thus lower friction factor compared to Newtonian fluid. Shear-thinning increases the anisotropy of turbulent velocity fluctuations by increasing the velocity fluctuations in the axial direction and decreasing in the radial and azimuthal directions. Because of higher mean viscosity and higher mean axial velocity gradient for shear-thinning liquids, higher mean viscous stress is observed for shear-thinning liquids compared to Newtonian fluid. In contrast, Reynolds shear stress is found to decrease with shear-thinning which is consistent with findings reported in past studies.

Analysis of the mean flow and turbulent kinetic energy budgets, which is carried out for GN liquids for the first time, shows that the effect of power-law rheology is confined to the near wall region, $y^+ \lesssim 60$. This is further confirmed via simulations where power-law rheology was used only near the wall and away from the wall a uniform viscosity was assumed. The thickness of GN rheology dependent region is found to increase with shear thinning which is consistent with the argument of Wilson and Thomas [103]. The overall effect of shear thinning is found greatest inside the viscous sublayer. The non-Newtonian dissipation terms arising due to viscosity fluctuations in mean flow and turbulent

kinetic energy budgets are found to decrease the total viscous dissipation. The effect of increasing Reynolds number is found to be similar for Newtonian and shear-thinning liquids. Increasing Reynolds number negligible affects the mean axial velocity profiles in the viscous sublayer for a shear-thinning fluid. The mean viscosity profiles near the wall for $y^+ \lesssim 100$ are found independent of the Reynolds number, the reason for which is not clear. Profiles of the axial turbulence intensity in wall units are found independent of rheology near the pipe centre the reason for which is also unknown.

Simulations of Bingham liquids showed that the effect of yield stress on a turbulent pipe flow is mostly similar to shear thinning. However, an important difference between the two effects is that unlike pure shear thinning, yield stress affects flow the greatest outside the viscous sublayer. The effect of yield stress on the mean axial velocity is negligible in the viscous sublayer and the mean axial velocity profiles follow $U_z^+ = y^+$ there. This is due to almost zero turbulent viscous stress there for Bingham liquids presumably because viscosity is dominated by the consistency K at high shear rates and $\tau_y/\dot{\gamma}$ is almost zero in the viscous sublayer.

A comparison of the mean axial velocity profiles for power-law liquids predicted by DNS and the profile proposed by Dodge and Metzner [35] showed that Dodge & Metzner profiles deviate significantly from the DNS predictions with the deviation being larger for more shear-thinning liquids. However, the predictions come close to the DNS predictions with increasing Reynolds number. The DNS friction factor predictions of shear-thinning liquids however agree well (within 5%) with the Dodge & Metzner correlation with the deviation between the predictions of DNS and the correlation again being larger for more shear-thinning liquids. This agreement is better than that observed in past DNS studies at lower Reynolds number. For less shear-thinning liquids, the DNS predictions are found closer to the correlation of Anbarlooei & Cruz [5] than Dodge & Metzner correlation. The predictions of the Wilson & Thomas correlation [103] which is used widely for yield stress liquids are found to deviate more from the DNS predictions for more shear-thinning liquids or for higher yield stress.

Compared to pipe flows, studies of open channel flows are rare. Simulations of rectangular open channels showed that the flow rate does not vary with varying channel aspect ratio for a fixed hydraulic radius. This means that a friction factor correlation defined using the hydraulic radius can be used confidently for rectangular open channel flows of GN liquids for different aspect ratios. The flows of Newtonian and shear-thinning liquids are affected similarly with varying channel aspect ratio and the effect of shear thinning is similar to that seen for pipe flow i.e. shear thinning increases the mean axial velocity and anisotropy of turbulent velocity fluctuations. Due to corners and the free surface, secondary flows are induced which penetrate more deeply into the flow from the boundary for a shear-thinning fluid compared to Newtonian fluid.

Shear thinning is shown to decrease the turbulent friction factor (also cited as drag reduction) in both pipes and open channels for a fixed Reynolds number (Re_τ or Re_G). The signature of drag-reduction is also found in other data, as in enhanced axial turbulence intensity, reduced radial and azimuthal turbulence intensities, reduced Reynolds shear stress and viscous dissipation of the turbulent kinetic energy. However, this drag reduction is much smaller than observed for viscoelastic liquids at similar Reynolds number (see [79]).

9.2 Future work

In the current study, the pipe flow simulations are carried out only for $Re_\tau < 750$ and the results showed that the mean axial velocity profiles of a shear-thinning fluid come closer to the Newtonian profile outside the viscous sublayer with increasing Reynolds number. The question remains whether the effect of GN rheology remains or vanishes at very high Reynolds number. Simulations showed that both shear thinning and yield stress increase the anisotropy of turbulent velocity fluctuations by increasing the fluctuations in the axial direction and decreasing in the transverse directions. This indicates a reduced turbulent energy transfer from the axial component to the transverse components but it is yet to be shown via an analysis of component-wise turbulent kinetic energy budget. For open channels, only the flow of a shear-thinning fluid in a rectangular channel is considered and the effect of yield stress and the shape of the channel cross-section

is yet to be investigated. Additionally, the current simulations of open channels assumed a uniform free surface which is reasonable for low Froude number flows such as considered here but will not be appropriate for high Froude number flows for which a significant deformation of free surface is expected. The effect of GN rheology for high Froude number flows also remains to be investigated. In the current study, only friction factor predictions predicted by DNS for turbulent pipe flows are compared with experiments and the validation of higher order data such as mean axial velocity and turbulence intensities are yet to be validated against experiments for pipes and open channels. Data produced in the current work will be useful in the development and validation of RANS and LES models for GN liquids.

References

[1] Abulnaga, B. E. (2002). *Slurry systems handbook*. McGraw-Hill,.

[2] Ahn, J., Lee, J. H., Lee, J., Kang, J.-h., and Sung, H. J. (2015). Direct numerical simulation of a 30R long turbulent pipe flow at Re_τ = 3008. *Physics of Fluids (1994-present)*, 27(6):065110.

[3] Akan, A. O. (2006). Fundamentals of open-channel flow. In Akan, A. O., editor, *Open Channel Hydraulics*, pages 1 – 23. Butterworth-Heinemann, Oxford.

[4] Alderman, N. and Haldenwang, R. (2007). A review of Newtonian and non-Newtonian flow in rectangular open channels. In *Hydrotransport*, volume 17, pages 87–106. The Southern African Institute of Mining and Metallurgy and the BHR Group Cape Town, SA.

[5] Anbarlooei, H. R., Cruz, D., Ramos, F., and Freire, A. P. S. (2015). Phenomenological blasius-type friction equation for turbulent power-law fluid flows. *Physical Review E*, 92(6):063006.

[6] Bagnold, R. A. (1954). Experiments on a gravity-free dispersion of large solid spheres in a Newtonian fluid under shear. In *Proceedings of the Royal Society of London A: Mathematical, Physical and Engineering Sciences*, volume 225, pages 49–63. The Royal Society.

[7] Barenblatt, G. I. (1996). *Scaling, self-similarity, and intermediate asymptotics: dimensional analysis and intermediate asymptotics*, volume 14. Cambridge University Press.

[8] Barnes, H. and Walters, K. (1985). The yield stress myth? *Rheologica Acta*, 24(4):323–326.

[9] Barnes, H. A. (1995). A review of the slip (wall depletion) of polymer solutions, emulsions and particle suspensions in viscometers: its cause, character, and cure. *Journal of Non-Newtonian Fluid Mechanics*, 56(3):221–251.

[10] Bingham, E. C. (1916). An investigation of the laws of plastic flow. *U.S Bureau of Standards Bulletin*, 13:309–353.

[11] Blackburn, H. M. and Sherwin, S. J. (2004). Formulation of a Galerkin spectral element–Fourier method for three-dimensional incompressible flows in cylindrical geometries. *J. Comput. Phys.*, 197(2):759–778.

[12] Bogue, D. C. and Metzner, A. B. (1963a). Velocity profiles in turbulent pipe flow. Newtonian and non-Newtonian fluids. *Industrial & Engineering Chemistry Fundamentals*, 2(2):143–149.

[13] Bogue, D. C. and Metzner, A. B. (1963b). Velocity profiles in turbulent pipe flow. Newtonian and non-Newtonian fluids. *Industrial & Engineering Chemistry Fundamentals*, 2(2):143–149.

[14] Bradshaw, P. (1987). Turbulent secondary flows. *Annu. Rev. Fluid Mech.*, 19(1):53–74.

[15] Brautlecht, C. A. and Sethi, J. R. (1933). Flow of paper pulps in pipe lines. *Industrial & Engineering Chemistry*, 25(3):283–288.

[16] Burger, J., Haldenwang, R., and Alderman, N. (2010a). Friction factor-Reynolds number relationship for laminar flow of non-Newtonian fluids in open channels of different cross-sectional shapes. *Chemical Engineering Science,* 65(11):3549 – 3556.

[17] Burger, J., Haldenwang, R., and Alderman, N. (2010b). *Laminar non-Newtonian open channel flow: investigating velocity, wall shear stress and fluid depth*.

[18] Burger, J., Haldenwang, R., and Alderman, N. J. (2014). Laminar and turbulent flow of non-Newtonian fluids in open channels for different cross-sectional shapes. *JHE,* 141(4):04014084.

[19] Burger, J., Haldenwang, R., Chhabra, R. P., and Alderman, N. J. (2015). Power law and composite power law friction factor correlations for laminar and turbulent non-Newtonian open channel flow. *Journal of the Brazilian Society of Mechanical Sciences and Engineering,* 37(2):601–612.

[20] Burger, J. H. (2014). *Non-Newtonian open channel flow: the effect of shape*. PhD thesis, Cape Peninsula University of Technology.

[21] Chanson, H. (2004). *Hydraulics of open channel flow*. Butterworth-Heinemann.

[22] Chilton, R. and Stainsby, R. (1998). Pressure loss equations for laminar and turbulent non-newtonian pipe flow. *JHE,* 124(5):522–529.

[23] Chin, C. (2011). *Numerical study of internal wall-bounded turbulent flows*. PhD thesis, The University of Melbourne, Australia.

[24] Chin, C., Monty, J. P., and Ooi, A. (2014). Reynolds number effects in DNS of pipe flow and comparison with channels and boundary layers. *Intnl J. Heat Fluid Flow*, 45:33–40.

[25] Chin, C., Ooi, A. S. H., Marusic, I., and Blackburn, H. M. (2010). The influence of pipe length on turbulence statistics computed from direct numerical simulation data. *Phys. Fluids*, 22(11).

[26] Clapp, R. M. (1961a). Turbulent heat transfer in pseudoplastic non-Newtonian fluids. In *International Development in Heat Transfer. A. S. M. E., Part 111, Sec. A.*, pages 652–661.

[27] Clapp, R. M. (1961b). Turbulent heat transfer in pseudoplastic non-Newtonian fluids. *Int. Dev. Heat Mass Trans.*, III:652–661.

[28] Coussot, P. (1994). Steady, laminar, flow of concentrated mud suspensions in open channel. *JHR*, 32(4):535–559.

[29] Couturier, É., Boyer, F., Pouliquen, O., and Guazzelli, É. (2011). Suspensions in a tilted trough: second normal stress difference. *J. Fluid Mech.*, 686:26–39.

[30] Cruz, D. O. A. and Pinho, F. T. (2003). Turbulent pipe flow predictions with a low Reynolds number $k - \varepsilon$ model for drag reducing fluids. *J. Non-Newt. Fluid Mech.*, 114(2):109–148.

[31] de Kretser, R., Scales, P. J., and Boger, D. V. (1997). Improving clay-based tailings disposal: Case study on coal tailings. *A. I. Ch. E. J.*, 43(7):1894–1903.

[32] den Toonder, J. M. J. and Nieuwstadt, F. T. M. (1997). Reynolds number effects in a turbulent pipe flow for low to moderate *Re*. *Phys. Fluids*, 9(11):3398–3409.

[33] den Toonder, J. M. J., Nieuwstadt, F. T. M., and Kuiken, G. D. C. (1995). The role of elongational viscosity in the mechanisms of drag reduction by polymer additives. *Appl. Sci. Res.*, 54:95–123.

[34] Dodge, D. and Metzner, A. B. (1959a). Turbulent flow of non-Newtonian systems. *AICHE Journal*, 5 (2):189–204.

[35] Dodge, D. W. and Metzner, A. B. (1959b). Turbulent flow of non-Newtonian systems. *A. I. Ch. E. J.*, 5:189–204.

[36] Eggels, J. G., Unger, F., Wiess, M. H., Westerweel, J., Adrian, R. J., Friedrich, R., and Nieuwstadt, F. T. M. (1994). Fully developed turbulent pipe flow: A comparison between direct numerical simulation and experiment. *J. Fluid Mech.*, 268:175–209.

[37] El-Emam, N., Kamel, A., El-Shafei, A., and El-Batrawy, A. (2003). New equation calculates friction factor for turbulent flow on non-Newtonian fluids. *Oil and Gas Journal*, 101(36):74.

[38] El Khoury, G. K., Schlatter, P., Noorani, A., Fischer, P. F., Brethouwer, G., and Johansson, A. V. (2013). Direct numerical simulation of turbulent pipe flow at moderately high Reynolds numbers. *Flow, Turbul. Combust.*, 91(3):475–495.

[39] Garcia, E. J. and Steffe, J. F. (1986). Comparison of friction factor equations for non-Newtonian fluids in pipe flow. *J. Food Process Eng.*, 9(2):93–120.

[40] Gavrilov, A. A. and Rudyak, V. Y. (2016). Direct numerical simulation of the turbulent flows of power-law fluids in a circular pipe. *Thermophysics and Aeromechanics*, 23(4):473–486.

[41] Gervang, B. and Larsen, P. S. (1991). Secondary flows in straight ducts of rectangular cross section. *J. Non-Newt. Fluid Mech.*, 39(3):217–237.

[42] Gnambode, P. S., Orlandi, P., Ould-Rouiss, M., and Nicolas, X. (2015). Large-eddy simulation of turbulent pipe flow of power-law fluids. *Intnl J. Heat Fluid Flow*, 54:196–210.

[43] Guang, R., Rudman, M., Chryss, A., Slatter, P., and Bhattacharya, S. (2011). A DNS investigation of the effect of yield stress for turbulent non-Newtonian suspension flow in open channels. *Particulate Science and Technology*, 29(3):209–228.

[44] Guermond, J. L., Minev, P., and Shen, J. (2006). An overview of projection methods for incompressible flows. *Comp. Meth. Appl. Mech. & Engng*, 195:6011–6045.

[45] Guzel, B., Frigaard, I., and Martinez, D. M. (2009). Predicting laminar turbulent transition in Poiseuille pipe flow for non-Newtonian fluids. *Chem. Eng. Sci.*, 64(2):254–264.

[46] Haldenwang, R. (2003). *Flow of non-Newtonian fluids in open channels*. PhD thesis, Cape Technikon, Cape Town, South Africa.

[47] Haldenwang, R. and Slatter, P. (2006). Experimental procedure and database for non-newtonian open channel flow. *JHR*, 44(2):283–287.

[48] Haldenwang, R., Slatter, P., and Chhabra, R. (2002). Laminar and transitional flow in open channels for non-Newtonian fluids. In *Hydrotransport*, volume 15, pages 755–768.

[49] Haldenwang, R., Slatter, P. T., and Chhabra, R. P. (2010). An experimental study of non-Newtonian fluid flow in rectangular flumes in laminar, transition and turbulent flow regimes. *Journal of the South African Institution of Civil Engineering*, 52:0 – 0.

[50] Hallbom, D. J. (2008). *Pipe flow of homogeneous slurry*. PhD thesis, Citeseer.

[51] Hanks, R. W. (1978). Low Reynolds number turbulent pipeline flow of pseudohomogeneous slurries. In *Fifth International Conference on the Hydraulic Transport of Solids in Pipes (Hydrotransport 5)*, pages C2–23–C2–34.

[52] Hanks, R. W. and Ricks, B. L. (1974). Laminar-turbulent transition in flow of pseudoplastic fluids with yield stresses. *J. Hydraulics*, 8(4):163–166.

[53] Hao, Z. and Zhenghai, R. (1982). Discussion on law of resistance of hyper-concentration flow in open channel. *Science China Mathematics*, 25(12):1332–1342.

[54] Hartnett, J. and Kostic, M. (1990). Turbulent friction factor correlations for power law fluids in circular and non-circular channels. *International Communications in Heat and Mass Transfer*, 17(1):59 – 65.

[55] Heywood, N. I. and Cheng, D. C. (1984). Comparison of methods for predicting head loss in turbulent pipe flow of non-Newtonian fluids. *Transactions of the Institute of Measurement and Control*, 6(1):33–45.

[56] Hutchins, N. and Marusic, I. (2007). Evidence of very long meandering features in the logarithmic region of turbulent boundary layers. *J. Fluid Mech.*, 579:1–28.

[57] Karniadakis, G. E., Israeli, M., and Orszag, S. A. (1991). High-order splitting methods for the incompressible Navier–Stokes equations. *J. Comput. Phys.*, 97(2):414–443.

[58] Kemblowski, Z. . and Kolodziejski, J. (1973). Flow resistances of non-Newtonian fluids in transitional and turbulent flow. *Int. Chem. Eng.*, 22(2):265–279.

[59] Keulegan, G. H. (1938). *Laws of turbulent flow in open channels*, volume 21. National Bureau of Standards US.

[60] Knight, D. W., Demetriou, J. D., and Hamed, M. E. (1984). Boundary shear in smooth rectangular channels. *Journal of hydraulic engineering*, 110(4):405–422.

[61] Kozicki, W. and Tiu, C. (1967). Non-Newtonian flow through open channels. *The Canadian Journal of Chemical Engineering*, 45(3):127–134.

[62] Krantz, W. B. and Wasan, D. T. (1971). Heat, mass, and momentum transfer analogies for the fully developed turbulent flow of power law fluids in circular tubes. *AIChE Journal*, 17(6):1360–1367.

[63] Leslie, D. C. and Gao, S. (1988). The stability of spectral schemes for the large eddy simulation of channel flows. *Intnl J. Num. Meth. Fluids,* 8(9):1107–1116.

[64] Lootens, D., Van Damme, H., Hémar, Y., and Hébraud, P. (2005). Dilatant flow of concentrated suspensions of rough particles. *Phys. Rev. Let.*, 95(26):268302.

[65] Lumley, J. L. (1969). Drag reduction by additives. *Annual review of fluid mechanics*, 1(1):367–384.

[66] Madlener, K., Frey, B., and Ciezki, H. (2009). Generalized Reynolds number for non-Newtonian fluids. *Progress in Propulsion Physics*, 1:237 – 250.

[67] Malin, M. (1997). Turbulent pipe flow of power-law fluids. *International Communications in Heat and Mass Transfer*, 24(7):977 – 988.

[68] Malin, M. (1998). Turbulent pipe flow of Herschel-Bulkley fluids. *International Communications in Heat and Mass Transfer*, 25(3):321 – 330.

[69] Melling, A. and Whitelaw, J. H. (1976). Turbulent flow in a rectangular duct. *J. Fluid Mech.*, 78(2):289–315.

[70] Metzner, A. B. and Reed, J. C. (1955). Flow of non-Newtonian fluids – correlations for laminar, transition and turbulent flow regimes. *A. I. Ch. E. J.*, 1:434–444.

[71] Mizuno, Y. and Jiménez, J. (2013). Wall turbulence without walls. *J. Fluid Mech.*, 723:429–455.

[72] Nezu, I. and Rodi, W. (1986). Open-channel flow measurements with a laser doppler anemometer. *JHE,* 112(5):335–355.

[73] Ohta, T. and Miyashita, M. (2014). DNS and LES with an extended Smagorinsky model for wall turbulence in non-Newtonian viscous fluids. *J. Non-Newt. Fluid Mech.*, 206:29–39.

[74] Park, J., Mannheimer, T., and Grimley, T. (1989). Pipe flow measurements of transparent non-Newtonian slurry. *J. Fluids Eng.,* 111(3):331–336.

[75] Pinho, F. T. (2003). A GNF framework for turbulent flow models of drag-reducing fluids and a proposal for a k–ε type closure. *J. Non-Newt. Fluid Mech.*, 114:149–184.

[76] Pinho, F. T. and Whitelaw, J. H. (1990). Flow of non-Newtonian fluids in a pipe. *J. Non-Newt. Fluid Mech.*, 34:129–144.

[77] Piomelli, U. (1997). Large-eddy simulations: Where we stand. In Liu, C. and Liu, Z., editors, *Advances in DNS/LES*, pages 93–104, Louisiana. AFOSR.

[78] Pope, S. B. (2000). *Turbulent flows*. Cambridge University Press.

[79] Ptasinski, P., Nieuwstadt, F., den Brule B.H.A.A., V., and M.A., H. (2001). Experiments in turbulent pipe flow with polymer additives at maximum drag reduction. *Flow, Turb. Combust.*, 66:159–182.

[80] Ptasinski, P. K., Boersma, B. J., Nieuwstadt, F. T. M., Hulsen, M. A., Van den Brule, B. H. A. A., and Hunt, J. C. R. (2003). Turbulent channel flow near maximum drag reduction: simulations, experiments and mechanisms. *J. Fluid Mech.*, 490:251–291.

[81] Rahman, N. (2013). *Wall slip in pipe rheometry of multiphase fluids*. PhD thesis, PhD thesis, The University of Manchester.

[82] Rico, M., Benito, G., and Dez-Herrero, A. (2008). Floods from tailings dam failures. *J. Hazardous Materials*, 154(1-3):79 – 87.

[83] Rudman, M. and Blackburn, H. M. (2006). Direct numerical simulation of turbulent non-Newtonian flow using a spectral element method. *Appl. Math. Mod.*, 30:1229–1248.

[84] Rudman, M., Blackburn, H. M., Graham, L. J. W., and Pullum, L. (2004). Turbulent pipe flow of non-Newtonian fluids. *J. Non-Newt. Fluid Mech.*, 118(1):33–48.

[85] Rudman, M., Graham, L. J. W., Blackburn, H. M., and Pullum, L. (2002). Non-Newtonian turbulent and transitional pipe flow. In *15th Int. Conf. Hydrotransport*, pages 271–286, Banff. BHR Group.

[86] Shaver, R. G. and Merrill, E. W. (1959). Turbulent flow of pseudoplastic polymer solutions in straight cylindrical tubes. *AIChE Journal*, 5(2):181–188.

[87] Shenoy, A. V. and Saini, D. R. (1982). A new velocity profile model for turbulent pipe-flow of power-law fluids. *The Canadian Journal of Chemical Engineering*, 60(5):694–696.

[88] Skelland, A. H. P. (1967). *Non-Newtonian flow and heat transfer*. John Wiley & Sons, New York.

[89] Slatter, P. (2000). The role of rheology in the pipelining of mineral slurries. *Mineral Processing and Extractive Metallurgy Review*, 20(1):281–300.

[90] Slatter, P. T. and Lazarus, J. H. (1993). Critical flow in slurry pipeline. In *12th Int. Conf. on Slurry Handling and Pipeline Transport, Hydrotransport 12*, pages 639–658. BHRG Fluid Engineering,Cranfield, UK.

[91] Steffe, J. F. (1996). *Rheological methods in food process engineering*. Freeman press.

[92] Szillas, A. P., Bobok, E., and Navaratil, L. (1981). Determination of turbulent pressure loss of non-Newtonian oil flow in rough pipes. *Rheol. Acta.*, 20:487–496.

[93] Te Chow, V. (1959). *Open channel hydraulics*. McGraw-Hill Book Company, Inc; New York.

[94] Thais, L., Gatski, T. B., and Mompean, G. (2013). Analysis of polymer drag reduction mechanisms from energy budgets. *Intnl J. Heat Fluid Flow*, 43:52–61.

[95] Tomita, Y. (1959). A study of non-Newtonian flow in pipe lines. *Bulletin J. S. M. E.*, 2(5):10–16.

[96] Torrance, B. M. (1963). Friction factors for turbulent non-Newtonian fluid flow in circular pipes. *South African Mech. Engr*, 13:89–91.

[97] Wallace, J. M. (2016). Quadrant analysis in turbulence research: History and evolution. *Annu. Rev. Fluid Mech.*, 48(1):131–158.

[98] Wallace, J. M., Eckelmann, H., and Brodkey, R. S. (1972). The wall region in turbulent shear flow. *J. Fluid Mech.*, 54(01):39–48.

[99] Warsi, Z. U. A. (2002). Turbulent flow of power-law fluids through circular pipes. *AIAA Journal*, 40(1):181 – 185.

[100] Wheeler, J. A. and Wissler, E. H. (1966). Steady flow of non-newtonian fluids in a square duct. *Transactions of the Society of Rheology*, 10(1):353–367.

[101] Wilson, K. C. (1991). Flume design for homogeneous slurry flow. *Particulate science and technology*, 9(3-4):149–159.

[102] Wilson, K. C., Addie, G. R., Sellgren, A., and Clift, R. (2006). Flow of non-settling slurries. In *Slurry Transport Using Centrifugal Pumps*, pages 51–82. Springer US.

[103] Wilson, K. C. and Thomas, A. D. (1985). A new analysis of the turbulent flow of non-Newtonian fluids. *Can. J. Chem. Eng.*, 63:539–546.

[104] Wilson, S. and Taylor, A. (1996). The channel entry problem for a yield stress fluid. *J. Non-Newt. Fluid Mech.*, 65(23):165 – 176.

[105] Yang, S.-Q., Tan, S. K., and Wang, X.-K. (2012). Mechanism of secondary currents in open channel flows. *Journal of Geophysical Research: Earth Surface*, 117(F4).

[106] Yoo, S. (1974). *Heat transfer and friction factors for non-Newtoman fluids in circular tubes*. PhD thesis, University of Illinois, Chicago.

[107] Zagarola, M. V., Perry, A. E., and Smits, A. J. (1997). Log laws or power laws: The scaling in the overlap region. *Phys. Fluids*, 9(7):2094–2100.

[108] Zagarola, M. V. and Smits, A. J. (1998). Mean-flow scaling of turbulent pipe flow. *J. Fluid Mech.*, 373:33–79.

A

Appendix 1

A.1   Mean flow kinetic energy equation

An equation for the mean flow kinetic energy $K = (1/2)U_iU_i$ can be obtained by multiplying the Reynolds averaged Navier–Stokes equation with U_i. The Reynolds averaged Navier–Stokes equation for a non-Newtonian fluid is written as:

$$\frac{\partial U_i}{\partial t} + U_j \frac{\partial U_i}{\partial x_j} = -\frac{1}{\rho}\frac{\partial P}{\partial x_i} + \frac{\partial}{\partial x_j}(2\bar{\nu}S_{ij} + 2\overline{\nu' s'_{ij}} - \overline{u'_i u'_j}) \tag{A.1}$$

Multiplying the above equation with U_i gives

$$\frac{1}{2}\frac{\partial U_i U_i}{\partial t} + \frac{1}{2}U_j \frac{\partial U_i U_i}{\partial x_j} = -U_i\frac{1}{\rho}\frac{\partial P}{\partial x_i} + U_i\frac{\partial}{\partial x_j}(2\bar{\nu}S_{ij} + 2\overline{\nu' s'_{ij}} - \overline{u'_i u'_j}) \tag{A.2}$$

Now for any quantity ϕ, the following is true

$$\begin{aligned}
u_i\frac{\partial \phi}{\partial x_j} &= \frac{\partial u_i\phi}{\partial x_j} - \phi\frac{\partial u_i}{\partial x_j} \\
&= \frac{\partial u_i\phi}{\partial x_j} - \phi s_{ij}
\end{aligned} \tag{A.3}$$

Using Eq. A.3 in Eq. A.2 gives the required mean flow kinetic energy equation

$$U_j \frac{\partial K}{\partial x_j} = -U_i \frac{1}{\rho} \frac{\partial P}{\partial x_i} + \frac{\partial}{\partial x_j}(2\bar{\nu} S_{ij} U_i + 2\overline{\nu' s'_{ij}} U_i - \overline{u'_i u'_j} U_i)$$
$$- (2\bar{\nu} S_{ij} S_{ij} + 2\overline{\nu' s'_{ij}} S_{ij} - \overline{u'_i u'_j} S_{ij}). \quad (A.4)$$

A.2   Turbulence kinetic energy equation

The Navier–Stokes equation for an instantaneous flow of non-Newtonian fluid is given as:

$$\frac{\partial u_i}{\partial t} + u_j \frac{\partial u_i}{\partial x_j} = -\frac{1}{\rho} \frac{\partial p}{\partial x_i} + \frac{\partial}{\partial x_j}(2\nu s_{ij}) \quad (A.5)$$

Using the Reynolds decomposition the above equation can be written as:

$$\frac{\partial(U_i + u'_i)}{\partial t} + (U_j + u'_j)\frac{\partial(U_i + u'_i)}{\partial x_j} = -\frac{1}{\rho}\frac{\partial(P + p')}{\partial x_i} + \frac{\partial}{\partial x_j}\left(2(\bar{\nu}+\nu')(S_{ij}+s'_{ij})\right) \quad (A.6)$$

Expanding Eq. A.6 leads to

$$\left(\frac{\partial U_i}{\partial t} + \frac{\partial u'_i}{\partial t}\right) + U_j\left(\frac{\partial U_i}{\partial x_j} + \frac{\partial u'_i}{\partial x_j}\right) + u_j\left(\frac{\partial U_i}{\partial x_j} + \frac{\partial u'_i}{\partial x_j}\right) = -\frac{1}{\rho}\left(\frac{\partial P}{\partial x_i} + \frac{\partial p'}{\partial x_i}\right)$$
$$+ \frac{\partial}{\partial x_j}\left(2\bar{\nu} S_{ij} + 2\bar{\nu} s'_{ij} + 2\nu' S_{ij} + 2\nu' s'_{ij}\right). \quad (A.7)$$

Subtracting Eq. A.1 from Eq. A.7 gives

$$\frac{\partial u'_i}{\partial t} + U_j \frac{\partial u'_i}{\partial x_j} + u'_j\left(\frac{\partial U_i}{\partial x_j} + \frac{\partial u'_i}{\partial x_j}\right) = -\frac{\partial p'}{\partial x_i}$$
$$+ \frac{\partial}{\partial x_j}\left(2\bar{\nu} s'_{ij} + 2\nu' S_{ij} + 2\nu' s'_{ij} - 2\overline{\nu' s'_{ij}} + \overline{u'_i u'_j}\right). \quad (A.8)$$

Multiplying Eq. A.8 with u_i and using $k = (1/2)\overline{u'_i u'_i}$ gives

$$\frac{\partial k}{\partial t} + U_j \frac{\partial k}{\partial x_j} + u'_i u'_j\left(\frac{\partial U_i}{\partial x_j} + \frac{\partial u'_i}{\partial x_j}\right) = -u'_i \frac{\partial p'}{\partial x_i}$$
$$+ u'_i \frac{\partial}{\partial x_j}\left(2\bar{\nu} s'_{ij} + 2\nu' S_{ij} + 2\nu' s'_{ij} - 2\overline{\nu' s'_{ij}} + \overline{u'_i u'_j}\right). \quad (A.9)$$

Using Eq. A.3 in Eq. A.9 gives

$$
\frac{\partial k}{\partial t} + U_j \frac{\partial k}{\partial x_j} + u_i' u_j' \left(\frac{\partial U_i}{\partial x_j} + \frac{\partial u_i'}{\partial x_j} \right) = -u_i' \frac{\partial p'}{\partial x_i}
$$

$$
+ \frac{\partial}{\partial x_j} \left(2\bar{\nu} s_{ij} u_i + 2\nu' S_{ij} u_i + 2\nu' s_{ij}' u_i' - 2\overline{\nu' s_{ij}'} u_i' + \overline{u_i' u_j'} u_i' \right)
$$

$$
- (2\bar{\nu} s_{ij}' s_{ij}' + 2\nu' S_{ij} s_{ij}' + 2\nu' s_{ij}' s_{ij}' - 2\overline{\nu' s_{ij}'} s_{ij}' + \overline{u_i' u_j'} s_{ij}'). \tag{A.10}
$$

Time averaging the above equation leads to

$$
U_j \frac{\partial k}{\partial x_j} + \overline{u_i' u_j'} S_{ij} + \overline{u_i' u_j' \frac{\partial u_i'}{\partial x_j}} = -\overline{u_i' \frac{\partial p'}{\partial x_i}} + \frac{\partial}{\partial x_j} \left(2\bar{\nu} \overline{s_{ij}' u_i'} + 2\overline{\nu' u_i'} S_{ij} + 2\overline{\nu' s_{ij}' u_i'} \right)
$$

$$
- (2\bar{\nu} \overline{s_{ij}' u_i'} + 2\overline{\nu' u_i'} S_{ij} + 2\overline{\nu' s_{ij}' u_i'}). \tag{A.11}
$$

Using Eq. A.3, one can write

$$
\frac{\partial (u_i' u_j' u_i')}{\partial x_j} = 2 u_i' u_j' \frac{\partial u_i'}{\partial x_j} + u_i' u_i' \frac{\partial u_j'}{\partial x_j}
$$

$$
= 2 u_i' u_j' \frac{\partial u_i'}{\partial x_j}. \tag{A.12}
$$

Therefore,

$$
u_i' u_j' \frac{\partial u_i'}{\partial x_j} = \frac{1}{2} \frac{\partial (u_i' u_j' u_i')}{\partial x_j}
$$

$$
= \frac{\partial (k u_j')}{\partial x_j} \tag{A.13}
$$

Using Eq. A.13 in Eq. A.11 gives the following turbulent kinetic energy budget equation.

$$
U_j \frac{\partial k}{\partial x_j} = -\overline{u_i' u_j'} S_{ij} - \overline{u_i' \frac{\partial p'}{\partial x_i}} + \frac{\partial}{\partial x_j} \left(-\overline{k u_j'} + 2\bar{\nu} \overline{s_{ij}' u_i'} + 2\overline{\nu' u_i'} S_{ij} + 2\overline{\nu' s_{ij}' u_i'} \right)
$$

$$
- (2\bar{\nu} \overline{s_{ij}' u_i'} + 2\overline{\nu' u_i'} S_{ij} + 2\overline{\nu' s_{ij}' u_i'}) \tag{A.14}
$$

An alternative form where the Newtonian and non-Newtonian terms are collected together is:

$$U_j \frac{\partial k}{\partial x_j} = -\overline{u_i' u_j'} S_{ij} + \frac{\partial}{\partial x_j} \left(\overline{p' u_j'} - \overline{k u_j'} + 2\bar{\nu} \overline{s_{ij}' u_i'} \right) - 2\bar{\nu} \overline{s_{ij}' u_i'}$$
$$+ \frac{\partial}{\partial x_j} \left(2\overline{\nu' u_i'} S_{ij} + 2\overline{\nu' s_{ij}' u_i'} \right) - \left(2\overline{\nu' u_i'} S_{ij} + 2\overline{\nu' s_{ij}' u_i'} \right). \quad \text{(A.15)}$$

B

Appendix 2

B.1   Axial mesh refinement

The axial mesh resolution independence is checked for Newtonian and shear-thinning (PL, $n = 0.6$) fluids at $Re_\tau = 323$ for a fixed domain length of $4\pi D$ which is sufficient to decay the two point correlations of the axial velocity fluctuations to zero (see section 3.6). The mesh had 300 spectral elements of the polynomial order 12. Simulations are run for the two fluids with the number of Fourier planes $N_z = 288, 384$ and 480 giving an axial mesh solution of $\Delta z^+ \approx 28, 21$ and 16 wall units. The results varied only slightly with decreasing Δz^+ from 28 to 21 with the deviation seen for $u_z'^+$, $u_\theta'^+$, Π^+, $\mathcal{D}_{nn}^+$ and ϵ_{nn}^+ (figures B.1 and B.2). Further axial-mesh-refinement negligibly affected the results.
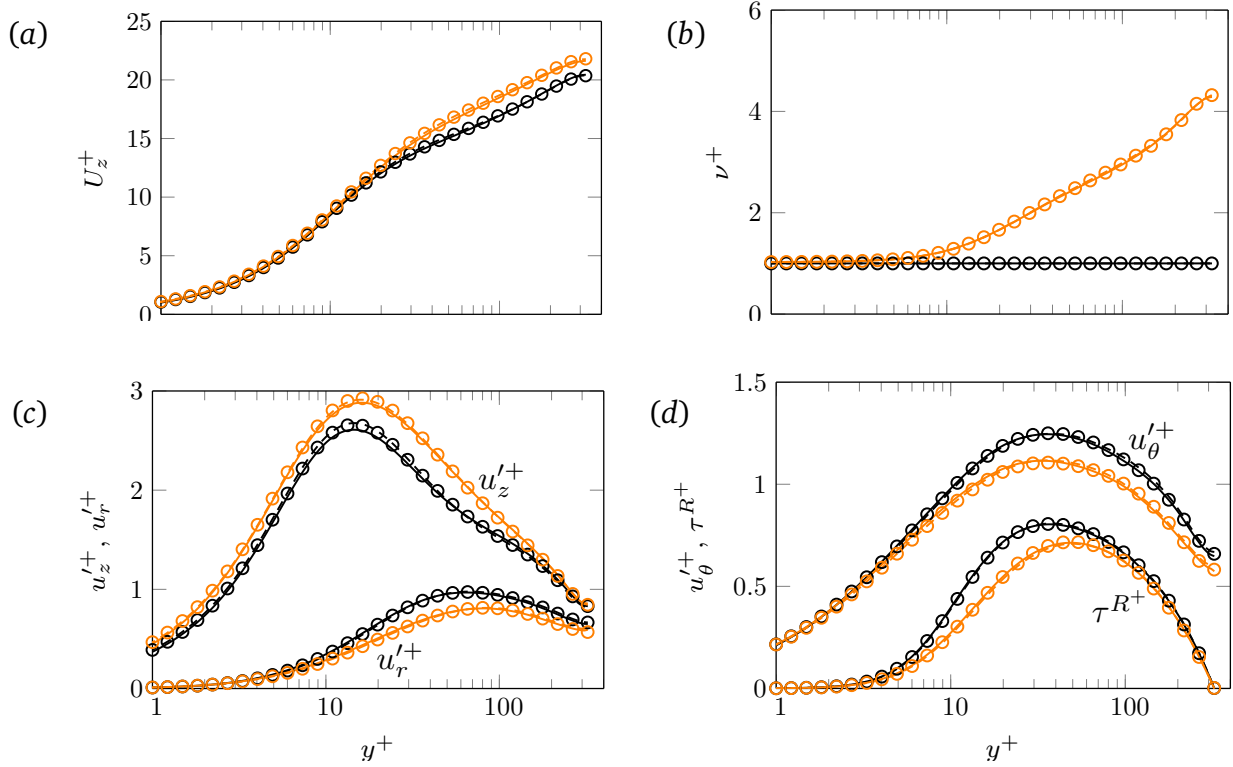
Fig. B.1 Profiles of the (*a*) mean axial velocity, (*b*) mean viscosity, (*c*) axial and the radial turbulence intensities (*d*) azimuthal turbulence intensity and the Reynolds shear stress plotted for Newtonian (black lines and markers) and PL ($n = 0.6$, orange lines and markers) fluids at $Re_\tau = 323$. The solid lines are for $\Delta z^+ \approx 28$, markers are for $\Delta z^+ \approx 21$ and dashed lines for $\Delta z^+ \approx 16$. The results of $\Delta z^+ = 21$ and 16 are indistinguishable.
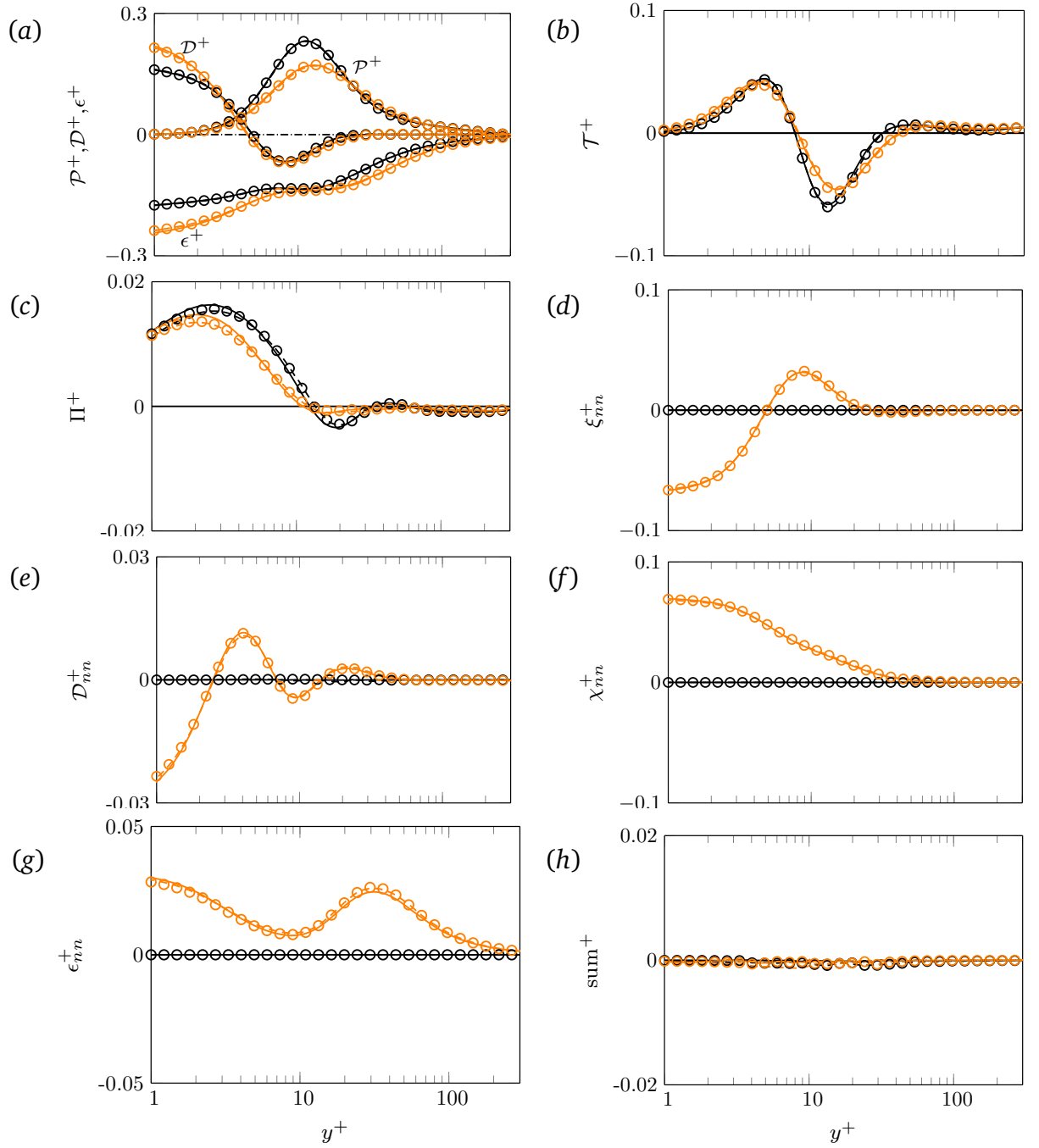
Fig. B.2 Profiles of turbulence kinetic energy budget terms plotted for Newtonian (black lines and markers) and PL ($n = 0.6$, orange lines and markers) fluids at $Re_\tau = 323$. Solid lines are for axial mesh resolution of $\Delta z^+ \approx 28$, markers are for $\Delta z^+ \approx 21$ and dashed lines are for $\Delta z^+ \approx 16$. The results of $\Delta z^+ = 21$ and 16 are indistinguishable.

B.2 Polynomial mesh refinement

The mesh resolution independence in the polynomial direction is checked only for the shear-thinning fluid at $Re_\tau = 323$. The same spectral mesh as used for checking the axial mesh resolution which had 300 spectral elements is used here. A $4\pi D$ long pipe with 384 Fourier axial planes ($\Delta z^+ \approx 21$) is used. Three values of the polynomial order, $N_p = 10, 12$ and 14 are considered, which give a near wall mesh resolution in the radial direction of $\Delta r^+ = 1.0, 0.83, 0.72$ and in the azimuthal direction of $\Delta(r\theta)^+ = 5.18, 4.31, 3.69$. As seen in figures B.3 and B.4, the results are only marginally varied with the mesh refinement in the polynomial direction. For the final mesh, $N_p = 12$ was chosen.
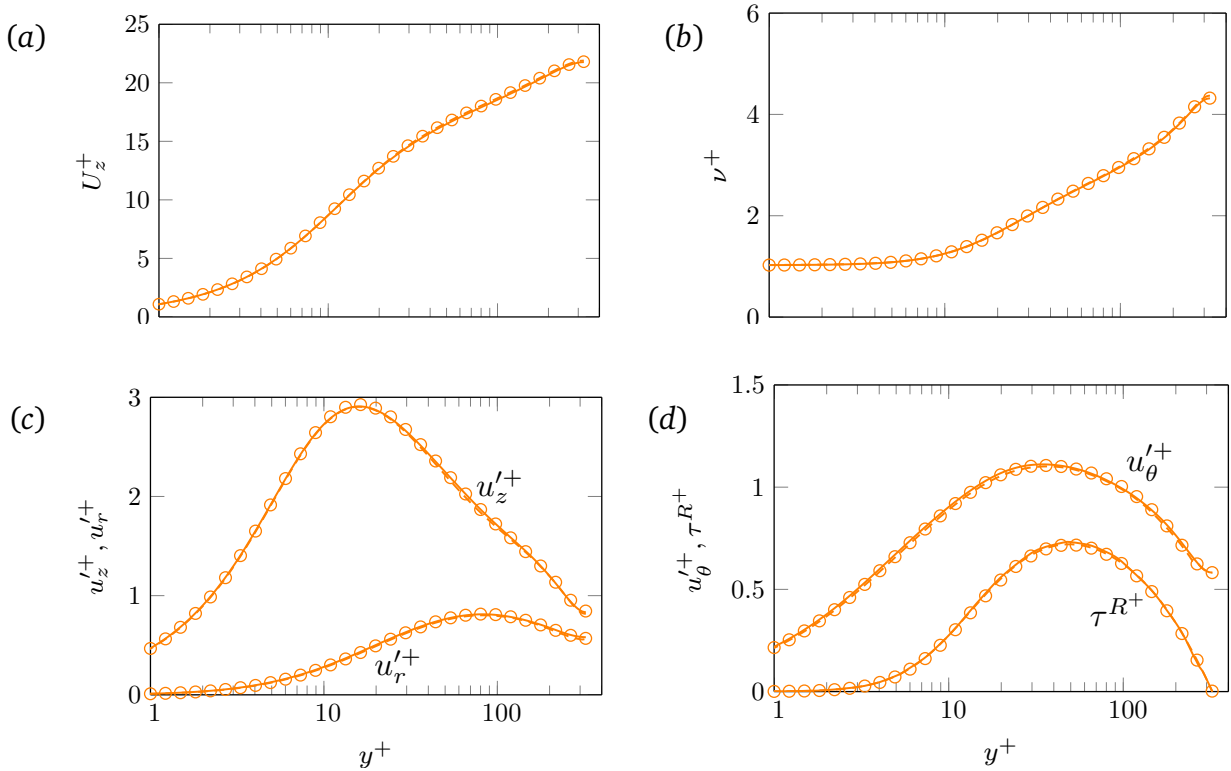

Fig. B.3 Profiles of the (a) mean axial velocity, (b) mean viscosity, (c) axial and the radial turbulence intensities (d) azimuthal turbulence intensity and the Reynolds shear stress plotted for a PL fluid with $n = 0.6$ at $Re_\tau = 323$. The solid lines are for $N_p = 10$, markers are for $N_p = 12$ and dashed lines for $N_p = 14$.
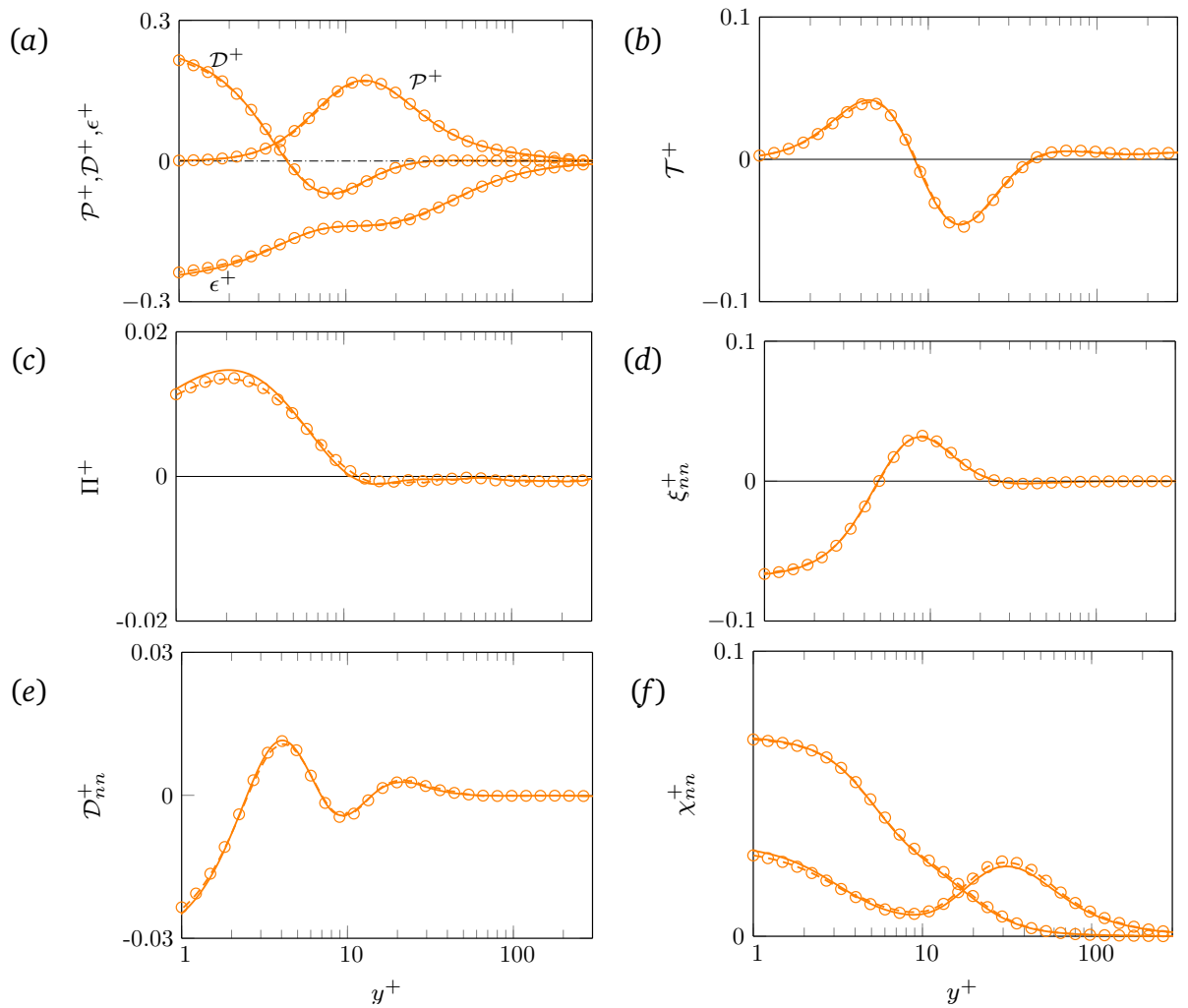
Fig. B.4 Profiles of various terms in the turbulence kinetic energy budget plotted for a PL fluid ($n = 0.6$) at $Re_\tau = 323$. The solid lines are for $N_p = 10$, markers are for $N_p = 12$ and dashed lines for $N_p = 14$.

B.3 Time step size independence

After verifying mesh resolution a time step independence is checked for the shear-thinning fluid by considering two different values of the time step $\Delta t/(\nu_w/u^{*2}) = 0.035$ and $\Delta t/(\nu_w/u^{*2}) = 0.0175$. The same spectral mesh as used for checking the mesh resolution independence is used with $N_p = 12$ and $N_z = 384$. As seen in figures B.5 and B.6, the effect of decreasing the time step size is very small and seen mainly in the profiles of the pressure gradient work Π^+ which is very small compared to other turbulent kinetic energy budget terms. A time step of $\Delta t/(\nu_w/u^{*2}) = 0.035$ is used in simulations at $Re_\tau = 323$ and reduced for higher Reynolds number simulations (see table 3.1).
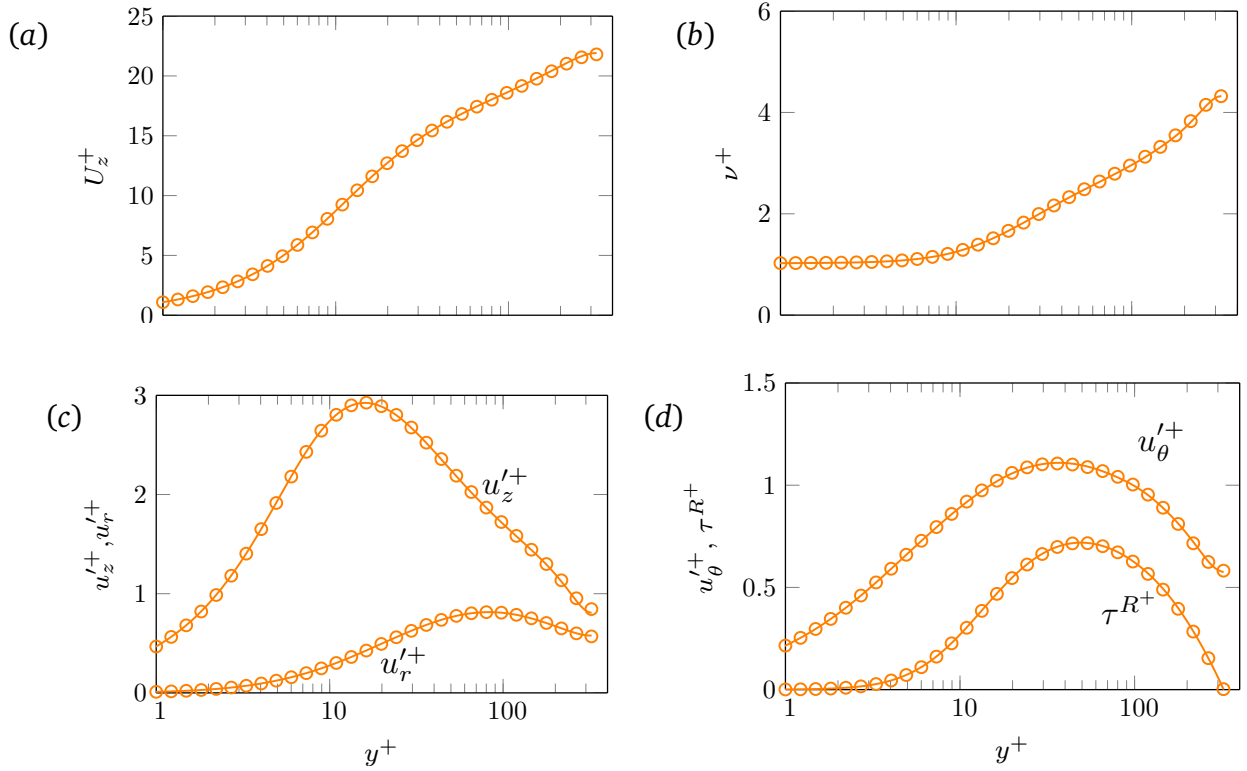

Fig. B.5 Profiles of the (*a*) mean axial velocity, (*b*) mean viscosity, (*c*) axial and the radial turbulence intensities (*d*) azimuthal turbulence intensity and the Reynolds shear stress plotted for a PL fluid ($n = 0.6$) at $Re_\tau = 323$ for two different time step sizes. The solid lines are for a time step of $\Delta t/(\nu_w/u^{*2}) = 0.035$ and markers are for $\Delta t/(\nu_w/u^{*2}) = 0.0175$.
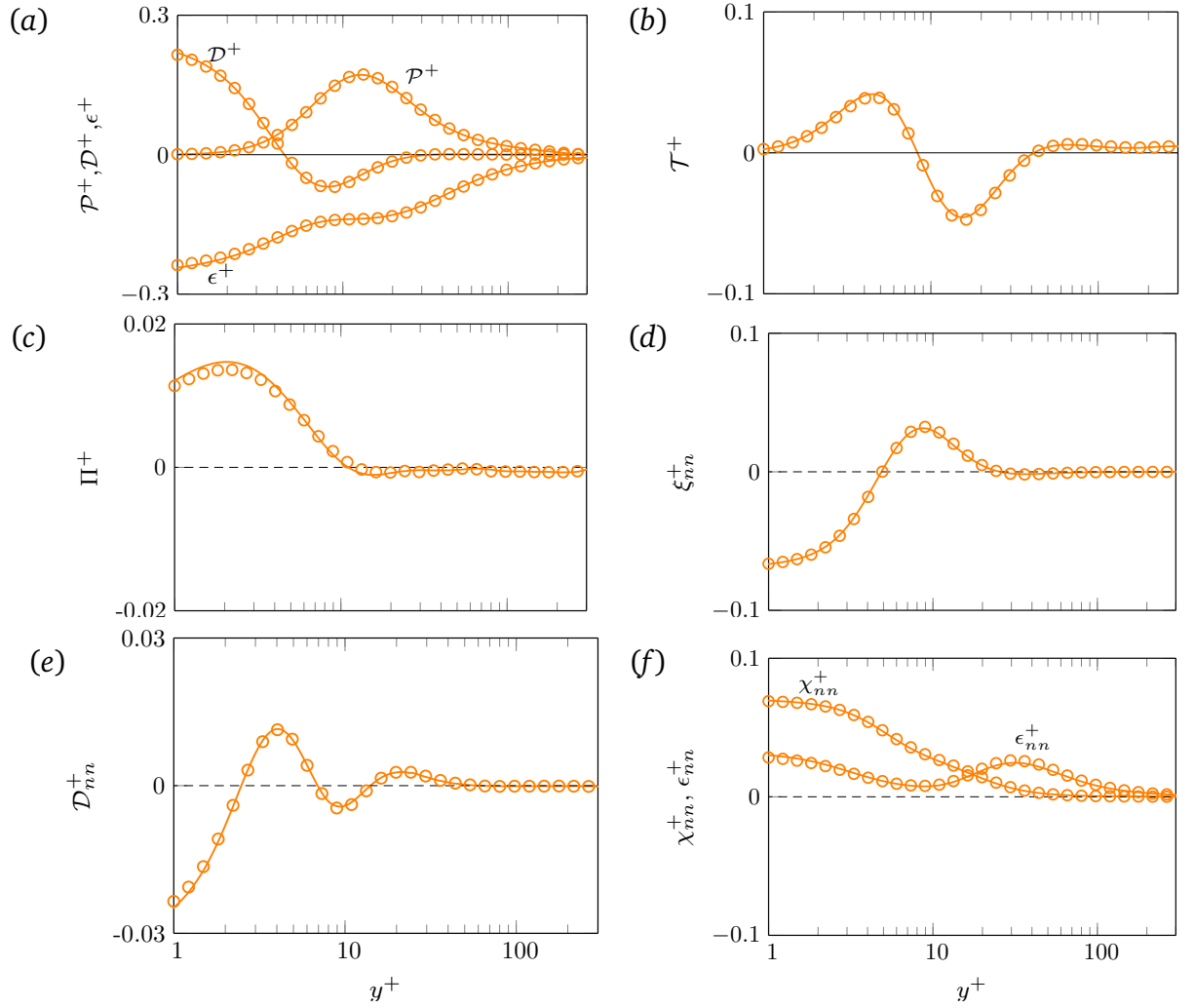
Fig. B.6 Profiles of various terms in the turbulence kinetic energy budget plotted for a PL fluid ($n = 0.6$) at $Re_\tau = 323$ plotted for two different time step sizes. The solid lines are for a time step of $\Delta t/(\nu_w/u^{*2}) = 0.035$ and markers are for $\Delta t/(\nu_w/u^{*2}) = 0.0175$.

175